Gas-Phase Detection Methods Using Diode Lasers

A thesis submitted for the degree of Doctor of Philosophy

by

Stuart George Baran

Balliol College, University of Oxford

Trinity Term, 2009

Gas-Phase Detection Methods Using Diode Lasers

Stuart George Baran, Balliol College

A thesis submitted for the degree of Doctor of Philosophy

Trinity Term, 2009

Abstract

Diode lasers are a convenient and economical source of near-infrared radiation, which may usefully be applied to a host of different sensitive detection methods; this thesis presents novel extensions of these methods, making use of the favourable characteristics of this type of light source. The first part of this thesis details the development of an optical feedback cavity-enhanced absorption spectroscopy (OF-CEAS) apparatus, including the development of the optical system, the sample handling, and the electronics for feedback phase control. A preliminary demonstration of the system is reported, presenting the detection of atmospheric water absorptions close to 1596 nm. Optimisation and application of the OF-CEAS spectrometer are then demonstrated, after which the spectrometer is applied to the sensitive detection of carbon dioxide absorptions suitable as a diagnostic aid in identifying *Heliobacter pylori* infection. A time-normalised α_{min} value of $5.8 \times 10^{-9}\mathrm{cm}^{-1}\mathrm{s}^{1/2}$ was measured for these spectra.

Further optimisation of the system leads to an ultimate detection sensitivity of $1.42 \times 10^{-9}\,\mathrm{cm}^{-1}\mathrm{s}^{1/2}$, measured on absorption transitions in acetylene close to 1532 nm. In order further to characterise the performance of the OF-CEAS system, analogous experiments are presented using the OF-CEAS setup and a standard diode-laser cavity-enhanced absorption spectroscopy (CEAS) apparatus. Detection is carried out on the P(6) line of the $\nu_1 + \nu_3$ vibrational band of the mixed isotopologue of acetylene, $^{12}\mathrm{C}^{13}\mathrm{CH}_2$. Direct comparison is made between the sensitivities of the two methods, and in light of this the suitability of each technique for detection in different environments is considered.

The well-characterised and consistent frequency scale which is inherent to the OF-CEAS technique is then applied to a line shape analysis for the presented absorption spectra. Pressure-broadening coefficients are determined for selected absorptions in the $\nu_1 + \nu_3$ band of acetylene. In spite of the low resolution associated with this technique, this accurate frequency scaling allows observation of subtle line shape effects such as Dicke collisional narrowing using the data presented in Chapter 3 for the R(60) line in the $3\nu_1 + \nu_3$ vibrational band of CO_2. These effects are quantified through use of a Galatry fit to each absorption spectrum. The statistical significance associated with the use of such a model, and the physical meaning of the results, are examined and discussed.

An alternative strategy for increasing the sensitivity of a diode-laser-based gas monitoring technique lies in moving detection to the mid-infrared region, where the absorption cross-sections are generally larger. With this motivation, difference frequency generation is presented, to produce radiation close to 3.5 μm which is then applied to a series of different enhanced spectroscopy techniques. The optimal sensitivity, of 32 ppb NO_2 at 45 Torr total sample pressure, was achieved using wavelength modulation spectroscopy. The different techniques are compared and possible improvements to them are put forward.

Finally, proof-of-principle work is presented seeking to combine the enhanced circulating power associated with the optical-feedback-locked techniques and nonlinear optical techniques to move detection to a more favourable spectral region. Light close to 429 nm is generated by second harmonic generation in a crystal of potassium niobate, with resonance-enhancement afforded by a feedback V-cavity of the sort employed in OF-CEAS. The potential of such a system for diode-laser-based generation of blue and ultraviolet light is demonstrated and discussed, along with improvements that might be implemented to increase the efficiency of the system.

Acknowledgements

This thesis simply would not exist without the kindness, help and moral support I have enjoyed from so many wonderful people over the past four years. Firstly, I must thank Gus for the chance to work in such a friendly and interesting group. I am thoroughly indebted to Grant for all of his advice and skilful project-steering, and especially for all the reading of drafts of this thesis and the pieces of work that led up to it. Rob also deserves unending thanks: for his quite supernatural ability to rectify the most vexatious of experimental problems with a frustratingly instantaneous touch, as well as his kind and patient answers to my (no doubt trivial) questions over five years!

Nicola van Leeuwen is someone without whom the OF-CEAS experiment would never have come into being, and I must thank her for her patience, her guidance and her electronics-related expertise. Our very own Crying Dutchman (it would be environmentally unfriendly to name him in full) has been an invaluable support, especially in the last twelve months. For introducing me to the hypnotic qualities of eccentrically-matched stripes and to the concept of infinite volume (have you seen his suitcase...?) I shall always be grateful. Graham's computational wizardry, and the childish Mrs-B-pranking humour we have shared, have also been integral to the completion of the work reported hereinafter.

Sarah T has always been a wonderful source of inappropriate gossip, sympathetic nods, and caffeinated drinks: coffee and gin have got us this far, and I certainly see no reason to give up on either! Mrs B, my nano-northern EndLab co-inmate, has enriched my life with her mellifluous vowel-sounds and her unfailingly humorous experimental setup, and for that I will remain in her debt. Luca's help with all of the NO_2 work, just like his company and boundless supply of Italian tongue-twisters, has been invaluable. Sarah "Gary" Gowrie deserves a special mention for teaching me to defend myself, *weegie-style*, and for her quite extraordinary intonation of words to the effect of "somewhat unusual." Everyone in this group has made it a more fun place to be, and so my thanks go to all the other Hancock-Ritchie group members from the past five years, and especially to the present cohort: Mike, Lineke, Michelle, Tom, Beth, Rich, and an unending supply of entertaining Part IIs. I have worked directly alongside some wonderful Part II students during my doctorate, and my thanks are due to Lindsay, to Katy and to Ann for their company, hard work and support. I must also thank the group's pet monkey and the West British Brogue [more about *pink noise sources* in section 1.4], for their advice about LaTeX, Macs, coffee, Moleskine diaries and other such, as well as for generally cheering me

up in the last few months whenever I've been feeling blue. Or possibly green, Lee.

Much of my experimental work has been aided considerably by the electronics and workshop staff here at the PTCL; we are very lucky to have you, and my particular thanks must go to Andy for so carefully crafting the OF-CEAS cell, and to Kevin for his limitless patience in the quasi-infinite iterations of designing, building and re-building the feedback phase control electronics.

I have been lucky enough to enjoy support from a wide range of people outside of this group, too. Professor Mark Brouard is a kind, brilliant and inspiring man; I will be neither the first nor the last to thank him for his excellent and careful tuition as an undergraduate, as well as his continued kindness and support since. Professor Richard Compton was kind enough to let me loose teaching his students, and was always there in support whenever I needed it; the care that he takes over his students – and, indeed, his academic assistant – has been wonderful to see. Teaching at St John's has been an unalloyed pleasure, and I must thank all my students for their company, their interest and their hard work; I can only hope that my tutorials successfully raised their glycaemic indices, if not their finals marks...

My musical exploits in and around Oxford have kept me as close to sane as I can ever claim to have been, and my friends in that sphere – Mads, Charlie, Rahul, Charlotte, James, John, Nick, Louise, Gabi and many more – have been a great source of fun, noise, food, wine and moral support. The same can be said of Barbara Lauriat and Dr Justine Pila in the Law Faculty; thank you both for placing your faith in me, and for allowing me the opportunity to work with some amazing people in the IP world; I hope that I will be able to justify the risk you took on me in the coming years!

Finally – indeed, ultimately – I must thank my family, and mostly my Mum and Dad, for everything they have been and continue to be in my life. From their support of the irritatingly noisy child with the goldfish-like attention span, to their support of the irritatingly noisy adult with the goldfish-like attention span, they have always stood right behind me. In the face of my apparently-terminal lack of gainful employment, they continue to be nothing but encouraging, and for that I could never thank them enough. This thesis is theirs.

Stuart Baran

Oxford, August 2009

Contents

Chapter 1

Introduction

Optical detection methods offer a convenient, sensitive and selective tool to understand the composition and environment associated with a gas sample. As such, they have provoked much fundamental study, and find applications across many fields. In light of this, the present chapter offers some context for the experimental work reported in this thesis. Specifically, the motivations for gas phase detection are examined and the particular advantages associated with lasers for use as probe light sources are discussed. Diode lasers lend themselves especially well to spectroscopic measurements; the reasons for this are examined in the context of a description of this type of light source. The physical basis of absorption spectroscopy is outlined, along with a survey of selected other laser-based detection techniques. Other, non-optical, types of detection technique are then discussed and compared with the spectroscopic approaches. Finally, a brief examination of noise and the expression of detection sensitivities precedes an outline of the scope of this thesis.

1.1 Quantitative Detection in the Gas Phase

Accurate monitoring of trace gases is often required in a variety of contexts; in particular, gas detection techniques have been applied to process monitoring [1–3] and to environmental and atmospheric sensing [4–6], as well as monitoring of biological processes [7] and medical diagnostics [8–10]. Trace gas monitoring is a

vast area of research [2, 11], and this section serves merely to highlight some pertinent examples of current techniques and applications.

In the process industry, rapid, sensitive, and selective sensing is necessary to ensure that quality standards are maintained in the product of a chemical process. During chemical vapour deposition processes, for instance, used for applying thin layers of tin oxide onto glass for solar cells and the like, a complex series of reactions is triggered by the initial heating step, and careful monitoring of this chemical process is required [3]; the non-invasive nature of optical analysis techniques lends itself particularly well to such an application.

Atmospheric sensing affords us a greater understanding of the chemistry controlling the composition of our surroundings; such fundamentally-motivated detection work is exemplified by the simultaneous measurements of N_2O, CH_4, CO, HCl and NO_2 carried out as part of the ALIAS-II mission [12]. Some environmental detection work also carries an economic motivation: the system demonstrated by Bishop and Stedman [13] monitors the composition of automobile exhaust, which is used to determine the environmental score (and thereby, taxation level) associated with a particular vehicle.

Biological and medical diagnostics applications based upon swift, accurate medical tests such as the Urea Breath Test (UBT) for *Heliobacter Pylori* infection [10] exploit all the advantages associated with non-invasive gas analysis methods. All these applications share a need for rapid, economical detection that is selective, sensitive and robust. The methods introduced in this chapter, and particularly those developed in the work presented later in this thesis, seek to achieve these aims.

1.2 Lasers in Gas Detection

1.2.1 Lasers

In a generic two-level system there are essentially three types of transition. *Absorption* is a transition from the lower energy level to the upper level, where the

absorbing particle takes up a photon; its rate is proportional to the energy density ($\rho(E)$) of photons incident on the absorber, on the population in the lower level, N_1, and on the Einstein B_{12} coefficient. *Spontaneous emission* is a random process whereby a particle in the upper level spontaneously emits a photon, and undergoes a transition to the lower level. Since this process is not driven by incident radiation, the rate of spontaneous emission is not dependent upon an energy density term, but merely proportional to the upper level population, N_2, and the Einstein A coefficient; the resulting emission adopts essentially random phase and direction, but has a wavelength resonant with the energy gap corresponding to the transition. The third class of transition is *stimulated emission*, where the emissive event is driven by incident radiation; the rate of stimulated emission is proportional to $N_2 B_{21} \rho(E)$, and the resulting radiation shares its direction, phase and wavelength with the driving radiation. It is this type of emission which is the basis of laser action.

If a *population inversion* can be established within a medium, so that the *gain condition* is satisfied:

$$\frac{N_2}{g_2} > \frac{N_1}{g_1} \tag{1.1}$$

where $g_{1,2}$ are the respective degeneracies of the levels, then the number of stimulated emission events in that medium can exceed the number of absorption events. As such, coherent radiation consistent with the wavelength, direction and phase of the initial (spontaneous) stimulating radiation results. This emitted radiation is then typically amplified through use of an optical resonator (see section 2.1). Lasers can therefore provide a useful source of intense, coherent radiation ideal for a spectroscopic experiment.

1.2.2 Absorption Spectroscopy

Absorption spectroscopy is based upon the measurement of the attenuation in the *intensity* of an electromagnetic (*em*) probe wave as the associated radiation is passed through the medium under study. Classically, this can be considered as the induction of electron oscillations in the absorbing medium by the probe *em* wave,

inducing dipoles oscillating in resonance with the probe field. Destructive interference between the field induced in this way and the probe field leads to a quantifiable depletion in the probe wave's intensity: *absorption*.

The time-dependent electric field associated with an *em* wave travelling along the $\vec{z}$-direction has the form [14]:

$$\mathrm{E}(z,t) = E_0 \exp\left\{i(\omega t - kz)\right\} \tag{1.2}$$

in which E_0 is the electric field amplitude, ω is the angular frequency of the wave, and k the corresponding wavevector. The wavevector accounts for the effect of the refractive index, n of the medium through which the probe radiation is passed, and has the form:

$$k = \frac{2\pi n}{\lambda} \tag{1.3}$$

In fact, the refractive index is best considered as a complex quantity, $n = n' - i\kappa$; correspondingly, the complex wavevector along $\vec{z}$, defined in terms of a reference value k_0, becomes $k_n = k_0(n' - i\kappa)$. When this is substituted into equation 1.2, the real part of the refractive index associates with the phase, and the imaginary part with the amplitude [15]:

$$\mathrm{E}(z,t) = E_0 \exp\{-k_0\kappa z\} \exp\left\{-i(\omega t - k_0 n' z)\right\} \tag{1.4}$$

The imaginary part of the refractive index determines the level of absorption, and the real part determines the change in the phase velocity of the probe radiation; n' is called the *chromatic dispersion* term.

Quantitative description of such absorption of light is encapsulated within the Beer-Lambert law [16]:

$$\frac{I_t}{I_0} = \exp\{-\alpha(\omega)L\} \qquad : \alpha = N\sigma(\omega) \tag{1.5}$$

wherein I_t and I_0 respectively represent the transmitted and incident light intensi-

ties, L is the absorption path length, and $\alpha(\omega)$ is the frequency-dependent absorption coefficient, itself composed of the absorber number density (N) and the frequency-dependent absorption cross-section, $\sigma(\omega)$, which is also dependent on the physical environment in which the absorber is found. For a given transition, the *integrated* absorption cross-section is typically quoted; this is the integral of the peak absorption cross section with respect to frequency (or, more generally, wavenumber) across the entire transition. As such, it is invariant to changes in line *shape*, and is a constant for a given line; it generally takes units of $\mathrm{cm^2cm^{-1}molec^{-1}}$.

1.2.2.1 Differential Optical Absorption Spectroscopy (DOAS)

In an atmospheric setting, absorption spectroscopy measurements are somewhat more complex in implementation, since there are often several species present whose spectra overlap, the collisional environment may significantly broaden spectral lines, and scattering by aerosol particles may also complicate the experiment [17]. In order to be able to identify a particular species, measurements need to be taken on significantly more than a single spectral line; observation over a broad spectral region – typically several tens of nm – improves the ability to distinguish between different absorbing species, and one such approach is *differential optical absorption spectroscopy* (DOAS) [17–20].

Scattering contributions to the spectrum typically exhibit a relatively smooth dependence upon wavelength, so that a significantly-structured spectrum viewed over a broad wavelength-range can straightforwardly be separated from the scattering signal by a combination of a high-pass filtering method and fitting of a simulation based upon known absorption cross-sections for the species under study. A background signal is taken either simply by recording the spectrum of the light source with the same detector, or by recording a spectrum knowing the absorber concentration within the air sample being studied [17].

This technique is useful for simultaneous monitoring of several atmospheric species. However, it is generally unsuitable for making local measurements; the

measurements are of the *average* absorption, typically over a long path length, and so no information about the local distribution of absorbers is included [21]. However, the ability to implement this technique over such long path lengths is what gives this method its sensitivity [21]; one implementation [18] of DOAS over 20.6 km for measurement of NO_2 and other atmospheric species gave an NO_2 detection limit of 40 pptv in 5 minutes of integration. However, since the technique is implemented over such long path lengths, this places demands on the minimum power of probe radiation required; in the NO_2 detection work of Harder *et al.* [18], for example, a 1000 W Xe-arc lamp was employed.

1.2.3 Some Other Laser-Based Detection Techniques

1.2.3.1 Laser-Induced Fluorescence (LIF)

Laser-induced fluorescence [22–24] (LIF) is based on a measurement of the spontaneous fluorescence spectrum after selective laser excitation of a molecular absorber. Careful tuning of the excitation wavelength may give rise to emission from a single upper level, making for a much simpler, clearer fluorescence spectrum compared to what might be observed after simultaneous emission from several upper states [16]. This technique is therefore inherently background-free, and in use LIF functions as a useful and highly sensitive form of spectroscopy. Although the detection sensitivity varies with the absorption cross-section associated with the species being studied, values on the order of $10^6\,\mathrm{molec\,cm^{-3}}$ are not uncommon [5, 25]. However, it is not so universal in application as absorption spectroscopy, since a sample with a fluorescent upper state (and an appreciable quantum yield associated with it) is an obvious prerequisite for LIF measurements. Competing pathways for de-excitation, such as collisional quenching or pre-dissociation, mean that not every excited electronic state gives rise to appreciable fluorescence. Additionally, the fluorescence rates at longer wavelengths are generally much slower, and so this technique is generally implemented in the ultraviolet or visible spectrum regions. LIF has been applied to measurements of many small molecules, especially forming the basis of

many reaction dynamics measurements on nascent species [23, 24, 26], though the need for very careful calibration and avoidance of collisional quenching of the sample present difficulties for its implementation as an atmospheric detection method for determination of *absolute* concentrations.

1.2.3.2 Photo-Acoustic Spectroscopy (PAS)

Photo-acoustic spectroscopy exploits the *photo-acoustic effect*, discovered by Alexander Graham Bell [27]; he found that a thin disc exposed to mechanically-chopped light emitted sound. This was found to work using sunlight, infrared and ultraviolet light. A photo-acoustic spectrum essentially comprises a plot of the amplitude of the sound against the wavelength of the light. Absorption of the *em* wave increases a sample's internal energy, with this energy then being transferred by collisions within the sample. Since the sample is effectively heated, for a constant-volume sample, the local pressure must increase. If the radiation source is modulated or pulsed, then, compressions and rarefactions in the gas are brought about, giving rise to an acoustic wave that can be detected at a microphone in the sample chamber. The amplitude of the sound is proportional to the level of heating, which is related to the degree of absorption of the light. An absorption spectrum can be inferred from a plot of sound intensity against laser wavelength. This can be a very sensitive form of spectroscopy, and is capable of measurements in all phases of sample [28, 29]. Minimum absorption coefficients on the order of $10^{-10}\,\mathrm{cm}^{-1}$ have been achieved using this technique [30]. Further enhancement to PAS has also been demonstrated by use of an appropriately-resonant cell [31]. Disadvantages associated with the use of this technique are related to its sensitivity to ambient conditions; the temperature, for example, must be very carefully controlled in order to make an accurate measurement, and the need to place the microphone very close to the sample may present experimental limitations for the use of flames and strongly heated samples.

1.2.3.3 Coherent anti-Stokes Raman Spectroscopy (CARS)

Raman Spectroscopy relies upon the inelastic scattering of light incident upon a molecule, whereby the incident radiation is shifted in energy by an amount consistent with the internal energy level spacings within the molecule. Raman spectroscopy can be considered as a two-photon process, proceeding *via* a virtual upper state [14–16, 32]. However, only a small proportion of the incident photons typically engage in such Raman scattering, and one of the principal difficulties associated with the technique is separating the very weak Raman signal from the high-intensity background of Rayleigh-scattered radiation.

Coherent Anti-Stokes Raman Spectroscopy (CARS) seeks to mitigate that disadvantage, presenting a multi-photon *stimulated* Raman technique which produces mutually-coherent signal waves. Under conditions where the incident radiation and the resulting Raman-scattered radiation are both at high intensities, the molecules' simultaneous interactions with two *em* waves must be considered. Both laser radiation at frequency ω_L, and Stokes radiation (at the difference frequency $\omega_L - \omega_{vib}$, where ω_{vib} corresponds to the vibrational transition being probed in the molecule) are provided, and now interact with the molecule. When subject to both these waves, a non-linear induced polarisation results, with terms in the (Stokes) difference frequency $\omega_L - \omega_{vib}$, and the (Anti-Stokes) sum frequency $\omega_L + \omega_{vib}$. Provided that the correct phase matching is achieved, a significant intensity of coherent Anti-Stokes radiation results. Spectroscopic study based on this principle is still an area of current interest [33], and the technique finds application to detection problems in gaseous and liquid phases, including flame thermometry [34], and femtosecond time-resolved measurements [35].

1.2.3.4 Degenerate Four-Wave Mixing (DFWM)

A related non-linear technique combines three coherent and identical laser beams to generate a fourth coherent beam of radiation. Degenerate four-wave mixing (DFWM) [36, 37] involves the crossing of two laser beams at a small angle, producing

a fringe pattern. This fringe pattern brings about a corresponding modulation, in space, of the populations of ground and excited states in an absorbing sample. The third laser beam is then scattered by Bragg diffraction at this effective grating, giving rise to a signal beam; this signal beam is then detected to produce the absorption spectrum. The coherent character of the signal light means that detection can be carried out at some distance from the sample chamber, remotely, and so this technique lends itself well to hostile environments such as flames and plasmas [25, 36]. Nonetheless, neither implementation of the setup nor analysis of the resulting spectra to find quantum state populations is straightforward. Furthermore, the signal scales as the square of the sample concentration, and so DFWM may not be ideally suited to the detection of trace species. In spite of these difficulties, the technique has been applied to trace species detection [37], as well as to flame analysis [36], photolysis products and combustion analysis [38].

1.2.4 Diode Lasers as Spectroscopic Sources

Diode lasers – or *semiconductor lasers* – are those which have a p-n semiconductor diode as their active medium [14–16, 39]. As current is supplied to the diode in the forward direction, electrons are transported from the n-section to the p-section, and "holes" travel in the converse direction. At the p-n junction, the electrons and holes can recombine radiatively – the electrons fall from the conduction band to the valence band, and the emitted recombination energy may be released as an *em* wave. The line width associated with this (spontaneous) emission is on the order of several cm^{-1}, and its wavelength is determined by the band gap (the energy difference between the valence and conduction bands). The choice of semiconductor and the concentration of introduced dopants therefore have a strong influence on the emitted wavelength. A schematic illustration of a semiconductor diode laser system is shown in Figure 1.1.

This is an example of a *homojunction* laser, such as might be constructed from gallium arsenide. A more efficient laser medium results when layers of different

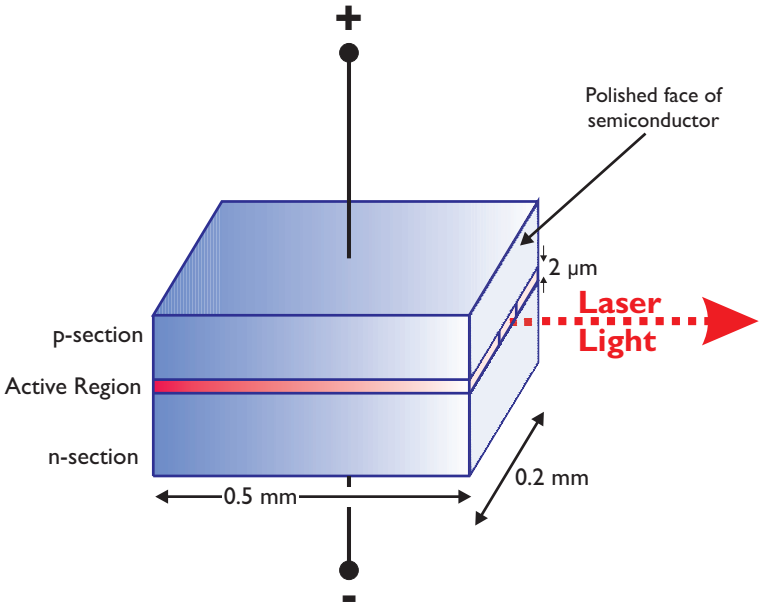

Figure 1.1: Simplified representation of a semiconductor diode laser, adapted from reference [15].

semiconductor materials are used and meet at the diode junction - this is a *heterojunction* arrangement [40]. Most commonly, a *double heterojunction* chip is used, with a thin (typically $\sim 2\,\mu m$) layer of one semiconductor such as GaAs sandwiched between cladding layers of another, such as AlGaAs; this sort of arrangement benefits from a wave-guiding effect as well as from enhanced carrier confinement owing to the greater AlGaAs band-gap. In each setup, donor and acceptor concentrations are present in sufficient concentration to place the Fermi level in the conduction band for the n-type layer, and in the valence band for the p-type layer. Forward-biassing of the junction (application of an external potential that renders the p-type layer more positive, and the n-type layer more negative) modifies the band energies, so that in a heavily-doped junction the electron concentration in the bottom of the conduction band may substantially exceed that in the top of the valence band. This amounts to establishment of a population inversion in the medium, and stimulated radiative recombination then forms the basis of the laser action.

The laser resonator in such a diode system often simply comprises the polished faces of the semiconductor crystal. However, the high refractive index of the semi-

conductor material and the large gain associated with such lasers often mean that such polishing is not necessary; for example, for gallium arsenide $n = 3.2$, corresponding to a Fresnel reflectivity of 0.32. Alternatively, a more effective resonator can be created by engineering a region of periodically-varying refractive index within a thin layer added to each end of the semiconductor crystal; this is called a *Bragg reflector*, and the construction of the Bragg reflector controls the reflected wavelength. The period of the Bragg reflector region, Λ, gives rise to a phase condition called the *Bragg condition* [15]:

$$2n_{eff}\Lambda = m\lambda \tag{1.6}$$

where n_{eff} is the effective value of the refractive index and m is an integer. An appropriate choice of Bragg period can therefore select a single mode for laser action. In a distributed Bragg reflector (DBR) laser there may be a region of periodically-varying n at each end of the crystal, encasing the active medium, or alternatively the periodic refractive index alternation may be extended throughout the gain medium. In the latter type of setup, resonant modes of the laser cavity are restricted to those additionally satisfying the Bragg condition; this is called a *distributed feedback* (DFB) laser.

Diode lasers are available over an increasing range of wavelengths, and the telecommunications industry has driven their efficient and economical construction in the near-infrared region particularly. Sources in this region are readily available, compact and robust, with DFB lasers in particular giving a reliably single-mode output over their tuning range. The selection of the particular frequency emitted by the diode laser is achieved *via* a series of strategies: firstly, as mentioned above, the choice of semiconductor and the level of doping are important factors determining the emitted frequency. Additionally, injecting light from a second laser – *injection locking* – may stimulate emission on a particular frequency; use of the resonant light from an external optical cavity, or the DFB and DBR arrangements present alternative methods. A diode laser may be tuned right across its gain profile by placing

the gain medium within an external cavity. The cavity further comprises a grating mounted so as to diffract a small amount (typically $\sim 15\,\%$) of the incident power into its first-order beam, directed back into the laser medium; this is illustrated schematically in Figure 1.2. Accordingly, this frequency-filtered feedback drives the laser emission increasingly monochromatic, and laser line widths as low as 10 kHz may be achieved [15, 40]. External cavity diode lasers (ECDLs) of this type can achieve tuning across a spectral range up to $\sim 100\,\text{nm}$, compared to the one or two nm typically achieved using a DFB laser. However, slightly more care may need to be taken with an ECDL to ensure a consistent, single-mode output, whereas the DFB output is typically very reliably single-mode right across its output range.

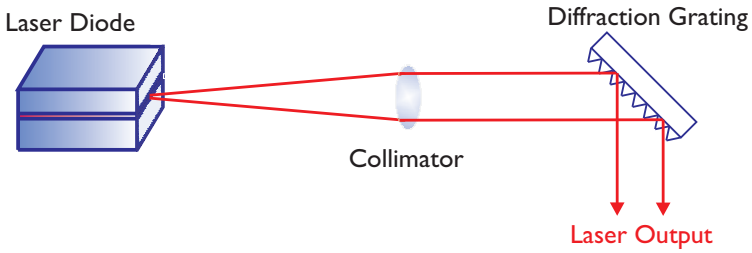

Figure 1.2: Schematic representation of an external cavity diode laser (ECDL).

All of these features of diode lasers, associated with their compactness, robustness, tunability, reliability and economy, make them ideal sources for spectroscopic detection experiments [41–44]. The work of this thesis seeks to exploit and build upon these advantages of diode laser radiation sources in the construction of sensitive, selective and robust detectors relevant to a variety of important analytical challenges.

1.3 Other Analytical Techniques

Other, non-optical, techniques are also in widespread use for gas-phase detection problems. One of the most commonly-implemented techniques is mass spectrometry [45], in which the species under study is ionised, typically by a process such as elec-

tron impact. The ions are accelerated under an electric or magnetic field, whereby they are sorted by their mass-to-charge ratio, m/z, and then detected, typically according to their time-of-flight. Electrospray ionisation allows movement of the ions already present in a liquid solution into the gas phase, so when combined with an MS technique it can present a method applicable to solution-phase detection as well as detection of gaseous species; this technique has been applied to biologically-relevant solution studies [46], and attracted a Nobel Prize in 2002. Since the species under investigation is typically fragmented during the ionisation process, the m/z information associated with the various fragments can give information about the structure of the species under study. Mass spectrometry measurements can be exceptionally sensitive, but are expensive and cumbersome in implementation. Non-covalent interactions within the sample are often disrupted by the ionisation process; indeed, the mass spectrometry technique's invasive nature, and the size and expense associated with the instrumentation, mean that it does not lend itself well to several process monitoring applications.

Electrochemistry offers an alternative detection method: electrochemical gas detectors measure the concentration of a sample gas by oxidising or reducing that gas at an electrode, and measuring the resulting current. Typically, the sensor comprises a set of electrodes composed of a precious metal and attached to a porous membrane, through which the air to be monitored may pass into the electrolyte (typically a mineral acid) [47]. The magnitude of the resulting current depends on the concentration of the species being oxidised or reduced. Normally, the sensors are designed so as to incorporate a diffusion-limited supply of gas to the sensor. An external circuit maintains the potential difference across the sensor; an equal, opposite electrochemical reaction takes place simultaneously at the working electrode and the counter electrode [48]. Such systems have been applied to gas detection problems of interest, such as the economical detection of toxic carbon monoxide in air. However, there may be considerable problems of selectivity associated with them, and generally only those species which are electrochemically active (and will

undergo the necessary redox transformation) may be detected [49]. As well as the problems of selectivity, blocking or poisoning of an electrochemical system may lead to (sometimes permanent) damage of such a system [47]. Nonetheless, electrochemistry may offer an economical approach to some detection problems, and Warburton [47] reported a steady-state sensitivity of 0.11 μA/ppm of carbon monoxide.

A further class of detection methods lies in chemiluminescence methods [50]; these are based upon bringing about a chemical reaction producing a photochemically-excited product which fluoresces or phosphoresces, and measuring the intensity of that luminescence. This technique has successfully been applied to several detection problems, including the detection of nitrogen oxides [51] and of gaseous isoprene [52]; the latter experiment exhibited an isoprene sensitivity of 400 pptv for a signal-to-noise ratio of 2 and with a time constant of 5 s. However, the indirect nature of these measurements means that very careful calibration is necessary before absolute concentrations of the sample species may be inferred.

1.4 Noise and Detection Sensitivity

The ideal output of a photodetector in an optical detection system is absolutely and directly proportional to the incident radiation power, and is exactly zero when no signal is incident on the photodetector. In reality, there is often a non-zero signal even with no optical input to such a device - this is termed the *dark current*. Further, even for an "optimally-constructed" photodetection system, there are fundamental sources of noise associated with both the dark current and the signal output; the laser will also, no matter how well constructed, be subject to fundamental noise which distorts its output.

A first source of noise is inherent to the quantised nature of light; since we consider the light as a series of discrete photons, the quantum fluctuations in the photon stream impose a fundamental electrical noise limit on photodetection. If the stream of photons is randomly-arranged, then we can use Poisson statistics to describe the number of photons, m, arriving at the detector in a given time interval

with respect to the mean rate, n [15]:

$$P(m) = \frac{n^m \exp\{-n\}}{m!} \tag{1.7}$$

Under such a model the noise level is simply given as the square-root of the mean, n. A term is generally included to describe the *quantum efficiency*, η, of the photodetector, so that the randomness in the detector *output* is given as the statistical fluctuations in a photon stream now described by ηn, with an associated noise level of $\sqrt{\eta n}$. This type of noise, ordinarily called the *shot noise*, presents a fundamental limit on the detection sensitivity for an optical monitoring system, associated directly with the photodetector and not influenced by the signal. The shot-noise-limited absorbance for a direct absorption measurement is given by [53]:

$$(\alpha L)_{min} = \left(\frac{2eB}{\eta P_0}\right)^{1/2} \tag{1.8}$$

where e is the elementary charge, B is the detector bandwidth, and P_0 is the incident power; here, η is the detector *responsivity*, expressed in $\mathrm{A\,W^{-1}}$. For a typical system such as those used in this thesis, with $P_0 = 10\,\mathrm{mW}$, a bandwidth of $(1/2\pi)\,\mathrm{Hz}$ and $\eta = 0.95$, an α_{min} value on the order of 10^{-9} results.

A further type of signal-independent noise associated with an optical detection technique is the *Johnson noise* [15, 54]. This is a white noise source associated with thermal excitation of electrons within elements of the detector and pre-amplifier, bringing about charge gradients that can generate noise on the electrical output signal. Statistical thermodynamics tells us that (except at the very lowest temperatures and highest signal frequencies) the average thermal energy associated with each degree of freedom of a system in equilibrium is $\frac{1}{2}k_BT$, and the energy stored in a capacitor is described in terms of its capacitance, C, and the supplied voltage, V, as $\frac{1}{2}CV^2$. Accordingly, the noise voltage, V_{noise}, associated with a single degree of freedom is then:

$$\frac{1}{2}C\langle V_{noise}^2\rangle = \frac{1}{2}k_BT \tag{1.9}$$

Simply by invoking Ohm's Law, we can find the corresponding Johnson noise current:

$$\left\langle I^2_{Johnson} \right\rangle = \left\langle V^2_{noise} \right\rangle R^{-2} = \frac{k_B T}{C R^2} \tag{1.10}$$

In such a case, the bandwidth is the number of degrees of freedom, given by $\Delta f = (4CR)^{-1}$, allowing us to rewrite expression 1.10 as [40]:

$$\left\langle I^2_{Johnson} \right\rangle = \frac{4 k_B T \Delta f}{R} \tag{1.11}$$

The Johnson noise may be associated with the photodetector, or with the circuit that processes its output, or both. Its importance with respect to the shot noise is determined by the photon flux. For a typical photodiode of the sort employed in this thesis, $C = 22\,\mathrm{pF}$ and the load resistance, R, is 1 MΩ. A circuit bandwidth of $\sim 11\,\mathrm{kHz}$ results, and the value for the corresponding Johnson noise photocurrent, $\left\langle I_{Johnson} \right\rangle$, is therefore $\sim 10^{-11}\,\mathrm{A}$.

Additionally, though, noise arises on the intensity of the laser output; temperature variation, acoustic vibration and other technical sources may contribute, and quantum noise associated with resonator losses is also important. Phase noise associated with the laser – which gives rise to the lower limit on its line width, and is discussed in more detail in section 3.2.1 – is also coupled to intensity noise. In general, an optical field oscillating at frequency ν incident on a detector at power P generates an output current of:

$$I(t) = \frac{e \eta P(t)}{h \nu} \tag{1.12}$$

wherein e is the electron charge, and η again denotes the quantum efficiency associated with the detector. Excess laser noise generally shows an inverse relationship with the lasing frequency, $I_{1/f} \propto 1/f$, and is therefore known as "$1/f$-noise", or sometimes "pink noise" [55].

The total signal-to-noise is generally presented as a root-mean-square value, com-

bining the squares of the noise photocurrents additively [54]:

$$\frac{S}{N} = \sqrt{\frac{\left\langle I_{Signal}^2 \right\rangle}{\left\langle I_{Johnson}^2 \right\rangle + \left\langle I_{Shot}^2 \right\rangle + \left\langle I_{1/f}^2 \right\rangle}} \tag{1.13}$$

The limit of detection for a given absorption spectroscopy experiment, also called the *sensitivity*, is determined by the total magnitude of noise sources in the signal and the detection over the timescale of the measurement. To consider the detection limit associated with different setups in a readily-comparable way, the notion of *noise-equivalent absorbance* (NEA) is useful. The noise-equivalent absorbance is the value of αL associated with a signal-to-noise ratio of one; any addition of absorber above this level will produce a signal that emerges from the baseline noise. This is usually normalised to an acquisition time of one second, simply by multiplying by the square-root of the total acquisition time associated with a particular measurement.

Implicit in this analysis is the assumption that continued averaging will always improve the noise level; this is true for the white noise contributions, but after a certain amount of time longer-timescale drifts become important, and the excess noise will reach a limiting value. In spite of this, for modest acquisition times the concept of noise-equivalent signal is a useful and general one, which will be adopted in this thesis. The sensitivity for each technique will generally be presented as an α_{min} value, giving the minimum detectable absorption coefficient, again associated with $S/N = 1$. This is ordinarily presented in its acquisition-time-reduced form, in units of $\mathrm{cm}^{-1}\mathrm{s}^{1/2}$.

1.5 Overview of this Thesis

In the following chapter, a broad account of optical cavities and their application to absorption spectroscopy is presented, taking in some of the background physics, as well as a survey of some of the different implementations of optical cavities within enhanced spectroscopic methods. Chapter 3 presents the development of an opti-

cal feedback cavity-enhanced absorption spectrometer (OF-CEAS); the nature and effect of optical feedback to a diode laser is described, along with the resulting contributions to the laser line width and frequency. The development of the spectrometer, including the mechanisms for control of the level and phase of the optical feedback, is detailed and illustrated, along with the data treatment routine. Finally, a successful first application of the OF-CEAS device to sensitive measurements of water and carbon dioxide absorptions near 1.596 μm is demonstrated, and the detection sensitivity of the system is quantified and discussed.

Chapter 4 extends and applies the work of Chapter 3; as well as enhanced sensitivity, the OF-CEAS method offers a well-defined inherent frequency calibration in all resulting spectra, and these two benefits are exploited in line shape measurements on acetylene absorptions close to 1.532 μm. Both the sensitivity and the line shape measurements are contrasted with measurements presented using a simple CEAS setup without optical locking, offering a verification of the OF-CEAS line shape measurements, as well as a direct appraisal of the increased sensitivity brought by the optical locking in the OF-CEAS. The accuracy of the method is demonstrated on measurements of collisional broadening and narrowing effects on the acetylene and carbon dioxide absorptions already encountered.

The fifth chapter of this thesis presents work on an alternative strategy for enhanced spectroscopic measurements, through generation of mid-infrared radiation to allow access to stronger transitions in nitrogen dioxide. The mid-infrared radiation produced by difference frequency generation (DFG) in a non-linear crystal is applied to detection of NO_2 in single-pass absorption, wavelength modulation and cavity-enhanced spectroscopic techniques. The relative merits of these different methods within an NO_2 detection setup are discussed and compared in light of the presented data.

Finally, Chapter 6 contains work towards the combination of the advantages of non-linear optical techniques for generation of more spectroscopically-convenient wavelengths of light with the benefits of the optical locking exploited in the OF-

CEAS system. Proof-of-principle experiments showing the viability of an optically-locked, resonator-enhanced second harmonic generation (SHG) setup are shown; others' approaches to enhanced SHG are discussed, and the present setup compared to them. In light of this work, the prospects for a full implementation of such a system for generation of blue and ultraviolet light are considered.

Chapter 2

Optical Cavities in Spectroscopy

This chapter presents a broad survey of how optical cavities are used in spectroscopy and the properties that make them appropriate for enhancement of the signal in an absorption spectroscopy measurement. Firstly, the concept of an optical cavity, or resonator, is introduced alongside some of the underlying physics: a discussion of the form of the transmitted light signal, its evolution with time, and its dependence upon the configuration of the cavity setup are examined. The application of cavity-enhancement to an absorption spectroscopy experiment is described and exemplified, with reference to research from this group and the published work of others. Finally, a survey of the different absorption spectroscopy techniques involving cavity-enhancement is presented, taking in the earliest temporal ring-down measurements, up to the most complex methods involving optical and electronic locking, and heterodyne techniques.

2.1 Optical Cavities: Fundamentals

An optical cavity – sometimes termed an *optical resonator* – in its simplest form comprises two or more reflective surfaces. Light is directed at the rear of at least one of these surfaces, which are mutually aligned so that the light is repeatedly reflected between them; the light propagates within a closed path. Throughout this continuous multi-passing process, some of the light escapes the cavity by leaking out

through the surfaces at each reflection. In a typical experimental realisation, the reflective surfaces are specially-optimised high-reflectivity mirrors, and the radiation source is a laser; some of the relevant properties of these components are discussed in sections 2.2.1 and 2.2.2.

The simplest type of optical cavity – the *Fabry-Pérot étalon* – comprises two plane mirrors with negligible losses, aligned completely parallel to one another. In a real experiment, confinement of the beam within the optical cavity is ordinarily achieved by using at least one spherical mirror, and the influence of the surfaces' curvatures on the transmitted light signal is examined at section 2.1.4. Nonetheless, the idealised results of the theory for the planar Fabry-Pérot resonator [56] are useful in describing optical cavities more generally, and in the next section we adopt this model to describe the cavity transmission.

2.1.1 The Transmitted Light Signal

Figure 2.1 shows successive electric field amplitudes alternately transmitted and reflected by such an étalon, assuming that the two mirrors are mutually spaced by a distance ℓ, and have equal reflectivities.

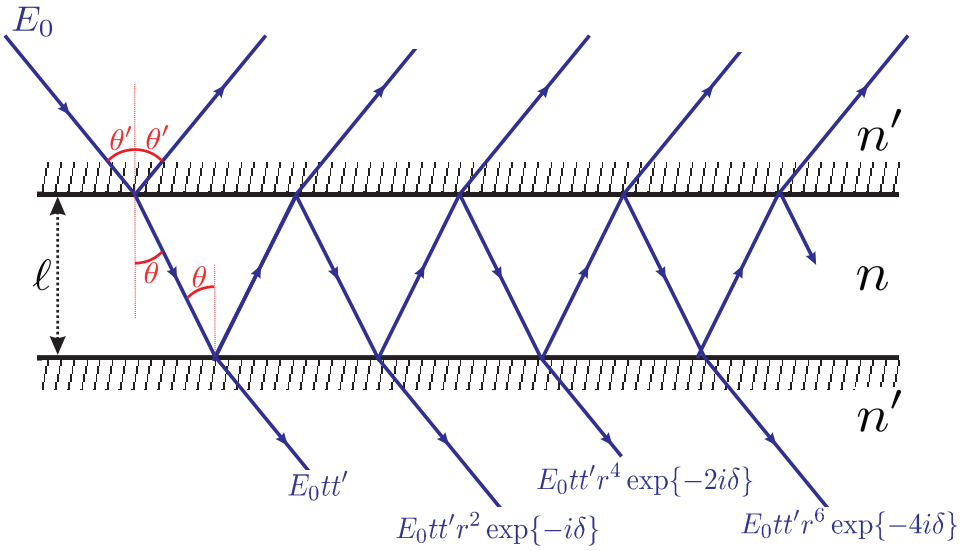

Figure 2.1: Simplified representation of a Fabry-Pérot étalon, showing the transmitted electric field amplitudes.

Consecutive transmitted waves have an optical path difference of $2n\ell\cos\theta$, where n is the refractive index referring to the medium between the mirrors. The total phase difference between the same pair of waves, including a phase change on reflection of η, is given by:

$$\delta = 2k\ell\cos\theta + 2\eta \tag{2.1}$$

wherein k is the wavevector relating to the medium. As such, the total transmitted complex electric field amplitude is given by a geometric progression:

$$\begin{aligned} E_t &= E_0tt' + E_0tt'r^2\exp\{-i\delta\} + E_0tt'r^4\exp\{-2i\delta\} + \ldots \\ &= \frac{E_0tt'}{1 - r^2\exp\{-i\delta\}} \end{aligned} \tag{2.2}$$

where E_0 is the incident electric field amplitude, r and t denote the reflection and transmission coefficients on travelling from refractive index n to n', and r' and t' are the corresponding coefficients in the opposite direction. The total transmitted intensity is then simply given by:

$$I_t \propto |E_t|^2 = \frac{I_0|tt'|^2}{|1 - r^2\exp\{-i\delta\}|^2} \tag{2.3}$$

Letting $|tt'| = T$ and $|rr'| = R$, and assuming negligible mirror losses so that $R + T = 1$, we can now express an *Airy function* to describe the variation in the transmitted light intensity with the phase difference, itself a function of the mirror spacing (equation 2.1):

$$\frac{I_t}{I_0} = \left(1 + \frac{4R}{(1-R)^2}\sin^2(\delta/2)\right)^{-1} \tag{2.4}$$

This function describes the transmitted intensity through the idealised Fabry-Pérot étalon, though it holds for an optical cavity that is injected with a perfect, coherent light source. The resulting comb-like transmission is shown in Figure 2.2 for a series of values of R.

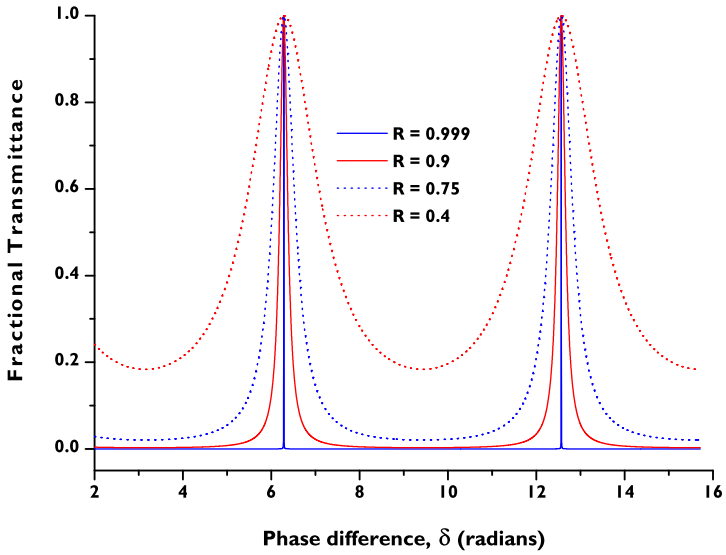

Figure 2.2: Plot of the idealised cavity transmission against the phase difference between successive waves, modelled using the Airy function (equation 2.4). The transmission is plotted for different values of the mirror reflectivity, illustrating the change in mode shape as the cavity finesse is increased.

The transmission function is essentially composed of a series of equally-spaced maxima. At each of these points, an integer number of wavelengths of the light fit within the cavity round-trip length, ensuring constructive interference between successive passes of the light; the light is said to be *in resonance* with the cavity. Accordingly, a substantially-enhanced transmission is seen at these points, and these are the *cavity modes*. The spacing between consecutive longitudinal modes of the cavity in frequency space is described by a single value, called the *free spectral range* (FSR). For light within an optical cavity of two mirrors separated by a distance L, travelling along a cavity round-trip of $2L$ through a medium with refractive index n at the speed of light, c, the free spectral range is then:

$$\Delta\nu_{FSR} = \frac{c}{2nL}\,\text{Hz} \tag{2.5}$$

2.1.2 Finesse, Quality and Mode Width

The resonance characteristics of a particular optical cavity can be described in terms of the number of round-trips within the cavity that each photon makes before it has an escape probability of $1/e$; this quantity, b, is sometimes informally referred to as the *bounce number*. It is the reciprocal of the sum of the coefficients describing *all* the loss processes within the cavity. As such, for our simple two-mirror cavity example,

$$b = \frac{1}{T_1 + L_1 + T_2 + L_2} = \frac{1}{2 - R_1 - R_2} \tag{2.6}$$

In the optical cavity with a round-trip of length $2L$ and equal mirror reflectivities $R_1 = R_2 = R$, the b-value then simply becomes $(2 - 2R)^{-1}$, and the effective path length travelled by a photon within the cavity is correspondingly $L_{eff} = L/(1 - R)$. This ability to trap a photon within the cavity is also related to the *width* of the resulting mode. We can rationalise that by considering the effect of a small perturbation in the laser frequency. In a cavity which is more effective at trapping each photon for longer on average – *i.e.* one characterised by more reflective mirrors – then a given perturbation to the laser frequency will give rise to a greater difference in the photon's total path length in that cavity. As such, the cavity with more reflective mirrors satisfies the constructive interference condition for the modes over a smaller distribution of frequencies, and so the mode width is reduced. The cavity's ability to support constructive interference over a long photon path length is quantified by the *cavity finesse*, F:

$$F = \frac{\pi\sqrt{R}}{1 - R} \tag{2.7}$$

For a low-loss cavity, the modes have a generally Lorentzian form, with a full width at half-maximum (FWHM) given by:

$$\Delta\nu_{FWHM} = \frac{\Delta\nu_{FSR}}{F} = \frac{\Delta\nu_{FSR}}{2\pi b} \tag{2.8}$$

A related quantity is the cavity's *quality factor*, Q; it quantifies the ability of the

cavity to build up and store energy. It has the following form:

$$Q = \frac{\nu}{\Delta\nu_{FWHM}} \tag{2.9}$$

This is a quantity not often referred to in the optics literature, except to make comparisons with similar electronic devices, where its use is more common.

2.1.3 Describing the Beam Path Within the Cavity

Laser radiation is typically inadequately described by treating the radiation as a plane wave; rather, the model of a Gaussian beam is more appropriate. A plane electromagnetic wave characterised by an angular frequency of ω and travelling along the $\vec{z}$ axis has the following complex field amplitude [14]:

$$E = E_0[\cos(\omega t - kz) + i\sin(\omega t - kz)] \tag{2.10}$$

where E_0 is a constant. A Gaussian beam, however, is one in which the field amplitude, $A(x, y, z)$, decays away from the propagation axis with a Gaussian distribution along any perpendicular direction. It adopts the same general mathematical form as the plane wave, but with the constant E_0 replaced by the Gaussian amplitude term, $A(x, y, z)$. The relative intensity distribution in the xy plane for a given displacement along the propagation axis, $\vec{z}$, is determined by finding AA^*. As we shall see in section 2.1.5, the zero-order intensity distribution in this plane corresponds with the TEM_{00} mode, the highest-intensity mode of a simple two-mirror optical cavity. For such a mode, the amplitude can be written as:

$$A(x, y, z) = \exp\left\{ -i\left[P(z) + \frac{k(x^2 + y^2)}{2\,q(z)}\right]\right\} \tag{2.11}$$

In this expression, $P(z)$ is a phase factor, k is the wavevector, given by $2\pi/\lambda$, and $q(z)$ is the complex radius of curvature. Commonly, this latter value is expressed as

a function of the *phase front curvature*, $R(z)$, and the corresponding *spot size*, $w(z)$:

$$\frac{1}{q} = \frac{1}{R} - i\,\frac{\lambda}{\pi w^2} \tag{2.12}$$

Correspondingly, the relative intensity distribution is then given by:

$$AA^* = \exp\left\{ -\frac{2}{w^2}(x^2 + y^2) \right\} = \exp\left\{ -\frac{2r^2}{w^2} \right\} \tag{2.13}$$

where w describes the radial distance from the beam centre to the point at which the field amplitude has decayed to $1/e$ times its maximal value, and therefore the intensity has fallen to I_0/e^2. A Gaussian beam always has a minimum spot size associated with it - this is typically denoted w_0, and is called the *beam waist*. At the beam waist, the curvature of the radiation wavefront is on the point of swapping from positive to negative (or *vice versa*), and so at this point the complex radius of curvature, $R(z)$, is infinite; as such, the Gaussian is pseudo-parallel at the beam waist. Far from the beam waist, the wavefront is more spherical in character; these near- and far-field regimes are separated by a notional distance termed the *Rayleigh range* [39]. Denoted z_R, it is the distance along the propagation axis between the beam waist and the point at which the beam radius has increased by a factor of $\sqrt{2}$. It takes the value:

$$z_R = \frac{\pi w_0^2}{\lambda} \tag{2.14}$$

To return to our two-mirror optical cavity, if we consider a pair of concave mirrors with equal radii of curvature r separated by a distance L, we can write the Rayleigh range in terms of a stability parameter, g, with $g = 1 - L/r$. The stability parameter is introduced more fully in the following section. The Rayleigh range in our cavity is found to be:

$$z_R^2 = \frac{g^2(1-g^2)}{(2g-2g^2)^2}L^2 \;\; = \frac{1+g}{4(1-g)^2}L^2 \tag{2.15}$$

Further ray-tracing matrix analysis yields the following expressions for the beam

waist, w_0, and spot size at each mirror, $w_1 = w_2$:

$$w_0^2 = \frac{L\lambda}{\pi}\sqrt{\frac{1+g}{4(1-g)}} \qquad \text{and} \qquad w_1^2 = w_2^2 = \frac{L\lambda}{\pi}\sqrt{\frac{1}{1-g^2}} \tag{2.16}$$

For the 1596 nm V-shaped cavity used in Chapter 3, for example, this leads to a beam waist of 0.47 mm, and a spot size on each mirror of 0.93 mm.

2.1.4 Optical Stability

We have seen in section 2.1.3, and specifically in equations 2.16, that the spatial distribution of a resonant mode in a simple two-mirror optical cavity extends substantially away from the cavity axis (which is the vector connecting the mirrors' centres). In order for the cavity to be resonant, the beam has to be trapped between the mirrors for many passes. For mirrors of finite size, some of the beam energy is not trapped in this way, and is lost from the resonator. These *diffraction losses* are larger for higher-order transverse modes (which are subject to a fuller description in section 2.1.5).

The ability of a given resonator to maintain such confinement of the light by periodic refocussing of the intra-cavity beam manifests itself in the requirement for *optical stability* [54, 57]. Except for the fact that the light path folds back upon itself, reflection at a curved cavity mirror is equivalent in geometric optics to passing through a lens with a focal length $f = r/2$, where r is now the radius of curvature of each of the two mirrors, which we take to be identical. If the mirrors are separated by a distance L, then, we can consider the resonator as a lens-equivalent waveguide, and form an appropriate ABCD-type matrix (see Appendix A) for a single pass through the cavity, describing the initial and one-pass vectors in terms of a displacement ($d_{0,1}$) and angle ($\theta_{0,1}$) from the optical symmetry axis.

$$\begin{pmatrix} d_1 \\ \theta_1 \end{pmatrix} = \begin{pmatrix} 1 & 0 \\ -2/r & 1 \end{pmatrix} \begin{pmatrix} 1 & L \\ 0 & 1 \end{pmatrix} \begin{pmatrix} d_0 \\ \theta_0 \end{pmatrix} \tag{2.17}$$

and therefore:

$$\begin{pmatrix} d_1 \\ \theta_1 \end{pmatrix} = \begin{pmatrix} 1 & L \\ \frac{-2}{r} & 1 - \frac{2L}{r} \end{pmatrix} \begin{pmatrix} d_0 \\ \theta_0 \end{pmatrix} \tag{2.18}$$

Appendix B details the analysis that derives an overall stability condition from this expression. The stability condition takes the general form:

$$0 < L < 2r \tag{2.19}$$

for a symmetrical two-mirror cavity. The equivalent analysis for the unsymmetrical case produces the following more general condition [11]:

$$0 < g_1 g_2 < 1 \tag{2.20}$$

where g_i is the stability parameter for mirror i, given by $1 - L/r_i$. These constraints are an important point of reference in cavity design.

2.1.5 Transverse Modes

The modes of an optical cavity are properly described as solutions to a three-dimensional wave equation. In full, the frequencies of the modes of a two-mirror optical cavity of length L, with the two mirrors' g-parameters being simply g_1 and g_2, can be expressed as [11, 58]:

$$\nu_{m,n,q} = \frac{c}{2L}\left[q + \frac{n+m+1}{\pi} \arccos\sqrt{g_1 g_2}\right] \tag{2.21}$$

where q is the longitudinal mode index, and m and n specify the number of optical nodes in the two directions perpendicular to the propagation axis. Two modes with the same m and n, but consecutive q, values (*longitudinal modes*) are separated by one free spectral range of the cavity. Modes of the same q, but differing in their values of m and/or n, are termed the *transverse modes* of the cavity, and are generally denoted TEM_{mn} modes. Figure 2.3 shows some typical spatial distributions of light

exiting an optical cavity after resonating in different TEM_{mn} modes; these images were taken using an infrared camera to observe the transmission through the V-shaped cavity introduced in Chapter 3.

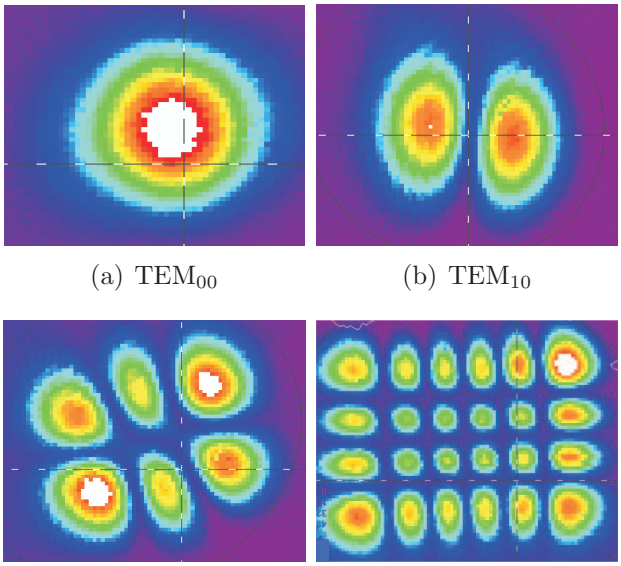

(a) TEM_{00} (b) TEM_{10}

(c) TEM_{21} (d) TEM_{53}

Figure 2.3: Cavity transmission measured using an infrared camera, showing the spatial distributions corresponding to different TEM_{mn} modes of the V-shaped optical cavity introduced in Chapter 3.

We can describe the origin of these transverse modes at different frequencies by considering the phase shift. The light coupled into a Gaussian mode of the optical cavity acquires a phase shift along its propagation direction, relative to that of a plane wave with the same frequency. This is called the *Gouy effect* [59–61], and the Gouy phase shift can be quantified as a function of the displacement from the beam waist along the propagation axis, z, and the Rayleigh range, z_R:

$$\phi_{G,00}(z) = -\arctan\left(\frac{z}{z_R}\right) \tag{2.22}$$

Setting the phase shift at the beam waist to be zero, at the respective far field limits on either side of the beam waist (*i.e.* the points at which $z \ggg z_R$), we can see that this phase shift approaches $\pm(\pi/2)$ radians. Accordingly, the total Gouy

phase shift on passing from the far field on one side of the beam waist, through the focus and out toward the other far field is π radians [61].

The Gouy phase shift undergone by a higher-order Gaussian beam is different to that in the zero-order case; for the TEM_{mn} mode, it is given by:

$$\phi_{G,mn}(z) = (m + n + 1)\phi_{G,00}(z) \tag{2.23}$$

The total phase difference that results between mirrors 1 and 2 of our cavity is the sum of the simple effect due to the displacement along the distance separating the mirrors, and the Gouy shift:

$$\phi_{tot,mn}(z_2 - z_1) = \frac{2\pi L}{\lambda} - (m + n + 1)\{\phi_{G,00}(z_2) - \phi_{G,00}(z_1)\} \tag{2.24}$$

Accordingly, the different phase shifts for different TEM_{mn} modes correspond with their resonating at different frequencies.

2.2 Optical Cavities: Implementation

2.2.1 The Light Source

The line width associated with a laser – like its time-integrated analogue, the band width – has a minimum value associated with phase noise in the laser medium. This minimum is called the Schawlow-Townes limit, and it is described and quantified more fully in Chapter 3. The amplitude of the laser radiation suffers fluctuations associated with its quantised nature; the light is emitted in discrete quantum "packets", and the quantum fluctuations associated are called the *shot noise* [54, 58, 62–64]. The spectral density associated with this noise is [54, 58]:

$$S(f) = 2\bar{I}h\nu \tag{2.25}$$

where $\bar{I}$ is an average laser intensity, $h\nu$ is the energy associated with a laser photon, and f is the shot frequency. Typically, shot noise only becomes obvious at the highest frequencies, where technical noise sources are generally less evident. The absolute limit of detection for a cavity-enhanced absorption spectroscopy setup, then, is set by the magnitude of this shot noise. Shot-noise limited detection in the cavity-enhanced context represents the situation where [11, 58]:

$$(\alpha L)_{min} = \frac{\pi}{F}\left(\frac{2Bh\nu}{\eta P}\right)^{1/2} \tag{2.26}$$

Under these conditions, $(\alpha L)_{min}$, the minimum detectable absorbance, is equivalent in amplitude to the shot noise; F is the finesse of the cavity, B is the detection bandwidth and η is the quantum efficiency associated with the detector; $h\nu$ is again the photon energy, and P the incident power. The bandwidth of the laser over the course of a cavity transmission measurement also has a strong influence on accuracy of analysis of the resulting spectra, and therefore on the detection sensitivity of a cavity-enhanced technique. Most fundamentally, applicability of the Beer-Lambert Law (equation 1.5) to describe molecular absorption relies upon the assumption of monochromatic light. The reflectivity of the each of the mirror surfaces also has a strong dependence upon the incident light's frequency. A broader distribution of incident light – corresponding to a laser source with a greater bandwidth – means a larger spread of associated effective reflectivities, making the calibration of a measurement of the cavity transmission more difficult.

In the case of temporal measurements (see section 2.3.1), if on each pass the light is not very close to equally attenuated, then a single exponential function will not accurately fit the resulting ring-down trace, and an accurate absorption cross-section cannot easily be inferred. Generally, if the laser bandwidth associated with the duration of a measurement is broader than, or similar to, the width of the absorption transition, then bandwidth effects become detrimental to the ability accurately to detect the absorber [62, 64–67]; the measurement of a ring-down trace may under such circumstances be dominated by the slow decay associated with the

wings of the absorption, rather than the absorption at the line centre.

2.2.2 Cavity Mirrors

The reflective surfaces comprising the optical cavity are typically distinct and specially-engineered mirror substrates. Mirrors are usually characterised by their reflectivity and transmission at a given wavelength, λ, and particularly by the complex field-amplitude reflection and transmission coefficients, respectively r and t. Ordinarily, it is the corresponding real *intensity* coefficients, $R = |r|^2$ and $T = |t|^2$, that are of most use, and it is to these that reference is generally made in this thesis. In the notional case of a perfect mirror, there are no losses of light, and so conservation of energy implies that $R + T = 1$. Of course, no real mirror satisfies this ideal picture; some of the incident light is absorbed by the mirror substrate, whose surface also has a finite roughness which brings about some scattering. All such losses for a given mirror are generally accounted for in a single intensity loss coefficient, L, so that:

$$R + T + L = 1 \tag{2.27}$$

Typical mirrors for a visible or infrared optical cavity experiment comprise a highly polished substrate coated with several very thin layers of reflective material; this material may be a metal (usually aluminium, silver or gold), or – especially for the highest reflectivities – a dielectric material such as silicon dioxide or a metal oxide [62]. Often, the layers of dielectric material are arranged to be alternately high-n and low-n; the reflection and transmission properties of such an arrangement vary with radiation wavelength in a straightforwardly-controllable way, by varying the thickness and refractive index of the dielectric layers. On interaction with such a mirror surface, the radiation generates many new waves by partial reflection and transmission at each of the boundaries between the layers, and the reflected wave results from interference between these [39]. Parts-per-million (ppm) losses are now common for well-engineered optical cavity mirrors in the visible and infrared regions; the very highest reflectivities now approach $R \sim 0.999999$, for mirrors

with surface roughness close to the atomic scale [62]. However, such extremely reflective mirrors are exceedingly expensive and would be liable to degradation, making them unsuitable for implementation in a robust detection instrument. In detection applications, mirrors with reflectivities between 0.999 and 0.9999 are more common.

Typically, in an optical cavity experiment, the rear face of the mirrors (and indeed, the faces of many of the other optics) are anti-reflection (AR-) coated. This is to minimise the appearance of unwanted étalons between pairs of optics adding structured noise to the eventual measured absorption spectrum. Like the reflecting surface itself, the AR-coating comprises application of a thin dielectric layer to the desired optical surface. In this case, though, only a single layer is used, of a material whose refractive index is intermediate to that of air and that of the substrate. This results in the first two reflected rays cancelling out each other's amplitude by destructive interference, and all the incident energy being disposed into the transmitted ray.

2.2.3 Non-Linear Cavity Configurations

So far in this discussion of the background optics and resonator physics, we have mostly considered the simplest case of an optical cavity composed of two mirrors aligned to face one another, forming a linear resonator. In terms of implementation and theory, this is often the simplest configuration to adopt. Sometimes, particular requirements for reduced, or frequency-selected, optical feedback motivate the adoption of a non-linear cavity arrangement. Figure 2.4 shows two such cavity arrangements for a three-mirror resonator.

In each of Figure 2.4(a) and Figure 2.4(b), the dark blue arrows show the direction of the incident and cavity-resonant light; the red arrows show the direction of the transmitted light, and the light blue arrow shows the reflected beam at the folding mirror of the V-cavity. It can be seen from Figure 2.4(a) that there is no path that the incident light can follow that will result in intensity being fed back along

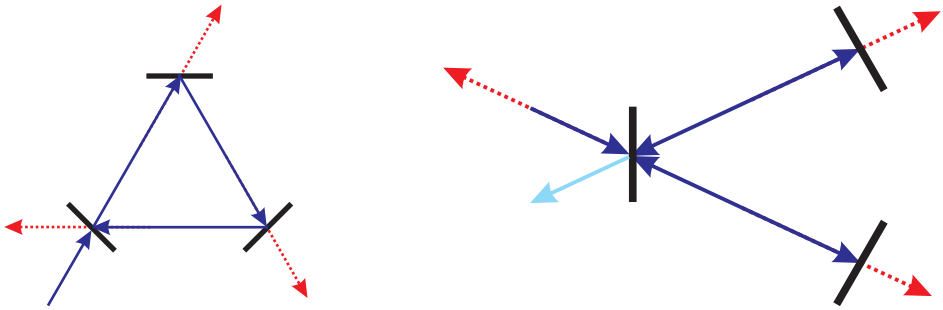

(a) Ring resonator (b) V-shaped resonator

Figure 2.4: Schematic illustration of two different three-mirror resonators, configured respectively in (a) a ring arrangement for minimal feedback and (b) a V-shape for cavity-selected feedback.

the original light path in the counter-propagating direction. Small imperfections on the mirror surfaces may in fact bring about the build up of some light propagating in the contrary direction, but a ring resonator is broadly associated with the elimination of feedback.

A V-shaped cavity can be used for frequency-selected feedback [68]. By inspection of Figure 2.4(b), it can be seen that the only light that feeds back along the incident light beam is the light which is resonant within the V-cavity. A cavity of this general configuration has been adopted for optical self-locking, and will form the basis of the optical feedback cavity-enhanced absorption spectroscopy work reported in chapters 3, 4 and 6 of this thesis.

2.2.4 Mode Matching

Radiation is coupled into an optical cavity when the laser mode and a cavity mode are in resonance. It has been demonstrated in section 2.1.5 that there is a spatial distribution associated with the cavity mode in the directions perpendicular to the cavity axis. Carefully matching this distribution and the shape of the incident light beam increases the power of radiation that couples into that cavity mode [65]. Specifically, the size of the beam is often telescoped using a pair of lenses to a size at or just over the mirror spot size w_1, calculated using expression 2.16. As well

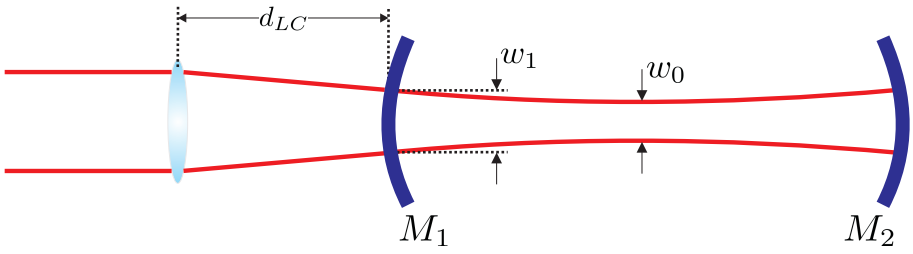

Figure 2.5: Schematic illustration of the simplest possible mode-matching scheme for a linear cavity.

as optimising the beam size, for the best coupling into the mode the light path should ideally mimic the divergence characteristics of the cavity mode. A general arrangement of the simplest possible form of mode-matching – use of a single convex lens – is illustrated in Figure 2.5, showing the beam waist and mirror spot size [58].

To achieve the best coupling efficiencies, the intensity profile of the incident radiation should further be matched to the Gaussian distribution associated with the cavity mode being injected. If a diode laser is being employed as the light source, then this beam-shaping process is especially important; ordinarily, the intensity distribution from such a laser is far from Gaussian [58]. The beam shape is typically altered by passing it through a pair of anamorphic prisms.

A full analysis of the light trajectory by ray transfer matrix analysis and consequent re-arrangement of beam-telescoping optics can allow access to very high coupling efficiencies. A single ABCD-type ray-transfer matrix can be determined describing the focussing at the lens and a cavity mirror, and the displacements through free space along the distance $d_{LC} + L/2$, where d_{LC} is the separation between the mode-matching lens and the cavity mirror. Invoking the ABCD law of Gaussian beam propagation (equation A.9), the problem can then be solved for the best values of d_{LC} and f, the focal length of the mode-matching lens, to achieve optimal mode matching.

2.3 Experimental methods

2.3.1 Temporal Evolution: Ring-Down Spectroscopy

The average path length travelled by a photon within the optical cavity can straightforwardly be related to the time which it spends trapped between the mirrors. For the two-mirror example, the photon lifetime, τ_0, is the time spent by a photon in the empty cavity until it has a $1/e$ probability of escaping, and is given by:

$$\tau_0 = \frac{L}{c(1-R)} \tag{2.28}$$

This quantity can be measured experimentally by applying a short pulse of light to an optical cavity, and measuring the decay in the transmitted light intensity at one of the mode frequencies; the resulting decay is exponential with time, and τ is the amount of time taken to reach a light intensity of $1/e$ of the initial level. This time is most commonly known as the *cavity ring-down time*.

Cavity ring-down measurements have been the subject of a series of excellent reviews [6, 11, 17, 25, 58, 62, 65, 69–71], and the theory of cavity ring-down spectroscopy has been considered by others [63, 72, 73]. In this section, the approach elucidated by Mazurenka *et al.* [11] and Wheeler *et al.* [25] is broadly adopted. For a pulsed laser source exciting the same two-mirror cavity taken as our example above at an incident intensity I_{pulse}, the transmitted single-pass intensity measured by a detector after the second cavity mirror will be given by:

$$I_0 = T^2 \exp\{-\alpha L\} I_{pulse} \tag{2.29}$$

where $\exp\{-\alpha L\}$ is a simple Beer-Lambert term for the one-pass absorbance through the medium contained between the two cavity mirrors, with α the corresponding frequency-dependent absorption coefficient. The transmitted intensity at the nth round-trip, then, is described by a geometric progression with initial term I_0 and common ratio $R^2 \exp\{-2\alpha L\}$. The total transmitted intensity after n round-trips

within the cavity is therefore:

$$\begin{aligned} I_n &= I_0 R^{2n} \exp\{-2n\alpha L\} \\ &= I_0 \exp\{-2n(-\ln R + \alpha L)\} \end{aligned} \tag{2.30}$$

Since the time taken to complete n round-trips within the cavity is simply:

$$t = \frac{2Ln}{c} \tag{2.31}$$

equation 2.30 can now be re-written fully in terms of time:

$$I(t) = I_0 \exp\left\{ -\frac{ct}{L}(-\ln R + \alpha L) \right\} \tag{2.32}$$

From this form of the decay, we can now extract the ring-down time:

$$\tau = \frac{L}{c(-\ln R + \alpha L)} \approx \frac{L}{c[(1-R) + \alpha L]} \tag{2.33}$$

where, for conditions of high reflectivity ($R \rightarrow 1$) we can use the approximation that $\ln R \approx (R-1)$. By comparing this expression for the ring-down time with that when there is no absorber present (equation 2.28), an estimate of the absorption coefficient, and therefore of the absorber concentration, can be obtained. Either the mirror reflectivity must be known precisely, or an absorption-free measurement of the cavity ring-down time needs therefore to be made in order to calibrate cavity ring-down measurements of absorbing species. Indeed, the value of τ_0 provides a convenient way accurately to calibrate the mirror reflectivity, and it was with this purpose originally in mind that the technique was born [25, 70, 73, 74].

Cavity ring-down spectroscopy experiments (CRDS) rely on such a measurement of the temporal evolution of the light intensity escaping an optical cavity when the light source is abruptly switched off. Specifically, the ring-down time, defined at equations 2.28 and 2.33 above, is measured with and without the absorbing medium present, and then using both these values the absorption coefficient can be extracted

[58]:

$$\alpha(\nu) = \frac{1}{c}\left(\frac{1}{\tau(\nu)} - \frac{1}{\tau(\nu_0)}\right) \tag{2.34}$$

Coincidence of a single mode of the laser with a single mode of the optical cavity yields a single proper exponential decay trace. If the laser is emitting over a broad frequency distribution, or if more than one mode of the optical cavity is being excited, then a multi-exponential decay trace results, with each mode corresponding to a subtly different ring-down time [11, 58, 62, 70]. The light that is resonant with each of these modes may also interfere, further complicating the transmitted time-dependent light signal. For CRDS measurements, then, it is especially important that the cavity transmission be considered when designing the cavity. A simulation of the expected cavity output, based on equation 2.21, will indicate the spacing between consecutive modes and therefore aid the design of a cavity where consecutive modes are well spaced so that a ring-down trace is less likely to involve contributions from more than one mode.

The original CRDS experiments employed a pulsed laser source, which brings advantages in that the laser naturally switches off the light source, and this pulsing can easily be implemented in such a way as to achieve a rapidly-extinguished light intensity. In an implementation of CRDS, if a cw laser is being used rather than a pulsed source, then a fast optical switch is required in order to extinguish the cavity-resonant light rapidly; as such, the light needs either rapidly to be switched off altogether [75], or to be moved swiftly out of resonance [76] with the cavity. In either case, the action must be sufficiently fast that substantial excitation of other modes – which might otherwise complicate the resulting ring-down trace – is avoided. Typically, for a continuous wave (cw-) laser source, this is achieved through use of an acousto-optic modulator (AOM). This device exploits the acousto-optic effect within certain crystalline materials, whereby the compressions and rarefactions induced in the solid structure when a sound wave is passed through it create an effective diffraction grating. Typically, the cavity ring-down experiment is set up and aligned to the first-order diffracted beam, with the AOM activated. Then,

when the AOM is triggered to switch off, the diffraction process abruptly ends, and so no light is directed into the optical cavity. Alternatively, a Pockels cell can be used; both realisations of an optical switch come with the additional benefit of contributing to the optical isolation of the laser from unwanted retro-reflections. Correspondingly, the detection apparatus must be fast enough fully and accurately to detect the change in the transmitted light intensity when the light source is switched off; typically, an amplified photodiode or photomultiplier tube can fulfil this task. Triggering is then usually set up in such a way that when light is coupled into the most intense low-order TEM mode (ordinarily TEM_{00}) above a certain threshold intensity level, a trigger signal is sent to deactivate the AOM or other optical switch, and the resulting ring-down trace is then recorded [58, 77].

A typical cw-CRDS arrangement is depicted schematically in Figure 2.6. Essentially, it comprises a laser source and optical isolator, a fast optical switch, an optical cavity encasing the absorbing sample, and detection apparatus. In order to run the experiment, some sort of wavelength-monitoring and trigger apparatus are required. The nature of the laser source has been discussed at section 2.2.1; the optical isolator is present simply to reduce or eliminate unwanted feedback to the laser. The effects of feedback to the laser are discussed more fully in Chapter 3, and so here we concern ourselves principally with the triggering, wavelength-stepping, and detection apparatus.

To bring about resonance between the laser and the optical cavity, accidental

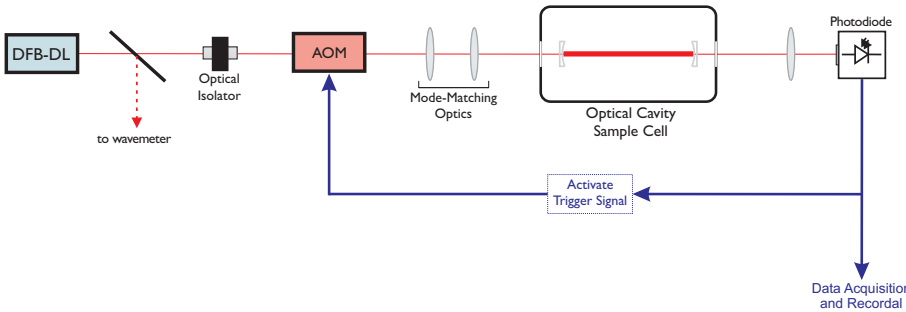

Figure 2.6: Generalised arrangement for a typical cavity ring-down spectroscopy arrangement.

resonance when the cavity is dithered slightly – either by deliberate vibration or by inevitable instabilities in the optical components of the experiment – can be relied upon [73]. However, for the majority of applications a more controlled approach is required [78], comprising scanning of the cavity length using a piezo-electric transducer [75, 79] over a distance at least equal to $\lambda/2$.

An example of a ring-down trace from an empty cavity of length 29 cm, using a cw laser at a wavelength of 1560 nm, is shown in Figure 2.7. The single exponential fit is shown, and results in a ring-down time of 0.54 ± 0.01 μs, corresponding to a geometric mean mirror reflectivity of 0.9985.

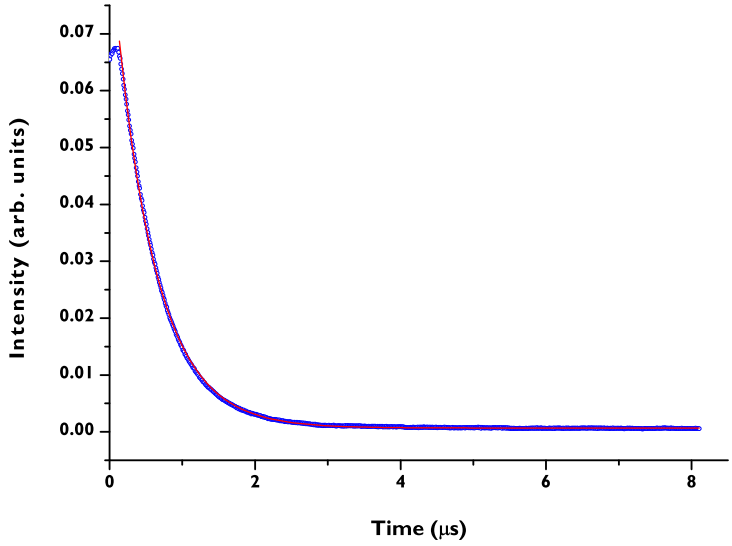

Figure 2.7: Ring-down trace for a 25 cm empty optical cavity illuminated close to 760 nm, and single exponential fit.

cw-CRDS is ideally suited to the use of narrow-band diode lasers, which bring all the advantages identified in Chapter 1. The use of cw diode lasers does have some disadvantages, particularly associated with the inherent lack of direct control over the time at which a ring-down event is to occur [58, 75] – but it has proved to be a useful and well-applied technique in atmospheric detection problems [80–87], as well as in plasma diagnostics [88–94] and more fundamental spectroscopic work

[95–98], regularly demonstrating minimum detectable absorptions on the scale of $\alpha_{min} \sim 10^{-9}\,\mathrm{cm}^{-1}$ and sometimes smaller.

2.3.2 Time-Integrated Cavity-Enhanced Spectroscopies

One of the disadvantages associated with making temporal measurements with a cavity ring-down technique lies in the demand that it makes on the speed of the photodetector and the optical switch. The requirement for rapid components to meet these demands, and the need to step the laser consistently, rapidly and accurately across the spectral region being measured add considerably to the expense and complexity of this experimental technique. In order to obviate the need for these more complex experimental components, there exists a family of techniques based on measuring the time-integrated cavity output, known as integrated cavity output spectroscopy (ICOS) [99], or cavity-enhanced absorption spectroscopy (CEAS) [100]; the latter term will generally be adopted for this group of techniques throughout this thesis.

Within a standard CEAS setup, rather than aligning the cavity for preferential excitation of a particular mode, the alignment is altered so that light may be coupled into many higher-order modes right across the relevant spectral region. Instead of a clean, periodic cavity mode structure, CEAS typically aims for a highly congested mode structure with a consistent average transmission across the spectrum, so that upon averaging the spectral baseline appears smooth. The laser is scanned repeatedly across the spectral region being probed, and the relatively narrow-band laser radiation couples into several modes of the cavity during the scan, by accidental coincidence of the laser frequency and the centre of a mode of the cavity [65, 100, 101]. Addition of mechanical instability to the system scrambles the cavity length, thereby randomising, and increasing the density of, accessible modes across a scan. As this procedure is repeated across the same region, a different series of these "accidental" resonances is accessed each time, and the "gaps" in the mode structure are filled in with each extra scan, giving rise to a smooth baseline after

averaging [100].

Interpretation of the resulting signals is predicated on the idea that the transmitted intensity through the cavity, with or without the presence of an absorbing medium between the mirrors, is directly proportional to the ring-down time [11, 58, 65, 100, 101]. Engeln *et al.* [100] first showed this to be the case at a restricted set of slow laser scan rates. Zalicki and Zare [102] derived a full and exact expression for the time-dependence of the ringing-up process, but Engeln *et al.* [100] assumed a block function for the laser spectrum, with a width greatly in excess of the cavity bandwidth, and convolved that laser spectrum with an Airy function, like that at equation 2.4, describing the cavity transmission. They calculated profiles describing the time evolution of the light intensity escaping the cavity, and then showed that the time-integrated transmitted intensity increased, to a good approximation, linearly at the slow scan rates they used. Engeln *et al.* [100] also noted that the profile of a cavity mode is well described by a Lorentzian function whose width is proportional to the total cavity losses (*i.e.* $\propto \tau^{-1}$), and whose intensity (peak height) is proportional to the square of the ring-down time. As such, the total area underneath the peak (related directly to the absorption coefficient) is expected to show the overall linear τ-dependence.

The work of Bakowski *et al.* [101] showed that this linear relationship holds more generally, developing a theoretical description that included rapid scanning rates. By considering the cavity as a Fabry-Pérot system that is equivalent to a scanning interferometer [101, 103–105], they show that the time-dependent transmitted amplitude can be written as:

$$A_t(t) = \sum_{n=1}^{\infty} R^{n-1}(1-R)\exp\{-(2n-1)\alpha L/2\}\exp\{i\phi_n(t)\} \qquad (2.35)$$

in which R is the reflectivity of the mirrors (assumed equal for the two mirrors, or replaced by the geometric mean of the two reflectivities if they differ), α is the absorption coefficient, which is considered to be invariant across the laser bandwidth, and t is time.

The corresponding time-dependent intensity of the cavity-transmitted light is then given by the square modulus of $A_t(t)$. Bakowski *et al.* [101] showed that such a model gives excellent agreement with experiment for a series of very different laser scan rates; this agreement is illustrated in Figure 2.8, reproduced from their article [101]. They then integrated the simulated time-dependent transmission, and showed that the resulting values scaled linearly with the ring-down time across the whole range of laser scan rates. In the limit of a truly monochromatic laser spectrum and a slow laser scan, the simple Airy function for the cavity transmission results [101].

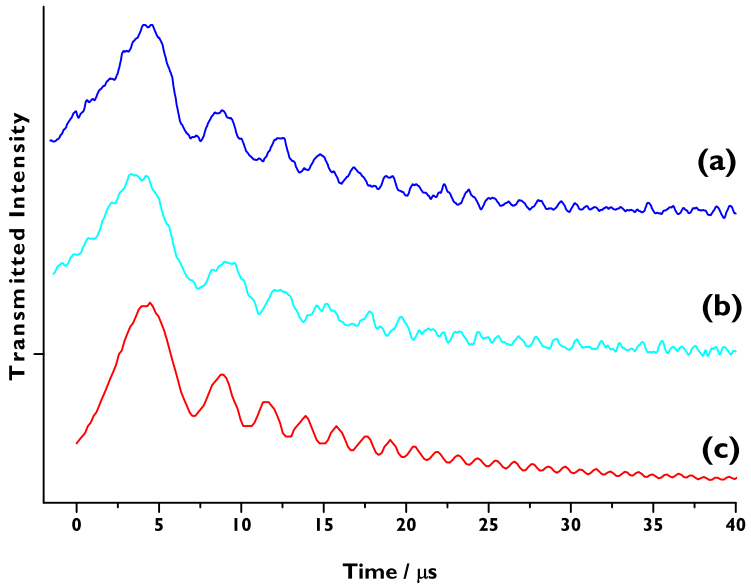

Figure 2.8: Transmission of an optical cavity showing (a) experimental results when scanning the cavity length, (b) experimental results when scanning the laser, and (c) theoretical results achieved by treating the cavity as a scanning interferometer. All three data sets are for an equal frequency scan rate close to 40 GHz s^{-1}, and the experimental data were taken using an ECDL close to 1750 nm in a 1 m cavity of finesse 10500. Reproduced from the work of Bakowski *et al.* [101].

This observation that the time-integrated intensity of light transmitted through the cavity is proportional to the ring-down time leads directly to the following form

for the absorption signal:

$$\frac{I_0 - I}{I} = \frac{\alpha L}{1 - R} \tag{2.36}$$

wherein I and I_0 are the respective signals with and without absorber, and α is the frequency-dependent absorption coefficient. This is the most generally-adopted form for describing the signal in a CEAS experiment, and is the expression which will be adopted for all of the CEAS spectra presented in this thesis, except where it is indicated otherwise.

Equation 2.36 has been arrived at by a series of alternative derivations and justifications. In the work of Fiedler *et al.* [106] (and also, later, in the review of Mazurenka *et al.* [11]) the fractional transmission was considered as a product of reflections (each giving rise to a term in $1 - R$) and single-pass absorptions $(1 - A)$, relating the transmitted light (I_{trans}) to the incident light (I_{in}) through:

$$I_{trans} = I_{in}(1 - R)^2(1 - A)\sum_{n=0}^{\infty} R^{2n}(1 - A)^{2n} \tag{2.37}$$

The sum term can then be cast as the infinite sum of a geometric progression with initial term 1 and common ratio $R^2(1 - A)^2$, and we can therefore rewrite equation 2.37 as:

$$I_{trans} = I_{in}\frac{(1 - R)^2(1 - A)}{1 - R^2(1 - A)^2} \tag{2.38}$$

The ratio between I_{trans} in the presence of absorber, and $I_{trans,0}$ without absorber present (*i.e.* when $A = 0$) is then found, substituting the Beer-Lambert expression of $\exp\{-\alpha L\}$ for $(1 - A)$. This yields the following expression for the CEAS signal, applicable for any values of R or A:

$$\frac{I_{out,0}}{I_{out}} = \frac{1 - R^2\exp\{-2\alpha L\}}{(1 - R^2)\exp\{-\alpha L\}} \tag{2.39}$$

From this expression, with experimental data for I_{trans} and $I_{trans,0}$ and a value for R, the absorption coefficient (and therefore the absorber concentration, knowing the relevant cross-section) can be determined.

O'Keefe *et al.* [99] adopted a similar derivation to that presented by Mazurenka *et al.* [11], but in the final steps invoked assumptions of high R and low A in order to solve an integral rather than finding the infinite sum of a geometric progression. In that case, the resulting expression that was used to present the CEAS signal is:

$$\frac{I_{trans,0}}{I_{trans}} = \frac{\ln R - \alpha L}{\ln R \exp\{-\alpha L\}} \tag{2.40}$$

A steady-state approach considering the circulating power in an off-axis CEAS experiment was adopted by Paul *et al.* [107], yielding the following expression, without including any assumptions about the alignment of the incident light.

$$\frac{I_{trans,0}}{I_{trans}} = \frac{1 - R\exp\{-\alpha L\}}{1 - R} \tag{2.41}$$

In the limits of high mirror reflectivity ($R \rightarrow 1$) and low absorbance ($\alpha \rightarrow 0$), this expression reduces to the form of the CEAS signal derived above, and expressed at equation 2.36.

CEAS therefore offers a robust technique which is generally more straightforwardly implemented than CRDS; the need for a trigger circuit, a fast optical switch, and a consistent frequency-stepping mechanism across a spectral feature is eliminated. The requirements for precise alignment and mechanical stability that a CRDS experiment requires are completely dispensed with in the CEAS case; indeed, a substantial "misalignment" and mechanical instability may often lead to an improved CEAS signal.

Employing CEAS, similar sensitivities have been achieved to those found using the CRDS method, and CEAS is a technique that has found many applications. By way of examples, recent papers have related to several different applications of the technique, including high resolution spectroscopy [108–113], atmospheric sensing [107, 114–116], plasma [101] and flame [117] diagnostics, and medical sensing [118].

An experimental realisation of a simple CEAS set-up, along with a comparison of its performance with that of an optically-locked CEAS technique (see section 2.4.2,

is addressed in Chapter 4.

2.3.3 Polarisation-Based Cavity Methods

Additional information about the nature of an absorber can be extracted from the results of a cavity ring-down experiment if the polarisation of the probe light is controlled, and compared quantitatively with the polarisation of the cavity output light [65, 71]. Engeln *et al.* [100, 119], for instance, demonstrated work on the $b \leftarrow X$ overtone magnetic dipole transition in O_2 close to 628 nm. On applying a magnetic field, Zeeman splitting removes the degeneracy of the levels with different M_J quantum numbers; the differential response of the different M_J-states to light polarised perpendicular and parallel to the applied magnetic field gives rise to polarisation-dependent absorption on these transitions. This in turn gives rise to an effective rotation of the plane of polarisation – an effect known as *magnetic dichroism* – which can be measured by comparing the cavity-transmitted signals in the two orthogonal polarisation directions. The work of Engeln [100, 119] gave a minimum detectable absorption close to $3 \times 10^{-9}\,\mathrm{cm}^{-1}$, and a minimum detectable rotation of the polarisation of $10^{-8}\,\mathrm{radians\,cm}^{-1}$. This is a system of considerable sensitivity; indeed, Müller *et al.* [120, 121] successfully adapted polarisation-dependent ring-down spectroscopy for application to the measurement of molecular chirality.

2.3.4 Cavity-Induced Phase Shifts

Another interesting variant on the cavity ring-down method is phase-shift CRDS (PS-CRDS) [122–125]. This technique is based on the cavity-attenuated phase shift measurements of Herbelin *et al.* [74, 126], and was proposed by Engeln *et al.* [122]. It involves a measurement of the phase-shift acquired by a sinusoidally-modulated cw laser beam, both for an empty cavity and for one with absorber present, and inferring the sample concentration from a comparison of these two measurements. The modulation is typically achieved using a mechanical chopper disc; this is the simplest arrangement, and is generally adequate for modulations up to $\sim 100\,\mathrm{kHz}$.

An AOM or an electro-optic modulator (EOM) is typically used to apply a faster modulation.

The modulated laser output can be written as:

$$I(\nu, t) = I_0(\nu)[1 + \beta(\nu)\sin(\omega t)] \tag{2.42}$$

in which I_0 represents the intensity of the unmodulated light, β the modulation depth and ω the (angular) modulation frequency. Meanwhile, the cavity response to a pulse of light can be modelled as:

$$C \exp\left\{ -\frac{t}{\tau(\nu)} \right\} \tag{2.43}$$

where C is simply a constant, and $\tau(\nu)$ is the frequency-dependent ring-down time. Convolving the laser output with the cavity response function yields an expression for the time-dependent light intensity escaping the cavity:

$$I_{trans}(\nu, t) = C \int_{-\infty}^{t} I_0[1 + \beta(\nu)\sin(\omega t')] \exp\left\{ -\frac{t - t'}{\tau(\nu)} \right\} \, \mathrm{d}t' \tag{2.44}$$

An expression for the constant C may then be derived, invoking the principle of energy conservation: in a given time period, the total intensity entering the cavity and that leaving the cavity must be in balance. This analysis yields $C = 1/\tau(\nu)$. Substituting this into equation 2.44 and integrating:

$$I_{trans}(\nu, t) = I_0[1 + \gamma(\nu)\sin(\omega t + \phi(\nu))] \tag{2.45}$$

with:

$$\gamma(\nu) = \frac{\beta(\nu)}{\sqrt{1 + \omega^2 t^2(\nu)}} \tag{2.46}$$

This analysis eventually yields an expression for the phase-shift experienced by the light, $\phi(\nu)$, in terms of the frequency-dependent ring-down time of the cavity, $\tau(\nu)$:

$$\phi(\nu) = \arctan[-\omega\tau(\nu)] \tag{2.47}$$

Accordingly, we can obtain an expression for the frequency-dependent absorption coefficient by substituting equation 2.47 into equation 2.34:

$$\alpha(\nu) = \frac{\omega}{c}\left(\frac{1}{\tan\phi(\nu)} - \frac{1}{\tan\phi_0(\nu)}\right) \tag{2.48}$$

where ϕ and ϕ_0 are the phase shifts experienced respectively for an empty cavity and with absorber present.

Lewis *et al.* [124] report that their PS-CRDS setup was sufficiently sensitive to allow measurements on methane gas down to a concentration of 5×10^{17} molecules/cm^{-3}. Amplified spontaneous emission (ASE) from a diode laser can pose a problem for the sensitivity of PS-CRDS measurements, but van Helden *et al.* [127] showed that this can be accounted for quantitatively in the analysis of a PS-CRDS experiment. An example spectrum from their work on oxygen detection by PS-CRDS is shown in Figure 2.9.

2.3.5 Broadband Cavity-Enhanced Spectroscopies

The advantages of high sensitivity brought by cavity-enhanced techniques have also been combined with the throughput advantage associated with broadband light sources. Especially when combined with the multiplexed detection approaches pioneered by Ball and Jones [17], these methods may present a rapid and economical detection tool for a whole variety of analytical problems. Principally, the advantageous aspects of these techniques arise out of the fact that the sources may in some cases be very cheap – light-emitting diodes (LEDs) are typically available for a few pence – and that complete spectra, sometimes corresponding to several vibrational bands, may be acquired very rapidly [11].

A variety of different broadband light sources has been employed, including pulsed dye lasers for atmospheric NO_3 and I_2 detection [129], xenon arc lamps [130] and an arc discharge plasma [131]. Work using LEDs has been demonstrated across the visible region [132–134] to provide an especially expedient and economical setup.

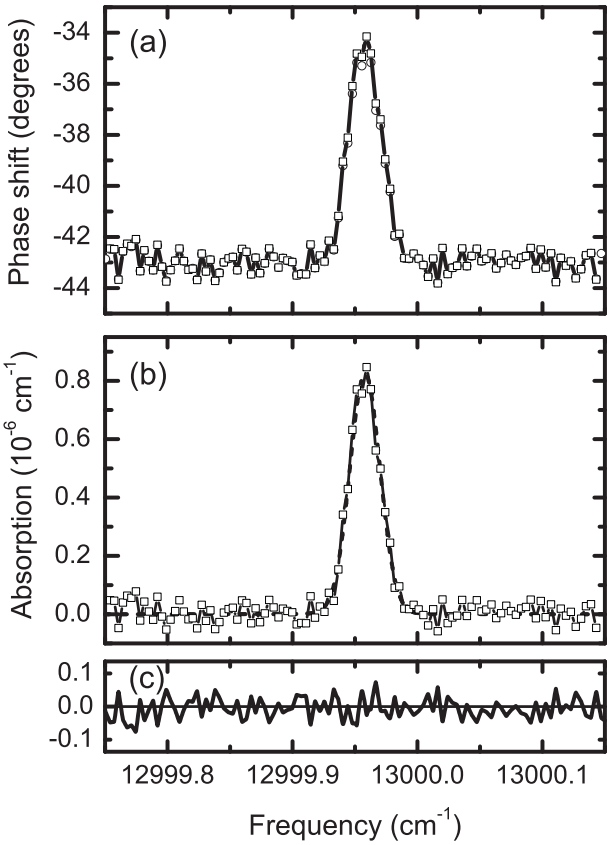

Figure 2.9: Experimental PS-CRDS spectrum (a), and simulation (b) based on HITRAN [128] data, of the ^{P}P(29,29) transition in the $b \leftarrow X$ band of O_2. (c) shows the difference between the experimental and simulated results, which is small, and therefore indicates the high performance of this technique. Reproduced from the work of van Helden *et al.* [127].

For the detection, several options have been presented in the literature: Czyzewski *et al.* [135] dispersed the broadband cavity output of a YAG-pumped pulsed dye laser through a spectrograph, and then image the transmitted light using a gated CCD camera. However, such a measurement is built up over a series of pulses, and so this method is still subject to shot-to-shot fluctuations in laser intensity, thereby losing one of the greatest advantages of the CRDS technique.

In order to retain this advantage, and obtain a full CRDS decay signal with each laser shot, Scherer [136] proposed a technique he called *ringdown spectral photography*, recording the time and frequency responses along orthogonal axes of a two-dimensional CCD detection array. The cavity output radiation is aligned to hit

a rotating mirror and then a diffraction grating before it reaches the CCD array; the mirror and the grating respectively disperse the signal with time and wavelength, in mutually perpendicular directions. With Scherer's system, a resolution of $1.5\,\mathrm{cm}^{-1}$ was achieved, limited by the speed of rotation of the mirror and the CCD pixel density. An alternative approach was put forward by Ball *et al.* [17, 129], who used a clocked CCD array. The clocked array shifts the captured image down to the next row of pixels every time a new shot is taken – in Ball's work, this was once every 0.5 μs – thereby giving a time-resolved series of images from which a ring-down decay trace can be calculated. Similarly to the Scherer [136] approach, this yields a two-dimensional output with time-dependent information along one axis, and wavelength-dependent information along the perpendicular axis. Others have coupled the cavity output into a commercial Fourier-Transform infrared (FTIR) spectrometer for analysis [137].

One difficulty associated with these broadband sources is that whilst the total power over a broad frequency range may be considerable, the spectral density (often informally quoted in mW/nm) often corresponds to a rather low-power source across the width of an absorption transition. The near-infrared work of Orphal and Ruth [137] employed a Xe-arc source in an incoherent BB-CEAS experiment; the combination of the low spectral power density of the lamp and modest mirror reflectivities meant that data acquisition over several hours was required to build up a high-resolution spectrum with a sensitivity of $\alpha_{min} \sim 10^{-6} - 10^{-5}\,\mathrm{cm}^{-1}\mathrm{Hz}^{-1/2}$ [137]. Recent work in this group has employed a higher-density source in the form of a superluminescent LED (SLED) for near-infrared BB-CEAS with both a dispersive spectrometer and an FT-interferometer, and has achieved a minimum detectable absorption coefficient of $\sim 10^{-8}\,\mathrm{cm}^{-1}$ in an acquisition time of several minutes. Super-continuum sources provide a broadband source at high spectral density [138, 139], and which may therefore offer an ideal high-power, broadband source for cavity-enhanced spectroscopic methods, especially for applications in the visible region. Though these sources are currently somewhat expensive, they has already

been applied with success to cavity-enhanced absorption spectroscopy by Johnston and Lehmann [140], and by Langridge *et al.* [141], and they provide an exciting alternative to the lower-spectral-density broadband sources used previously, with the potential to study interfaces and condensed phase samples [142–144].

A further broadband cavity technique of interest uses optical frequency combs for cavity-enhanced spectroscopic detection [145–147]. Thorpe *et al.* [145] used such a system to extract simultaneous ring-down measurements from 125,000 individual modes of the sample cavity, taking a high-sensitivity spectrum over 100 nm in the visible and near-infrared. The rapid data acquisition that is possible with such a technique lends it to some interesting time-resolved applications; Thorpe *et al.* [145] demonstrated their system by examining collision-induced population redistributions in C_2H_2, O_2, H_2O, and NH_3. Gohle *et al.* [148] applied frequency combs to Vernier spectroscopy of oxygen close to 760 nm, whilst Mandon *et al.* [149] carried out Fourier-transform spectroscopy with a comb setup to study the overtone region of the acetylene spectrum close to 1.5μm.

2.4 Locked Cavities

One strategy for improving the signal-to-noise in a cavity-enhanced spectroscopy experiment lies in locking the laser wavelength and cavity to one another so that they are held in resonance throughout the experiment. This results in a greater power build-up into each mode of the cavity, thereby reducing the effect of laser noise on the transmitted cavity modes relative to the size of the signal [70]. Particularly, the shot-noise limit is reduced since the light levels being detected are typically much greater; this also allows a ring-down trace to be recorded over a longer timescale, which brings advantages for the fitting procedure. Locked techniques confer the additional advantage of detection on a single, stable mode, meaning that a smaller spread of ring-down times is generally measured, allowing for a more accurate fit to a single exponential decay. Where it is the time-integrated cavity output that is being measured, rather than a ring-down measurement, a cavity-locked approach brings

about larger signals and all but eliminates the effects of residual mode structure [58]. However, locking of a diode laser to a cavity mode (especially for cavities of very high finesse) is not necessarily straightforward, principally owing to the bandwidth mismatch between the two [11, 58]. A variety of schemes has been proposed for the locking process, and this section very briefly surveys some of these approaches.

2.4.1 Electronically-Locked Systems

Locked cavity-enhanced spectroscopy was first reported by Nakagawa *et al.* [150], using a diode-laser-pumped YAG laser to probe weak acetylene transitions close to 1.064 μm, and was later implemented by Gianfrani *et al.* [151] for ultra-sensitive heterodyne measurements on molecular oxygen close to 763 nm. In Gianfrani's work, the laser was scanned continuously through a Doppler-broadened absorption, with a total scan width of approximately 8 GHz, and simultaneous detection was carried out at the carrier and FSR frequencies. Using this method, Gianfrani *et al.* [151] achieved a minimum detectable absorption of $6.9 \times 10^{-11}\,\mathrm{cm^{-1}Hz^{-1/2}}$ in a 26 cm cavity with a finesse of approximately 6000.

Pound-Drever-Hall locking [152, 153] has been applied to cw-CRDS using three-mirror triangular ring cavity arrangements by Paldus *et al.* [154] and Spence *et al.* [155], and then in a simple two-mirror linear configuration by Ye *et al.* [156] and van Leeuwen *et al.* [157]. Ultimate sensitivities as low as $8.8 \times 10^{-12}\,\mathrm{cm^{-1}Hz^{-1/2}}$ have been reported for such systems. However, the electronics and other components required to bring about the Pound-Drever-Hall locking may be very complex to implement and maintain, and so this sort of system is generally only implemented for the most challenging of detection problems.

2.4.2 Optical Locking

One simpler approach for achieving maintenance of the laser in resonance with the optical cavity is through passive optical locking [158–160]. It relies upon laser self-locking, due to *injection seeding* by the frequency-selected optical feedback from the

optical cavity. This reduces the laser's line width and locks its frequency to that of a cavity mode centre. These methods are introduced more fully in Chapter 3, where its implementation in a sensitive near-infrared spectrometer is reported.

2.4.3 Ultra-Sensitive Heterodyne CEAS: NICE-OHMS

The most sensitive cavity-enhanced detection work reported so far has been achieved through the technique of noise-immune cavity-enhanced optical heterodyne molecular spectroscopy (NICE-OHMS) [53, 77, 161–166]. First put forward by Ye *et al.* [53], NICE-OHMS was developed to overcome the problems associated with wavelength-jitter on the probe laser [70], and is essentially a combination of frequency modulation spectroscopy (FMS) and CEAS. However, the combination of those two techniques brings extra complexities; the modulation must be set so that the frequency-spacing between the carrier frequency and the sidebands is fixed at the cavity free spectral range. This means that, when transmitted through the optical cavity, the sidebands and carrier are all subject to equal cavity-enhancement; any fluctuations in the laser output are therefore detected equally in the sidebands *and* the carrier. After demodulation at the original modulation frequency, any such noise will therefore be eliminated from the signal. A second Pound-Drever-Hall-type locking loop holds the laser carrier frequency at the cavity mode centre to keep it fully in resonance throughout the experiment, with the cavity length (and the modulation frequency, continuously locked to the FSR) being scanned to probe the spectrum. The general features of such a NICE-OHMS experiment are represented in Figure 2.10.

The NICE-OHMS signal is finally demodulated at the 60 Hz frequency of the WMS-like modulation applied by the cavity PZT. The transmitted sidebands are of opposite phase, and therefore cancel in the absence of any absorber. However, if any absorber is present, then differential absorption on the two sidebands will give rise to their having different amplitudes in the cavity transmission, and the resulting overall phase shift alters the demodulated signal. The technique does not depend on

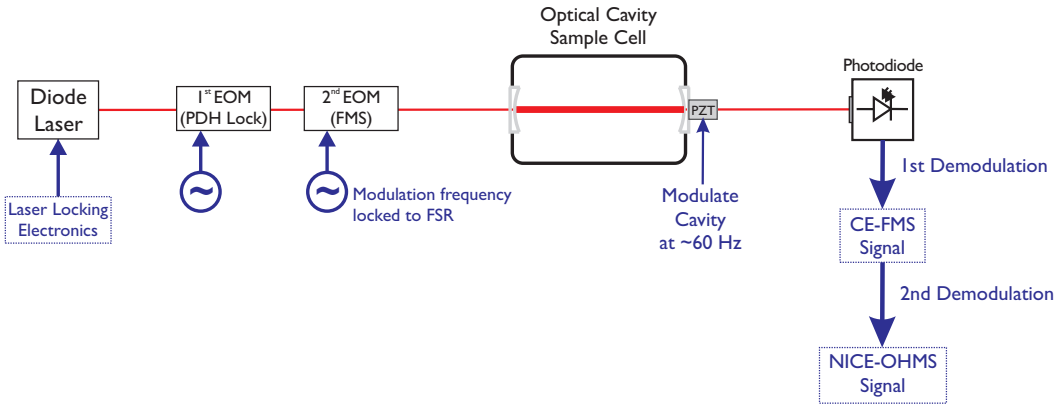

Figure 2.10: Flow diagram denoting the key stages in a NICE-OHMS experiment.

the quality of the laser locking. Noise on the frequency of the laser jitters the entire FM triplet, and so the final demodulated signal will not incorporate any of this jitter; this is why the technique is referred to as *noise-immune*. The performance of a NICE-OHMS spectrometer may be limited by residual amplitude modulation (RAM), though there exist strategies to minimise the contribution that it makes to the signal [166]. Since this is a method that, when optimised, is genuinely shot-noise limited, it can achieve the ultimate low sensitivities, and a minimum detectable absorption of $1 \times 10^{-14}\,\mathrm{cm^{-1}Hz^{-1/2}}$ was reported by Ye *et al.* [53]. However, no other implementation of NICE-OHMS [163–166] has been able to replicate this number, and the multiple layers of electronic locking make this a technique that is expensive and cumbersome in implementation, and somewhat too fragile for many field applications.

2.5 Summary

The burgeoning literature relating to use of optical cavities in absorption spectroscopy is a testament to these techniques' ubiquity. Cavity-enhanced methods of absorption spectroscopy have given rise to an array of tools for many different detection problems. This chapter has surveyed some of the most important of these

methods, from the most expedient and economical methods in CEAS and cw-CRDS to the ultra-sensitive experiments using the intricate heterodyne techniques such as NICE-OHMS.

Cavity-enhanced methods lend themselves to use of a variety of different light sources, including the most convenient and economical diode lasers. The ability to achieve very impressive sensitivities with even the most compact and economical of lasers recommends cavity-enhanced spectroscopy as a technique for a whole variety of the most important and stimulating detection problems. Some of these have been encountered in this chapter, in the medical, environmental, physical and chemical fields, but there are many more uses to which these techniques have been applied, and the number is only likely to grow further.

Chapter 3

OF-CEAS I: Background and Development

This chapter details the development of an optical feedback cavity-enhanced absorption spectroscopy (OF-CEAS) apparatus; initially, this is demonstrated by the detection of atmospheric water absorptions close to 1596 nm. Further optimisation and application of the OF-CEAS spectrometer will be demonstrated: specifically, the apparatus will be applied to the sensitive detection of carbon dioxide absorptions suitable as a diagnostic aid in identifying *Heliobacter pylori* infection. The work presented in this chapter was published in an article in *The Analyst* [167].

3.1 Background

As illustrated in Chapter 2, the extent of the sensitivity enhancement associated with a CEAS experiment can be improved by increasing the coupling efficiency of the light into each mode of the cavity to obtain higher signal levels, and actively locking the cavity length so that, as the laser is scanned across the spectral region, it remains resonant with a single mode of the cavity [151]. The high-speed electronics required to achieve this level of locking are complex, however; they may add considerable expense to the setup, and make it less robust and more difficult to use. It is the aim of the work presented in this chapter to offer an alternative, passive technique based

upon self-locking of the diode laser by optical feedback from the external cavity.

Morville *et al.* [158] first demonstrated Optical Feedback CEAS (OF-CEAS) for measurements of atmospheric water and real-time monitoring of hydrogen fluoride, using a diode laser centred near 1312 nm. Their OF-CEAS system was later extended to detection of methane [168] and nitrogen dioxide [169], as well as to airborne water isotope measurements [170]. Members of that group later collaborated with Wehr *et al.* [171] to apply OF-CEAS to carbon isotope measurements close to 2 μm. A full physical characterisation of the optical feedback CEAS technique was presented recently by Motto-Ros *et al.* [172].

In this technique, alluded to in section 2.4.2, a standard two-mirror optical cavity is "folded" into a V-shaped arrangement by addition of a third cavity mirror. The light from the laser is then injected through the external face of this folding mirror and along one "arm" of the V-shape. In this configuration the direct reflection from the optical cavity is directed away from the path of the incident light, but the light that is resonant with a cavity mode can oscillate within the cavity and then exit the folding mirror to retrace the incident light path, back into the laser. Thus, feedback of light to the laser active medium occurs at frequencies corresponding to the modes of the cavity. If this light is of the correct phase, an *injection seeding* effect brings about a narrowing in the laser line width, and an accompanying locking of the laser frequency to the centres of the cavity modes. As the laser is swept across the frequency range of interest, the laser emits at successive modes of the V-shaped cavity, spending negligible time in between [158].

The line width reduction allows successive modes of the cavity to be observed cleanly in the transmitted light. Accordingly, a significantly enhanced light intensity is seen coupled into each mode. An absorption spectrum may then be measured by recording the maxima of the successive transmitted cavity modes across a laser scan. Pairs of consecutive cavity modes are spaced consistently by the well-defined free spectral range (FSR) of the cavity, given by $c/2L$ where L is the total cavity length (as such, L is the sum of the arm lengths in the V-shaped cavity). Spectra resulting

from an OF-CEAS system are therefore ready-calibrated for relative frequency. A single well-characterised transition centre is then all that is required to achieve an absolute and accurate frequency scale for each spectrum.

The related technique of cavity ring-down spectroscopy (CRDS), involving a rapid measurement of the lifetime of a light field inside the cavity, has also been employed by others using such a V-shaped cavity system. Optical feedback-locked CRDS (OF-CRDS) [68] has been applied to detection on weak absorption lines in the oxygen *B*-band [173], and also to characterisation of the light extinction due to single aerosol particles [174].

This chapter presents the development and implementation of an OF-CEAS system using a DFB-DL centred close to 1596 nm (*i.e.* within the optical communications *L*-band). This setup offers significant gains in sensitivity compared to traditional absorption spectroscopy, whilst avoiding some of the disadvantages of experimental complexity, expense and fragility associated with the ultra-sensitive modulation-based optical cavity techniques such as NICE-OHMS [53, 77, 161–166] and locked-cavity optical heterodyne ring-down spectroscopy [175]. The sensitivity and expediency of the system are demonstrated on relatively weak transitions of water in a sample of laboratory air, and on samples of carbon dioxide with the motivation to measure $^{13}CO_2$ and $^{12}CO_2$ concentrations.

3.2 Feedback Injection to a Diode Laser

There exists a considerable literature describing the physics of optical feedback systems [176–180], and the use of optical feedback or optical injection from another laser to seed semiconductor lasers is the subject of a substantial and comprehensive review by Tartwijk and Lenstra [181]. A full review of that scale will not be repeated here, but it is the aim of this section to highlight features of the optical feedback injection seeding mechanism, including a description of how it brings about *linewidth narrowing* and *frequency locking* effects, that are pertinent to the detection work presented in this chapter.

The action of external optical feedback upon a diode laser may give rise to a complex array of (often unwanted) perturbations observed in the diode laser output light. However, selected feedback of part of the emitted light into the laser medium is a technique which has been used widely for stabilisation and line width narrowing of the light from a diode laser [181–183]. Typically, a wavelength-selective element such as an external optical cavity [182–185] or a grating [186] is used to filter the light so that only the "useful" light is included in the feedback. This optical filtering has also been carried out by polarisation spectroscopy, as for example in the work of Liu *et al.* [187] and Kozuma *et al.* [188].

The light which is fed back into the active medium of the laser may then itself stimulate that medium; the resulting stimulated emission will share its phase, wavelength and direction with the feedback radiation [14]. Increasingly, over several cycles of feedback and stimulated emission, the emission from the laser comes to resemble the feedback radiation. By using a wavelength-selective element such as a grating or cavity to supply optical feedback to the laser medium, the output radiation from the laser can be controlled, and the laser caused to emit preferentially at a series of pre-determined wavelengths. This *injection seeding* effect is key to the OF-CEAS technique.

When an external optical resonator has been employed for selective feedback, it has ordinarily been configured in a confocal arrangement [182–185]. The present work, in common with that of Morville [158], adopts a V-shaped external optical cavity to effect the wavelength selection. The choice of a V-shaped external cavity confers several advantages with respect to use of either a grating or a confocal cavity arrangement. Firstly, use of a grating generally allows only relatively coarse wavelength selection, bringing about less effective frequency locking, and therefore reducing the advantage conferred by a relatively monochromatic feedback-locked source for an absorption spectroscopy experiment. Secondly, the cavity arrangement allows the use of very high-reflectivity mirrors which not only further narrow the width of the resulting cavity resonances which will comprise the feedback radiation,

but may also be used to achieve a path length enhancement through the absorption sample. Specifically, with respect to the confocal cavity configuration, a V-cavity setup allows the construction of a cavity of higher finesse; the tolerance required of the radius of curvature in a confocal setup rapidly becomes unworkable in systems of very high finesse [158]. In such a system, several transverse modes are degenerate, and a V-shaped trajectory comprising a superposition of several transverse modes allows for construction of an optical feedback setup. However, as the cavity finesse is increased, the concomitant decrease in the modes' widths makes the degeneracy condition less likely to be fulfilled, and therefore the superposition becomes more difficult to achieve. The V-cavity allows for relatively small mirror surfaces, even with long cavity arm lengths (which, as we shall see later, bring increased sensitivity and spectral resolution), in turn allowing for the use of cheaper substrates as well as the sensitive measurement of relatively small sample volumes.

The wavelength-selected optical feedback then causes a reduction in the laser line width and an effective lock to the wavelength at the centre of each resonant mode of the cavity. As such, when the laser is scanned across the spectral range of interest, a persistent, high signal-to-noise signal is observed for each resonant mode of the external cavity, with the laser being dragged straight from one mode centre to the next, and spending negligible time at the wavelengths in between.

3.2.1 Contributions to Diode Laser Line Width

The coherence time of a diode laser is typically only on the order of a microsecond. This is directly connected with the laser line width; in the case of an exponential coherence decay, as might be observed in a laser subject to no technical noise sources, it is related to the Lorentzian laser linewidth through:

$$\Delta\nu_{Lorentz} = \frac{1}{\pi\tau_{coh}} \tag{3.1}$$

where τ_{coh} is the coherence time. Correspondingly, the emission line width (*i.e.* the

FWHM width of the laser spectrum) is typically on the order of a few MHz for this type of laser. The resonator within a diode laser typically comprises two relatively low-reflectivity surfaces, often including a polished face of the semiconductor chip as one "mirror". As such, the losses associated with the resonator within a diode laser are typically quite large, but they are usually compensated for by a high level of gain in the active medium. One by-product of this arrangement is that the spontaneous emission rate is generally high. In contrast to the stimulated emission which provides the coherent laser radiation, spontaneous emission occurs with random phase and direction. The high level of spontaneous emission therefore provides a lower limit to the laser line width, $\Delta\nu_{laser}$. This contribution is described by the Schawlow-Townes equation [189]:

$$\Delta\nu_{laser} = \frac{\pi h\nu(\Delta\nu_c)^2}{P_{out}} \tag{3.2}$$

with photon energy $h\nu$, $\Delta\nu_c$ denoting the FWHM bandwidth of the laser resonator, and P_{out} the laser output power. This has been expressed more generally [190] as:

$$\Delta\nu_{laser} = \frac{h\nu\,\theta\,I_{tot}\,T_{oc}}{4\pi\,T_{rt}^2\,P_{out}} \tag{3.3}$$

where T_{oc} denotes the output coupler transmission, I_{tot} the total losses due to the laser resonator, T_{rt} the resonator round-trip time, and θ is a *spontaneous emission factor* which takes into account the level of spontaneous emission particular to the type of laser system being described.

It is not just spontaneous emission into the laser mode which gives rise to phase noise and the fundamental lower limit to the laser line width, however. The laser gain and the losses of the laser resonator contribute noise to the resulting intra-cavity light field. Indeed, if one were to replace the laser gain system with a notionally noiseless amplifier, the phase noise would only reach a limiting value of half that determined by the Schawlow-Townes equation [191].

The Schawlow-Townes limit has been shown to be approached by some solid-state laser systems, but for semiconductor lasers it ordinarily underestimates the

line width associated with the output laser radiation, even when there is minimal technical noise associated with the laser [159]. Henry [192] described the greater observed line widths in semiconductor laser diodes as the result of a coupling between the laser radiation intensity and the phase noise, owing to a dependence of the semiconductor's refractive index upon the carrier density. He included this intensity-phase coupling mechanism in his model for laser line width by introducing a *line width enhancement factor*, α, to account for it. In his model, α is simply a factor to describe the proportional relationship between changes in the emitted light's phase, and changes in the overall gain; it is also sometimes referred to as the *Henry factor* or the *phase-amplitude coefficient*. The resulting line width is increased by a factor of $(1 + \alpha^2)$ [192]. Semiconductor lasers generally have small, but non-zero, values for α associated with their emission spectra [54, 158, 193]; for a multi-quantum-well diode laser (MQW-DL), typically $\alpha \approx 1$, whereas for a heterostructure diode laser (HS-DL), depending on the semiconductor material, a typical value for the Henry factor is between three and eight [158].

3.2.2 The Effect of Optical Feedback: Line Width Narrowing and Frequency Locking

Allowing feedback of the full output of a diode laser into its active medium typically gives rise to a strongly perturbed, chaotic output with a short associated coherence time. In contrast, controlled optical feedback action, involving re-injection of the diode laser medium with frequency-selected light, may increase the coherence time associated with the laser radiation; when the light is frequency-selected finely by use of a high finesse optical cavity, re-injecting the cavity-resonant light may bring about an even greater improvement in the laser coherence.

A reduction is observed in the laser line width when subject to cavity-selected optical feedback; essentially, the optical cavity can be considered to be converting frequency-domain noise to amplitude fluctuation [158, 159, 194]. The initial output from the diode laser has relatively stable amplitude, but a substantial frequency

dispersion associated with it; in contrast, the transmitted light through an optical cavity has a very narrow frequency distribution – given by the cavity mode width, in turn determined by the cavity finesse – but relatively large fluctuations in amplitude. Once the cavity transmitted light is returned to the laser as feedback, these amplitude fluctuations are then damped by the laser medium, giving rise to light which has a narrower distribution of amplitudes *and* frequencies associated with it. This cavity-selected feedback may therefore very effectively carry out the injection seeding action described above at section 3.2, yielding relatively monochromatic light with little phase noise, a stabilised amplitude and a long coherence time.

There is an additional, highly useful, characteristic of the laser output resulting from such a selective optical feedback system. Over a relatively broad spread of values for its phase, the optical feedback also brings about a frequency locking effect, effectively holding the laser at the frequencies corresponding to the mode centres during a laser scan, and spending negligible time at the frequencies in between.

Ordinarily, during a laser scan without feedback, increasing the current supplied to the laser heats the active medium. This increase in temperature corresponds to an increased refractive index, and therefore to an increase in the effective laser cavity length; the result of all of this is that the laser emission is driven to longer wavelengths. However, when the optical feedback coupling is effective, at the mode centres the light is resonant not just within the laser cavity, but also within the external V-shaped optical cavity; the laser cavity has effectively been placed inside the larger external cavity. The effective laser cavity length now includes a much larger "unheated" section, which for a high-finesse external cavity is subject to a substantial path length up to the order of kilometres. At these wavelengths, then, corresponding to the centres of the modes of the external cavity, the effect of the current-induced heating is much smaller, as it is now only active upon a very small proportion of the total cavity length. As such, at these points, the heating effect is greatly slowed down, and so the laser is effectively stalled at the frequencies corresponding to the external cavity mode centres, allowing a signifcantly enhanced

intensity of light to couple into each mode as the laser is scanned across the region of interest.

3.3 Carbon dioxide

3.3.1 The spectroscopy of CO_2

Carbon dioxide is one of the most comprehensively studied molecules in the spectroscopy literature. It is a centrosymmetric linear triatomic molecule with $D_{\infty h}$ symmetry, and it has four fundamental vibrational modes, including a doubly-degenerate pair of bends. These fundamental vibrations are depicted in the following table:

ν_1	symmetric stretch	Σ_g^+ symmetry	1337 cm^{-1}	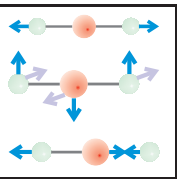
ν_2	doubly-degenerate bend	Π_u symmetry	667 cm^{-1}	
ν_3	anti-symmetric stretch	Σ_u^+ symmetry	2349 cm^{-1}	

Table 3.1: The fundamental vibrational modes of carbon dioxide.

Both the ν_2 and ν_3 vibrations are infrared-active, as both bring about a change in the molecular dipole moment; the *mutual exclusion rule* for centrosymmetric molecules implies that the remaining ν_1 vibration must therefore be active in the Raman spectrum [195, 196], and experimental observation has confirmed this [197, 198]. As further support for the assignment of these vibrational bands, the Π band is observed to have PQR structure – *i.e.* rotational branches corresponding to $\Delta J = \pm 1, 0$ – whilst the two Σ vibrational bands are observed to have PR structure ($\Delta J \neq 0$) [198].

The Raman spectrum of the ν_1 vibrational band in carbon dioxide is not a single band centred at 1337 cm^{-1}, but instead a pair of features at 1285 and 1388 cm^{-1} (whose average is the 1337 cm^{-1} symmetric frequency indicated above.) Fermi [199] provided the explanation for this splitting, noticing that the first overtone of the bending vibration, $2\nu_2 = 2 \times 667\text{cm}^{-1}$, lies very close in energy (at 1334

cm^{-1}) to the ν_1 fundamental (1337 cm^{-1}). A very small perturbation is therefore all that is required to bring about an interaction between these two, giving rise to wavefunctions for the new system composed of a linear combination of the original wavefunctions. Since the two interacting energies are so very close, and the resonance almost perfect, the new wavefunctions are composed almost exactly half-and-half of the original two. Accordingly, we expect the two Raman lines to be observed at roughly equal intensity, and that has indeed been seen to be the case [198]. This effect is often termed *Fermi resonance* [16]. The spectrum is further complicated by the fact that alternate rotational levels' transitions are missing from the spectrum; this is a nuclear spin-statistical effect that arises from the Pauli principle, and is discussed in more detail in sections 4.2.2 and 5.2.

It is the combination band ($3\nu_1 + \nu_3$) that is most conveniently located for the present detection study, with R-branch transitions being found in the region of $\sim 1.6\mu m$ for both the $^{12}CO_2$ and $^{13}CO_2$ isotopologues. For an isotopologue ratio measurement, the ideal spectral region contains strong transitions for each isotopologue within a small frequency range, accessible in a single diode laser scan, and largely free of interferences from other transitions due to other species. The full assignment for the transitions chosen for the present study is given at section 3.5.2.

3.3.2 Motivations for CO_2 detection

Carbon dioxide isotopologue measurements are becoming increasingly common for the rapid detection and diagnosis of certain medical conditions, and can be used as indicators of gastric emptying and liver function. By far the most familiar carbon isotope test is that for *Heliobacter pylori*, an important pathogen associated with many diseases of the gut, including gastritis, peptic ulcers and gastric cancers [10]. Its swift detection, diagnosis and eradication are considered essential for all patients with peptic ulcers. One method of *H. pylori* detection is known as the Urea Breath Test (UBT): ^{13}C-labelled urea is administered to the patient, whose breath is then monitored for the presence of $^{13}CO_2$. The *H. pylori* bacteria enzymatically cleave

the urea to release ammonia for local pH regulation, and in this process the carbon is oxidised to CO_2. Humans possess no such urease enzymes, and so the presence of elevated levels of $^{13}CO_2$ in the exhaled breath can reliably be attributed to the presence of the bacteria. An accurate method for determination of isotope ratios in a sample of CO_2 is therefore of substantial interest for medical application; for such a clinical measurement, this isotope ratio is typically quoted as a *delta* value:

$$\delta = \frac{\frac{[^{13}CO_2]}{[^{12}CO_2]} - \frac{[^{13}CO_2]^*}{[^{12}CO_2]^*}}{\frac{[^{13}CO_2]^*}{[^{12}CO_2]^*}} \tag{3.4}$$

wherein the asterisks denote a standard value of the isotope ratio, and the resulting delta value is ordinarily expressed in units "*per mil*" ($1‰ = 10^{-3}$).

3.4 Experimental

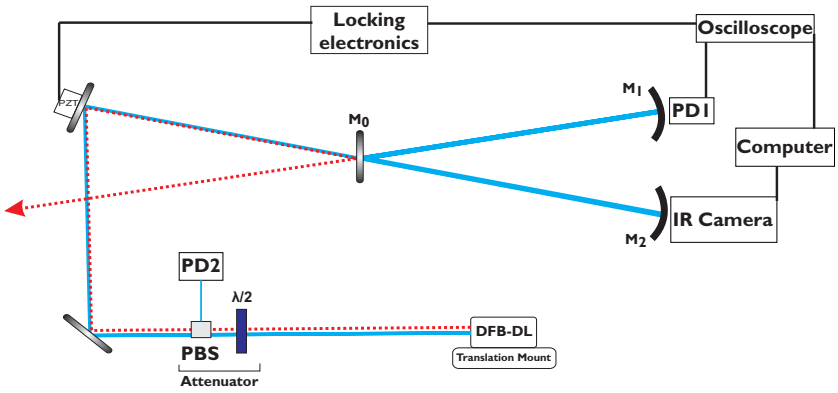

Figure 3.1: The OF-CEAS setup. PBS = Polarising Beamsplitter, DFB-DL - Distributed Feedback Diode Laser, $\lambda/2$ = Half-Waveplate, PZT = Piezoelectric Transducer and PD = Photodiode. The PZT is translated on a sufficiently small scale that the V-cavity alignment is not appreciably affected when the optical locking is active. The dotted line denotes the path of the majority of the incident light, which is reflected away from the cavity, and the accompanying solid line shows the path of the cavity-resonant light.

Our experimental arrangement is illustrated in Figure 3.1, and includes a DFB-DL centred at $\approx 1596\,\text{nm}$ [*Marconi-Bookham*] and driven by a commercial temper-

ature and current controller [*Thorlabs ITC-510*], connected to an integrated laser mount [*Thorlabs, LDM21*]. Coarse adjustment of the laser frequency is achieved by changing the DFB-DL temperature, and fine adjustments by altering the current. The DFB-DL is generally operated at the highest current possible, just below 200 mA, in order to maximise output power.

The three cavity mirrors [*Newport Supermirrors*] are supported upon standard finely-adjustable mounts [*Newport Ultima*], and the whole cavity assembly is housed within a stainless steel vacuum vessel. This vessel was constructed with several inlet/outlets to allow evacuation, throughput of several gases, and pressure monitoring all to be carried out.

The folding mirror, M_0, is separated from each of the other cavity mirrors, M_1 and M_2, by an equal cavity arm length ($L/2$) of approximately 75 cm. In general for a linear optical cavity, the mode described by transverse and longitudinal electric field indices, m, n and q has a frequency given by equation 2.21, wherein g_1 and g_2 are functions of the cavity length and the mirrors' radii of curvature r_1 and r_2, and are respectively given by $1-(L/r_1)$ and $1-(L/r_2)$. The values of m and n correspond to the numbers of spatial (transverse) nodes in the two directions perpendicular to the cavity axis, and q to the longitudinal mode number. In our OF-CEAS experiment, we treat the cavity as a folded linear cavity, having mode frequencies described by equation 2.21; the cavity is aligned for dominant excitation of the TEM_{00} modes, with $m = n = 0$. The frequencies of these modes are separated consistently by the cavity free spectral range (FSR), and are given by $qc/2L$. However, the frequency spacing for low order transverse modes arising from equation 2.21 is also considered when designing the cavity; a lack of significant interference between the TEM_{00} modes and other lower-order transverse modes makes for a satisfactory choice of cavity configuration.

A long absorption cavity confers the advantages not just of increased path length, but also of better spectral resolution. Since we measure one spectral point every free spectral range of the V-cavity, and that FSR is inversely related to the cavity

length, a longer cavity allows us to acquire more points across a given absorption line. A further limitation on the choice of cavity length arises when we consider its optical stability; the relevant condition for a linear cavity with mirrors having radii of curvature r_1 and r_2 spaced by length L is:

$$0 < \left(1 - \frac{L}{r_1}\right)\left(1 - \frac{L}{r_2}\right) < 1 \tag{3.5}$$

In the experiments described in the present chapter, the folding mirror is planar, and the other two mirrors have a radius of curvature of 1 m, meaning that we can apply the stability condition 3.5 directly, as if to a two-mirror system. The overall cavity length is 1.48 m, so the relevant stability product is 0.2401, and the cavity configuration is stable.

Alignment of the setup is carried out using a visible helium-neon (HeNe) laser injected through the cavity mirror at the end of an arm of the cavity, and then aligned counter-propagating to the infrared light between the folding mirror and the laser. Reflections of the visible light are used approximately to align the cavity, and then fine alignment of the cavity mirrors is carried out while observing the light transmitted through the cavity onto the infrared camera [*Electronviewer Micronviewer 7290A*] and infrared indium gallium arsenide (InGaAs) photodiode 1 [*Thorlabs, DET-410*]. In this way, the cavity is aligned for primary excitation of the TEM_{00} mode.

For spectral acquisition, the cavity transmission is recorded on photodiode 1, and the light intensity on photodiode 2 is recorded simultaneously; both photodiodes are connected to a digital oscilloscope [*Tektronix TDS2014*], with 8-bit digitisation resolution. These data are then transferred, using a GPIB interface, to a personal computer for processing. Data acquisition is initiated and controlled by a data treatment routine programmed with LabVIEW. It is the *ratio* of the signals on photodiodes 1 and 2 that is measured, to eliminate the effects of intensity noise in the analysed spectrum.

For each of the OF-CEAS experiments, a laser scan rate is chosen to minimise the

data acquisition time whilst allowing sufficient time for a substantial amount of light to build up within the cavity. For the water detection work, for example, a peak-to-peak triangular ramp of 1 V was applied using a function generator [*TTi, TG230*] set at a frequency of 3.17 Hz; this produced a laser scan across approximately 175 modes (0.59 cm^{-1}) locking to each mode for approximately 250 μs, considerably in excess of the cavity ring-down time (our finesse of ≈ 3500 corresponds to a ring-down time of ≈ 11 μs).

3.4.1 Controlling the optical feedback

The level of optical feedback to the laser is controlled, using an attenuator comprising a half waveplate and a polarising beamsplitter, to ensure that each successive TEM_{00} mode is seen during a scan, whilst maximising the time spent in resonance with each mode. Morville *et al.* [158] reported that they produced the best data when each mode was in resonance for a time close to 500 μs.

Maintenance of the correct phase of the feedback radiation at the frequency of a given mode is also crucial. The optical feedback to the laser must be of the correct phase so that the laser operation is seeded and locked at the cavity mode centre frequencies; if it is not, then it merely disrupts correct operation of the laser at that mode. Furthermore, if the light returning to the laser is out of phase with the original laser output, then destructive interference will occur and will deplete the intensity of light reaching the cavity [158]. The laser-cavity distance needs to be maintained at a precise integer-multiple of the cavity arm length throughout a laser scan; otherwise, the resulting cavity transmission shows a beating effect, so that only groups of modes are visible with markedly varying intensities. The symmetries of the modes are also affected; when the phase relationship is correct, the appearance of each TEM_{00} mode transmission is symmetric about its frequency centre. Where the laser-cavity distance is not optimised, and groups of modes due to the beating effect are observed, each mode's transmission maximum is shifted towards the centre of the mode group.

Morville *et al.* [158] showed that the feedback phase is optimal when the laser-cavity distance reaches $kL/2$, with k an integer. Where k is odd, all longitudinal modes of the cavity have optimal feedback phase, whilst for an arrangement with even k, every other longitudinal mode has optimal feedback and the alternate modes are out of phase, consequently halving the OF-CEAS spectral resolution.

In the work described in this chapter, the laser-cavity distance is maintained at $3L/2$ by an electronic servo loop, which actuates the piezoelectric transducer (PZT). A schematic illustration of the electronic servo loop is given in Figure 3.2.

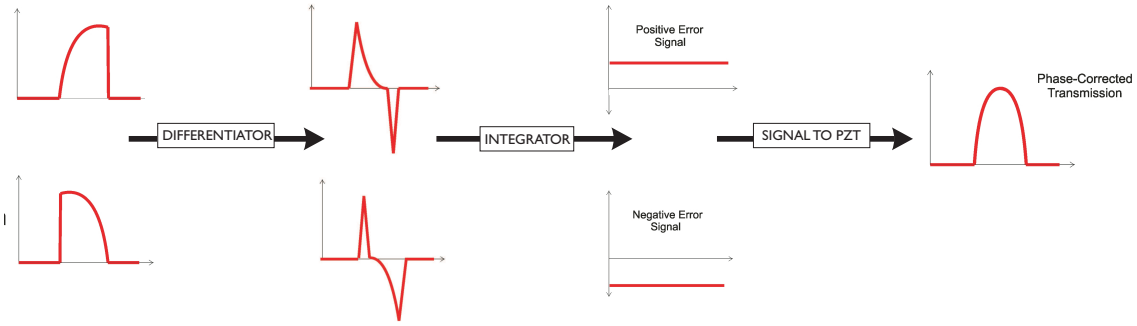

Figure 3.2: A schematic illustration of the electronic servo loop employed for the OF-CEAS feedback phase control. In each case, the sketched plots are of signal intensity against time, as would be observed on the oscilloscope within our experimental setup.

In essence, the cavity transmission is rapidly differentiated and then slowly integrated to generate an error signal; this signal will be zero where the modes are symmetric, and will be non-zero where they are asymmetric. The polarity of this error signal is dependent upon the direction of the asymmetry, and therefore indicates the direction in which the phase needs to be adjusted to maintain resonance between the laser and the cavity modes. A simple feedback loop then supplies the appropriate correcting voltage to the PZT, and translates the steering mirror; this maintains the correct laser-cavity distance throughout the experiment, so that all modes remain in phase.

The servo loop is composed of two major circuits: the first (the "feedback circuit") takes the signal from the photodiode after the cavity and analyses it for the

symmetry of the modes to generate the appropriate error signal, whilst the second (the "lock" circuit) acts in response to the error signal, generating an error signal to cause the piezoelectric transducer to move in the appropriate direction. An annotated version of the circuit diagram for the feedback circuit is shown as Figure 3.3; Figure 3.4 shows the locking circuit, similarly annotated.

The circuit diagrams without annotations, together with that for the servo loop power supply, are found in Appendix C. Two important elements which are included in the feedback circuit are the baseline noise reduction stage, and a saturation stage. The first is carried out by an operational amplifier ("op-amp") clearly indicated in the annotated circuit diagram of Figure 3.3; the workings and uses of op-amps are described in Appendix C. The function of this first op-amp involves the application of a modest negative offset, and then the removal of all signal below zero. This allows removal of the noise on the signal baseline, including any small resonances observed corresponding with other higher-order modes of the optical cavity. The saturation step is carried out by altering the gain across the amplifier immediately following the differentiator op-amp; this is adjusted by altering the ratio in resistances between R7 and R8. The signal is amplified until it saturates; this eliminates the very fast, sharp spikes at the maximum and minimum of the differentiated signal, and instead leaves an amplified part of the signal corresponding to the top of each cavity mode in the cavity transmission. It is the symmetry of these mode tops in which we are most interested, and so this saturation step allows the correction to be focussed on the most useful part of the transmission signal. This step is illustrated schematically in Figure 3.5, showing the form of the oscilloscope trace (intensity *vs.* time) corresponding to the differential of a single cavity mode, before and after the saturating amplifier.

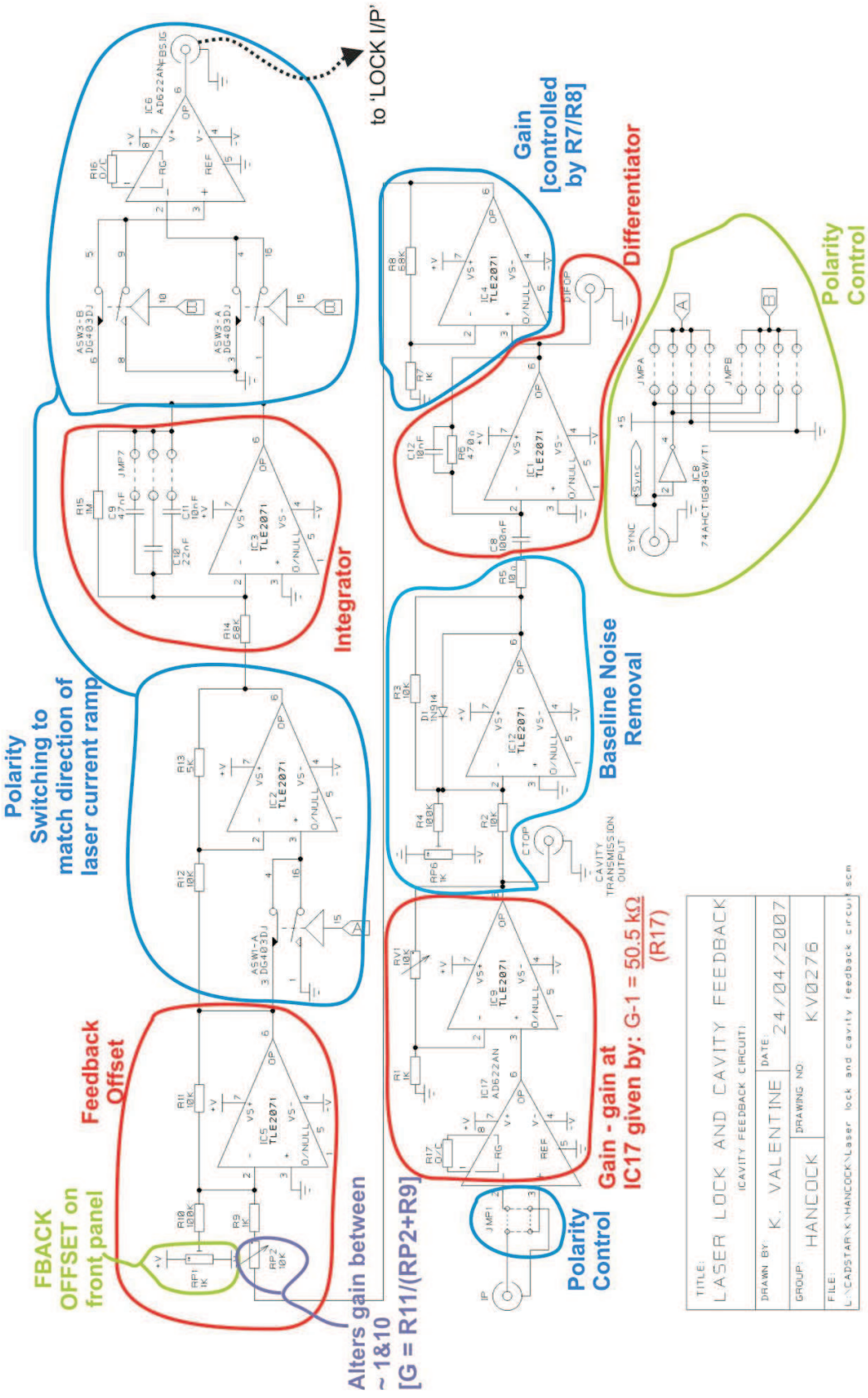

Figure 3.3: Annotated circuit diagram for the feedback circuit within the electronic servo loop for optical feedback phase control.

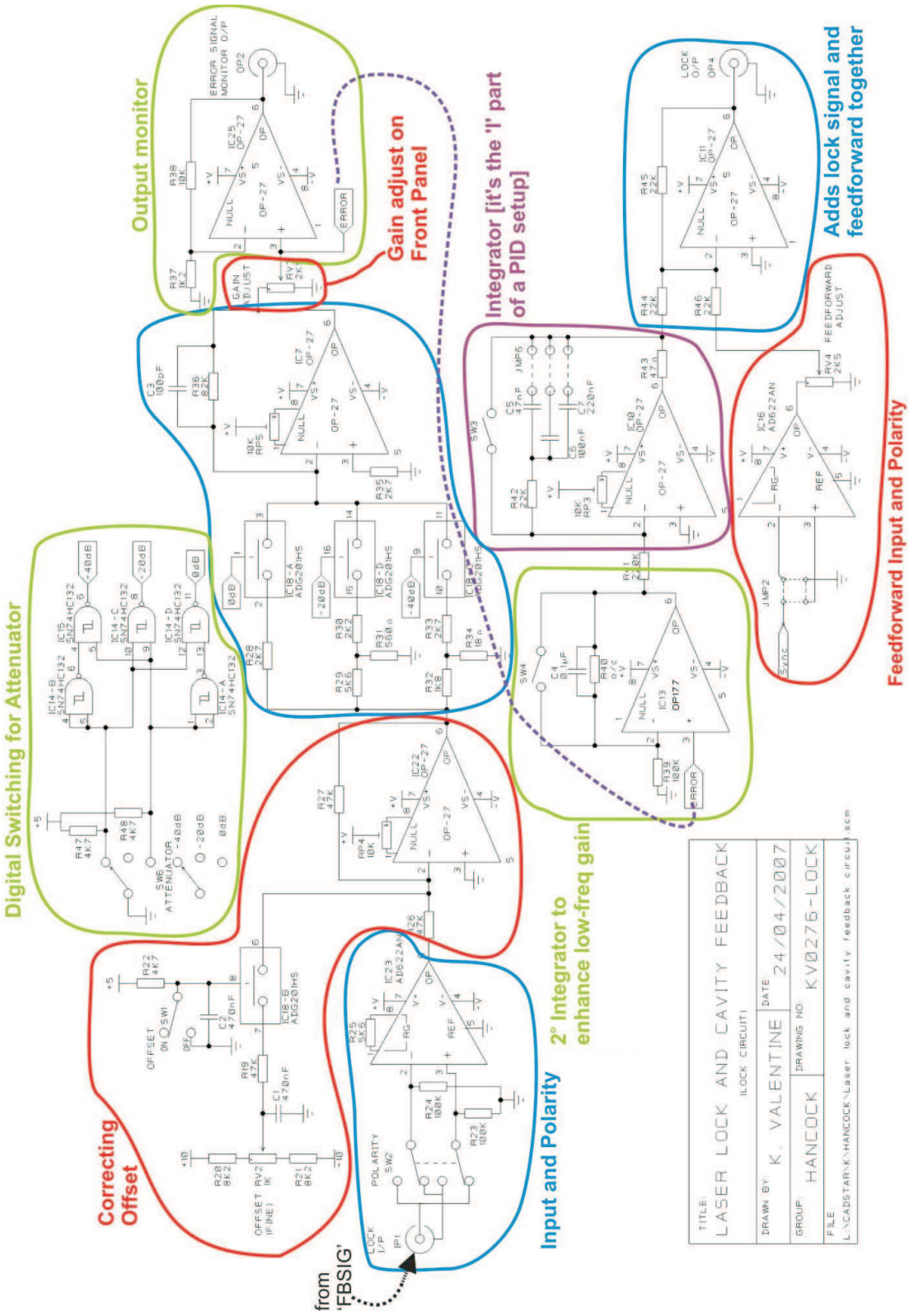

Figure 3.4: Annotated circuit diagram for the lock circuit within the same electronic servo loop.

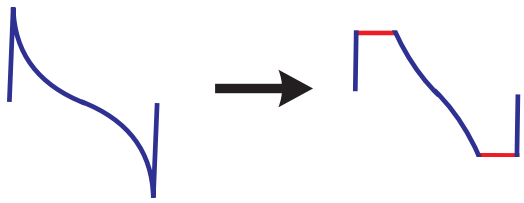

Figure 3.5: Illustration showing the form of the oscilloscope trace corresponding to a single cavity mode after differentiation, giving the signal before and after the saturating amplifier.

As alluded to above, the *level* of the optical feedback must carefully be controlled as well as its phase; too low a feedback rate produces insufficient locking. In this case, the laser does not lock to the cavity modes for very long, and so the benefit of the long cavity power build-up in each mode is not properly realised. If the feedback rate is very low, competition from modes other than TEM_{00} may also be observed, obscuring the spectrum and making analysis more difficult. Conversely, when the feedback rate is too great, the locking range – *i.e.* the region throughout which frequency locking is seen to a particular mode centre – may exceed the free spectral range of the cavity. When this occurs, modes may be missed entirely from the transmission, meaning that an accurate spectrum becomes all but impossible to obtain. In the limit of excessive feedback, the output appears chaotic, with little evidence of any mode structure.

The evolution in the V-cavity transmission with increasing feedback level is shown in Figure 3.6. This optical feedback level is altered using the attenuator, comprising the half-waveplate and the polarising beamsplitter shown in Figure 3.1. First, the optical isolator (if used) is detuned to allow some feedback, usually to an amount slightly greater than the desired level. The half-waveplate within the attenuator is then rotated until an optimal feedback level is achieved; this is the feedback level which produces modes sufficiently wide in time that minimal time is spent at the frequencies between, indicating a locking range approaching, but exceeded by, the V-cavity free spectral range. As such, this allows the optimal combination of a high degree of optical locking conferring high signal to noise on the transmitted

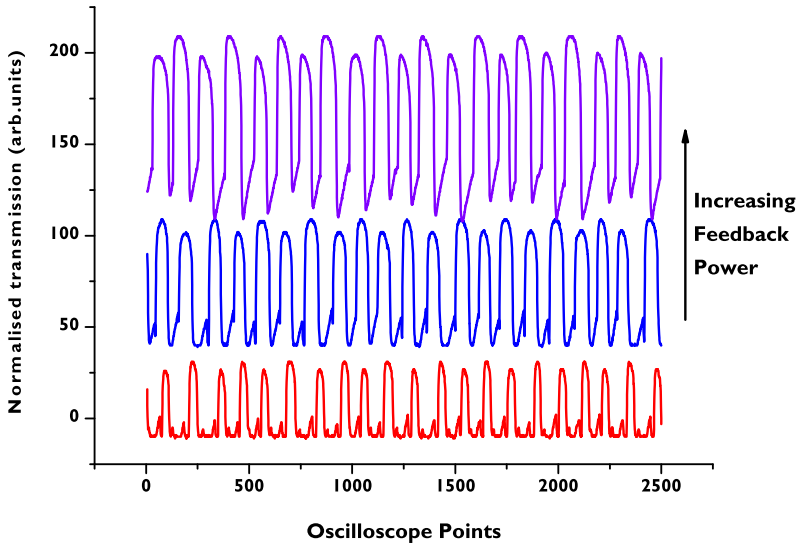

Figure 3.6: Plots showing the cavity transmission through the empty OF-CEAS V-cavity with increasing levels of optical feedback.

modes, without risking "losing" any modes in the transmitted light.

3.5 Results and Discussion

3.5.1 Water Measurements

A screen-shot from the data treatment routine is shown in Figure 3.7.

The top left panel displays a single scan of the cavity transmission recorded on the oscilloscope, normalised for the laser power by dividing the transmission on photodiode 1 by that on photodiode 2. An atmospheric water absorption feature is clearly discernible near the centre of the trace in each of the three panels. These data are the very first absorption data taken using the OF-CEAS setup, before the optimisation of the feedback phase control electronics, and so they are relatively noisy compared to the carbon dioxide data presented in section 3.5.2 which were taken with the fully-optimised setup.

The normalised transmission data are passed through a peak-picking algorithm,

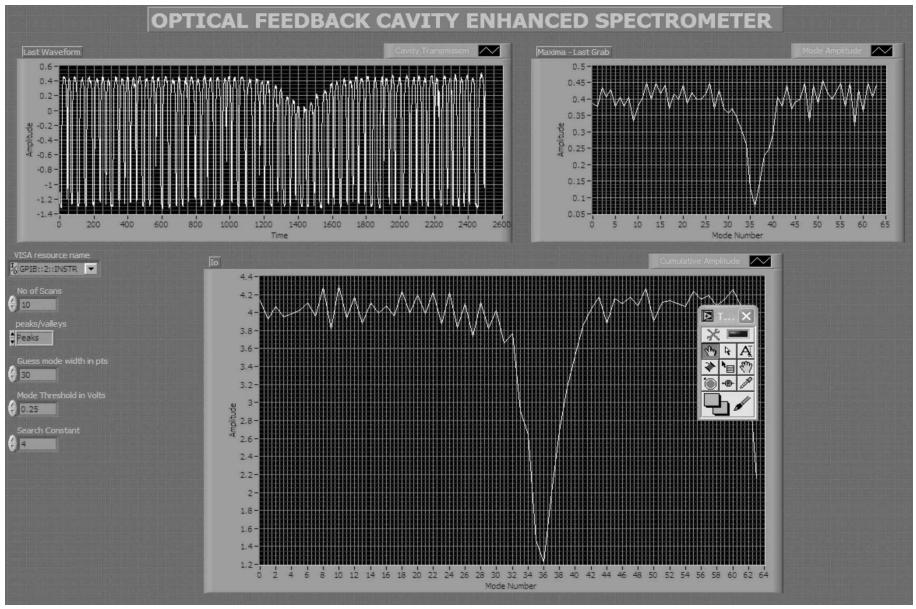

Figure 3.7: Screenshot of the data acquisition routine, showing the water absorption centred close to 6260.8 cm^{-1}. The three panels, clockwise from the top left, show the cavity transmission, the one-shot mode maxima, and the sum of ten shots of mode maxima.

and the resulting transmission maxima are plotted against mode number in the top right-hand panel. The peak-picking algorithm was a simple routine supplied with the LabVIEW package; after a first pass through this routine, the peak maxima were refined by passing the data a short distance to either side of the picked maxima from the first pass through a second repetition of the peak-picking routine. Groups of these maxima are averaged to create the final intensity data set, I. The sample-free background, I_0, is fit analytically. The I and I_0 data are then used to generate a spectrum in the form of equation 2.36.

It can be seen from the data in the acquisition panel of Figure 3.7 that there is an alternation in the intensities of successive TEM_{00} modes in the cavity transmission, and a corresponding oscillation in the maxima shown in the bottom panel. This effect arises because modes described by odd and even q in equation 2.21 are respectively nodal and anti-nodal at the folding point of the cavity, and they therefore have subtly different losses associated with them. This difference in electric field intensity gives rise to the observed alternation in the intensity of the transmitted

modes. To correct for this, the odd mode maxima and the even mode maxima were treated separately; this yields two sets each of I and I_0 data, corresponding to subtly different effective values for R (and, therefore, for the effective path length). Once these have been converted to a value of $(I_0 - I)/I$ as in equation 2.36, the two data sets are effectively normalised for these different R values, and so can be recombined directly to form a single spectral data set.

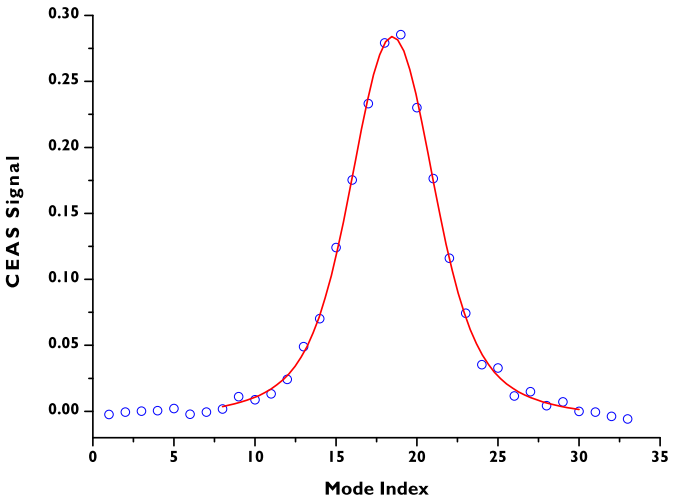

Figure 3.8: Absorption spectrum of ≈ 16 Torr laboratory air, showing the water absorption centred close to $6260.8\,\mathrm{cm}^{-1}$. A Voigt fit to the transition is shown. The spectrum is plotted as the CEAS signal (in the form given in equation 2.36) against mode index, with a mode separation equal to the cavity free spectral range of $3.34 \times 10^{-3}\,\mathrm{cm}^{-1}$.

A first example of such a spectrum, applying the OF-CEAS technique to detection of water in the cell when filled with ≈ 16 Torr of laboratory air, is presented in Figure 3.8. It shows the weak water absorption at 6260.823 cm^{-1}, for which $\sigma_{int} = 3.345 \times 10^{-25}\,\mathrm{cm}^2\mathrm{molec}^{-1}\mathrm{cm}^{-1}$ [128]; this is the $(3,2,1) \leftarrow (3,1,2)$ transition in the $4\nu_2$ overtone band, where the assignments are given as (J, K_a, K_c). For convenience, the CEAS signal is plotted against mode number. This spectral line has a calculated Doppler width of 0.0182 cm^{-1} at 296 K, and a reported air pressure broadening coefficient of $0.193\,\mathrm{cm}^{-1}\mathrm{atm}^{-1}$ (FWHM) [128]. The total Voigt FWHM

is therefore calculated, using the form cited by Olivero and Longbothum [200]:

$$w_{Voigt} = \sqrt{(w^2_{Doppler}/\ln 2) + w^2_{Lorentz}} \tag{3.6}$$

The resulting total Voigt FWHM is calculated to be 0.0205 cm^{-1} at an air pressure of 16 Torr, neglecting self-broadening effects within the water. For the experimental data, the Voigt function fits well to the spectral profile, as is shown in Figure 3.8. Fixing the Gaussian contribution at the calculated value for the Doppler width, the returned total Voigt FWHM is $0.0211 \pm 0.0003\,cm^{-1}$, in satisfactory agreement with the calculated value given the small number of data points.

The sensitivity of our atmospheric water system is expressed in terms of a minimum detectable absorption coefficient, α_{min}. For this system, an optimal α_{min} of $1.1 \times 10^{-8}\,cm^{-1}$ was calculated, with an acquisition time of 2.38 s. This yields a time-reduced value of $\alpha_{min} = 1.72 \times 10^{-8}\,cm^{-1}s^{1/2}$ for one second of data acquisition, expressed as the coefficient for absorption of equivalent size to the root-mean-square noise level in the spectrum after one second of data averaging.

3.5.2 Carbon Dioxide Isotope Measurements

The OF-CEAS system was then extended to the measurement of carbon dioxide isotopologues. Some medical motivations for their accurate, swift and sensitive detection were elucidated in section 3.3.2. The electronics were fully re-optimised before operation of these measurements. Comparing the screen-shot shown in Figure 3.9 with that shown earlier for the water measurements in Figure 3.7 makes clear the improvement in the quality of the data once the phase control electronics were running at a speed appropriate to real-time maintenance of the feedback phase during a complete spectral scan. The raw data show much cleaner modes, with the alternation in their intensities consistent and clear, giving rise to a much smoother spectral baseline.

The carbon dioxide data presented show the sum of 20 shots' mode maxima,

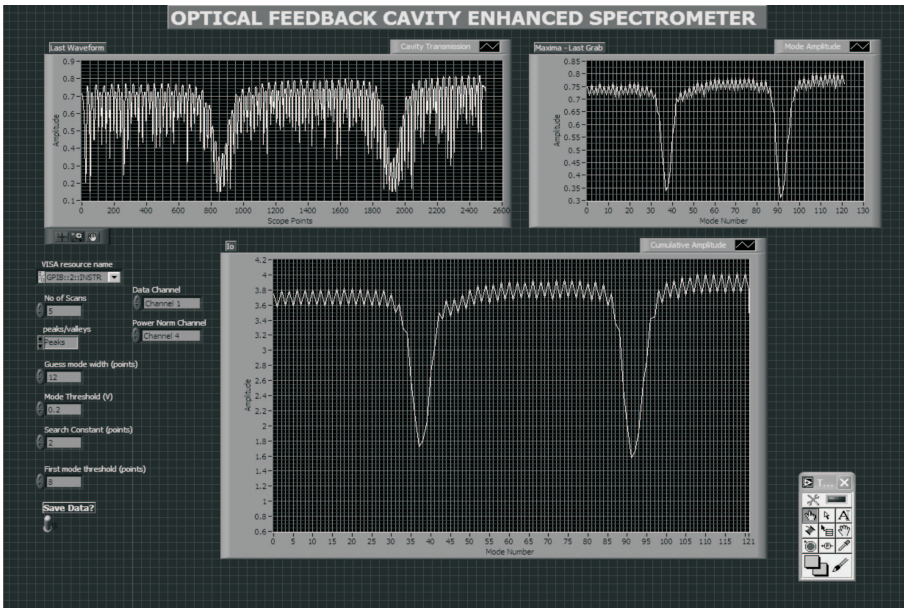

Figure 3.9: Screenshot of the data acquisition routine, showing data relating to the two carbon dioxide isotopologue absorptions close to 6261.6 and 6261.8 cm^{-1} studied in this chapter. The three panels are equivalent to those shown in Figure 3.7. A clear improvement in the data quality is visible, after optimisation of the speed of the feedback phase-control electronics.

at a ramp frequency of 5 Hz, in the spectral region containing two carbon dioxide isotopologue transitions close to 6261.6 and 6261.8 cm^{-1}. These peaks correspond to particular rotational transitions within the $3\nu_1 + \nu_3$ vibrational band of each isotopologue of carbon dioxide. The absorption at 6261.644 cm^{-1} is an R(60) line for the $^{12}CO_2$ isotopologue, and that at 6261.827 cm^{-1} is an R(30) transition for $^{13}CO_2$, and they have respective integrated cross-sections of 1.56×10^{-25} and 1.11×10^{-25} $cm^2 cm^{-1} molec^{-1}$ at 296 K (taken from the HITRAN [128]) database, each having a quoted error close to $\pm 5\%$. These cross-sections are already normalised for isotopic abundance and so they imply that, in a static sample at 296 K, the two absorbances should be observed in a ratio close to 1.56/1.11.

Figure 3.10 shows the transmission maxima corresponding to a series of measurements at different carbon dioxide pressures, and Figure 3.11 shows the spectrum that results from treatment of a single set of these transmission maxima. The alternation in the amplitudes of successive data points is no longer evident after analysis,

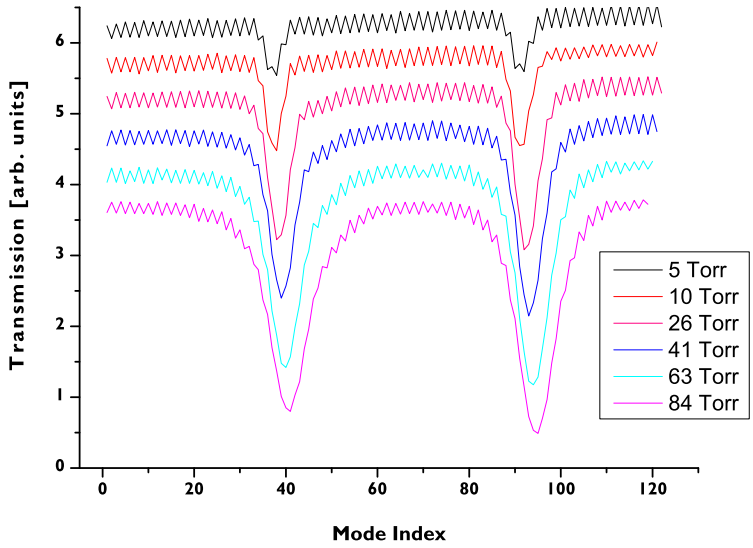

Figure 3.10: Offset transmission maxima plots, before spectral analysis, showing the change in the two CO_2 isotopomer absorptions near 6261.6 cm^{-1} and 6261.8 cm^{-1} as the CO_2 pressure is increased. The transmission alternation between consecutive modes is clearly visible.

and the resulting spectra show excellent signal-to-noise. Indeed, in the case of the the data taken with 84 Torr of carbon dioxide, a signal-to-noise ratio of $\sim$ 3000 resulted. In the spectrum, we also observe an additional, smaller absorption close to 6261.80 cm^{-1}, for which an assignment is not currently known. This feature was also observed, and reported without an assignment, by Crosson *et al.* [201].

For all of the present work, the mirror reflectivities were calibrated using known amounts of absorber, measuring a spectroscopically well-characterised transition. The resulting value of R was 0.9991 ± 0.00004, corresponding to a finesse of approximately 3500. For the calibration, the area was determined underneath a fit to the $^{12}CO_2$ absorption at 6261.644 cm^{-1} at a series of different CO_2 pressures.

A linear fit to the baseline of the carbon dioxide data in Figure 3.11 yields a standard deviation of 6.8×10^{-4} in the units of the CEAS signal. This value describes the error in an absorption measurement due to noise in the experiment, and corresponds to an α_{min} value of $4.07 \times 10^{-9} cm^{-1}$ in the total acquisition time of

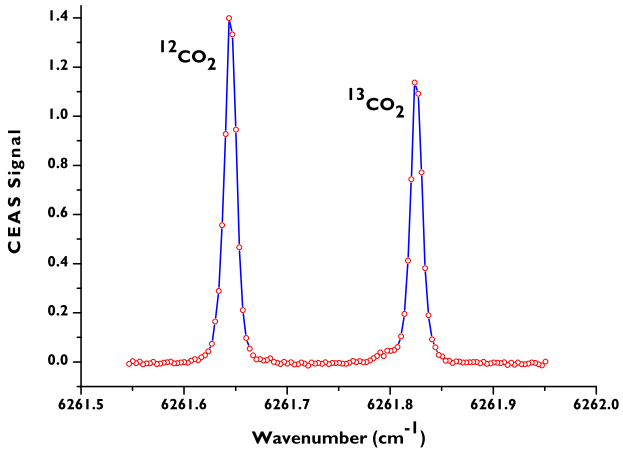

Figure 3.11: Analysed absorption spectrum corresponding to the transmission maxima in Figure 3.10, showing the data after analysis for 26 Torr of carbon dioxide.

2 s; the corresponding time-normalised value is therefore $5.8 \times 10^{-9}\text{cm}^{-1}\text{s}^{1/2}$. This value therefore reflects the improvements to the electronic servo loop for maintenance of the correct optical feedback phase, made between the water measurements and the carbon dioxide measurements. Particularly, optimisation of the speed at which the servo loop operates improved the stability of the transmission signal, thereby reducing the noise level on the resulting spectral data. Further improvement may be attributed to refinements made to the data acquisition software at the same time as optimisation of the electronics, made to improve the reliability of the peak-picking algorithm within the acquisition routine.

3.6 Conclusions and Outlook

The effect of optical feedback on the transmission of a V-shaped optical cavity has been discussed; the resulting injection seeding effect on a diode laser may cause laser line width narrowing and frequency locking of the laser to the mode centres in the external V-cavity transmission. These effects have been exploited in the development of an optical feedback cavity-enhanced absorption spectroscopy (OF-

CEAS) apparatus, which has then successfully been applied to the detection of very weak absorptions with high signal-to-noise and an accurately-calibrated relative frequency scale. OF-CEAS was initially carried out for measurements of water vapour absorption close to 1.596 μm. A time-normalised minimum detectable absorption coefficient of $1.72 \times 10^{-8}\,\mathrm{cm^{-1}s^{1/2}}$ resulted for these preliminary measurements.

The importance of control over the magnitude and phase of the optical feedback to the laser have been elucidated. The connection between the feedback phase and the symmetry of the transmitted V-cavity modes has been discussed, and used as the basis for the design and implementation of an electronic servo loop for real-time maintenance of the feedback phase, which is crucial to the production of a useful signal for OF-CEAS. After optimisation of the speed of these electronics, the OF-CEAS spectrometer's precision was demonstrated in the measurements of isotopologue absorptions in carbon dioxide, a spectroscopic measurement problem relevant to medical diagnostics. The accurate detection of $^{12}CO_2$ and $^{13}CO_2$ isotopologues has been shown, as is required for example in analysis of exhaled breath as a biomarker for *Heliobacter pylori* infection. A time-normalised α_{min} value of $5.8 \times 10^{-9}\mathrm{cm^{-1}s^{1/2}}$ was achieved; this is not so sensitive as the value of $5 \times 10^{-10}\,\mathrm{cm^{-1}}$ reported for one second of averaging by Morville *et al.* [158]. However, their setup comprised a cavity of substantially greater finesse ($F \sim 22000$), in light of which the sensitivity of the present measurements is reasonable. Further improvements to the experiment, to improve upon this initial detection limit, are presented in Chapter 4.

Work continuing beyond this thesis, seeking further improvement of the OF-CEAS spectrometer, is directed towards further reducing the limit of detection, firstly by altering the electronic servo loop to be suitable for implementation with a higher-finesse V-cavity. An important factor limiting the time-stability of the setup developed and reported in this chapter is the temperature-stability of the diode laser; by improving this, and by speeding up the data transfer from the oscilloscope to the analysis programme on the computer, the sensitivity may further be enhanced by allowing for longer periods of averaging. Implementation of the optical feedback

phase control loop within the experimental control software, rather than using an electronic servo loop, may allow for a more versatile control setup which is more easily applied to systems of higher V-cavity finesse, and may therefore offer further opportunities to improve the detection sensitivity.

Furthermore, owing to the strong temperature-dependence of the ratio of the line intensities for the $^{12}CO_2$ and $^{13}CO_2$ absorptions employed in the work reported in this chapter, the error in a ratio measurement is dominated by uncertainties in the temperature-dependent absorption cross-sections relating to the two lines. The data presented in this chapter suggest a ratio between the cross-sections of the two isotopologues' absorptions of 1.26 ± 0.03; the values taken from HITRAN [128] imply a ratio close to 1.41 at 296 K. However, earlier work in this group [202] found a value of ~ 1.1, highlighting the difficulties in making a ratio measurement in a non-temperature-stabilised cell. As such, an accurate measurement of the isotope ratio would need to be carried out in a temperature-stabilised cell [201]. The strong temperature dependence of these lines is demonstrated by the value of $\Delta\delta/\Delta T$, the change in the δ-value expressed in equation 3.4 per unit temperature. Bergamaschi *et al.* [203] showed that this may be estimated from the following expression:

$$\frac{\Delta\delta}{\Delta T} \approx 1000\frac{\Delta E}{k_B T^2}‰ \tag{3.7}$$

wherein ΔE signifies the difference in the two transitions' ground state energies. From this expression, an estimate of $\sim 16‰/\mathrm{K}$ is obtained for the isotope ratio measured from the two absorption lines studied in this chapter. At very low absorptions, the digitisation resolution associated with the oscilloscope may also become important; the data presented in this chapter were acquired using an 8-bit oscilloscope, and therefore the limiting digital resolution is one part in 256. Accordingly, the use of an acquisition setup at greater digitisation depth may also enhance the achievable detection sensitivity.

Chapter 4

OF-CEAS II: Characterisation and Application

4.1 Overview

In this chapter, the high-sensitivity OF-CEAS spectrometer developed and discussed in Chapter 3 is further characterised and applied to line shape studies. In order further to characterise the performance of the spectrometer, high-sensitivity studies of acetylene absorptions close to 1532 nm are carried out simultaneously using the OF-CEAS setup and a standard diode-laser cavity-enhanced absorption spectroscopy (CEAS) apparatus. Detection is carried out on the P(6) line of the $\nu_1 + \nu_3$ vibrational band of the mixed isotopologue of acetylene, $^{12}C^{13}CH_2$. CEAS data are presented employing a linear two-mirror optical cavity of finesse ≈ 15700 alongside data taken for the same transition using the OF-CEAS setup, whose three-mirror V-cavity had a finesse of ≈ 3500; direct comparison is made between the sensitivities of the two methods, and in light of this the suitability of each technique for detection in different environments is considered.

Collisional (pressure-) broadening effects are introduced, and pressure broadening data are presented for broadening of the studied acetylene absorptions by air and the noble gases. Parmenter-Seaver analysis of the pressure-broadening data is introduced, and Parmenter-Seaver plots are presented alongside the resulting well-depth

estimate for the acetylene dimer. The agreement between the data sets corresponding to the two experimental techniques is discussed, and the relative merits of the techniques for this sort of measurement are considered. A further set of pressure broadening measurements for the P(12) line in the $\nu_1 + \nu_3$ vibrational band of the pure isotopologue $^{12}C_2H_2$ is shown so as to allow a direct comparison of our data with earlier work.

The well-characterised and consistent frequency scale which is an inherent feature of the OF-CEAS technique is then applied to a line shape analysis for the transitions presented in Chapter 3. In spite of the low resolution associated with this technique, this accurate frequency scaling allows observation of subtle line shape effects such as Dicke collisional narrowing using the data presented in Chapter 3 for the R(60) line in the $3\nu_1 + \nu_3$ vibrational band of CO_2. These effects are quantified through use of a Galatry fit to each absorption spectrum. The statistical significance associated with the use of such a model, and the physical meaning of the results, are examined through a statistical F-test.

4.2 Acetylene and its Spectroscopy

4.2.1 Earlier Work on Acetylene Detection

The detection and monitoring of acetylene have many applications in diverse areas, from breath analysis for medical diagnostics [204] to plastics production [205]. Acetylene is an impurity which is commonly found in the ethene that results from the cracking of higher hydrocarbons [206], and so accurate and expedient schemes for its detection are of scientific and industrial interest. Owing to its resistance to oxidation in the atmosphere, acetylene is considered a useful marker compound for atmospheric pollution studies; such atmospheric detection [207] demands selective, rapid and absolute measurement of the number density of acetylene present in an atmospheric sample. The identification of the P(3), P(4) and P(5) lines of the acetylene ν_3 fundamental band in the infrared spectral measurements of comet Hyakutake

were an important part of the characterisation of the comet's composition [208]. The estimated acetylene abundance relative to water was found to be in the region of 0.3–0.9%. However, the fundamental region of the acetylene spectrum does not lend itself particularly well to atmospheric detection problems ordinarily; Brooke *et al.* [208] had difficulties with resolving the acetylene fundamental spectrum fully, owing to the presence of conflicting lines due to the hydroxyl radical.

A substantial body of work also exists relating to the study of acetylene in flames. Lucht *et al.* [209] employed coherent anti-Stokes Raman spectroscopy (CARS) to characterise the acetylene concentration within a pre-mixed methane/acetylene/air flame; their limit of detection was defined as the acetylene concentration at which one hundred signal photons were collected, and was measured as 0.2 % acetylene. Later work on characterising acetylene flames has improved greatly on this detection sensitivity; Williams and Fleming [210] employed laser-induced fluorescence (LIF) to measure the acetylene intermediate formed in propane and methane flames in air, using a detection wavelength close to 228 nm. They found that the methane flame produced a much weaker acetylene signal than that formed in propane, and that their LIF setup was not sufficiently sensitive to detect acetylene in the methane flame except under very fuel-rich conditions. Very careful calibration was also required of the system, especially to account for interferences owing to nitric oxide.

The need for speed, selectivity and accuracy for these diverse applications and measurements means that diode laser absorption spectroscopy and its associated techniques lend themselves particularly well to acetylene detection. Tai *et al.* [211], for instance, used 1.66 μm and 1.53 μm diode lasers, in conjunction with a 4 km-long optical fibre for remote absorption spectroscopy for acetylene detection; they achieved a detection limit of 3 ppm in a 10 cm absorption length with an integration time of one second. Oh *et al.* [212] reported wavelength modulation spectroscopy measurements on acetylene in 1995, employing a near-infrared ECDL in the 1.5 μm region; with a time constant of $\tau = 300\,\mathrm{ms}$, they reported a minimum detectable absorbance of 4.8×10^{-4}, corresponding to a bandwidth-reduced minimum detectable

acetylene concentration of $\sim 5 \times 10^{12}$ molec cm^{-3}.

Pavone *et al.* [213] published work on acetylene detection in the visible region, using a stabilised aluminium gallium arsenide (AlGaAs) diode laser to undertake spectral measurements on the overtone region close to 0.79 μm. They reported a limit of detection of 200 ppb/km, and their setup was employed to make line shape measurements on the P(11) and R(5) lines in this region, determining the relevant self and air broadening coefficients for each line. De Rosa *et al.* [214] also employed a diode-laser-based system, carrying out frequency modulation spectroscopy to make line shape and pressure shift measurements on the acetylene $\nu_1 + 3\nu_3$ combination band close to 787 nm.

The work of Chen *et al.* [215] and of Rusciano *et al.* [216] combines the use of solid-state lasers with difference frequency generation in a non-linear optical material to generate longer-wavelength light for detection in the mid-infrared region corresponding with higher-cross-section fundamental transitions. Chen's system [215] employed two Ti:Sapphire lasers which were mixed in a birefringent gallium selenide crystal to produce radiation tunable between 8–19 μm. The difference frequency radiation was then employed to carry out absorption measurements on the Q-branch within the ν_5 vibrational band of acetylene near to 13.7 μm, achieving an ultimate sensitivity of 28 ppm m Hz$^{-1/2}$. They note that this would correspond to a detection limit of 1 ppb in a 100 m White Cell. The Rusciano [216] system combined a Nd:YAG laser at 1064 nm and a semiconductor ECDL tunable between 770–785 nm in a periodically-poled lithium niobate (PPLN) crystal, to create difference frequency radiation close to 3 μm with a conversion efficiency of $\nu_{exp} = 0.0146\%\mathrm{W}^{-1}\mathrm{cm}^{-1}$. This radiation was then used to perform pure absorption spectroscopy and $1f$ wavelength modulation spectroscopy on fundamental transitions in the ν_3 vibrational band of acetylene ($\sigma \sim 10^{-20}\mathrm{cm}^2\mathrm{cm}^{-1}\mathrm{molec}^{-1}$). With a path length of 30 m and a total sample pressure of 500 mbar, a detection limit of 4 ppb was demonstrated with measurements of acetylene in nitrogen. Hornberger *et al.* [217] measured acetylene overtone spectra in the region 6300–6400 cm^{-1}. Us-

ing a NaCl-OH^- colour centre laser emitting radiation with power on the order of hundreds of mW into a radial resonant photoacoustic multipass cell, photoacoustic spectroscopy measurements were presented, with a minimum detectable absorption coefficient of $\alpha_{min} \approx 10^{-9}$, which corresponds to a minimum detectable acetylene concentration of 10^{11}–10^{12} molec cm^{-3} for detection in the 6460 cm^{-1} region.

Not all of the techniques presented in the literature for detection of acetylene are spectroscopic, however. Ishiji *et al.* [218], for example, presented an electrochemical sensor for detection of acetylene in gases extracted from isolation oils. There are difficulties associated with the selectivity of electrochemical sensors, however; indeed, with one of the electrodes used in Ishiji's work, the selectivity – defined for a particular interfering species as the ratio between the detection sensitivities for acetylene and that species – was found to be lower than 5 for both carbon monoxide and ethene. With a gold counter-electrode, a selectivity in excess of 100 was measured by Ishiji *et al.* [218], but this still represents a substantial interference with the signal if those contaminants are present in relatively high abundance.

The acetylene absorption transitions in the region close to 1.5 μm that is adopted for the work in this thesis have been investigated and characterised by many groups seeking to offer a frequency standard for the near-infrared region for use in accurate frequency-calibration of other atomic and molecular spectra, in metrology and in optical communications. Specifically, saturation spectroscopy has been employed to make absorption measurements at very narrow line widths [219–222]. Of these, Thapa *et al.* [220] made measurements within a photonic bandgap fibre on the $\nu_1 + \nu_3$ band near 1532 nm, and the work of Onae [221], Edwards [223] and De Labachelerie [222] refers to the $^{13}C_2H_2$ isotopologue.

4.2.2 The Acetylene Spectrum

Acetylene is a linear, symmetrical molecule with point group $D_{\infty h}$. For such a linear molecule with $N = 4$, there are $3N - 5 = 7$ normal modes. These are ilustrated below; the two bending motions are doubly degenerate.

ν_1	symmetric stretch	σ_g symmetry	3374 cm^{-1}	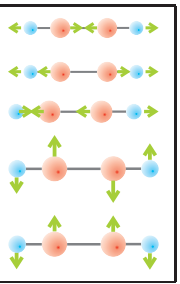
ν_2	symmetric stretch	σ_g symmetry	1974 cm^{-1}	
ν_3	anti-symmetric stretch	σ_u symmetry	3287 cm^{-1}	
ν_4	anti-symmetric bend	π_g symmetry	612 cm^{-1}	
ν_5	symmetric bend	π_u symmetry	729 cm^{-1}	

Table 4.1: The fundamental vibrational modes of acetylene.

Nuclear spin statistics are important in the acetylene spectrum. Pauli's exclusion principle tells us that the total molecular wavefunction must be symmetric with respect to the interchange of identical bosons, and antisymmetric with respect to the exchange of identical fermions. For symmetry purposes, we may consider the C-H combination (boson × fermion) as a single fermion. The imbalance in the number of nuclear spin wavefunctions with respectively symmetric and antisymmetric behaviour under interchange of the two C-H units means that there is a 3:1 intensity alternation between consecutive rotational lines in the acetylene spectrum. In the mixed isotopologue, $^{12}C^{13}CH_2$, which is not centrosymmetric, the two C-H units cannot be interchanged by a symmetry operation of the molecule, as they are not identical, so there is no intensity alternation evident in the spectrum of the mixed acetylene isotopologue.

In the spectral region studied in this chapter, close to 1.5 µm, several vibrational bands overlap. Transitions from the ground state to $\nu_1+\nu_3$ in $^{12}C_2H_2$ and $^{12}C^{13}CH_2$ are observed near 1.5 µm. In the spectrum of the $^{12}C_2$-isotopologue, hot band transitions corresponding to $\nu_1+\nu_3+\nu_4^1 \longleftarrow \nu_4^1$ (π_g–π_g) and $\nu_1+\nu_3+\nu_5^1 \longleftarrow \nu_5^1$ (π_u–π_u) are also seen [224].

In the hot bands, which are π–π transitions, the energy levels in the initial and final states may be further complicated by *Coriolis interaction*, a coupling between rotational and vibrational motions [195, 196, 225–227]. For example, as a stretching mode is excited while the molecule is simultaneously rotating, the effect of the tangential component of the rotational motion is to induce coupling of angular

momentum into the bending mode. The additional angular momentum - *vibrational angular momentum* - associated with the rotation can be accounted for in the term values for the rotational spectrum:

$$F_v(J) = B_v[J(J+1) - \ell^2] - D_v[J(J+1) - \ell^2]^2 \tag{4.1}$$

where $\ell\hbar$ is the magnitude of the induced vibrational angular momentum. This coupling is more efficient for a better energy match between the relevant stretching and bending vibrations. Accordingly, the Coriolis coupling between the antisymmetric stretching vibration, ν_3, and one of the bending motions (ν_4, ν_5), for instance, is small. However, the bending motions are doubly degenerate with their perpendicular counterparts. Rotational angular momentum about the internuclear axis, $\vec{z}$, arising from excitation of a bending vibration may convert one of the two perpendicular bending motions into the other one with which it is degenerate. This Coriolis interaction is now between two vibrations which are degenerate, and so it is a large, first-order, interaction. The associated rotational term expression is now modified to [195]:

$$F_v(J, \ell^{\pm}) = B_v[J(J+1) - \ell^2] \pm (q_i/4)(v_i+1)J(J+1) - D_v[J(J+1) - \ell^2]^2 \tag{4.2}$$

in which q_i is a coefficient describing the magnitude of the interaction between rotational motion and vibration i [195]. Accordingly, term values differing only in the sign of ℓ are split, by $(q_i/2)(v_i+1)J(J+1)$, and this is known as *l-type doubling*. This splitting decreases in magnitude with increasing ℓ, and is only appreciable in size for $|\ell| = 1$. This ℓ-type doubling is observed, for example, associated with the ν_5 symmetric bending vibration in acetylene. In the π–π transitions such as the $\nu_1+\nu_3+\nu_5^1 \longleftarrow \nu_5^1$ hot band transitions, this ℓ-type doubling effect occurs in both the initial and final states of the transition, and the transitions in the spectrum appear as doublets, as illustrated in Figure 4.1. Figure 4.8 shows an example spectrum of one of the resulting absorption doublets using the optimised OF-CEAS setup. The

components of these doublets are assigned according to the symmetry behaviour of the associated wavefunction $\Psi = \psi_{elec}\psi_{nuc}$ under inversion, and are labelled as + or -. The accepted convention [195, 226] for labelling of these levels in closed-shell molecules is that those with parity $+(-1)^J$ are assigned the label e, and those with parity $-(-1)^J$ are labelled f. The resulting selection rules are then [195]:

$$\begin{aligned} &\text{For } \Delta J = 0: \quad e \leftrightarrow f \quad e \nleftrightarrow e \quad f \nleftrightarrow f \\ &\text{For } \Delta J = \pm 1: \quad e \nleftrightarrow f \quad e \leftrightarrow e \quad f \leftrightarrow f \end{aligned}$$

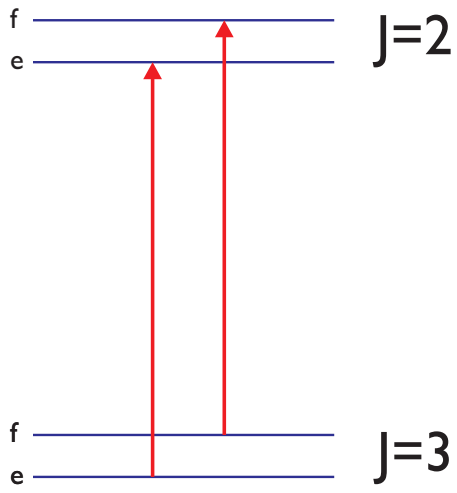

Figure 4.1: Schematic illustration of the energy levels in the P(3) doublet within the $\nu_1 + \nu_3 + \nu_5^1 \longleftarrow \nu_5^1$ band.

4.3 Broadening Effects in Spectroscopy

In spectroscopy, the lines owing to absorption or emission transitions never exhibit the zero line width that true monochromaticity would imply. Instead, even for atomic lines measured at very low pressures, a distribution of emitted or absorbed frequencies is observed about a central frequency, ν_0, corresponding to the energy difference between the two quantum states involved. The function that describes the form of the spectral line is called the *line profile*, $I(\nu - \nu_0)$. The line profile is further characterised by a line width, which is given by the difference in frequency space between the two frequencies at which $I(\nu_1) = I(\nu_2) = \frac{1}{2}I(\nu_0)$; this is the *full width at*

half maximum (FWHM). The *kernel* associated with the line is the area underneath the line function between ν_1 and ν_2, and the *wings* are the regions bounded by the line function on either side of the kernel. These terms are illustrated in Figure 4.2.

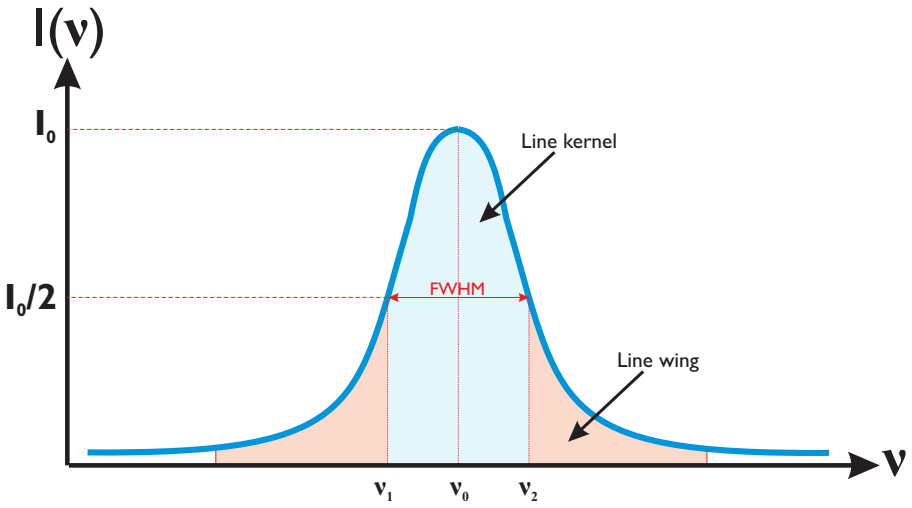

Figure 4.2: Schematic illustration showing the different quantities associated with the profile of a spectral transition.

There are several phenomena which lead to a broadened line shape, and these are generally divided into two categories: *homogeneous* and *inhomogeneous* mechanisms [54]. Homogeneous broadening mechanisms are those in which the distribution of frequencies observed is characteristic of every particle in the sample, and the line profile therefore describes the line shape associated with any one of those particles, each being indistinguishable from the others. By contrast, inhomogeneous broadening mechanisms are ones in which there is a distribution in the central frequencies corresponding to each of the distinguishable emitting or absorbing particles [14].

4.3.1 Homogeneous Broadening

The absorption or emission lines resulting from even a notionally isolated, motionless particle would have a non-zero line width, due to uncertainty arising from the lifetime associated with the upper state of the transition [54]. A state with a precise energy, and associated time-dependent wavefunction $\Psi(t) = \psi e^{-iEt/\hbar}$, is a steady

state with a probability density that is time-independent, $|\Psi|^2 = |\psi|^2$ [227]. However, on introducing transitions to other states which cause a temporal decay in the population of the initial state, supposing that this decay is describable by an exponential with a time-constant τ, the probability density becomes:

$$|\Psi|^2 = |\psi|^2 e^{-t/\tau} \tag{4.3}$$

The time-dependent amplitude of the wavefunction then adopts the form:

$$|\Psi| = |\psi| e^{-iEt/\hbar - t/2\tau} \tag{4.4}$$

This exponential term is a function whose amplitude reduces as the oscillation proceeds, and its energy can be extracted by Fourier theory, modelling the function as a superposition of oscillating waves:

$$\begin{aligned} e^{-iEt/\hbar - t/2\tau} &= \int g(E') e^{-iE't/\hbar} \, \mathrm{d}t \\ \therefore g(E') &= \frac{\hbar/\tau}{(E - E')^2 + (\hbar/2\pi)^2} \end{aligned} \tag{4.5}$$

in which $g(E)$ is the *spectral density function*. All of the energy values must appear in the superposition; the function that describes the decay in the wavefunction corresponds to a range of energies. As such, a state with a finite lifetime is associated with a non-zero energy uncertainty. By analogy with Heisenberg's uncertainty principle, the lifetime broadening relation can be stated as:

$$\tau \Delta E \approx \frac{\hbar}{2} \tag{4.6}$$

This encapsulates the idea that any state with a finite lifetime necessarily has a non-zero energy uncertainty associated with it, and so the line profile associated with any such transition has a non-zero line width. This line width is called the *natural line width*, brought about by this *lifetime broadening* effect arising from the

uncertainty principle.

A second homogeneous line broadening mechanism is *collisional broadening*, also termed *pressure broadening*. This arises due to a reduction in the lifetime associated with the radiating state; the lifetime broadening relation (4.6) indicates that a reduction in the lifetime must result in a corresponding increase in the energy uncertainty ΔE, and therefore in the line width. Typically, models of collisional line broadening assume that the collisions are *adiabatic*; the collision does not contribute to inducing the transition. The lifetime broadening relation (4.6) implies that collisions contributing to the wings of the lineshape, at large frequency detuning values from the line centre, are those on a short timescale [228].

The part of the absorption signal corresponding to the line kernel corresponds to small frequency deviations from the line centre, and therefore to a longer interaction time between the radiation and the absorber. Within this regime, the transition *duration* is long compared to the duration of each collision and the time between successive collisions. Over the course of the time during which the particle is interacting with the radiation, the absorbing particle suffers several collisions, each of which is comparatively short. Accordingly, this defines the *impact* regime [229]. Conversely, when the transition time is exceeded by the average collision duration, which in turn is much smaller than the time between collisions, the absorbing particle is interacting with the same collider throughout the time it spends interacting with the radiation; under these conditions, the *quasi-static approximation* applies [228]. The regime that is most important to the broadening measurements presented in this chapter, concerned mostly with the width of the line *kernel*, is that appropriate to an impact approximation.

Both elastic and inelastic collisions contribute to the broadening of spectral lines, and elastic collisions may also shift the line centre. A classical model considers inelastic collisions to bring about a reduction in the amplitude of the oscillation associated with the radiative transition; this corresponds to an increase in the linewidth in the frequency domain. By contrast, elastic collisions leave the amplitude unchanged but

alter the *phase* of the radiation corresponding to the transition.

Both homogeneous broadening mechanisms lead to a Lorentzian line shape. The line profile associated with collisional broadening, for instance, has the following general normalised form [54]:

$$g(\nu) = \frac{\Delta\nu}{2\pi[(\nu - \nu_0 - \nu*)^2 + (\Delta\nu/2)^2]} \tag{4.7}$$

where $\Delta\nu$ is the Lorentzian line width (FWHM), owing to *inelastic* collisions, and ν_0 is the frequency at the line centre. The extra term $\nu*$ accounts for the frequency shift brought about by the phase-altering *elastic* collisions. This line profile is generally adopted under conditions where collisional effects are dominant, but typically for total pressures under 1 atm, and since the $\nu*$ term is often very small at these pressures, it is often neglected altogether.

A further source of homogeneous broadening, specifically relevant in solids, arises from the interaction between a particle within a crystal and a phonon, involving the emission or absorption of acoustic energy. Such collisions do not terminate the lifetime of the species in its absorbing or emitting state, but do bring about a sudden change in the phase of the radiation corresponding to the spectroscopic transition; this is the source of the line broadening.

4.3.2 Inhomogeneous broadening

In a gaseous sample, the transition frequency, ν, associated with a single particle in the sample is Doppler-shifted according to:

$$\nu \rightarrow \nu_0 + \frac{|\vec{v_x}|}{c}\nu_0 \tag{4.8}$$

where $|\vec{v_x}|$ is the magnitude of the velocity component along the direction connecting the moving particle and the observer, c is the speed of light, and ν_0 is the transition frequency corresponding with that particle when stationary. This forms the basis of the major inhomogeneous line broadening mechanism in gas-phase spec-

troscopy, a consequence of the different Doppler shifts observed in the transition frequencies measured for particles within a sample having different velocities. To describe the range of velocities represented in a bulk gas sample, we adopt the Maxwell-Boltzmann distribution:

$$f(v_x, v_y, v_z) = \left(\frac{M}{2\pi k_B T}\right)^{3/2} \exp\left\{ -\frac{M}{2k_B T}(v_x^2 + v_y^2 + v_z^2)\right\} \tag{4.9}$$

for a gas with atomic mass M, at equilibrium at temperature T, and with $k_B = 1.381 \times 10^{-23}$ J K^{-1}molec^{-1}. We can consider $f(v_x, v_y, v_z)\ \mathrm{d}v_x\ \mathrm{d}v_y\ \mathrm{d}v_z$ as the probability that the velocity $\vec{v}$ of a given particle in the sample is directed toward the volume element $\mathrm{d}v_x\ \mathrm{d}v_y\ \mathrm{d}v_z$ centred about (v_x, v_y, v_z), and so:

$$\iiint_{-\infty}^{+\infty} f(v_x, v_y, v_z)\ \mathrm{d}v_x\ \mathrm{d}v_y\ \mathrm{d}v_z = 1 \tag{4.10}$$

Considering equation 4.8, then, the probability that the transition frequency is found in the interval between ν and $\nu + \mathrm{d}\nu$ is the same as that for finding v_x between $v_x + \mathrm{d}v_x$. Accordingly, we substitute $v_x = (\nu - \nu_0)(c/\nu_0)$ into equation 4.10 and integrate over all v_y, v_z. This eventually returns the following normalised expression for the Doppler-broadened line shape:

$$g(\nu)\ \mathrm{d}\nu = \frac{1}{\nu_0}\left(\frac{Mc^2}{2\pi k_B T}\right)^{1/2} \exp\left\{ -\left(\frac{Mc^2}{2k_B T}\right)\left(\frac{(\nu - \nu_0)^2}{\nu_0^2}\right)\right\}\ \mathrm{d}\nu \tag{4.11}$$

This is a Gaussian function, symmetric about the line centre ν_0 and with a corresponding FWHM line width (in this case, simply termed the *Doppler width*) of:

$$\Delta\nu_{Dopp} = 2\nu_0 \sqrt{\frac{2k_B T}{Mc^2} \ln 2} \tag{4.12}$$

In regimes where the Doppler broadening is still an important contribution to the line shape, a convolution of the relevant Lorentzian and Gaussian functions is required to describe the overall line profile so as to extract quantitative information from spectra. The resulting line profile takes the form of a *Voigt* function. After

normalisation, this is expressed as follows:

$$g(\nu) = A\int_{-\infty}^{\infty} \frac{\exp\{-t^2\}}{\left(\sqrt{\ln 2}\frac{\Delta\nu_L}{\Delta\nu_G}\right)^2 + \left(\sqrt{\ln 2}\left(\frac{\nu-\nu_0}{\Delta\nu_G}\right) - t\right)^2} \; \mathrm{d}t \tag{4.13}$$

where A is a constant, $\Delta\nu_L$ is the Lorentzian HWHM, and $\Delta\nu_G$ is the Gaussian HWHM (as opposed to the FWHM given in equation 4.12), the latter two quantities corresponding respectively to collisional and Doppler broadening phenomena. The Voigt function is the most commonly-used form of line profile for absorption spectroscopy at the sample pressures typically used for simple detection applications. That this profile accounts for the two major physical effects leading to line broadening quantitatively but separately is convenient; it allows us straightforwardly to quantify the influence of each on the total line shape by fitting a Voigt function. The Doppler width may be calculated analytically through equation 4.12, but may be confirmed by fitting a Gaussian function to the profile resulting from a low pressure (< 1 Torr) spectrum.

The collisional broadening is quantified by measuring the evolution in the size of the Lorentzian contribution to the line width with pressure. Spectral measurements are taken on a static sample, with increasing pressures of buffer gas being added, and a Voigt profile is fit to each of the resulting spectra, fixing the Gaussian width contribution at the Doppler width. The returned Lorentzian half-width from these Voigt fits then increases linearly with pressure of buffer gas; the constant of proportionality found from such a plot is the pressure broadening coefficient, γ. The pressure broadening coefficient is particular to a spectral transition, and to the buffer gas, and is usually reported in units of MHz/Torr; for foreign gas broadening interactions, a typical γ value would be on the order of 1–10 MHz/Torr.

4.4 Collisional Broadening in C_2H_2 at 1.5 μm: Earlier Work

This region of the spectrum of acetylene has been the subject of a series of earlier lineshape studies. Rank *et al.* [230] produced a study of several lines in the acetylene $\nu_1 + \nu_3$ band, with which the present work is concerned, in 1960; their work included a characterisation of pressure broadening of the studied lines by krypton and xenon gas. A fuller investigation was presented by Varanasi and Bangaru [231]; in their work, self broadening and broadening by hydrogen are both considered at a series of temperatures up to room temperature. Thibault *et al.* [232] measured pressure broadening coefficients for lines in the $\nu_4 + \nu_5$ combination band as part of an investigation of the acetylene-neon dimer system. These studies are directed towards the "pure" ^{12}C isotopologue of acetylene, but a full study of line parameters and line strengths in the corresponding band of $^{13}C_2H_2$ forms part of the work of Kusaba and Henningsen [233]. Some data are presented by Minutolo *et al.* [234] for the mixed $^{12}C/^{13}C$ isotopologue for self-broadening, as part of a study of acetylene lineshapes in both that isotopologue and the $^{12}C_2$ isotopologue close to 1.54 μm.

A more recent paper by Bond *et al.* [235] presents data on pressure broadening and pressure shift effects on acetylene lines in the $\nu_1 + \nu_3$ band for the $^{12}C_2$ isotopologue; data are presented for broadening at 195 K, and the authors discuss the temperature dependence of the broadening effects, making reference to the work of Arteaga *et al.* [236]. Arteaga's study provides a close comparison for some of the data presented here, and includes a comprehensive survey of broadening coefficients in the $\nu_1 + \nu_3$ band of the $^{12}C_2$ isotopologue of acetylene, including data for broadening by hydrogen, deuterium, nitrogen, air and the noble gases.

4.5 Experimental

4.5.1 CEAS Experiments

A schematic illustration of the CEAS experimental setup is shown in Figure 4.3

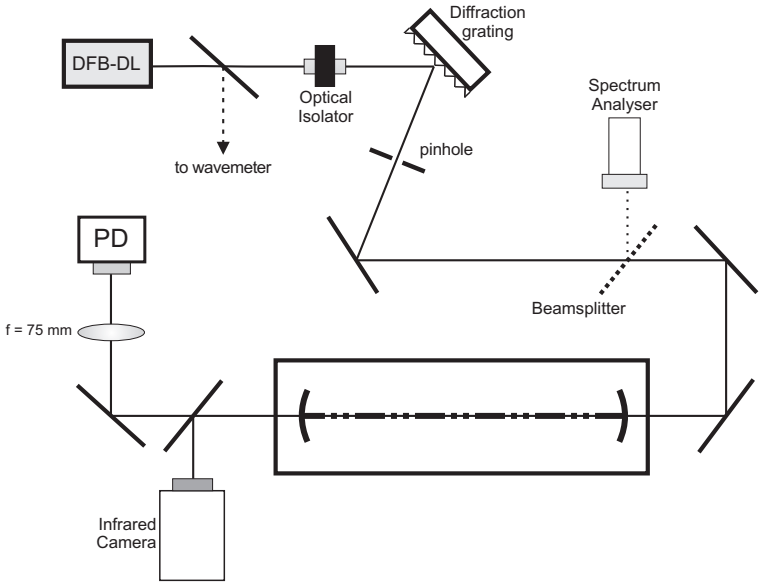

Figure 4.3: The cavity-enhanced absorption spectroscopy (CEAS) setup employed in this work.

A DFB-DL [*Bookham*] centred close to 1532 nm was employed as the radiation source and was driven by a commercial temperature and laser controller [*Thorlabs, ITC-510*] connected to an integrated laser mount [*Thorlabs LDM-21*]. The DFB-DL was operated at around 24 °C, and at injection currents close to 180 mA. The laser current was scanned, by applying a triangular ramp voltage of 3.5 V peak-to-peak at a frequency of 5–6 Hz using a function generator [*TTi, TG230*]. A flipper mirror was placed immediately after the laser, to allow its wavelength to be characterised using a wavemeter [*Burleigh WA-1000*]. An optical isolator was placed between the laser and the cavity to reduce the intensity of the uncontrolled feedback of light back into the laser from optical components in the setup, since this can disrupt the correct operation of the laser.

The radiation was dispersed using a diffraction grating, to reduce the level of

amplified spontaneous emission (ASE) from within the laser active medium reaching the detector. The ASE was close to 25% of the total laser output. To calibrate the frequency scale, measurements were carried out on the spectral line studied under conditions where pressure broadening effects were negligible. The resulting line width was used to calibrate a spectrum analyser [*Melles Griot, 1450–1650 nm*, nominally 2 GHz free spectral range], whose accurate free spectral range was then used as a frequency standard in subsequent CEAS experiments. The optical cavity for the CEAS work comprised a pair of highly reflective "supermirrors" [*Research Electro-Optic 10881*], each with reflectivity 0.9999 in this wavelength region, and separated by 25 cm. This optical cavity was housed within a stainless steel and Perspex vacuum-tight chamber that was equipped with inlet/outlet fittings for gas flow and pressure monitoring. A second flipper mirror, positioned behind the optical cavity, allowed the cavity output to be directed towards an infrared camera [*Electrophysics, Micronviewer 7290A*]. This camera was employed to monitor the spatial profile of the cavity transmission and to confirm that the desired cavity alignment was achieved. The light exiting the final mirror of the optical cavity was then collected on a photodiode [*Thorlabs, DET10C/M*]; the signal was amplified and recorded by a digital oscilloscope [*Tektronix TDS2014*] along with the signal from the spectrum analyser. Data acquisition was carried out using LabVIEW.

4.5.2 OF-CEAS Experiments

The OF-CEAS spectrometer employed for the measurements described in this chapter was broadly the same as that described in Chapter 3, and illustrated in Figure 3.1. The same DFB-DL was employed as detailed in Section 4.5.1 for the CEAS experiments. Whilst a formal mode-matching setup was not adopted, collimation and telescoping optics were added to the set up to improve the beam shape and size so as to seek broadly to optimise the efficiency of coupling of light into the cavity.

For data taken with both techniques, acetylene dilutions in argon with accurately-measured ratios (close to one part in fifty) were used, so that manageable pressures

of gas could be added to the cell, whilst maintaining the resulting transitions in the relatively low-absorption regime to which our analysis is appropriate. Background signals were, with both sets of apparatus, taken by measuring the transmission through the evacuated cell. For the pressure-broadening measurements, an initial spectrum was taken using between 0.5 and 1 Torr of the acetylene gas solution, and then the broadening gas was introduced in increasing amounts with a spectrum being taken at each pressure, after the gases had had time to diffuse and mix through the cell.

Firstly, a set of line shape measurements was taken on the P(6) absorption line in the $\nu_1 + \nu_3$ band of the mixed isotopologue ($^{12}C^{13}CH_2$) at 6528.735 cm^{-1}; these were recorded and analysed to produce pressure broadening coefficients for air and for each of the noble gases studied. Subsequently, to compare our line shape results with others' earlier work, a second series of pressure broadening experiments was carried out using the OF-CEAS apparatus in exactly analogous fashion. Measurements were in this case made on the P(12) line of the same vibrational band of the pure isotopologue $^{12}C_2H_2$, found at 6526.538 cm^{-1}.

After the P(6) measurements were taken, and the line shapes measured and analysed, the electronics were re-optimised, changing the balance between the amplification factors across the various operational-amplifiers. The collimation optics were replaced and the alignment of the cavity re-optimised. To measure the ultimate sensitivity achievable with this system, a further set of detection measurements, this time without a full line shape study, were carried out on the P(3) Coriolis doublet within the $\nu_1 + \nu_3 + \nu_5^1 - \nu_5^1$ ($\pi_u - \pi_u$) hot band of $^{12}C_2H_2$, located at 6527.59 [P(3f)] and 6527.61 [P(3e)] cm^{-1} [128].

4.6 Results

4.6.1 CEAS Results

CEAS spectra were produced by plotting the CEAS signal, in the form presented in equation 2.36, against frequency. The frequency scale for each of the CEAS spectra was calibrated using the spectrum analyser, which gave peaks separated by an accurate free spectral range close to 2 GHz. A LabVIEW routine was used to generate a calibrated spectral frequency scale for our CEAS data from the spectrum analyser signal. An example of such a spectrum is given in Figure 4.4, which shows data for the P(6) line in the $\nu_1 + \nu_3$ band of $^{12}C^{13}CH_2$ at 6528.735 cm^{-1}, fitted with a Voigt profile.

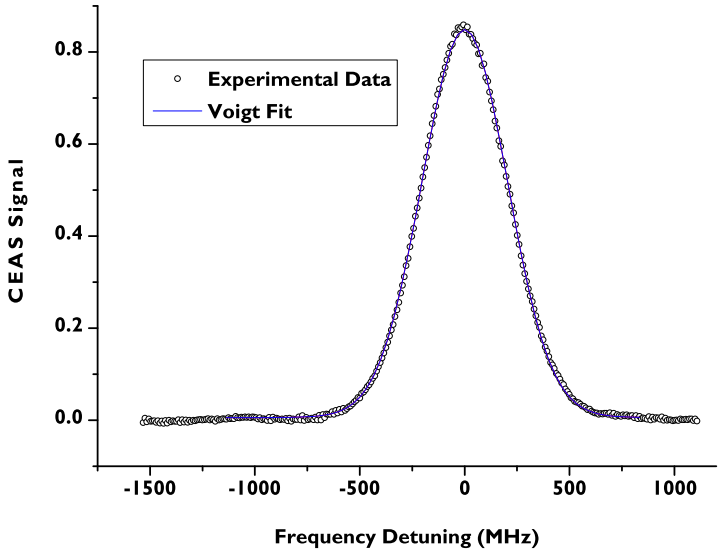

Figure 4.4: CEAS spectrum taken with 51.3 mTorr of acetylene, in approximately 2.5 Torr of argon, showing the P(6) line in the $\nu_1+\nu_3$ band of the $^{12}C^{13}CH_2$ acetylene isotopologue. For clarity, a selection of only 300 points is shown across the profile: a Voigt fit to the data is also shown.

The returned Lorentzian contribution to the full-width-at-half-maximum (FWHM) is 11.8 ± 1.4 MHz, and is in good agreement with the Lorentzian contribution of 12.2 MHz expected on the basis of the argon pressure broadening coefficient for this

line which is presented below. For these line width measurements, the resolution of the experimental setup is likely to be limited by the bandwidth of the detection apparatus, which is calculated to be approximately 10 MHz; this value considerably exceeds the laser bandwidth, which is close to 1 MHz.

The P(6) absorption line within this band was selected for the present work as it is found in a region of the acetylene spectrum that is relatively free of spectral congestion. Further, its integrated cross-section of $1.32 \times 10^{-22}\,\mathrm{cm^2 cm^{-1} molec^{-1}}$ (from the HITRAN [128] database, quoted with an error of approximately $\pm 1.5\%$) means that the absorption signal is large enough to be observed with a good signal-to-noise ratio at these low acetylene concentrations, but still within the low absorption regime appropriate to our analysis. Knowing accurately the concentration of acetylene in a series of spectral samples, the cavity finesse (and therefore the geometric mean mirror reflectivity) can be calibrated. The geometric mean reflectivity of the mirrors, R, is related to the cavity finesse, F, through equation 2.7.

The background signal, I_0, is determined using a polynomial fit to the spectral baseline, with the absorption signal removed. The noise level on the data is then found by examining the standard deviation of the data points from a linear fit to a region of the spectrum free of absorption features. This value for the noise level is then applied to the CEAS equation (equation 2.36); since the acquisition time and the cavity length are well known, it follows that the sensitivity can be calculated. With a cavity finesse of ≈ 15700, a cavity length of 25 cm and root mean square (RMS) noise level of 3.4×10^{-3}, the data in Figure 4.4 were taken in a total acquisition time of 16.9 s; this results in an acquisition-time-reduced sensitivity of $5.6 \times 10^{-8}\mathrm{cm^{-1} s^{1/2}}$.

Pressure broadening data sets were taken with helium, argon and air each acting as the buffer gas. Fitting a Voigt profile to each such spectrum, with the Gaussian part fixed to the calculated Doppler width, returns a value for the Lorentzian width. A plot of the Lorentzian FWHM against pressure yields a gradient of 2γ, from which the pressure broadening coefficient, γ, is obtained. Figure 4.5 shows examples of such

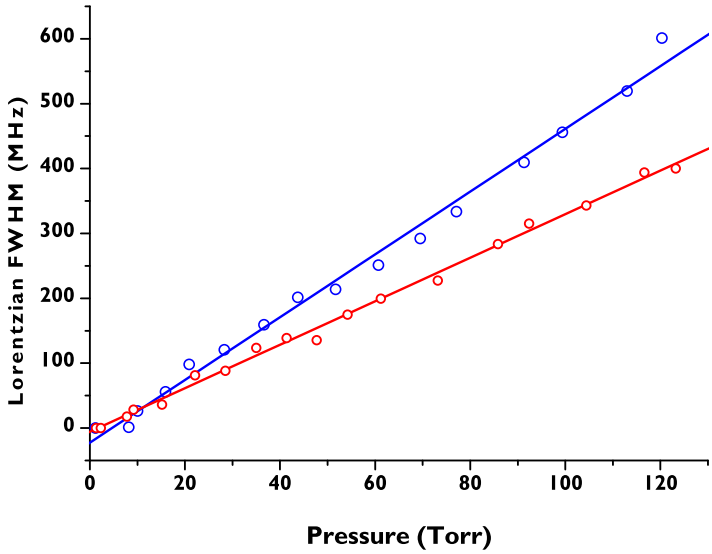

Figure 4.5: Plot showing Lorentzian FWHM against pressure of buffer gas with helium (red) and argon (blue) for the same absorption line as that shown in Figure 4.4. The gradient of this graph, for each gas X, is $2\gamma_X$.

plots, for helium and argon, of the Lorentzian FWHM against buffer gas pressure, with helium generating a broadening coefficient of 1.68 ± 0.03 MHz/Torr, and argon 2.42 ± 0.06 MHz/Torr, where the errors are the returned values ($\pm\sigma$) associated with the linear fit. There is a small non-zero intercept (for Ar, -22.5 MHz; for He, -5.66 MHz) associated with each linear fit; this may be attributable to small systematic errors in the pressure measurement, as well as the error associated with the linear fit. Indeed, in the pressure broadening measurements presented here it is the systematic errors arising from any inaccuracy in measurement of the pressure that are likely to dominate the error on the returned widths. The value of R for these spectra was determined by calibrating the apparatus using known amount of absorber; a value of 0.99981 ± 0.00005 was returned. A similar plot produced an air pressure broadening coefficient for this transition of 3.12 ± 0.04 MHz/Torr. As can be seen from the data presented both in Figure 4.5 and Table 4.2, there is a general increase in the pressure broadening coefficients with increasing polarisability of the noble gases [237]. This is mainly a consequence of the concomitant increase in the dispersion interaction

between the species, and is explored later.

	Air MHz/Torr	**Helium** MHz/Torr	**Neon** MHz/Torr	**Argon** MHz/Torr	**Xenon** MHz/Torr
P(6) $^{13}C^{12}CH_2$ (6528.735 cm^{-1}) OF-CEAS	3.10 ± 0.25	1.63 ± 0.047	1.56 ± 0.053	2.37 ± 0.095	2.64 ± 0.19
P(6) $^{13}C^{12}CH_2$ (6528.735 cm^{-1}) CEAS	3.12 ± 0.042	1.68 ± 0.026		2.42 ± 0.059	
P(6) $^{12}C_2H_2$ (6541.960 cm^{-1}) Arteaga [236]	3.40 ± 0.07	1.71 ± 0.026	1.64 ± 0.016	2.46 ± 0.008	2.99 ± 0.026
P(11) $^{12}C_2H_2$ (6529.172 cm^{-1}) Arteaga [236]	3.15 ± 0.10	1.72 ± 0.026	1.51 ± 0.016	2.05 ± 0.016	2.60 ± 0.049
P(12) $^{12}C_2H_2$ (6526.538 cm^{-1}) Arteaga [236]	3.07 ± 0.057	1.72 ± 0.035	1.48 ± 0.016	2.05 ± 0.006	2.51 ± 0.012
P(12) $^{12}C_2H_2$ (6526.538 cm^{-1}) OF-CEAS	3.01 ± 0.096	1.74 ± 0.025	1.41 ± 0.021	1.98 ± 0.036	2.42 ± 0.067

Table 4.2: Summary of pressure broadening coefficients found (HWHM), including the data described in this thesis and the work of Arteaga *et al.* [236].

As noted in section 4.4, prior studies give few data for the pressure-induced line broadening in this mixed isotopologue, $^{12}C^{13}CH_2$. However, the work on $^{12}C_2H_2$ by Arteaga *et al.* [236] provides pressure broadening values for transitions in the same spectral region which can be used as a comparison; these are collated with our data in Table 4.2. Values from Arteaga's work are presented for the equivalent P(6) line in the pure isotopologue, as are the lines at P(12) and P(11), whose central frequencies lie respectively just above and below that of the line at 6528.735 cm^{-1} studied in the present work. Good agreement is seen between the two sets of measurements, as is clear from the data in Table 4.2.

In addition, pressure broadening data were taken for both methane and ethene. Acetylene is an impurity in ethene production, and so the pressure broadening coefficients of acetylene in methane and ethene are of industrial interest. A pressure broadening coefficient of 2.21 ± 0.11 MHz/Torr was determined for the P(6) line with methane, whilst ethene yielded a coefficient of 3.58 ± 0.06 MHz/Torr. These hydrocarbon buffer gases produce generally larger pressure broadening coefficients because they have more internal degrees of freedom in addition to greater polar-

isability [237]; this increases the magnitude of the interaction between the collider and absorber, resulting in both more efficient elastic and inelastic energy transfer and larger broadening coefficients.

4.6.2 OF-CEAS results

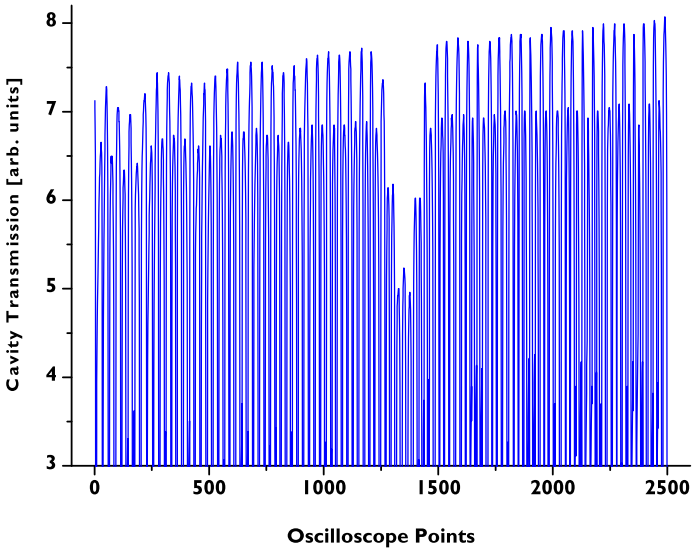

Figure 4.6: Raw, unprocessed OF-CEAS data from the oscilloscope, showing a single shot of the cavity transmission. In the centre of the trace, the P(6) transition within the $\nu_1 + \nu_3$ combination band for the $^{12}C^{13}CH_2$ isotopologue is clearly visible. The data were taken using 0.519 Torr of the 1:49 acetylene-in-argon mixture.

An analogous set of experiments was performed on the P(6) line, using the OF-CEAS setup. Spectra are presented, once again, in the same form as for the CEAS measurements: the CEAS signal is plotted against frequency or equivalently the mode index, since consecutive modes are spaced by the consistent free spectral range corresponding to the cavity. Figure 4.6 shows an example of an unprocessed spectrum, recorded directly from the oscilloscope in the experiment. We can clearly see the intensity alternation between consecutive modes, and during the analysis these are dealt with by splitting up the odd- and even-indexed mode maxima for

background fitting, in the manner described in chapter 3.

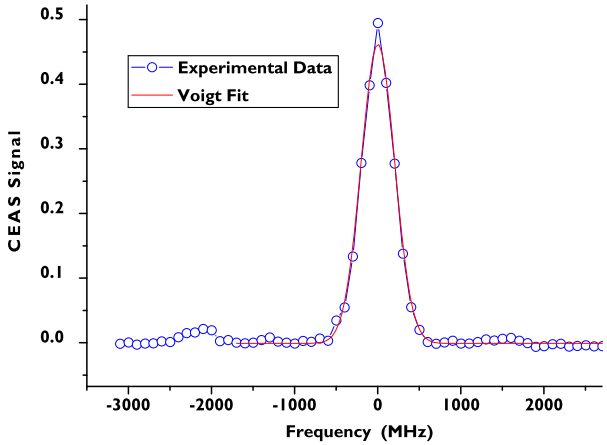

Figure 4.7: Analysed example OF-CEAS spectrum showing the P(6) transition within the $\nu_1 + \nu_3$ band for the $^{12}C^{13}CH_2$ isotopologue, corresponding to the raw data shown in Figure 4.6. A Voigt fit to the data is also shown.

Figure 4.7 shows an example OF-CEAS spectrum for 0.519 Torr of 1:49 acetylene/argon mix (0.011 Torr of acetylene), with a Voigt profile fitted. At this low pressure, Doppler broadening is dominant, and so the Lorentzian FWHM is negligible and a Gaussian fit produces a linewidth of 460.9 ± 5.7 MHz, which is in good agreement with the calculated value of 464 MHz. Recording ten averages at a laser scan frequency of 4.27 Hz, a time-reduced sensitivity of $7.15 \times 10^{-9}\,\mathrm{cm^{-1}s^{1/2}}$ was achieved for the data shown in Figure 4.7. This is an increased sensitivity relative to that achieved using the standard CEAS technique, since a greater signal-to-noise ratio (from $\sim$ 250 to $\sim$ 450 in this case) results from higher cavity transmission with optical locking to successive TEM_{00} modes, and from reducing the noise and intensity fluctuations associated with the laser linewidth. The limiting noise source in the case of conventional CEAS arises from the residual mode structure [238], and this problem is dispensed with in the case of the OF-CEAS experiments.

Measurement of the area under the absorption signal allows a mean mirror reflectivity and therefore a finesse to be calculated. Using the absorption signals for the

P(6) transition in the isotopologue, a mean mirror reflectivity of 0.9991 ± 0.00003 results, corresponding to a cavity finesse of ≈ 3500. The sensitivity of the system may be improved by increasing the total data acquisition time, but there is a limit beyond which a further increase in the averaging does not bring about an improvement in the limit of detection. Over time, as more averages are taken, the influence of longer-term instabilities in the laser output – such as intensity fluctuations, laser frequency drift or the laser unlocking from the cavity – eventually becomes important, leading to deterioration of the detection sensitivity. Consistent with the observations of Morville *et al.* [158], we typically see that, when using our setup, the detection sensitivity only continues improving up to an optimal acquisition time of the order of a second. Future work with the spectrometer will be directed to improving the ultimate sensitivity of the system by tackling some of the long-term noise contributions – especially temperature-drift on the DFB-DL – and therefore allowing for longer averaging periods.

As described at the end of section 4.5.2, one further optimisation of the collimation optics and the electronics within the setup was implemented, in order to find the best possible detection sensitivity. Having done this, a final set of detection data were measured on the P(3) Coriolis doublet in the $\nu_1 + \nu_3 + \nu_5^1$–ν_5^1 (π_u–π_u) hot band of ^{12}C-acetylene; an example spectrum is shown in Figure 4.8.

A linear fit to the spectral baseline on this spectrum produced an optimal α_{min} value of $1.42 \times 10^{-9}\,\mathrm{cm^{-1}s^{1/2}}$, a significant improvement on the sensitivity measured on the $^{12}C^{13}CH_2$ isotopologue measured before the further optimisation of the experiment. This was obtained by performing the linear fit on all of the spectral points to the lower-frequency side of the absorption doublet, and the standard deviation to this linear fit taken as the signal size corresponding to a notional signal-to-noise of one. A double Gaussian fit to the data is shown in Figure 4.8, and returned a Gaussian FWHM of 479 MHz for each peak, in good agreement with the theoretical Doppler width of 474 MHz.

Pressure broadening data were recorded on the P(6) line, using the OF-CEAS

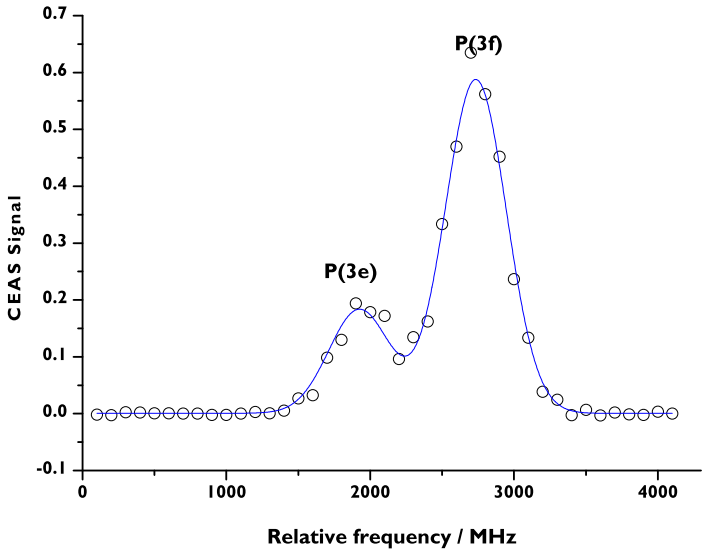

Figure 4.8: OF-CEAS spectrum of the P(3) Coriolis doublet in the $\nu_1+\nu_3+\nu_5^1-\nu_5^1$ (π_u–π_u) hot band of ^{12}C-acetylene, after further optimisation of the setup. Spectrum taken on 0.35 Torr of the 1:49 C_2H_2/Ar mix.

setup, for broadening by air, helium, neon, argon and xenon. Examples of spectra taken with helium as the broadening species are shown in Figure 4.9; the increase in linewidth, and concomitant reduction in peak cross section, are clear as more helium is added.

The relative frequency scale is accurate and consistent throughout, and together with the well-characterised line-centre, this allows us to calibrate the absolute frequency scale for these measurements. Plotting the returned Lorentzian FWHM from the Voigt fits against air pressure, a pressure broadening coefficient of 3.11 MHz/Torr is found. The noble gases studied – helium, neon, argon and xenon – returned pressure broadening coefficients of 1.63, 1.56, 2.37 and 2.64 MHz/Torr, respectively; these values are shown in Table 4.2, together with the appropriate errors.

A further set of line shape measurements was made on the P(12) line in the $\nu_1+\nu_3$ band of the pure isotopologue, $^{12}C_2H_2$, to facilitate direct comparison of the present data with others' work. The pressure broadening plots corresponding to these experiments are given in Figure 4.10, and the resulting values are listed in

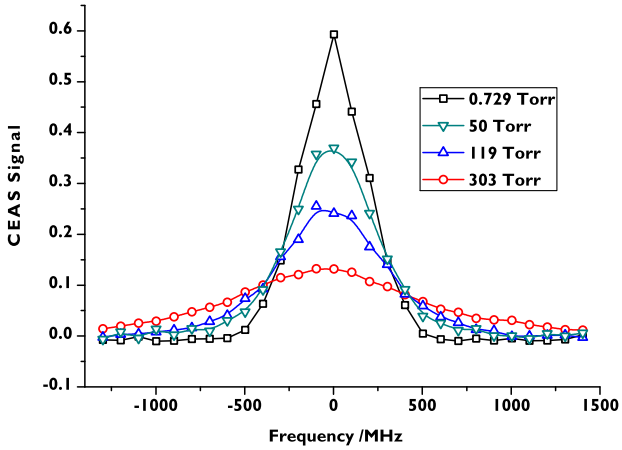

Figure 4.9: Example OF-CEAS spectra on the P(6) line of the $\nu_1 + \nu_3$ combination band, showing the evolution in spectral line shape with addition of helium to 0.729 Torr of the 1:49 acetylene/argon mix. Broadening in the line width, and a corresponding reduction in the peak height, are clearly seen.

Table 4.2. The errors on the pressure broadening coefficients generated using the OF-CEAS setup are, broadly speaking, larger than those from the CEAS experiment without the optical locking; this is consistent with the reduction in frequency resolution on adopting the OF-CEAS technique. This effect is mitigated, though, by the well-defined nature of our frequency scale in the OF-CEAS experiments, allowing these accurate line shape measurements. The values follow the expected trend of increasing pressure broadening coefficient with an increase in broadening gas polarisability, except that helium is out of sequence. One explanation for this may arise from the collision kinematics – the collision frequency is proportional to the mean relative particle speed, in turn proportional to $\mu^{-1/2}$ – and the significantly lower mass of helium.

4.6.3 Parmenter-Seaver Analysis

The Parmenter-Seaver formalism [239] has been used to interpret rare gas collisional broadening data such as those in Table 4.2 [108, 240]. Under this model, the colliding

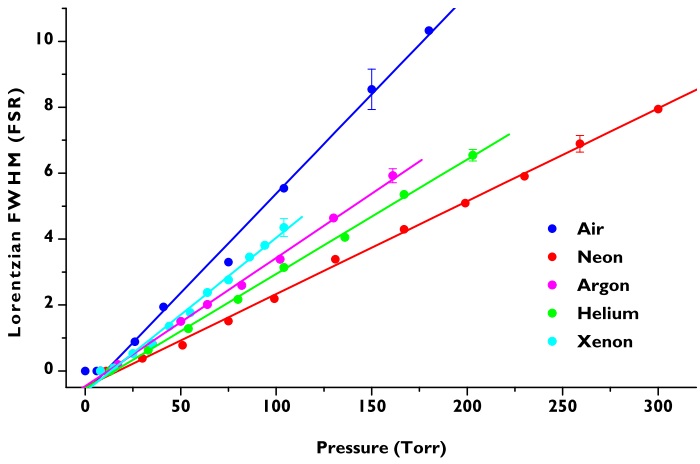

Figure 4.10: Pressure broadening plots for the OF-CEAS measurements on the P(12) line in the $\nu_1 + \nu_3$ band of the pure isotopologue, $^{12}C_2H_2$. To illustrate the confidence in these data based on the goodness of the straight line fit, errors are shown corresponding to $\pm 2\sigma$, where σ is the standard deviation of the data from the fit; for clarity, this is shown for just a single point within each gas.

species are considered to form a complex, with the associated rate coefficient linked to the equilibrium constant for the complexation process. The measured pressure broadening coefficients can be considered as rate coefficients for the formation of the complex; these may then be converted into corresponding "reaction" cross-sections, σ_M, which are related to the bond strength of the excited complex through:

$$\ln \sigma_M = \ln C + \frac{\epsilon_{A^*M}}{k_B T} \tag{4.14}$$

wherein C is a constant, and ϵ_{A^*M} is the intermolecular well depth between the acetylene molecule (A^*) and the broadening collider (M). For the rare gas–acetylene complexes, the values of the equilibrium well depth D_e have been found [232, 241], and Figure 4.11 shows a plot of $\ln \sigma_M$ against D_e at room temperature.

The expected monotonic increase of $\ln \sigma_M$ with D_e is observed, but the best linear fit, as shown in the figure, has a gradient roughly double $(k_B T)^{-1}$ at room temperature. Reduction of the well depth to allow for zero-point energy effects (which may give a more realistic value for ϵ_{A^*M}) serves only to increase the gradient

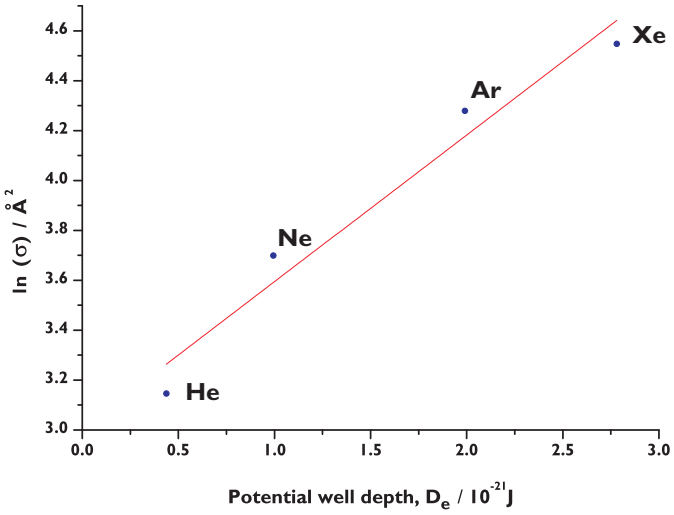

Figure 4.11: Plot of $\ln \sigma$ against D_e for the rare gas–acetylene complexes.

further. The Parmenter-Seaver formalism is useful insofar as it may have predictive power (for example to estimate the pressure broadening by krypton, unmeasured in the present work), though it should generally be regarded as a qualitative model.

Here, the values of ϵ_{A^*M} may be estimated to be the calculated well depths D_e. In the majority of cases, where the Parmenter-Seaver formalism is adopted, the well depths of the complex are not known, and in these cases the geometric mean combination approximation $\epsilon_{A^*M} \approx \sqrt{\epsilon_{A^*A^*}\epsilon_{MM}}$ is used [242], where for the present case $\epsilon_{A^*A^*}$ and ϵ_{MM} would be the well depths of the acetylene dimer and the rare gas dimers respectively. If that approximation holds, then the cross-sections for pressure broadening take the following form:

$$\ln \sigma_M = \ln C'' + \beta \sqrt{\frac{\epsilon_{MM}}{k_B}} \tag{4.15}$$

where β is expressed as follows:

$$\beta = \sqrt{\frac{\epsilon_{A^*A^*}}{k_B T^2}} \tag{4.16}$$

The well-depth of the acetylene dimer should then be found from the gradient,

β, of a graph of $\ln \sigma_M$ against $\sqrt{\frac{\epsilon_{MM}}{k_B}}$. The OF-CEAS data for the P(6) line were used to construct such a plot, yielding the potential well depth of the acetylene isotopologue dimer as 10.2 ± 1.7 kJ mol^{-1}. Calculated values for the ground state molecule dimer are generally of the order of 7 kJ mol^{-1} [243]. As such, the correlation with rare gas dimer well depth appears to give a reasonable estimate of the acetylene dimer well depth. However, this agreement seems largely to be fortuitous, given that the application of equation 4.14 does not give the expected value for the gradient. As such, we have seen that whilst observation of a Parmenter-Seaver correlation between rare gas broadening coefficients may lend qualitative credence to the relative sizes of a set of broadening coefficient data, and the model may be expected to have reasonable predictive power, the approximations within the model render it unsuitable for a full quantitative interpretation of collisional broadening data.

4.7 Collisional Narrowing

Collisional broadening effects are treated within an analysis of the change in the amplitude and phase of the light on interacting with the colliding medium. Provided that these interactions are rapid compared to the time between successive collisions, this change can be represented as an essentially random perturbation to the light's phase, and results in the Lorentzian line profile discussed at section 4.3.1; this is then convolved with the Gaussian profile resulting from treatment of Doppler broadening (equation 4.11) to produce the Voigt profile detailed at equation 4.13. Whilst this analysis holds at moderate pressures, at lower pressures the Voigt fit has sometimes shown a reproducible and characteristic mismatch with the spectral data, particularly close to the line centre and at the line wings. This was attributed by Dicke [244] to a reduction in the Doppler width brought about by a collisional reduction in the range of velocities associated with the molecules in the sample, and the effect is often known as *Dicke narrowing*.

There are two major models for the quantitative description of such collisional

narrowing effects, distinguished according to whether the collisions are considered to be hard or soft [245]. Under the former regime, hard collisions are assumed to have no direct effect upon the velocity of the absorbing or emitting particle; the velocity distribution after each and every collision is assumed to conform to a Maxwell-Boltzmann description, each particle's final velocity being essentially uncorrelated with its initial velocity. This model results in a *Rautian* line shape [245], and is most appropriate when the mass of the collider greatly exceeds that of the absorber.

Galatry [246] presented a description of simultaneous Doppler- and collisional broadening effects on the line shape of an absorption transition based on classical Fourier theory, most appropriate to a soft collision regime. Under this model, each collision has a significant effect on the absorber's velocity, and so the initial and final values of that velocity are strongly correlated. The cumulative effect across the bulk sample is modelled using Brownian motion, and a *Galatry* profile results with the following form:

$$G(x,y,z) = \frac{1}{\sqrt{\pi}}\,\mathrm{Re}\left[\int_0^\infty \exp\left\{-ix\tau - y\tau + \frac{1}{2z^2}[1 - z\tau - \exp(-z\tau)]\right\}\ \mathrm{d}\tau\right] \quad (4.17)$$

In this expression, x is the frequency displacement from the line centre, normalised to the Doppler width; y is the similarly-normalised Lorentzian width, related to the effective frequency of the broadening collisions. z is the additional parameter that has been introduced to account for the Dicke narrowing effect. This *narrowing parameter* is related to an effective frequency of the velocity-changing collisions within the soft collision approximation; accordingly, the value of z scales with pressure. The gradient of a plot of z against pressure, analogous to a pressure broadening coefficient, is usually represented by β. This value can in turn be related to the self-diffusion coefficient, D, through:

$$D = \frac{k_B T}{2\pi c M \beta} = 4.374 \times 10^{-4} \frac{T}{M\beta} \quad (4.18)$$

where k_B is the Boltzmann constant, c and T are respectively the speed of light and

the temperature, and M is the molecular weight of the absorber.

4.7.1 Fitting to the CO_2 spectra

For the absorption spectra taken on carbon dioxide as described in Chapter 3, a study was carried out to determine the best function with which to fit the absorption line shape. This is of interest for fundamental physical reasons, since it can give us considerable information about the physics of the interactions between absorber molecules, or between the absorber and other molecules. It is also of importance in the design of an accurate detection process; a fully accurate determination of the sample concentration requires a precise fit to the sample data to find the area under the absorption signal.

An example carbon dioxide spectrum is shown in Figure 4.12. Voigt and Galatry fits to the data are shown, along with the relevant residuals (data − fit). The characteristic 'W' shape in the residual to the Voigt fit is seen clearly, indicating the effect of Dicke narrowing.

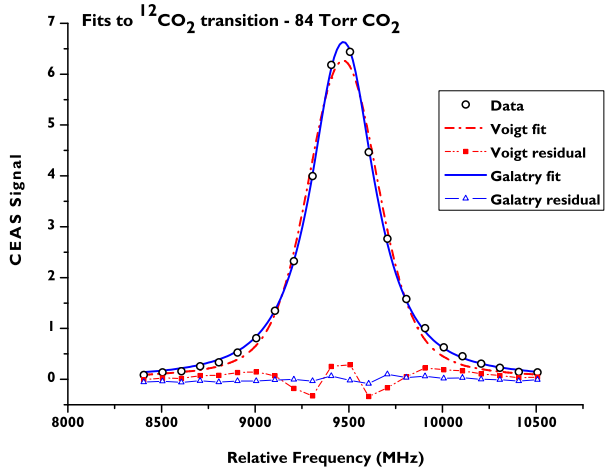

Figure 4.12: Analysed absorption spectrum showing the R(60) line in the $3\nu_1+\nu_3$ vibrational band of $^{12}CO_2$. The data correspond to 84 Torr of carbon dioxide gas, and residuals to the two (unweighted) fits are shown.

That the Galatry function provides a superior fit is clear from the magnitudes

of the residuals. The Galatry fit returns an estimate for the carbon dioxide self-broadening coefficient of $2.2 \pm 0.2\,\mathrm{MHz/Torr}$, which based on this small number of points and at relatively low resolution is in reasonable agreement with the HITRAN [128] value of 2.6 MHz/Torr. The β value returned by the Galatry fits to these data was $0.044 \pm 0.013\,\mathrm{cm^{-1}atm^{-1}}$. Through equation 4.18, this results in an estimate for the self-diffusion coefficient in CO_2 of $0.067 \pm 0.02\,\mathrm{cm^2s^{-1}}$, in reasonable agreement with a simple kinetic theory [247] estimate of $0.081\,\mathrm{cm^2s^{-1}}$.

However, it is important to verify that the improvement in fit is not simply brought about by the introduction of extra parameters, but because the model including collisional narrowing is in fact physically more appropriate. For this, a statistical analysis was carried out.

4.7.2 The F-test

A statistical F-test [248] may be used to compare the validity of two models of differing complexity for modelling a set of data. An F-test provides an estimate of the probability that the improvement in fit on moving to a more complex model is a result simply of the increase in the number of fitting parameters, rather than owing to the more complex model actually being more appropriate. This probability is called the p-value. The expression for F is given by:

$$F = \frac{SS_1 - SS_2}{SS_2} \Big/ \frac{DF_1 - DF_2}{DF_2} \tag{4.19}$$

In each case, the subscript '1' refers to the simpler model, and '2' refers to the more complex model with more parameters. The SS terms are the respective sums of squared deviations between the fit and the data for each point i:

$$SS = \sum_i (x_{fit,i} - x_{data,i})^2 \tag{4.20}$$

DF in each case denotes the number of degrees of freedom associated with each model; this is simply given by the difference between the number of data points and

the number of fit parameters. A p value may then be determined, knowing the two DF values and the F value; the p values corresponding to different values of F are tabulated in many statistical texts [248]. An F value close to one indicates that the improvement in fit can largely be attributed to the increase in fitting parameters, and that the more complex model is not intrinsically any more appropriate to the data; this would also result in a p-value close to one.

An F-test was performed on our CO_2 data (Figure 3.10) at each pressure, comparing our Voigt fit (six parameters) with the Galatry fit (seven parameters) that has an additional term to allow for collisional narrowing. In every case except the data with 5 Torr of carbon dioxide, the test returned a p-value less than the accepted significance limit of 0.05, indicating that there is a statistically-significant improvement in the fitting when using the Galatry model, with a $> 95\%$ probability that the improvement is attributable to the Galatry model being more appropriate. For the data at 5 Torr, the statistical test indicated that there was no statistically-significant improvement in the fitting when using a Galatry fit rather than a Voigt fit; this is consistent with the supposition that no effective Dicke collisional narrowing would be observed at this low sample pressure.

4.8 Conclusions and Outlook

The OF-CEAS spectrometer developed and reported in Chapter 3 has been applied to high-sensitivity studies of acetylene absorptions in the region of 1532 nm, and characterised relative to a standard cavity-enhanced absorption spectroscopy (CEAS) apparatus. Detection was initially focussed on the P(6) line of the $\nu_1 + \nu_3$ vibrational band in the mixed-carbon isotopologue of acetylene, $^{12}C^{13}CH_2$. CEAS experiments without optical locking gave a detection sensitivity for measurements on this absorption line of $5.6 \times 10^{-8}\,\mathrm{cm^{-1}s^{1/2}}$, employing a cavity of finesse ≈ 15700. An improvement in the detection sensitivity has been realised using OF-CEAS, which returns a value for α_{min} of $7.15 \times 10^{-9}\mathrm{cm^{-1}s^{1/2}}$, even when employing a cavity of only moderate finesse (≈ 3500).

After further optimisation of the OF-CEAS setup, measurements were presented on the Coriolis doublet of P(3e) and P(3f) lines in the $\nu_1 + \nu_3 + \nu_5^1 - \nu_5^1$ $(\pi_u - \pi_u)$ hot band of the $^{12}C_2$ isotopologue. An ultimate minimum detectable absorption coefficient of $1.42 \times 10^{-9}\,\mathrm{cm^{-1}s^{1/2}}$ was determined. Considering a direct scaling of detection sensitivity with cavity finesse, and taking account of the difference in the two cavity lengths, suggests an improvement of approximately thirty times on moving from CEAS without locking to the optically-locked OF-CEAS apparatus.

Line shape data were measured for the P(6) line in the mixed-carbon acetylene isotopologue; specifically, pressure broadening coefficients were measured for this line, in air and noble gases, using both techniques. The data from the two setups were found to be in good agreement, suggesting that the inherent sacrifice in resolution when adopting the OF-CEAS setup is compensated for by its exceptionally well-defined frequency scale, allowing accurate line width measurements with both techniques. These data also compare satisfactorily with data from others' earlier work, especially with that of Arteaga *et al.* [236] on absorption transitions in the pure carbon-12 isotopologue of acetylene in this wavelength region. Further measurements of pressure broadening coefficients for the P(12) line in the same vibrational band, but in the pure carbon-12 isotopologue of acetylene, allowed a direct comparison with Arteaga's work [236], and excellent agreement was seen.

The Parmenter-Seaver formalism, sometimes used to interpret collisional broadening data [108, 240], has been discussed in light of its applicability to the data measured in this work, and limitations of the model indicated.

Finally, the carbon dioxide data from Chapter 3 were subject to line shape analysis to account for collisional broadening and narrowing effects. A Galatry fit was found to provide a superior description of the carbon dioxide spectral data at sample pressures in excess of 5 Torr, relative to the Voigt fits which make no allowance for collisional narrowing effects. These effects were able reliably to be observed and quantified, even at the low resolution offered by the OF-CEAS technique. From the OF-CEAS data, a narrowing parameter of $\beta = 0.044 \pm 0.013\,\mathrm{cm^{-1}atm^{-1}}$

was returned, corresponding with a CO_2 self-diffusion coefficient of $D_{CO_2:self} = 0.067 \pm 0.02\,\mathrm{cm^2 s^{-1}}$, in reasonable agreement with an estimate determined within simple kinetic theory. Statistical testing through use of an F-test confirmed that the improvement in fit when adopting a Galatry function was statistically significant, implying a physically meaningful improvement when moving to a model that accounts for collisional narrowing effects.

Chapter 5

Mid-Infrared Detection of NO_2

The present chapter concerns the use of convenient, economical near-infrared diode lasers combined with non-linear optical techniques in the efficient generation of mid-infrared light for sensitive spectroscopic detection. The theory and realisation of such non-linear optical techniques are discussed, alongside a consideration of their merits for use in a spectroscopic detection tool.

More specifically, the generation of mid-infrared radiation close to 3.47 μm is described, making use of quasi-phase-matched difference frequency generation (QPM-DFG) in a crystal of periodically-poled lithium niobate (PPLN). QPM-DFG is carried out in a 40 mm PPLN crystal, using pump and signal radiation from diode lasers centred at wavelengths of ∼1064 and ∼1535 nm. The resulting 60 μW of mid-infrared radiation is characterised and applied to the detection of (gas-phase) nitrogen dioxide using direct absorption spectroscopy and wavelength modulation spectroscopy in a long path-length multi-pass cell. Finally, a further sensitive detection method is demonstrated: by adopting a time-integrated cavity-enhanced spectroscopy technique, some of the additional experimental and economic limitations presented by use of cavity ring-down spectroscopy are avoided. The characteristics of each of these detection methods are discussed and quantified. Work in this chapter forms the basis of an article shortly to be submitted.

5.1 Motivation

Nitrogen dioxide is considered as an atmospheric pollutant, on account of its action as a respiratory irritant and its importance in the chemistry controlling the atmospheric concentration of ozone [249]. Particularly, NO_2 is important in the catalytic reduction of stratospheric ozone to dioxygen:

$$NO + O_3 \rightarrow NO_2 + O_2$$

$$NO_2 + O \rightarrow NO + O_2$$

NO_2 is also involved in the "protection" of ozone by removing atmospheric ClO to form a so-called temporary inert reservoir of chlorine nitrate:

$$ClO + NO_2 \rightarrow (ClONO_2)$$

The net effect (in this case) is of an attenuated rate of catalytic ozone removal. Nitrogen dioxide may also react directly with ozone, reducing it to oxygen ($NO_2 + O_3 \rightarrow NO_3 + O_2$) [250].

Tropospheric ozone chemistry is also significantly influenced by NO_x (the generic term for $NO + NO_2$). Ozone arises in the troposphere due to downward transport from the stratosphere, but also due to *in situ* catalytic photo-oxidation of the carbon monoxide and hydrocarbons produced by the combustion of fossil fuels; in this latter process NO_x is the catalyst, and its availability is often the rate-limiting factor. As such, NO_x is a major contributor to the generation of photochemical smog. Typically, urban environments show enhanced concentrations of nitrogen dioxide, in the region up to 100 ppbv, owing to the greater volume of road traffic and industry, as well as the reduced tendency for air mixing, associated with such areas [251].

Accordingly, a full and quantitative understanding of the atmospheric nitrogen dioxide concentration is of great importance in developing a description of the air composition and atmospheric chemistry associated with a particular location.

5.1.1 Earlier Work on NO_2 Detection

Owing to its environmental and atmospheric relevance, the detection of nitrogen dioxide has been the subject of considerable study. Several methods have been put

forward for the detection of nitrogen dioxide in an atmospheric, and sometimes biological, context. Chemiluminescence (CL) methods [252] were among some of the first to be investigated, though they often involve a chemical conversion or calibration step, and lack the directness of a spectroscopic approach. The work of Fontijn *et al.* [252] on nitric oxide detection produced a sensitivity of 4 ppb, and they reported how the apparatus could be extended to NO_2 detection [252]. Detection methods based on bio-sensing have also been demonstrated [253], typically using immobilized bacteria which oxidise the NO_2, with the response at an oxygen electrode attached to the bacteria being used to infer the NO_2 concentration. However, such a method again relies on an indirect measurement, and presents problems associated with the useful lifetime of the bacteria, as well as a long response time; in the work of Okada *et al.* [253], the response time was 3 minutes; additionally, the sensitivity that resulted was 0.51 ppm [253], considerably in excess of typical atmospheric NO_2 concentrations. Electrochemical methods offer a more direct approach to measuring the NO_2 concentration [254–256], but whilst these allow the user to make measurements on small sample volumes in a compact device [257], they are often associated with poor specificity.

More recent work on indirect detection methods has been presented, based on adsorbing the nitrogen dioxide and then extracting and analysing it chemically [258], or on a chemical reaction which generated a coloured complex, whose presence was then quantified photometrically [259]. Resistive-type sensors, based on the changing resistance of the sensor substrate in the presence of NO_2 have also been shown [260, 261], though the response of such a system is strongly dependent upon the exact morphology of the semiconductor crystal and its preparation method [260]. The work of Kida *et al.* [260], for instance, reported a WO_3-based sensor; WO_3 is an n-type semiconductor, and adsorption of NO_2 on the substrate induces a change in the charge distribution within the solid, changing its resistance [260, 262].

Spectroscopic detection methods often lend themselves well to the production of compact and accurate devices; the direct nature of such a measurement, and the

lack of need for chemical reagents and passive samplers, have made such techniques attractive for nitrogen dioxide detection, and several groups have put forward experimental schemes for a spectroscopy-based NO_2 sensor. Occasionally, even the spectroscopic techniques are combined with a chemical step for trapping, conversion or amplification of the analyte. Verma *et al.* [263], for instance, reported diffuse-reflectance Fourier-transform infrared (FTIR) spectroscopy with a pre-conversion step in which the NO_2 is reacted with NaOH-$Na_2As_2O_3$, thereby reducing the NO_2 to nitrite, NO_2^-. The more "traditional" spectroscopic approach for such measurements is typically focussed on sensing by long-path differential optical absorption spectroscopy (DOAS) [18, 19] or by laser-induced fluorescence (LIF) [264]. However, DOAS is not generally suitable for making localised measurements, since its output represents an *average* absorbance, typically over a very substantial path length. A more spatially-selective approach is offered by LIF; Dari-Salisburgo *et al.* [264] conducted atmospheric measurements using such a system, employing a doubled YAG emitting at 532 nm; they reported their limit of detection to be 10 pptv for an integration time of 60 s. These LIF measurements were compared with similar measurements at the same sites using a CL-based technique, and this comparison highlighted the disadvantage of a lack of specificity that is often associated with indirect measurements. Their CL procedure involved a reduction of NO_2 to NO at a molybdenum convertor; they observed that the CL measurements frequently over-estimated the local NO_2 concentration, which they attributed to other NO_y species being reduced to NO by the molybdenum, and producing a signal. However, the application of LIF is not without difficulties: it often requires very careful calibration, and quenching of the fluorescence signal by air can complicate the output signals.

Measurements have also been reported by several groups on the NO_2 absorption spectrum in the red and blue spectral regions, often combined with cavity-enhanced techniques for more sensitive detection. The NO_2 spectrum in the visible region is composed of transition features that are weak or indistinct, even in the windows

free of spectral interferences due to other atmospheric absorbers; if subject to any pressure broadening, these transitions become even less distinct. In order to mitigate the difficulties associated with definitively sampling part of a relatively unstructured spectrum, work in the blue has often been carried out using a broadband light source, so as to seek to over-sample the spectrum. Xu *et al.* [265] and Wu *et al.* [266] presented data respectively for single-pass absorption spectroscopy and incoherent broadband CEAS (IBB-CEAS) measurements using a blue light-emitting diode (LED), achieving respective sensitivities of 3 ppm in 2 s for a 50 cm cell and 2.2 ppbv in 100 s. Langridge *et al.* [134] published work on a broadband absorption spectrometer using LEDs, applicable to a series of trace gases including NO_2. Their system was implemented in the region close to 650 nm, for NO_3 detection, but extrapolating their sensitivity they suggest a limit of detection on the order of 100 pptv for a 10 s measurement in the 440 nm region.

A cw-CRDS spectrometer was employed by Wada and Orr-Ewing [21] for NO_2 detection with an external-cavity diode laser (ECDL) centred close to 410 nm, achieving a minimum detectable NO_2 concentration of 0.1 ppbv in 50 s of averaging. Kasyutich *et al.* [115] presented work close to 405 nm on time-integrated cavity-enhanced absorption spectroscopy; an "off-axis" alignment is claimed to have been adopted to enhance the baseline smoothness and therefore detection sensitivity, for which a value of ~ 0.75 ppb was found. OF-CEAS has also been employed for a nitrogen dioxide spectrometer in the blue spectral region [169] and achieved an excellent sensitivity of 200 pptv in 70 ms of integration time. However, the low resolution which is an inherent feature of that technique is particularly unfortunate for the measurement of a relatively unstructured part of the NO_2 spectrum. Other cavity-enhanced work on nitrogen dioxide includes the phase-shift measurements presented at 430 nm by Kebabian *et al.* [133] and at 404 nm by Kasyutich *et al.* [267]; Kebabian [133] achieved shot-noise-limited detection, corresponding to a 0.3 ppb detection limit, with 10 minutes of averaging, whilst Kasyutich presents a sensitivity of 0.24 ppb in 80 s at atmospheric pressure. In order to seek to combine

the advantages of broadband detection with a higher power of radiation, one interesting new approach involves the application of supercontinuum sources, though these remain rather expensive and continuous wave supercontinuum sources are not yet available commercially. Langridge *et al.* [141] realised a supercontinuum CEAS system for detection of trace gases including NO_2, centered in the region between $\approx 640 - 675$ nm; the authors stated in their article that this region "provides far from optimal sensitivity for NO_2 detection," since the cross-sections here are not the largest available for NO_2. Nonetheless, they presented measurements on a 125 ppbv NO_2 sample, with an uncertainty in the absorber concentration of 0.7 ppbv. This wavelength region does, however, offer the possibility of simultaneous detection of NO_2 and NO_3, which is mentioned in the work of Triki *et al.* [268], who demonstrated an incoherent BB-CEAS system using a 643 nm LED which they suggest might be suitable for simultaneous detection of these two species, achieving a detection limit in the ppbv range after two minutes of averaging. Further work in this wavelength region was demonstrated by Varma *et al.* [269], using a 20 m-long cavity for open-path monitoring of a series of trace gases, including NO_2. A similar implementation has been realised in the near-ultraviolet; the experiments reported by Gherman *et al.* [270] were carried out between 360 and 380 nm, using a high-power LED for NO_2 and HONO detection.

Further work on NO_2 has been presented in the fundamental spectral region associated with the symmetric stretch, found close to 6.2 μm. One relatively high-power source of tunable radiation available in this region which shows promise for sensitive spectroscopic detection is the quantum cascade laser (QCL). Karpf and Rao [271] achieved a minimum detectable concentration of NO_2 at the level of 100 ppb in a short-path absorption cell with an external cavity cw-QCL, combining the advantages of sensitive detection with a broad tuning range, allowing their NO_2 spectra to be taken over 16 cm^{-1}. Pushkarsky *et al.* [272] and Lima *et al.* [273] present work on photo-acoustic spectroscopy with QCLs respectively centred at 6.25 and 6.2 μm. Pushkarsky's system [272] employs a cw-QCL, emitting 300 mW of

radiation over approximately 350 nm, and they demonstrated sub-ppb detection of NO_2. Lima *et al.* [273], by contrast, used a pulsed QCL system, reporting a sensitivity of 80 ppbv for nitrogen dioxide detection.

The final major region in which a significant amount of NO_2 detection work has been reported is that close to 3.4 μm, associated with the $\nu_1 + \nu_3$ combination band; earlier work in the mid-infrared region is discussed in sections 5.3 and 5.4.

5.2 The Spectroscopy of NO_2

Nitrogen dioxide is an asymmetric rotor with C_{2v} symmetry. Unusually for a stable molecule, its ground state has an open shell electron configuration, with $^2A_1$ symmetry, due to its single unpaired electron. There are three normal modes of vibration associated with the NO_2 molecule:

ν_1	symmetric stretch	A_1 symmetry	1618 cm^{-1}	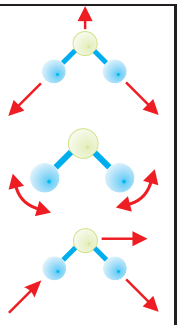
ν_2	bend	A_1 symmetry	750 cm^{-1}	
ν_3	anti-symmetric stretch	B_1 symmetry	1318 cm^{-1}	

Table 5.1: The fundamental vibrational modes of nitrogen dioxide, adopting the co-ordinate system wherein the z-axis lies along the principal axis of the molecule, the $+y$-direction runs left-to-right in the plane of the page, and the $+x$-direction points out of the page toward the reader.

The strongest line intensities are associated with the 1618 cm^{-1} ν_1 fundamental band, but its spectroscopy is complicated by strong interferences due to atmospheric absorbers (principally water) in the region. As such, the relatively strong $\nu_1 + \nu_3$ combination band, centred close to 3.4 μm in a spectral window free of such interferences, is potentially more convenient for a detector to be applied in any atmospheric or industrial environment, and is adopted here.

The quantum-mechanical description of the relevant angular momenta adopted in this chapter is the same as that used in the HITRAN database [128, 274]. The molecule is described as an asymmetric top [195, 275, 276] *i.e.* a molecule in which the three angular momenta are different, $I_a \neq I_b \neq I_c$ but can be described by approximation to the prolate ($I_a < I_b = I_c$) and oblate ($I_a = I_b < I_c$) cases. The basic angular momenta for description of the system are **R**, the molecular rotational angular momentum, **L**, the electronic orbital angular momentum, and **S**, the spin angular momentum arising from the unpaired electron.

R and **L** couple to produce a total angular momentum without spin, **N**. The latter then couples with **S** to give the total angular momentum, **J**, associated with the molecule. **R** and **L** are poorly-defined angular momenta, and so it is the coupled momenta which we use to describe the system, with corresponding quantum numbers J, N, and K.

- N describes the rotational angular momentum;
- J describes the resultant angular momentum after spin-rotation coupling, but excluding nuclear spin. Therefore, $J = N \pm S = N \pm \frac{1}{2}$;
- K is the projection of J on the symmetry axis; K_a and K_c apply to respectively prolate and oblate limiting cases.

Rotational assignment of the nitrogen dioxide spectroscopic transitions is made on the basis of the change in N; conservation of the incoming photon angular momentum implies selection rules of:

$$\begin{array}{lll} \Delta N = 0, \pm 1 & \Delta K_a = 0 & (\text{for } K_a \neq 0) \\ \Delta N = \pm 1 \text{ only} & \Delta K_a = 0 & (\text{for } K_a = 0) \\ \Delta N = 0, \pm 1 & \Delta K_a = \pm 2, \pm 4 & (\text{for all } K_a) \end{array}$$

and analysis of the transition dipole moment leads to the vibrational selection rule:

$$\Delta v = \pm 1 \text{ (and overtones)}$$

Hyperfine structure may also arise from the coupling between **J** and the nuclear spin of the nitrogen (^{14}N, $I = 1$), to give rise to a total angular momentum **F**. This hyperfine splitting is in turn described by the quantum number $F = J, J \pm 1$ [274].

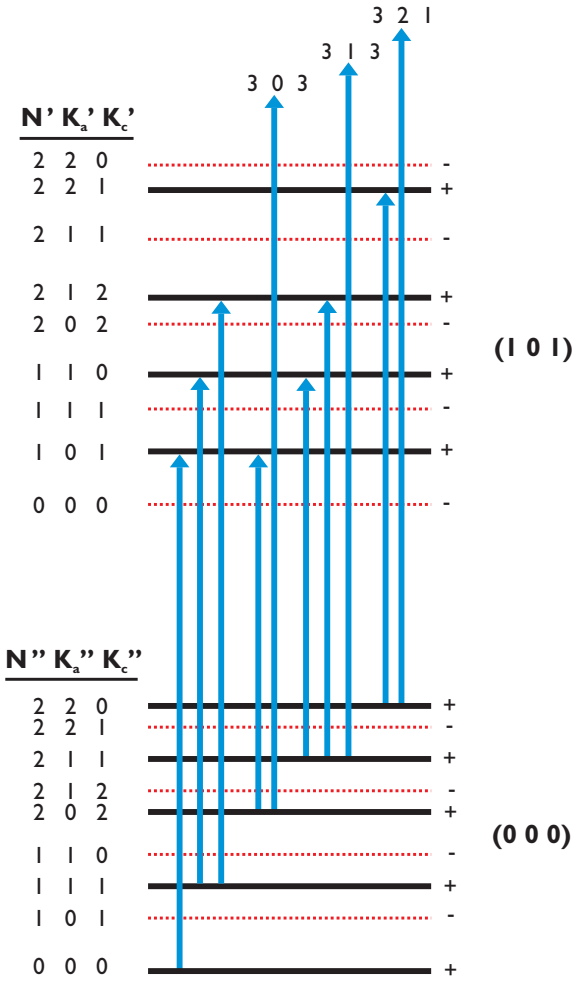

Figure 5.1: Some energy levels for the NO_2 molecule in the $\nu_1 + \nu_3$ vibrational band. Rotational levels are assigned using the quantum numbers shown to the left hand side of each level, and the +/- symbol to the right of each level indicates the symmetry behaviour of the total wavefunction, $\Psi_{TOT} = \psi_{rot}\psi_{vib}\psi_{el}\psi_{NS}$, with respect to exchange of the oxygen atoms.

Nuclear spin statistics are also important in this spectrum. The oxygen nuclei in the molecule are identical bosons (with zero nuclear spin). Accordingly, the Pauli principle tells us that the total wavefunction $\Psi_{TOT} = \psi_{rot}\psi_{vib}\psi_{elec}\psi_{NS}$ for the system must be symmetric with respect to their interchange. The vibrational, electronic

and nuclear spin wavefunctions in the ground state are all symmetric with respect to the $\hat{C}_2$ operation that represents interchange of the identical oxygen nuclei. The rotational wavefunction completes the set; its symmetry behaviour is dependent upon the combination of values for K_a and K_c; symmetry labels for these states were presented by King, Hainer and Cross [277], who developed the notation which takes their name. King, Hainer and Cross notation indicates odd (*o*-) or even (*e*-) symmetry for each combination of K_a and K_c values; an *ee* state or an *oo* state then has even rotational symmetry, whilst the two mixed combinations (*eo, oe*) are antisymmetric. The resulting symmetry behaviour for the total wavefunction is indicated with a $+/-$ in Figure 5.1.

The upper vibrational state $(\nu_1 + \nu_3)$ has B_2 symmetry, and its vibrational wavefunction is antisymmetric with respect to the same $\hat{C}_2$ operation. Once again, the King, Hainer and Cross description of the rotational wavefunction symmetry applies. Some of the allowed transitions for the $\nu_1 + \nu_3$ combination band are shown in Figure 5.1.

Additionally, each line in the vibration-rotation spectrum appears as a spin-doublet, though the splitting is sometimes small enough that these doublets can only be seen at high spectral resolution. Specifically, the electronic spin angular momentum may couple with the rotational angular momentum, giving rise to the form of the total angular momentum, $J = N \pm 1/2$. Vibration-rotation transitions are then subject to the additional constraint $\Delta N = \Delta J$; those transitions with $\Delta N \neq \Delta J$ may be observed within the spectrum, but are generally much weaker. A generalised illustration of these transitions is given in Figure 5.2.

5.3 Non-linear Optical Techniques

Spectroscopic detection in the mid-infrared provides a considerable advantage compared to that in the near-infrared, since it is in the mid-infrared window (particularly in the region close to 3 μm) that many small molecules' fundamental vibrations are to be found. Accessing these stronger transitions may allow for more sensitive

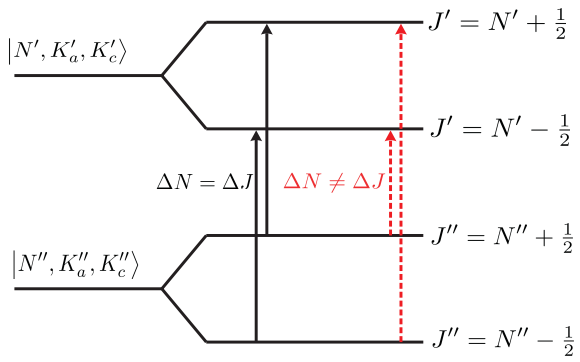

Figure 5.2: Schematic illustration showing the allowed [solid, black] and forbidden [dashed, red] transitions between spin-doublet states within nitrogen dioxide.

detection of a given target species when using an absorption spectroscopy-based technique. However, direct sources of mid-infrared radiation remain relatively expensive, and are occasionally complex to operate. Quantum cascade lasers (QCLs) are now available in the mid-infrared region, though they are only relatively recently available close to 3 μm, and not commercially; QCLs do not currently represent an economical option for gas detection.

These difficulties with direct mid-infrared sources motivate work to generate mid-infrared radiation from other, more convenient, light sources. Difference frequency generation (DFG) is a technique that can make use of diode lasers in the near-infrared, in conjunction with non-linear optical (NLO-) materials, to generate mid-infrared radiation [278–286]. Such systems allow the optimal combination of the advantages of economy, compactness and ease-of-use associated with diode-based radiation sources in the near-infrared with access to the greater absorption cross-sections typically associated with absorption transitions in the mid-infrared window.

Non-linear processes such as DFG are a consequence of the non-linear optical response of the polarisation of a material to the application of an intense electric field by laser radiation [287]. As the electromagnetic wave travels through the crystal, the electric field induces oscillating dipoles in the material; the induced polarisation, $P(t)$, quantifies the overall dipolar field in unit volume according to the susceptibility of the material, χ. Higher-order terms are represented by expressing the polarisation

as a series expansion in χ, such that:

$$P(t) = \epsilon_0 \chi^{(1)} E(t) + \epsilon_0 \chi^{(2)} (E(t))^2 + \epsilon_0 \chi^{(3)} (E(t))^3 + \dots \tag{5.1}$$

in which $E(t)$ is the magnitude of the applied electric field, $\chi^{(n)}$ is the nth-order susceptibility, and ϵ_0 is the vacuum permittivity.

Application of a more intense laser field can induce significant contributions to the polarisation at higher harmonics of the driving frequency. It is the contribution of the higher-order terms, and most significantly the second-order term in this expression, that gives rise to non-linear optical effects such as DFG. When two electric fields, $E_n(z,t) = E_0 \cos(\omega_n t - kz)$, are applied with frequencies ω_1 and ω_2, the induced polarisation contains terms in $2\omega_1$, $2\omega_2$, $(\omega_1 + \omega_2)$ and $(\omega_1$ - $\omega_2)$; the first two correspond to frequency-doubling (second-harmonic generation, SHG) terms, whilst the latter two are respectively the sum- and difference-frequency terms. To achieve efficient conversion to the difference frequency, the relative phases of the two radiations must carefully be matched throughout the NLO material, *i.e.* the wavevector mismatch, which is the Δk defined in equation 5.2, must be zero. This phase matching typically introduces additional constraints of temperature and geometry to the non-linear optical material, especially for birefringent phase matching; these constraints make difference frequency generation difficult to realise with appreciable conversion efficiencies in a NLO material without specific phase-matching.

Quasi-phase-matching (QPM) [288, 289] overcomes some of these constraints by using a material whose susceptibility is alternated periodically in its polarity along its length – a *periodically-poled* material. In ferroelectric materials such as $LiNbO_3$, the periodic poling is achieved by application of a conductive mask to a surface of the crystal to act as a patterned electrode. A strong (typically in excess of 250 kV per cm) electric field is then applied, and this produces an alternation in the crystal structure corresponding with the pattern of that electrode mask. In lithium niobate, it is displacement of the lithium ions between layers of oxygen ions that brings about the ferroelectric properties; asymmetry of the crystal structure's unit cell has

associated with it a permanent dipole, dependent upon the relative positions of the lithium and oxide ions. As such, the applied electric field brings about rearrangement of the lithium ions relative to the oxygen layers so as to improve the alignment of these dipoles with the applied field. QPM is a convenient technique, since it allows access to the greatest non-linear coefficients associated with the material. The non-linear optical process can then be carried out over distances up to several centimetres, enhancing the interaction efficiencies that may be achieved.

The periodic poling of the crystal is accounted for in the analysis of QPM-DFG by inclusion of an extra term in the wavevector mismatch, which becomes:

$$\Delta k = k_1 - k_2 - k_3 - \frac{2\pi m}{\Lambda} \tag{5.2}$$

where Λ is the crystal poling period, k ($= 2\pi n/\lambda$ for radiation of wavelength λ subject to a refractive index of n in the crystal) is the wavevector describing each frequency of radiation. The quantity m is the order of the Fourier component which describes the variation of the non-linear coefficient in space [288]; there is a series of solutions that satisfy the requirement for a zero mismatch, and these are indexed by the quantity m. The QPM-DFG realised in the present work is a first-order ($m = 1$) interaction, and accesses the d_{33} non-linear coefficient of periodically-poled lithium niobate (PPLN). The efficiency of such a wavelength-conversion device is usually expressed in $\%W^{-1}$, and is η in the following expression:

$$P_{idler} = \frac{\eta P_{signal} P_{pump}}{100} \tag{5.3}$$

where P_{signal}, P_{pump} and P_{idler} represent the respective powers of radiation at the signal, pump and idler wavelengths.

5.3.1 Periodically-Poled Lithium Niobate

Periodically-poled lithium niobate is one of the most commonly adopted NLO materials for this sort of application. Its transparency to the mid-infrared radiation

(indeed, to all radiation in the range of approximately 2-5 μm), its large non-linear response and its high damage threshold lend it to implementation for QPM-DFG [290].

A further method for optimising the interaction efficiency associated with an NLO process is the use of optical guiding within the NLO crystal; PPLN in waveguide form, where the crystal is engineered to enhance the confinement and therefore interaction of the pump and signal radiation, has recently been shown to produce especially high conversion efficiencies [286]. Typically, however, a waveguide system is operable over a relatively narrow wavelength range – typically close to 12 cm^{-1} – and the construction of the waveguide systems may limit the input powers that may be used. In contrast, the multi-track PPLN crystal used in the present work provides PPLN with a series of different poling periods between 29.5 and 31.5 μm, allowing for operation over a much broader range of wavelengths; indeed, if suitable input radiation were available, the PPLN crystal would be operable over 1300 cm^{-1}. As such, the PPLN crystal is especially convenient for use combined with a widely tunable light source such as an external cavity diode laser (ECDL), which allowed operation over almost 100 cm^{-1}.

5.4 Earlier Work with Mid-Infrared Radiation

In 1997, Petrov *et al.* [280] presented work on DFG close to 3.4 μm, with the pump and signal light being provided respectively by a 100 mW diode laser at 808 nm and a 500 mW diode-pumped Nd:YAG laser at 1064.5 nm. They produced approximately 3.4 μW of mid-infrared light, corresponding to a conversion efficiency of 0.0068 $\%W^{-1}$. This work was followed some two years later by that of Lancaster *et al.* [291], who presented a widely-tunable source of mid-infrared light between 3.25 and 4.4 μm based on an erbium-doped-fibre-amplified (EDFA-) distributed Bragg reflector diode laser (DBR-DL) and a tunable ECDL; again, the output power was only $\approx$ 3 μW, with a conversion efficiency of 0.0836 $\%W^{-1}$ in a 19 mm PPLN crystal.

Fradkin-Kashi *et al.* [292] present data for methane detection using a Nd:YAG

laser and a diode laser near 1.5 μm, but with the quasi-phase matching achieved in a 10 mm crystal of periodically-poled $KTiOAsO_4$ (PP-KTA); their setup, however, only produced 0.14 μW of radiation close to 3.5 μm at a conversion efficiency of 0.0091 $\%W^{-1}$. Yanagawa *et al.* [293] and Flaud and Orphal [294] reported respective conversion efficiencies of 0.041 and 0.1 $\%W^{-1}$ for their PPLN DFG systems; the Yanagawa [293] system also achieved tunability across a 130 nm range. Still greater tunability was reported by Deng *et al.* [295], who presented a continuously tunable source between 2.75 and 4.78 μm based on the interaction between a cw Ti:Sapphire laser, itself tunable between 767 and 861 nm, and a Nd:YAG laser. Previous work published by this group [283] achieved 18.7 μW of mid-infrared radiation close to 3.36 μm, using a distributed feedback diode laser (DFB-DL) centred at 1560 nm and a Nd:YAG laser centred at 1064 nm and achieving a conversion efficiency of 0.17 $\%W^{-1}$; the realisation of mid-infrared generation described in the present chapter therefore offers a system at improved conversion efficiency and output power, as well as greater tunability owing to the combination of the multi-poling-period PPLN crystal and a tunable ECDL.

One arrangement which allows for the generation of substantially greater powers of mid-infrared radiation by a NLO method is the use of an optical parametric oscillator (OPO). An OPO uses an optical cavity to enhance at least one of the signal and idler waves generated from a single pump wavelength, often achieving a photon conversion efficiency of tens of percent. Output powers on the order of Watts can be achieved; one example is found in the work of van Herpen *et al.* [296], who presented a single-frequency cw-OPO using PPLN to generate radiation between 4 and 5 μm, and achieved an optimal output power of 1.2 W of radiation near 3.9 μm; this was observed with a pump power of 11 W. Use of an OPO in this way presents additional experimental constraints: van Herpen *et al.* [296] found an oscillation threshold of 5 W of pump light, and the implementation of an OPO can be complex and expensive compared to the setup discussed in the present chapter.

Kasyutich's [297] all-diode-laser DFG system achieved a modest typical output

power of 1.7 μW in the mid-infrared, and is presented alongside detection work using a QCL-based setup; the DFG efficiency is 0.021 $\%W^{-1}$ in a 40 mm crystal. Maddaloni *et al.* [298] and Stry *et al.* [299] both presented combinations of DFG-based mid-infrared light generation with an enhanced spectroscopic technique: in the former case, two-tone frequency modulation spectroscopy (TT-FMS), and in the latter a CRDS system. Maddaloni's [298] is a high-power system, using typical input powers of 2.5 and 0.1 W for the pump and signal radiations; this combination produced 0.25 mW of mid-infrared light, and running the system with maximal input powers of 5 and 0.7 W produced in excess of 3 mW of mid-infrared radiation which was applied to detection of atmospheric methane. A bandwidth-reduced minimum detectable absorption coefficient of $5.3 \times 10^{-9}\,\mathrm{cm^{-1}Hz^{-1/2}}$ is reported when the TT-FMS is applied in a 13 m multi-pass cell, bringing about an improvement in sensitivity of approximately 100 times with respect to direct absorption measurements on the same lines.

The "cavity leak-out spectrometer" presented by Stry *et al.* [299] utilised an all-solid state laser DFG system converting 20 mW of light at 808 nm and 660 mW of 1064 nm radiation to a maximum output power of 27 μW near 3.3 μm. Ethane spectra were presented, with ring-down traces being taken in frequency steps of 150 MHz. From their 1σ-uncertainty on the decay time associated with 2 s of signal integration, a noise-equivalent absorption coefficient of $1.41 \times 10^{-8}\,\mathrm{cm^{-1}s^{1/2}}$ resulted.

5.5 Modulation Spectroscopy

Modulation spectroscopy techniques such as wavelength modulation spectroscopy (WMS) [300–304] present opportunities for enhanced detection; they generally involve a rapid sinusoidal modulation of the wavelength of the incident light. The modulation is superimposed on a low-frequency ramp that tunes the laser across the spectral feature of interest. Phase-sensitive detection and demodulation of the absorption signal at a harmonic of the modulation frequency then produces the spectrum. The major advantages of such a technique are twofold: firstly, the resulting

spectrometer produces a signal that is directly proportional to the concentration of the absorber under study; secondly, by shifting the detection to a higher frequency regime, where the technical noise is generally lower, such a modulation-based system may be used for sensitive detection of low concentrations of absorbing species over significant background noise, since components of the noise that do not fall into the appropriate higher-frequency regime are automatically rejected from the modulation spectroscopy signal [44].

The detected signal can be modulated either by a variation in the spectroscopic light source, or by modulating some property of the absorbing species. In the former case - *source modulation* - the modulation may be applied to either the frequency or the amplitude of the light; by contrast, a molecular modulation may typically involve a change in the centre frequency of the spectroscopic transition under study, perhaps induced magnetically or electrically, or by controlled variation of the population in the initial state of the transition. For example, laser electron paramagnetic resonance spectroscopy - more commonly *laser magnetic resonance* (LMR) spectroscopy - involves a magnetically-induced modulation [305–308]. The sample is subjected to a magnetic field, $\vec{B}$, of varying intensity. This then lifts the degeneracy of levels with like J and different M_J, as described by the Zeeman effect [225]. A more widely applicable analogue of this technique is laser Stark spectroscopy [309], which makes use of a varying electric field to modulate the absorption transition's central frequency. In this case, the electric field is modulated while the DC electric field is tuned. As well as its application to detection, laser Stark spectroscopy can also be applied to the accurate determination of molecular dipole moments [14].

The work presented in this chapter employs the source-modulation-based technique of wavelength modulation spectroscopy. Wavelength modulation spectroscopy techniques have been in use since the early nineteen-seventies [310–312], typically using modulations on the order of 50 kHz applied to the laser; especially when using a diode laser source, this modulation is usually applied directly to the laser injection current. Frequency modulation spectroscopy (FMS) [313–315] is a related technique,

generally conducted in the regime where the absorption line width is significantly exceeded by the modulation frequency.

Within WMS, when a sinusoidal modulation is applied to the frequency of a narrow-band light source, we can consider the instantaneous frequency, ω, of the light as oscillating sinusoidally with frequency ω_m, about a central laser frequency ω_L; the maximal excursion from the central frequency is called the *modulation amplitude*, $\delta\omega$.

$$\omega = \omega_L + \delta\omega \cos(\omega_m t) \tag{5.4}$$

In an experiment, the transmitted radiation can then be expressed as a Fourier series of cosine terms:

$$I(\omega_L, t) = \sum_{n=0}^{\infty} A_n(\omega_L) \cos(n\omega_L t) \tag{5.5}$$

Each contribution from an nth harmonic of the modulation frequency is the quantity, A_n, measured using a phase-sensitive detector such as a lock-in amplifier. These are described by the following expression, taking $\theta = \omega_m t$:

$$A_n(\omega_L) = \frac{2}{\pi} \int_0^{\pi} I_0(\omega_L + \delta\omega \cos\theta) \exp\{-\sigma(\omega_L + \delta\omega \cos\theta)N\} \cos n\theta \ \mathrm{d}\theta \tag{5.6}$$

wherein N is the number density of absorber particles, and σ is the absorption cross-section. As such, the signal quantified by equation 5.6 can be evaluated (and indeed simulated) provided that I_0 and $\sigma(\omega)$ are known for the particular wavelength. Ideally, the spectral scan is performed with no change in the incident light intensity across the spectrum, such that:

$$A_n(\omega_L) = \frac{2I_0}{\pi} \int_0^{\pi} \exp\{-\sigma(\omega_L + \delta\omega \cos\theta)N\} \cos n\theta \ \mathrm{d}\theta \tag{5.7}$$

In the conditions of low absorbance ($\sigma N \lll 1$) we can make the series approximation

$\exp[-\sigma(\ldots)N] \approx 1 - \sigma(\ldots)N$, so that the signal now becomes:

$$\begin{aligned} A_n(\omega_L) &\approx \frac{2I_0}{\pi}\int_0^{\pi}\{1-\sigma N(\omega_L+\delta\omega\cos\theta)\}\cos n\theta\ \mathrm{d}\theta \\ &= \frac{2I_0}{\pi}\int_0^{\pi}\cos n\theta\ \mathrm{d}\theta - \frac{2I_0}{\pi}\int_0^{\pi}\sigma N(\omega_L+\delta\omega\cos\theta)\cos n\theta\ \mathrm{d}\theta \end{aligned} \tag{5.8}$$

The first integral becomes $[\frac{1}{n}\sin n\theta]_0^{\pi}$ and is therefore zero, leaving us with [44]:

$$A_n \approx -\frac{2I_0N}{\pi}\int_0^{\pi}\sigma(\omega_L+\delta\omega\cos\theta)\cos n\theta\ \mathrm{d}\theta \tag{5.9}$$

In the limit of low absorbance, each of the harmonic components in the Fourier series comprises a signal directly proportional to the absorber concentration.

Different source-based modulation spectroscopy techniques are characterised typically by the size of the frequency excursion from the central laser frequency - *i.e.* by the size of $\delta\omega$ - relative to the width of the absorption profile being studied, Γ [304]. In the case where $\delta\omega \lll \Gamma$, we may express the absorption cross-section as a Taylor series, yielding:

$$A_n(\omega_L) = \frac{I_0\,2^{1-n}NN_A}{n!}\,\delta\omega^n\,\frac{\mathrm{d}^n\sigma}{\mathrm{d}\omega^n}\bigg|_{\omega=\omega_L} \tag{5.10}$$

In this limit of a frequency excursion much smaller than the absorption line width, the nth harmonic component of the Fourier series describing the intensity of the transmitted radiation is proportional to the nth derivative of the absorption signal [310]. This regime is termed the *derivative limit*, and is the modulation regime characteristic of wavelength modulation spectroscopy (also referred to sometimes as *derivative spectroscopy*). We can consider the instantaneous frequency in this limit to be varying slowly with respect to the absorption timescale, and so the time-dependent wavelength-modulated intensity follows the profile of the derivative of the absorption spectrum with no significant phase lag. An increased modulation depth gives a larger signal, up to the limit where $\delta\omega \approx \Gamma$; approaching this limit, modulation broadening makes an increasingly important contribution to the line

width.

5.6 The Pump and Signal Lasers

The input (pump and signal) radiation was generated using an external-cavity-based Distributed Bragg Reflector Diode Laser (DBR-DL) [*Lumics, LU1064M150*] centred near to 1064.29 nm, and an External Cavity Diode Laser (ECDL) [*Sacher LION, Littman configuration*] operating between 1480 and 1560 nm. A current of 320 mA was applied to the DBR-DL, housed in a temperature-stabilised butterfly package (thermistor resistance $\sim$ 9.45 kΩ); a polarisation-maintaining optical fibre pigtail delivered the output radiation at a power of 136 mW. The ECDL was run at an operating current of 192 mA, and a temperature of 25.7 °C; fine-tuning of its output wavelength was achieved using a piezo-electric transducer attached to the mirror of the laser's external cavity. Applying 66.2 V to this piezo-electric transducer, an output wavelength of 1535.11 nm was achieved. This combination of pump and signal wavelengths gave rise to mid-infrared (idler) radiation close to 3.47 μm (2881.9 cm^{-1}).

5.7 Experimental

A schematic illustration of the experimental setup employed in the present work is shown in Figure 5.3.

The light from the ECDL was passed through a free space dual-stage optical isolator [*Isowave, I-15-UHP-4*] and aligned into an optical fibre connected to the input of the erbium-doped fibre amplifier (EDFA) [*Nuphoton Technologies*]. The EDFA amplified approximately 5 mW of input light from the ECDL to produce approximately 250 mW of radiation at 1535.11 nm. The radiation from the DBR-DL was also passed through an optical isolator [*Thorlabs-OFR, IO-2.5-1064-VLP*], after which the power of 1064.29 nm radiation was measured to be 83 mW. When no isolator was used with the DBR-DL laser, the output was affected by too much

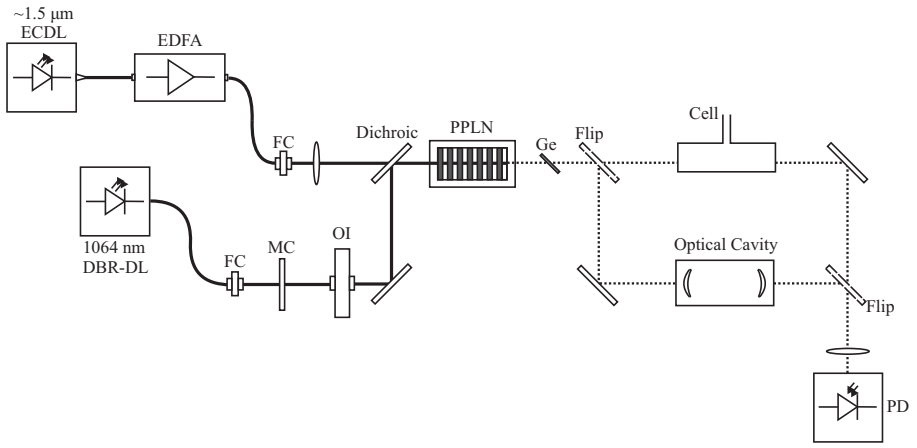

Figure 5.3: Schematic illustration of the experimental setup for the nitrogen dioxide mid-infrared detection work, detailed in section 5.7. FC = fibre coupler; MC = mechanical chopper; OI = optical isolator; Flip = flip mirror; PD = photodiode.

feedback to the laser, which gave rise to a stepped appearance to the signal that resulted when the radiation was directed into a spectrum analyser. This is shown in Figure 5.4. The output polariser of each optical isolator was carefully aligned to vertical polarisation, to facilitate quasi-phase matching within the PPLN crystal.

The pump and signal beams were then combined at a dichroic mirror and co-aligned so that they passed through the 40 mm-long PPLN crystal [*Stratophase, OPO3-40*]. The PPLN crystal is anti-reflection coated for the applied pump and signal wavelengths, and is constructed to have a series of distinct millimetre-wide tracks, each characterised by a different poling period (Λ) ranging from 29.5 to 31.5 μm in intervals of 0.25 μm. Coupled with the tunable ECDL, this setup is capable of accessing a range of output wavelengths; the accessible values are between 3.3 and 3.48 μm, limited by the operating range of the EDFA. For the current work, the signal and pump light were co-aligned along the crystal track characterised by Λ =29.75 μm (defined at room temperature). To optimise the efficiency of conversion, the pump and signal beams were each focussed using a suitably anti-reflection-coated lens before the PPLN crystal, and the two were then carefully overlapped. The crystal was maintained at a constant temperature close to 74 °C

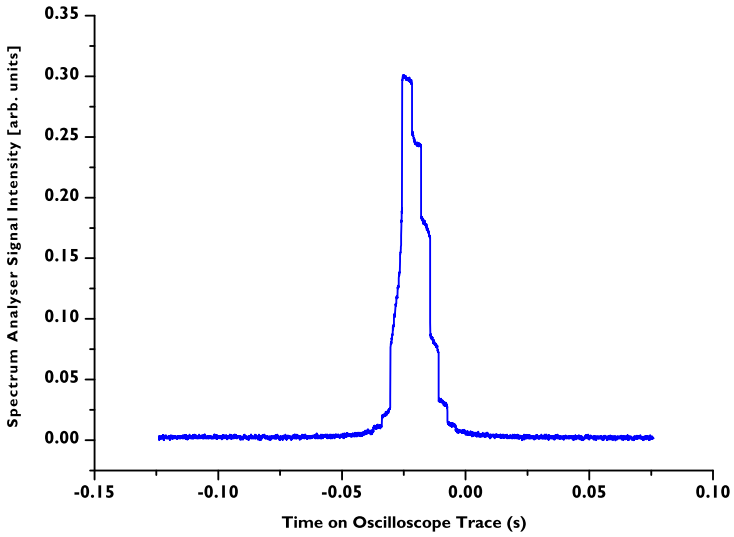

Figure 5.4: Spectrum Analyser trace relating to the LUMICS 1064 nm DBR-DL without optical isolation; the stepping on the signal, thought to be owing to a feedback locking effect, is clearly visible.

using a commercial oven and temperature controller [*HC Photonics, TC-038*].

Beyond the crystal, the generated mid-infrared light was separated from the remaining pump and signal beams using a germanium filter, then passed through the relevant sample cell arrangement and detected at a HgCdZnTe photodiode [*VIGO, PVI-2TE-4*] with a built-in pre-amplifier [*VPDC-0.1I*]. Scanning the wavelength of the mid-infrared radiation was achieved by varying the output wavelength from the ECDL; this was realised by applying a triangular voltage ramp to the piezo-electric transducer attached to the laser's feedback element. The triangular ramp was supplied by a function generator [*TTi, TG1010A*] and the frequency scale was calibrated using a spectrum analyser [*Spectral Products*] into which the 1535 nm radiation was aligned, to provide an accurate, well-characterised étalon with a free spectral range close to 2 GHz.

Detection was carried out on the absorption doublet feature in the $\nu_1 + \nu_3$ band of nitrogen dioxide, centred at ≈ 2881.92 cm^{-1}. This feature is listed in HITRAN [128] as being composed of a pair of transitions at 2881.9236 and 2881.9246 cm^{-1},

with respective cross-sections of 4.28×10^{-21} and 4.11×10^{-21} $cm^2molec^{-1}cm^{-1}$; it was selected for detection on account of its large absorption cross-section, and because it is in a spectral region free of interference from atmospheric methane signals. The relatively low levels of interference from atmospheric absorbers, and the well-defined structure of the absorption spectra obtained, present advantages of mid-infrared detection with respect to detection in the visible region. The quantum numbers assigned to the transitions in HITRAN [128] are shown in Table 5.2. The bandwidth of our detection setup for the absorption spectroscopy experiments was not sufficiently low to resolve these two transitions, which appear in the spectra presented in this chapter as a single unstructured feature. Accordingly, in analysis, the feature is fit with a single Voigt function, with the Gaussian width component taken as the sum of the calculated Doppler width and the frequency offset between the centres of the two contributing absorptions.

		$\nu_1 + \nu_3$				Ground State			
Wavenumber (cm^{-1})	σ_{int} (cm^2cm^{-1})	**N**	$\mathbf{K}_a$	$\mathbf{K}_c$	**J**	**N**	$\mathbf{K}_a$	$\mathbf{K}_c$	**J**
2881.9236	4.28×10^{-21}	24	1	24	24.5	25	1	25	25.5
2881.9246	4.11×10^{-21}	24	1	24	23.5	25	1	25	24.5

Table 5.2: Spectroscopic data for the transitions giving rise to the absorption doublet used for the present NO_2 detection work. Notation is adopted consistent with HITRAN [128].

The wavelength of the pump light emitted by the Lumics laser was measured using a wavemeter [*Burleigh, WA-100*] and found to be 1064.288 nm (≈ 9396 cm^{-1}). In order to produce idler radiation that was suitable to access the desired transition within the NO_2 spectrum, close to 3.47 μm ($\approx$2881.92 cm^{-1}), signal light at 1535.1 nm ($\approx$6514 cm^{-1}) was required. The ECDL was tuned to a wavelength close to this by adjusting the coarse alignment of the laser grating; fine tuning was carried out, using the wavemeter in conjunction with observation of the absorption signal in the presence of NO_2 gas, by altering the voltage supplied to the piezo-electric transducer within the ECDL.

A simulation of the QPM-DFG interaction efficiency with crystal temperature was carried out using the pump and signal wavelengths and the crystal length as

inputs; the crystal was tuned to the returned value for the optimum crystal temperature, and then varied within a range of approximately ±20 °C from this initial value to find the temperature at which the highest power of mid-infrared radiation was generated. Based on this procedure, the PPLN crystal was maintained at a temperature close to 74 °C throughout this work.

For the direct absorption measurements, the 2.5 cm sample cell was a cylindrical glass cell with calcium fluoride windows. Signal and background spectra were recorded with the sample cell filled and empty, and the baseline signal at the detector was recorded when the laser was blocked.

5.7.1 WMS Measurements

For wavelength modulation spectroscopy (WMS) a modulation was applied to the ECDL current driver, using a function generator [*TTi, TG1010A*]; this modulation was applied at a reference frequency close to 1 kHz. A lock-in amplifier [*EG&G Instruments, 7265*] was used to demodulate the signal at the second harmonic of the reference frequency. The modulation amplitude was optimised to provide the largest WMS signal-to-noise ratio, and the time constant on the lock-in amplifier was chosen to provide the best signal to noise; typically, a time constant of 20 ms was used. A slow ramp was applied to the ECDL at a frequency of 0.5 Hz. For the low-concentration WMS measurements, the sample cell was replaced by a multi-pass White Cell, with a total path length of 20 m. To reduce the influence of étalons, the collecting lens after the PPLN crystal was mechanically vibrated, using a small motor placed against its mount, throughout the WMS experiments.

5.7.2 CEAS Measurements

Finally, CEAS measurements were made on the same pair of absorption transitions. The optical cavity was formed from a pair of high reflectivity mirrors coated for ≈ 99.9% reflectivity close to 3.5 μm [*Layertec*], which were spaced by 25 cm and housed in a cell constructed in-house to include all the appropriate gas and evacuation

inlets. When in place, the mirrors form the ends of the cell, obviating the need for windows, and the mounts are fitted with micro-adjusters. Alignment was carried out using the (suitably attenuated) 1535 nm light exiting the crystal by removing the germanium filter. First, the cavity mirror nearest the detector was mounted and aligned; the second cavity mirror was then mounted in the cell, and aligned to overlap the incoming beam on its reflection.

Monitoring the mid-infrared, the alignment of the cavity was then altered until a regular cavity transmission, associated with excitation of just a very small number of low-order modes, was achieved. The resulting cavity mid-infrared transmission is shown in Figure 5.5 at line (a).

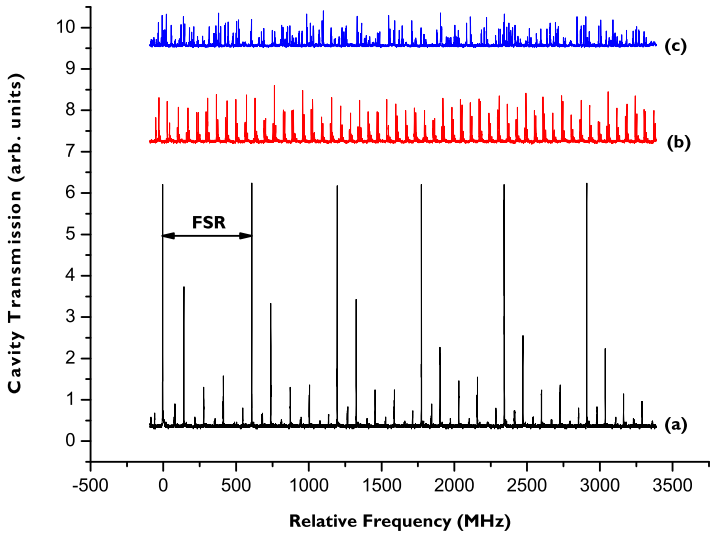

Figure 5.5: Cavity transmission of mid-infrared light at three different optical cavity alignments. The three plots are offset vertically for clarity

From this state, the cavity was carefully misaligned until the excitation of many higher-order modes was observed (Figure 5.5, line (b)). To enhance the congestion of the mode structure, and thereby increase the baseline smoothness for taking measurements, extra mechanical disturbance was introduced by placing a second small motor against one of the cavity mirror mounts; the corresponding mid-infrared cav-

ity transmission is shown at line (c) in the same figure. For these CEAS experiments, owing to the relatively low power of the input mid-infrared radiation (tens of μW) the transmitted signal at the photodiode was passed to the lock-in amplifier used for the WMS measurements, with the fast (approximately 1.5 kHz) modulation having been applied by a mechanical chopper installed directly in front of the 1064 nm laser.

5.8 Results

5.8.1 Efficiency of Mid-Infrared Light Generation

Under the conditions described above, input powers of P_{pump} = 83 mW and P_{signal} = 250 mW yielded an output mid-infrared power of 60 μW, as measured on a high-sensitivity power-meter [*Gentec-E Solo 2*]. This corresponds to an experimentally-determined conversion efficiency, as according with equation 5.3, of η_{exp} = 0.29 $\%W^{-1}$. This value compares favourably with even the best of the efficiencies reported by others [293, 298, 299] generating mid-infrared radiation by QPM-DFG in a non-waveguide PPLN crystal.

5.8.2 Direct Absorption

The mid-infrared radiation produced by our PPLN QPM-DFG setup was first applied to direct absorption measurements of the spin doublet absorption feature corresponding to the assignments as in Table 5.2. The absorption signal was first characterised by direct absorption spectroscopy in the 2.5 cm glass cell described above. A sample absorption spectrum, taken with 7 Torr of pure nitrogen dioxide gas, is shown in Figure 5.6(a). The pure NO_2 was then buffered with air; the air was added to a series of total pressures up to 212 Torr, and the absorption spectrum recorded at each pressure. The associated line shape was measured for each spectrum; such data are necessary to understand the evolution of the peak-cross section, and therefore the attainable limits of detection, in different sample environments.

These absorption spectra were then characterised empirically by fitting the feature to a single Voigt function. This empirical measurement was carried out in order to quantify the evolution of the absorption cross-section in different pressure environments; the measurement was analysed by analogy to a simple pressure-broadening measurement, but the approximations used mean that the returned value is of practical, descriptive use in implementing such a detection system, rather than being an accurate measure of the collisional broadening of the two contributing lines. The Gaussian width for each Voigt fit was set at a fixed value; and the Lorentzian width component of the Voigt fit recorded at each pressure. The Gaussian width was fixed at a value of 6.26×10^{-3} cm^{-1}; this is the sum of the calculated Doppler width at room temperature for this wavelength (5.27×10^{-3} cm^{-1}), and the frequency offset (9.995×10^{-4} cm^{-1}, taken from the HITRAN [128] database) between the two contributing absorptions. The Lorentzian full-width obtained in this way is plotted against air pressure in Figure 5.6(b). The gradient of the straight-line fit to these data is 2γ, where γ is the effective pressure broadening coefficient, and for these data was found to take a value of 2.52 ± 0.07 MHz/Torr (with the error given as $\pm 2\sigma$ for the linear fit shown in Figure 5.6(b)); a small non-zero intercept (1.78×10^{-3} cm^{-1}) is associated with the linear fit, and may be attributable to systematic errors in the pressure readings. HITRAN [128] data for the integrated cross-section and the pressure broadening coefficients of each of the contributing transitions were used to simulate the spectrum in this region at the same series of pressures, and to give a value for this effective pressure broadening coefficient for comparison with our work; a similar analysis on the resulting simulations yielded a value for γ of 2.71 MHz/Torr, in reasonable agreement with our experimental value.

5.8.3 WMS Spectra

The raw data from a WMS spectrum taken in the 20 m White Cell are shown in Figure 5.7; this spectrum was measured with 45 Torr of a calibrated 5 ppm mixture of nitrogen dioxide in zero-grade air [*CK Gas*]. This spectrum corresponds to five

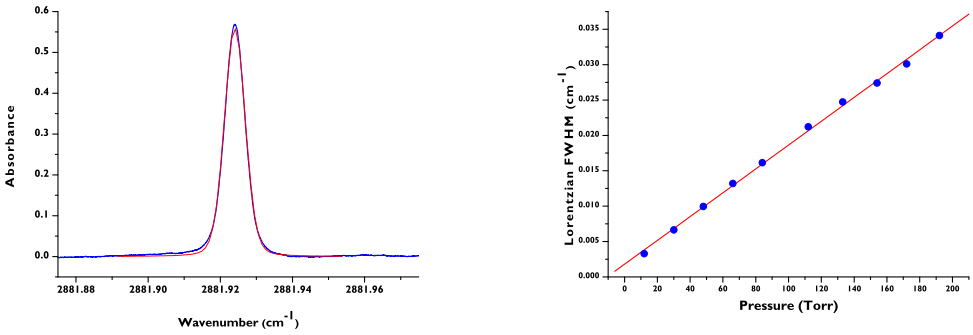

(a) Direct absorption spectrum (b) Pressure broadening plot

Figure 5.6: A direct absorption spectrum measured in a 2.5 cm cell with 7 Torr of pure NO_2; and corresponding plot showing the evolution of the Lorentzian contribution to the total Voigt line shape with air pressure.

averages, taken at a slow ramp frequency of 0.5 Hz.

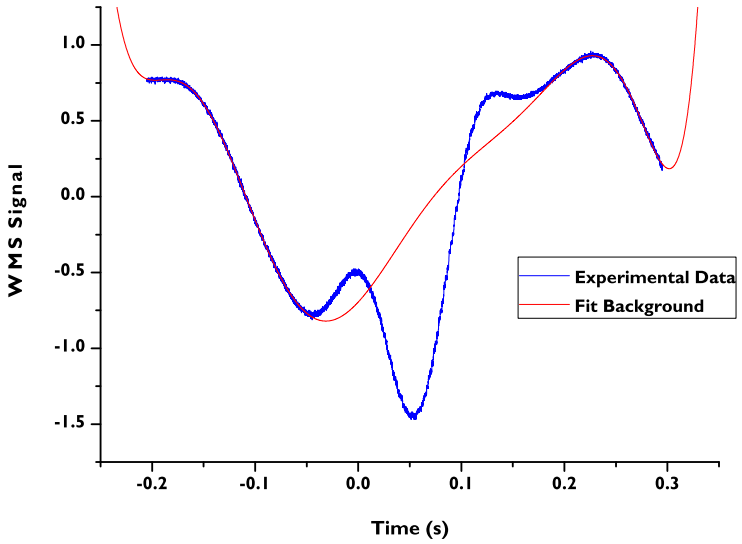

Figure 5.7: Raw data from a WMS spectrum measured with 45 Torr of 5 ppm nitrogen dioxide in air, in the 20 m White Cell, over $\sim 10\,\mathrm{s}$ acquisition time. The same absorption transition was used as for the previous two figures. An étalon effect is clearly seen on the data; the fit background is also shown.

Whilst several étalons were removed from the transmitted WMS signal by the action of the motor against the lens following the PPLN crystal, one large étalon

persisted, and this can clearly be seen on the data shown in Figure 5.7. Accordingly, a background signal was generated by fitting a polynomial function to the transmitted WMS signal with the signal due to the absorption transition removed analytically, and the resulting spectrum is shown in Figure 5.9. The amplitude of the modulation was measured from a spectrum analyser trace taken as the experiment was carried out; this is shown in Figure 5.8. The modulation index – the ratio of the modulation amplitude (FWHM) to the absorption line width (FWHM) – was in this case found to be approximately 1.9. These measurements were therefore not made within the derivative limit described at section 5.5.

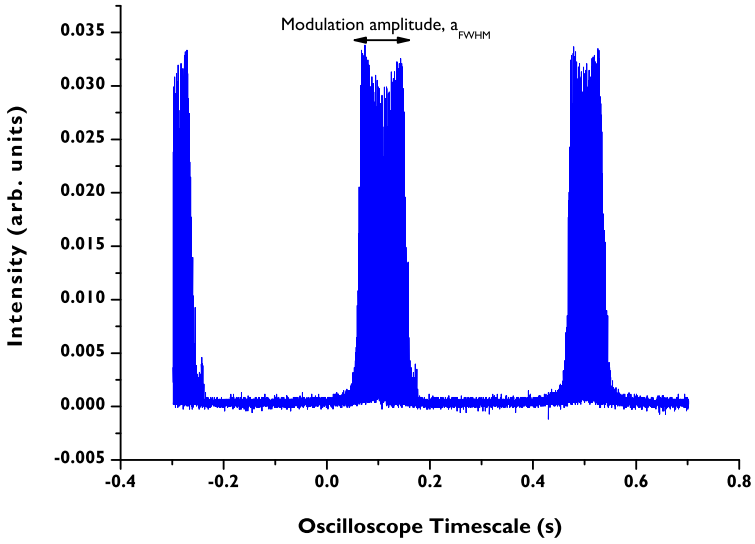

Figure 5.8: Spectrum analyser trace corresponding to the NO_2 WMS experiments, from which the modulation amplitude, and therefore the modulation index, were determined.

The noise level on the spectrum in Figure 5.9 was determined by finding the standard deviation about a linear fit to the baseline, as shown in the figure. The red line in Figure 5.7 shows the analytically-generated background; this was determined by cutting out the absorption signal from the spectral data and carrying out a polynomial fit to the remaining data, and was verified by taking an evacuated-cell spectrum, which was found to be in good agreement. Following this procedure,

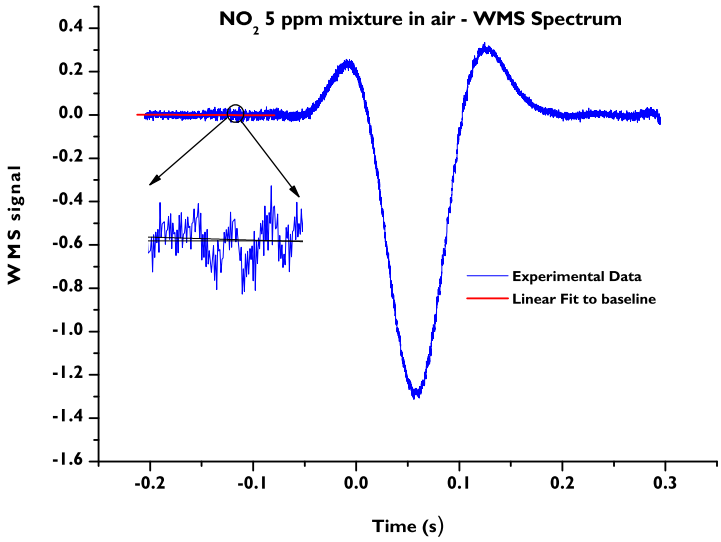

Figure 5.9: WMS spectrum resulting from the data shown in Figure 5.7, after background subtraction. The linear fit used to find the noise level, and a magnified sample of part of the baseline, are also shown.

a signal-to-noise ratio of 160 results for this spectrum. This implies that, keeping a total pressure of 45 Torr, the noise-equivalent absorption signal (*i.e.* that which would generate a signal-to-noise ratio of one) would correspond to 32 ppb of NO_2. Assuming a linear scaling of the peak cross-section with the line width, and adopting our measured effective pressure-broadening coefficient of 2.52 MHz/Torr, a noise-equivalent absorption signal for a measurement taken at atmospheric pressure (760 Torr) corresponds to a nitrogen dioxide concentration of 40.5 ppb. This method shows great promise as a technique for detection of nitrogen dioxide, based upon the use of compact and economical near-infrared lasers and achieving a minimum detectable NO_2 concentration on the order of typical urban atmospheric concentrations even under conditions of atmospheric pressure, although further work is needed to eliminate étalons from the system.

One difficulty that is typically encountered when detecting NO_2 in a sample cell is associated with adsorption of the gas to surfaces; owing to the polarity of the NO_2 molecule, it is a very "sticky" molecule which readily adsorbs to (especially metal)

surfaces. This effect was observed in the present work. Figure 5.10 shows raw data from a WMS experiment equivalent to that which generated the data in Figures 5.7 and 5.9. The calibrated 5 ppm NO_2 mix was added to the White Cell at a pressure of 72 Torr, and successive traces in Figure 5.10 show the transmitted WMS signal approximately every thirty seconds, with no further addition or removal of gas to the cell. This figure clearly demonstrates the effect of adsorption of the NO_2 to the walls, mirrors, and fixtures of the cell: the size of the WMS signal is diminished with time, as this effect removes the NO_2 from the optical path. From these results, it appears that the deposition of the nitrogen dioxide gas on the mirrors affects the two experiments in two different ways; whilst an argument based purely on the surface-area-to-volume ratio would suggest that the signal depletion ought to be more severe in the CEAS setup compared to the White cell, the results here indicate the opposite. One explanation for this lies in the different materials that comprise the surface coatings on the mirrors; the mirrors in the White cell have a significantly greater area than those in the CEAS experiment, and are gold-coated. The results exemplified in Figure 5.10 suggest that adsorption to this gold surface depletes the absorption signal more effectively than in the case of the high-reflectivity cavity mirrors. From Figure 5.10, it can be seen that the signal has been reduced in size by a factor of approximately a half after one minute; this is broadly consistent with earlier work in this group [202], as well as with the work of Reid *et al.* [316] which was conducted in a similarly-constructed sample cell.

This effect could be reduced by coating some of the surfaces in the cell with PTFE or another stick-resistant material, and/or by a reduction in the surface area associated with the mirrors, which are subject to significant "sticking" from the NO_2. Consistent with this, our cavity-enhanced absorption spectroscopy experiments were carried out with 1" diameter, dielectric-coated mirrors, thereby reducing the mirror surface area with which the nitrogen dioxide might interact compared to the White Cell's larger gold mirrors. Accordingly, the difficulties associated with sticking of the nitrogen dioxide to the mirrors can be expected to be reduced with respect to the

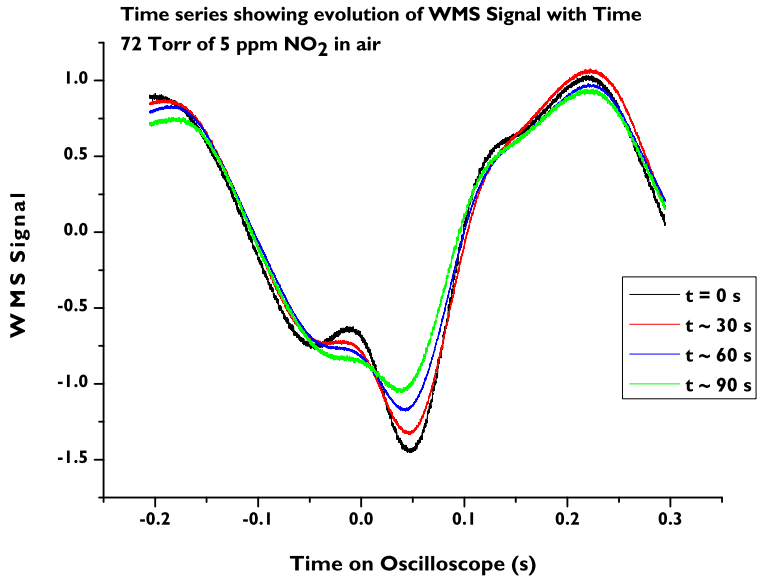

Figure 5.10: Data taken using a fixed sample of 72 Torr of the same 5 ppm mix of nitrogen dioxide in air, taking a WMS spectrum every 30 seconds. The effect of adsorption to the interior of the White Cell is clearly seen.

White Cell measurements, allowing in principle for longer integration times without great signal depletion.

5.8.4 CEAS Spectra

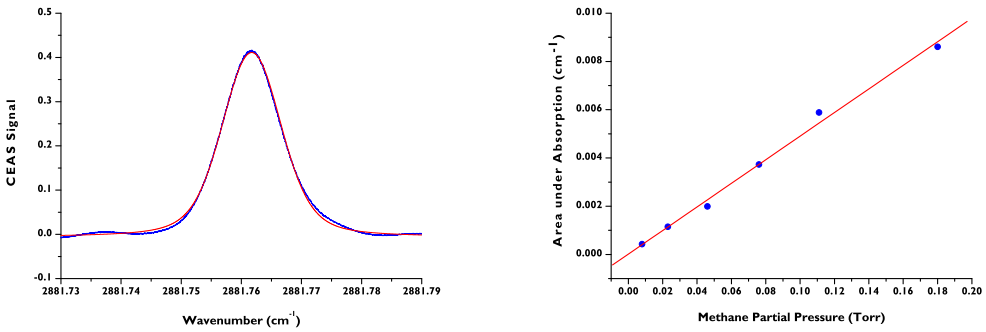

(a) Example methane spectrum (b) Reflectivity calibration plot

Figure 5.11: Reflectivity calibration data, showing the $\nu_2 + \nu_4$ Q(9) absorption for 11.1 Torr of a 1% CH_4:N_2 mixture and the variation in the area under the absorption signal with pressure.

The cavity was calibrated using known amounts of a 1% methane-in-nitrogen mixture. A nearby absorption transition due to methane, the Q(9) transition located at 2881.76 cm^{-1} within its $\nu_2 + \nu_4$ vibrational band, was measured with known pressures of the methane-in-nitrogen mixture. Its integrated cross section of $9.86 \times 10^{-23} cm^2 molec^{-1} cm^{-1}$ was taken from the HITRAN [128] database, and used to calibrate the absorption signals and therefore the cavity reflectivity, invoking the typical CEAS expression (equation 2.36.

Sample calibration data are shown in Figure 5.11; the area under the absorption in each spectrum was used to calibrate the mirror reflectivity. It should be noted that the Gaussian component of the width returned by the Voigt fit to the data shown in Figure 5.11(a) ($9.5 \times 10^{-3}\,cm^{-1}$) considerably exceeds that resulting from a simulation based on HITRAN [128] data for the integrated cross section and pressure broadening coefficients; this effect arises due to instrumental broadening associated with the mismatch between the frequency of the applied modulation for lock-in detection and the detection band width. The integrated signal should, however, not be affected. This calibration resulted in a geometric mean mirror reflectivity of 0.998, and correspondingly a cavity path-length enhancement of 500 and effective path length ($L_{eff} = L/1 - R$) of 125 m.

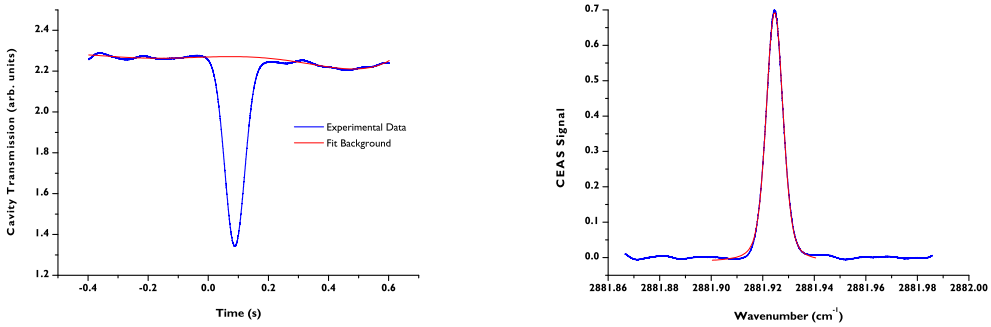

(a) Raw data (b) Corresponding spectrum

Figure 5.12: Raw CEAS transmission data with background fit, and the analysed CEAS spectrum corresponding to 8.5 Torr of a 160 ppm mix of nitrogen dioxide in nitrogen. The data were taken in a total acquisition time of 5 s, at a ramp frequency of 10 Hz.

The CEAS spectrometer was used to take a series of spectra on a mixture of approximately 160 ppm nitrogen dioxide in air. A spectrum is shown in Figures 5.12(a) and 5.12(b); the former shows the raw data and the latter the corresponding analysed spectrum. The signal-to-noise ratio for the spectrum shown in Figure 5.12(b) is 520, since the standard deviation to the linear fit shown is found to be 1.34×10^{-3}. This value implies that, at this total pressure (8.5 Torr), a noise-equivalent absorption signal would be observed due to 313 ppb of nitrogen dioxide. This value is similar, for example, to the value of 259 ppb attained by Lancaster *et al.* [291] for detection of NO_2 over an optical path length of 18 m at 88 Torr total pressure (7.6 ppm NO_2) in this spectral region using DFG in a PPLN crystal. Nonetheless, the CEAS spectrometer does not match the performance of the WMS setup, despite the optical path length being subject to a greater enhancement in the optical cavity than the White Cell. This can be attributed to the small intensity of transmitted light resulting from the CEAS spectrometer, so that the effect of the noise on detection was felt more keenly when set against such a small signal.

5.9 Summary and Outlook

Generation of mid-infrared radiation close to 3.47 μm has been demonstrated, by quasi-phase-matched difference-frequency generation (QPM-DFG) in a PPLN crystal of length 40 mm, using pump and signal radiation produced using diode lasers centred at wavelengths respectively close to 1064 and to 1535 nm. 60 μW of mid-infrared radiation was produced, corresponding to a QPM-DFG efficiency of $\eta_{exp} = 0.29\%\ \mathrm{W}^{-1}$. After characterisation of the radiation, its application to detection of nitrogen dioxide gas has been demonstrated; this is a problem of interest and importance in atmospheric and environmental analytical science.

The resulting mid-infrared radiation was employed for detection of the doublet absorption feature close to 2881.9 cm^1 in the $\nu_1 + \nu_3$ band of NO_2, by direct absorption spectroscopy, wavelength modulation spectroscopy and cavity-enhanced absorption spectroscopy. Wavelength-modulation spectra measuring a 5 ppm NO_2-in-air

mix have been presented; 45 Torr of such a mixture generated a WMS spectrum with signal-to-noise of 160, corresponding to a noise-equivalent absorption for 32 ppb of NO_2 at this total pressure, an amount on the order of typical atmospheric concentrations, in 10 s of data acquisition. Cavity-enhanced absorption spectroscopy was then demonstrated with the generated mid-infrared light, using high reflectivity mirrors calibrated with a well-characterised methane sample. Spectra on 8.5 Torr of a 160 ppm mixture of NO_2 in nitrogen were presented, with a signal-to-noise ratio of approximately 520. The best detection sensitivity was achieved using the WMS setup, but was limited by a low-frequency étalon that is likely to be associated with the PPLN crystal. One possibility for eliminating this would be to use a pair of matched-response detectors before and after the absorbing sample, allowing subtraction of the étalon from the signal. The small transmitted signal through the CEAS spectrometer led to a slightly poorer detection sensitivity, but was carried out using mirrors of only 99.8% reflectivity; currently, mirrors for the near-infrared region are available at much higher reflectivities (see section 2.2.2), and so when this technology becomes more readily available in the mid-infrared region, the potential for greater path length enhancements will allow further improvement of our CEAS spectrometer.

Chapter 6

Towards Optically-Locked SHG

In this chapter, proof-of-principle work is reported investigating the feasibility of a system combining non-linear optical techniques, as were introduced in Chapter 5, with a V-shaped optical feedback cavity like that developed in Chapters 3 and 4. Such an arrangement seeks to exploit the enhanced circulating power of near-infrared light inside a cavity subject to optical feedback to produce an increased level of blue light by second harmonic generation (SHG) in a crystal of potassium niobate ($KNbO_3$).

This chapter surveys some typical applications that take advantage of the optical characteristics of light in the blue spectral region, and then briefly revisits and extends the discussion of non-linear optical techniques begun in Chapter 5 to include a quantitative description of the phase-matching process inside the non-linear crystal. A characterisation of the 860 nm laser source and the $KNbO_3$ crystal is presented. The design and implementation of a V-shaped cavity for feedback locking is reported, and the resonator constructed and characterised. Finally, the system is applied to generation of blue light, and the optimal second harmonic generation using this setup is discussed and quantified.

The prospects for a full implementation of such an optically-locked second harmonic generation apparatus are discussed, and ways in which the experiment might be extended and improved are identified.

6.1 Background

6.1.1 Technical Advantages of Light in the Blue Region

Durable, compact sources of blue laser light find many applications in industry; recent advances in high-density optical data storage systems have exploited the relatively low diffraction-limited spot size associated with a blue Gaussian beam for more efficient storage of data on a compact disc [317]. The same aspect of blue laser radiation has been applied to improved-resolution laser printing and colour display technology in computer monitors and televisions [318]. Blue light is the least attenuated part of the spectrum when visible light is transmitted through sea water, and so it also forms the basis of underwater communication devices [319].

The blue region is also relatively rich in spectroscopic transitions suitable for detection studies. The occurence of atomic transitions of metals – including aluminium, titanium, yttrium, tungsten and gallium – in the region between 350 and 450 nm makes blue light ideal for non-invasive spectroscopic monitoring of vapour deposition processes [318]. Several other small molecules of spectroscopic and atmospheric interest, including NO_2, ClO, BrO, HONO and CH_2O, exhibit absorptions in the 300–400 nm region. However, blue diode lasers are generally only currently available between approximately 390 and 414 nm, based on an indium-doped gallium nitride active medium [318]. Furthermore, even these available diodes suffer from structural imperfections that worsen as the indium concentration is increased to drive the laser emission to longer wavelengths [320].

As such, the usefulness of blue laser light for a variety of applications and the relative paucity of compact, durable, diode-based sources of such light have motivated the investigation of alternative methods for producing this radiation. Particularly, non-linear optical techniques allowing access to the second harmonic of the output of a diode laser further to the red have shown great potential for generation of blue light that retains the advantages of simplicity associated with the original light source.

6.1.2 Second Harmonic Generation

It was shown in section 5.3 that the non-linear response of the polarisation of a material to the application of an intense electric field by radiation from a laser can be expressed as a series expansion (equation 5.1) about the applied field. Section 5.3 showed that higher-order terms give rise to interactions between a pair of electric fields, and that the induced polarisation (equation 5.1) then includes terms in the second harmonic of the incident light. The second-order susceptibility in that expression, $\chi^{(2)}$, can itself be expressed as $2d$, where d is the *non-linear coefficient* associated with the NLO material; this is a symmetry property of the crystal, typically quoted in $\mathrm{pm\,V^{-1}}$. The time-dependent electric field associated with the fundamental laser radiation, and propagating in the $\vec{z}$-direction, is given by:

$$\mathrm{E}_\omega(z,t) = \frac{1}{2}E(z,\omega)\big[\exp\{-i(\omega t - k_\omega z)\} + \exp\{+i(\omega t - k_\omega z)\}\big] \tag{6.1}$$

wherein k_w is the wavevector associated with angular frequency ω, and the NLO material's refractive index, n_ω; and E is the electric field amplitude. The wavevector takes the usual form:

$$k_\omega = \frac{\omega n_\omega}{c} = \frac{2\pi n_\omega}{\lambda_\omega} \tag{6.2}$$

If we consider the second order contribution to the induced polarisation in equation 5.1 and substitute it into equation 6.1, then a component of the induced polarisation emerges oscillating at the second harmonic frequency:

$$\mathrm{P}_2 = 2\epsilon_0 d\,\mathrm{E}^2_\omega(z,t) \;\; = \frac{\epsilon_0 d}{2}\,\mathrm{E}^2(z)\big[\exp\{-2i(\omega t - k_\omega z)\} + \exp\{+2i(\omega t - k_\omega z)\} + 2\big] \tag{6.3}$$

The electric field at the second harmonic, with wavevector $k_{2\omega} = 2\omega n_{2\omega}/c$, can then be expressed as:

$$\mathrm{E}_\omega(z,t) = \frac{1}{2}E(z,2\omega)\big[\exp\{-i(2\omega t - k_{2\omega} z\} + \exp\{+i(2\omega t - k_{2\omega} z\}\big] \tag{6.4}$$

Comparing equations 6.1 and 6.4 yields the phase-matching condition [40]:

$$k_{2\omega} = 2k_{\omega} \Rightarrow 2\omega n_{2\omega} = \omega n_{\omega} \qquad \text{so that} \qquad \Delta k \ = k_{\omega} - k_{2\omega} \tag{6.5}$$

Ordinarily, dispersion within the material means that the refractive index increases with the frequency of the radiation, and so a phase mismatch arises, depleting the efficiency of the second harmonic generation. One convenient method to overcome this mismatch is the use of a birefringent crystal, where the refractive index is instead dependent on the *direction* of the electric field (and therefore the induced polarisation) [287]. Birefringent crystals are – necessarily – anisotropic, allowing two waves of differing polarisations to propagate through a crystal in the same direction, but subject to different refractive indices. Accordingly, if the crystal is chosen such that the harmonic of highest frequency is subject to the lowest refractive index, then the effect of the regular dispersion can be cancelled out, allowing the phase condition to be fulfilled.

In the work presented in this chapter, a crystal of orthorhombic potassium niobate ($KNbO_3$) is adopted as the birefringent NLO material. This is a crystal of C_{2v} symmetry with two optic axes [321, 322], and its unit cell is illustrated in Figure 6.1. In $KNbO_3$, the wave propagating parallel to the crystal axis (the *ordinary* wave, subject to refractive index n_o), experiences a greater refractive index than that propagating perpendicular to the crystal axis (the *extraordinary* wave, subject to n_e). The crystal is α-cut, so the incident laser beams propagate perpendicular to the crystal axis, as shown in Figure 6.1. The fundamental light was polarised along the *b*-axis, corresponding to the *ordinary* refractive index, and gives rise to second harmonic radiation polarised along the *c*-axis.

This crystal is applied to 90° non-critical type I phase matching; the fundamental beam is introduced at 90° to the optic axis of the crystal. For an SHG process, the phase matching is always of type I, as the two interacting photons come from the same beam. As such, they share the same polarisation, and experience the *ordinary* refractive index, n_o; for the phase matching condition to be met, each resultant

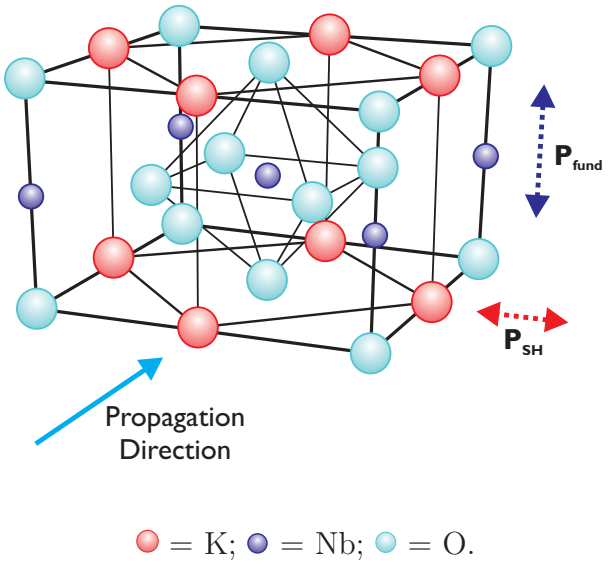

Figure 6.1: Representation of the orthorhombic potassium niobate unit cell. The polarisation directions of the fundamental harmonic and the second harmonic are ahown, and respectively denoted P_{fund} and P_{SH} [323].

second harmonic photon must have orthogonal polarisation, and be subject to the *extraordinary* refractive index, n_e.

The wavelength at which the phase condition is met is (strongly) temperature-dependent, as the relative magnitudes of n_o and n_e are dependent upon the inter-atomic spacings within the crystal structure. For a given wavelength, therefore, careful temperature tuning of the crystal is required in order to optimise the phase matching and the resulting second harmonic generation efficiency. The temperature-dependence of the refractive indices in $KNbO_3$ is described by the relevant Sellmeier equation [321–325]:

$$\begin{aligned} n_\omega^2 - 1 = (S_1 + b_1 F + b_2 G)\frac{\lambda^2\lambda_1^2}{\lambda^2 - (\lambda_1 + b_3 F + b_4 G)^2} \\ + (S_2 + b_5 F)\frac{\lambda^2\lambda_2^2}{\lambda^2 - (\lambda_2 + b_6 F)^2} - (D + b_7 F)\lambda^2 + b_8 F\lambda^4 \end{aligned} \tag{6.6}$$

In this expression, λ gives the wavelength in units of μm, λ_1 and λ_2 are coefficients describing electrical properties of the material, each having units of length; S_1, S_2, F, G and D are parameterised functions of the temperature, T, in units of °C,

and the values of these coefficients are found in reference [318], and reproduced for clarity in Table 6.1.

	Fundamental	**Second Harmonic**
S_1 (μm^{-2})	19.456	16.086
E_1 (eV)	4.5492	4.8553
S_2 (μm^{-2})	134.95	166.258
E_1 (eV)	9.0392	10.3834
D (μm^{-2})	2.837×10^{-2}	1.939×10^{-2}
b_1 (μm^{-2})	-5.263×10^{-5}	-3.267×10^{-5}
b_2 (μm^{-2})	-1.65×10^{-3}	-2.8×10^{-3}
b_3 (μm)	2.38×10^{-7}	1.89×10^{-7}
b_4 (μm)	-6.78×10^{-5}	-2.48×10^{-5}
b_5 (μm^{-2})	2.0536×10^{-4}	1.990×10^{-4}
b_6 (μm)	1.767×10^{-7}	1.75×10^{-7}
b_7 (μm^{-2})	-1.22×10^{-8}	-2.7×10^{-8}
b_8 (μm^{-4})	-3.3×10^{-10}	-5.7×10^{-10}

Table 6.1: Constants associated with the Sellmeier equation (6.6) for the fundamental harmonic and the second harmonic in potassium niobate.

The output value of the refractive index from this expression is calculated for both the fundamental (–) and second harmonic (–), respectively at 860 and 430 nm, and illustrated in Figure 6.2. Employing the constants in Table 6.1, the following definitions also apply:

$$\begin{aligned} F &= (T + 273.15)^2 - (22 + 273.15)^2 \\ G &= (T - 22) \\ \lambda_i &= \frac{1.239852(\mu m)}{E_i(eV)} \end{aligned} \tag{6.7}$$

It can be seen from Figure 6.2 that, at temperatures close to room temperature, the refractive index experienced by the fundamental harmonic exceeds that experienced by the second harmonic, suggesting that effective phase matching at these wavelengths can be achieved in this temperature regime.

The power of the generated second harmonic radiation is proportional to the square of the power of the fundamental light; it was shown in equation 5.3 that the

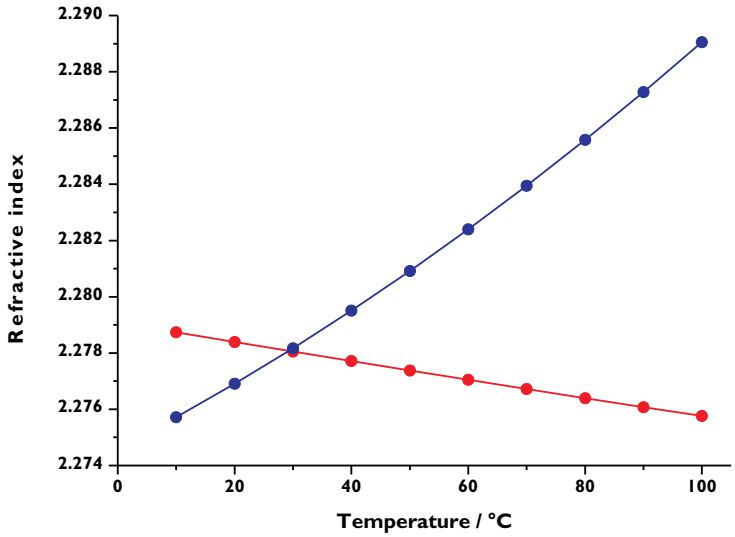

Figure 6.2: Temperature-dependence of the refractive index of $KNbO_3$, as calculated from the Sellmeier equation (6.6). The red curve corresponds to the fundamental ($\sim 860\,\text{nm}$); the blue curve represents the frequency-doubled second harmonic radiation ($\sim 430\,\text{nm}$). [318]

output power is proportional to the powers of both sets of interacting radiation, and in this case both interacting photons are from the same beam. As such:

$$P_{SH} = \gamma P_{FH}^2 \tag{6.8}$$

where γ is the conversion efficiency. A theoretical expression for this conversion efficiency was derived by Boyd and Kleinman [326] by considering the physics of two interacting Gaussian beams:

$$\gamma = \frac{8\omega^3 d^2 l h(\xi)}{\epsilon_0 \pi c^4 n_\omega^2} \tag{6.9}$$

where d is the non-linear optical coefficient which describes the non-linearity of the birefringent crystal, n_ω is the refractive index relevant to the fundamental radiation, and ϵ_0 is the permittivity of free space; and the fundamental angular frequency $\omega = 2\pi c/\lambda$. The focussing parameter, $h(\xi)$, describes the balance between the

focussing at the beam waist, and the changing shape of the beam over the crystal length. The beam waist, of width w_0, is assumed to be in the centre of the crystal, and $\xi = l/b$ where l is the crystal length and b the confocal parameter. A graphical presentation of the values of $h(\xi)$ for different ξ was given by Boyd and Kleinman [326].

Potassium niobate has an unusually large non-linear optical coefficient associated with SHG ($d_{32} = 18.3\,\mathrm{pm\,V^{-1}}$) at room temperature for the 858 nm fundamental radiation employed in the work reported in this chapter. Accordingly, efficient SHG can be achieved in this material with the economical and convenient diode laser sources available at this wavelength [325]. Further enhancement of this process, by increasing the fundamental intensity taking part in the second harmonic generation through use of an enhancement cavity, is the focus of the work presented in this chapter.

6.1.3 Earlier Work: Enhancement Techniques

A range of techniques has been applied to enhance the transmitted signal in experiments for the second harmonic generation of blue light in a NLO material. The adoption of a pulsed laser source or a diode-pumped solid state laser such as a Ti:Sapphire laser allows access to high powers of radiation; however, these advantages must be offset against difficulties associated with the cost, size and band width associated with such lasers. There are relevant techniques for amplification of the incident light in a second harmonic generation experiment; for instance, a laser source with good beam quality may be paired with a diode laser in a master oscillator power amplifier (MOPA) arrangement, though this is often far from straightforward in implementation and is a somewhat inefficient consumer of electrical power [318].

An alternative approach, and that adopted for the work reported in this chapter, is based upon enhancement by an optical resonator in which the non-linear crystal is placed. Typically, this involves the use of a separate cavity, external to the laser medium. However, intracavity frequency up-conversion is also sometimes adopted

[327, 328], where the non-linear crystal is placed inside the laser's own resonator. The basis of resonator-enhanced SHG is that the external cavity be resonant at the fundamental wavelength, trapping that radiation in such a configuration that it is caused to pass repeatedly through the non-linear crystal, leading to a generally higher-efficiency interaction with the material, and a greater level of SHG. The optical enhancement associated with the mode structure of such a cavity increases the circulating radiation power, and therefore the conversion efficiency.

One of the more challenging experimental aspects of such a setup lies in maintaining the cavity and the light in resonance, and particularly in maintaining the cavity length such that constructive interference of the fundamental wavelength may occur on each pass. This may be achieved by the active cavity-locking schemes mentioned in Chapter 2, as well as passive locking approaches such as that described and developed in Chapters 3 and 4. The work of this chapter applies the V-cavity-based optical locking method, as used in OF-CEAS in Chapters 3 and 4, to increase the circulating power of light within such an enhancement cavity for SHG in a crystal of potassium niobate.

Optically-locked resonator-enhanced SHG was realised by Dixon *et al.* [329] using a $KNbO_3$ crystal held within a linear, two-mirror, optical cavity; this resulted in a conversion efficiency of 1.7 % and 0.251 mW of radiation was obtained close to 432 nm. A variable feedback system was included in their setup, which is illustrated in Figure 6.3, and comprised an optical isolator and an attenuator. The isolator allowed the laser to be shielded from the reflected non-cavity-resonant radiation, but the cavity-resonant radiation was polarisation-selected using a half wave plate so that it would pass through the isolator and return to injection-seed the diode.

Another strategy that has been taken up by some [330–332] is the adoption of a ring cavity. As explored in section 2.2.3, such resonators are associated with a standing wave propagating only in the forward direction; whether used in a triangular ring cavity or a so-called "bow-tie" arrangement, there is no intensity coupled into the counter-propagating direction, and therefore no route for cavity-resonant feed-

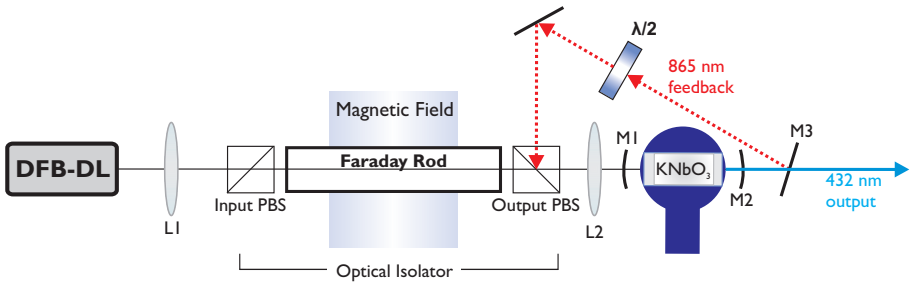

Figure 6.3: The variable feedback SHG setup of Dixon *et al.* , modified from reference [329].

back to emerge. Accordingly, some sort of external retro-reflector is needed to direct cavity-resonant light in the counter-propagating direction so that feedback can be used to seed the laser; alternatively, the cavity-resonant light may be directed into the laser without passing back through the resonator. These experimental schemes have led to conversion efficiencies for the SHG process of 0.57–7.3 %. Dixon *et al.* [329] attributed the relatively low conversion efficiencies obtained for such systems to imperfections in the bulk structure, and particularly the surfaces, of the potassium niobate crystals; their system produced 0.215 mW of blue light, when a theoretical value of 0.82 mW was expected [329].

A major contribution to the low conversion efficiencies is caused by the great reduction in the cavity finesse on introducing the crystal within the cavity. The losses at the crystal faces on each pass through the resonator rapidly dominate the overall cavity losses, leading to a substantially smaller cavity finesse. One solution to this problem has been the construction of *monolithic resonators*, such as that employed by Goldberg *et al.* [333], where the reflectors comprising the resonator are merely polished surfaces of the non-linear crystal, meaning that there are fewer surface interactions with the light, significantly reducing the intra-cavity losses, and thereby increasing the conversion efficiency that may be achieved. Indeed, Goldberg *et al.* [333] achieved a conversion efficiency of 45 % in a monolithic linear potassium niobate resonator, converting 167 mW of light at 842 nm to 24 mW of 421 nm radiation.

6.2 Characterisation of the laser and crystal

The Fabry-Pérot diode laser [*JDS Uniphase 856 nm*] was first characterised, in order that the best parameters for its operation could be chosen for the SHG experiments. The laser output wavelength was varied by tuning the driver current, in order to find a region in which the output radiation was stable and single-mode. A mode-hop between two such stable operating regions is seen in Figure 6.4. From this tuning experiment, an optimal current of 150 mA was selected, for operation at 41 °C; this generated an output power of approximately 85 mW of radiation close to 858.8 nm.

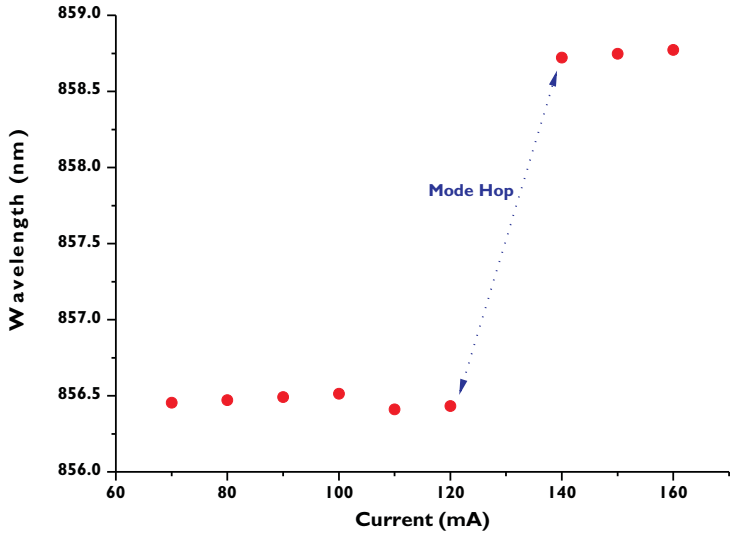

Figure 6.4: Wavelength tuning curve for the Fabry-Pérot Laser operating at 41 °C, showing a mode-hop between two regions of stable output.

Having optimised the operating parameters for the laser, the crystal – particularly, the temperature-dependence of its SHG efficiency – was characterised by a single-pass SHG experiment. The crystal was held in a small mount fitted with an electric Peltier-controlled crystal oven; this allowed control of the crystal temperature to within ± 0.1 °C. A half wave plate [*Thorlabs AHWP05M-630*] before the crystal was used to select the polarisation of the incident light that achieved

optimal second harmonic generation. Biaggio *et al.* [325] previously determined a theoretical optimum temperature of 21 °C for SHG at 857 nm. For the radiation at ~ 858.8 nm in this experiment, the light was focussed into the centre of the crystal using a short-focal-length lens [*Thorlabs*], and the intensity of light generated at the second harmonic (429.4 nm) was measured using a cailbrated InGaAs photodiode [*Thorlabs DET-210*].

A coloured glass filter was used to absorb the fundamental radiation transmitted through the $KNbO_3$ crystal before reaching the photodiode; the transmission properties of this filter were measured using a UV-visible spectrophotometer [*Varian Cary 100 Bio*]. The filter was found to be 50 % transmissive to the second harmonic radiation.

The crystal temperature was varied in steps of 0.1 °C between 20.5 and 22.1 °C, and the second harmonic intensity at the photodiode was recorded on a digital oscilloscope [*Tektronix TDS 2014*] and transferred to a personal computer using a routine written in LabVIEW. Using the calibration data for the power-response of the photodiode, the transmitted power was calculated in each case, and the resulting temperature tuning curve is shown in Figure 6.5. The optimum second harmonic intensity was observed at 21.6 °C, and corresponded to a power of 1.1 μW. The crystal's bandwidth, determined from the FWHM associated with the temperature tuning curve, was found to be 0.2 °C, which is in good agreement with the theoretical calculations of Biaggio *et al.* [325], who reported a HWHM value "on the order of 0.1 °C."

A theoretical value for the conversion efficiency associated with this setup was determined by running a simulation of the focussing parameter; the maximum value of the focussing parameter, $h(\xi)$, was found; from this, the associated confocal parameter (and therefore beam waist) were determined. The resulting beam waist of 15.2 μm corresponded, for this 10 mm crystal, to a focussing parameter of 0.8. Some of the physical parameters associated with α-cut $KNbO_3$ are given in Table 6.2.

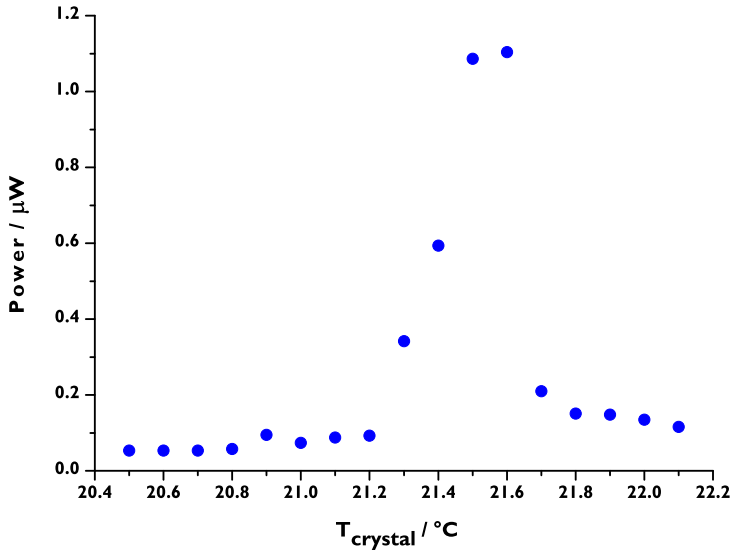

Figure 6.5: Temperature tuning curve for the $KNbO_3$ crystal, with the laser producing 858.7 nm radiation whilst operating at a current of 150 mA; the y-axis shows the power of resulting second harmonic radiation close to 429 nm.

d_{32}	Non-linear coefficient	$1.62 \times 10^{-22}\,\mathrm{C\,V^{-2}}$
ω	Fundamental angular frequency	$2.2 \times 10^{15}\,\mathrm{Hz}$
$n_\omega(21.6\,^\circ\mathrm{C})$	Refractive index	2.278338

Table 6.2: Parameters associated with the α-cut $KNbO_3$ crystal [318].

Employing these values, a theoretical single-pass conversion efficiency of $\gamma = 0.194\,\mathrm{W^{-1}}$ results from equation 6.9. The conversion efficiency achieved in these experiments – $3.43 \times 10^{-4}\,\mathrm{W}$ – therefore represents 0.17 % of the theoretical value, and suggests significant defects associated with the $KNbO_3$ crystal.

6.3 The Feedback Resonator: Characterisation and Optimisation

Before the crystal was introduced into the optical V-cavity, the resonator was characterised and the feedback locking tested. A small, symmetrical V-cavity, directly

analogous to that used in Chapters 3 and 4, was constructed with $L_1 = L_2 = 4.5\,\text{cm}$. Such a cavity has a free spectral range (FSR) of 1.7 GHz. This cavity length was chosen to achieve a balance between the need to focus the light tightly into the crystal to access optimum conversion efficiency, and the need to maintain the resonator's optical stability (see section 2.1.4).

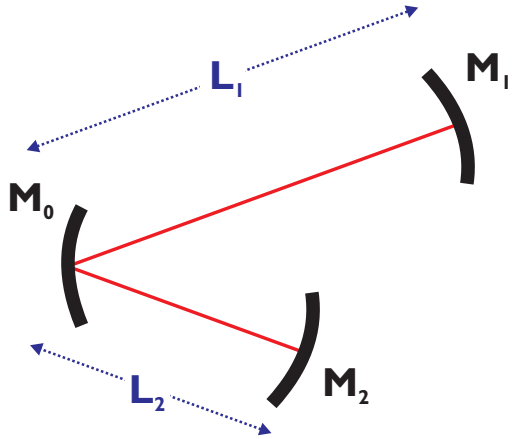

Figure 6.6: Generalised cavity arrangement for the optical stability calculations.

Ray transfer matrix analysis, introduced in Appendix A, gives the following relevant matrices for the generalised resonator arrangement shown in Figure 6.6. The appropriate sign convention assigns a *positive* radius of curvature to a *concave* mirror.

$F_{M_{0,1}}$	Reflections at mirrors $M_{0,1}$	$\begin{pmatrix} 1 & 0 \\ -\frac{2}{r_{M_{0,1}}} & 1 \end{pmatrix}$
$T_{L_{1,2}}$	Translation through a distances $L_{1,2}$ through free space	$\begin{pmatrix} 1 & L_{1,2} \\ 0 & 1 \end{pmatrix}$

The total $ABCD$-matrix for the round-trip is then given by:

$$ABCD = F_{M_0} T_{L_1} F_{M_1} T_{L_1} F_{M_0} T_{L_2} F_{M_2} T_{L_2} \tag{6.10}$$

and the relevant stability condition is $-1 < \cos\theta < 1$, wherein:

$$\cos\theta = \frac{\mathbf{Tr}(ABCD)}{2} \tag{6.11}$$

All three mirrors had radii of curvature of 50 mm, and symmetrical arm lengths of 45 mm; as such, $\cos\theta = 0.921$, and the cavity is stable. Mirrors [*LaserOptik*] of 0.5" diameter were employed; these were mirrors specified by their manufacturer to be of high reflectivity for both the 425–435 nm and 850–870 nm regions. These reflectivities were calibrated experimentally at the fundamental wavelength, using a high-accuracy power meter [*Gentech XLP12-1S-H2*]; the resulting reflectivity of 0.995 corresponds to a cavity finesse close to 600. The experimental arrangement is depicted in Figure 6.7.

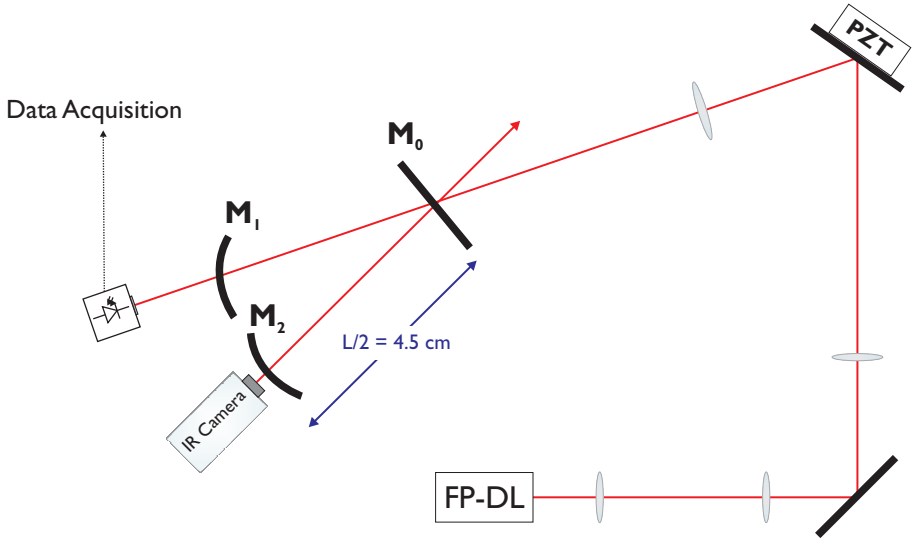

Figure 6.7: Schematic illustration of the setup for characterising the symmetric V-shaped optical resonator, with $L_1 = L_2 = L/2 = 4.5\,\text{cm}$.

Figure 6.8 shows the persistent, well-defined mode structure that was exhibited in the cavity-transmitted light across a laser scan of approximately one second's duration. This well-defined, evenly-spaced structure is consistent with successful injection seeding by the optical feedback, bringing about the optical locking effect discussed in section 3.2. Using a 10 GHz spectrum analyser [*Melles Griot, 10 GHz*],

the mode spacing was found to take a consistent value of 1.7 GHz, corresponding to the free spectral range associated with a folded 9 cm-long cavity.

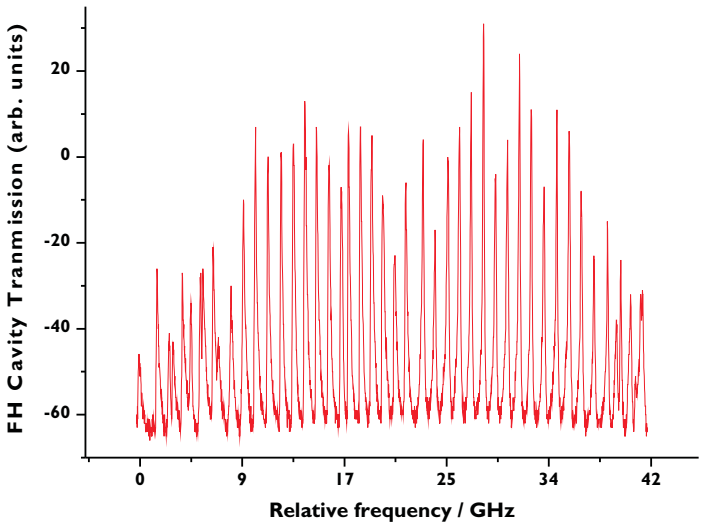

Figure 6.8: Cavity transmission of the fundamental (858.7 nm), showing clean, well-defined mode structure spaced consistently by a free spectral range of 1.7 GHz.

Similarly to the OF-CEAS experiments described in Chapters 3 and 4, a mirror before the resonator was mounted on a PZT, to allow control of the laser–cavity distance. Consistent with the behaviour expected from an optically locked system, when the feedback phase is altered by changing the laser–cavity distance it was found that the mode structure could be shifted controllably and reproducibly. This was achieved by manually altering the voltage supplied to this PZT by a small power supply [*Weir Mini-reg Power Supply, Type 401*], and the effect is illustrated in the two traces in Figure 6.9.

Having characterised the resonator, and fully optimised the operating parameters for the crystal heater and laser, the cavity was re-configured in order to achieve the most efficient non-linear interaction between the fundamental laser light and the $KNbO_3$ crystal. In order to compensate for the reduction in cavity finesse brought about by introducing the high losses associated with the $KNbO_3$ crystal, the input

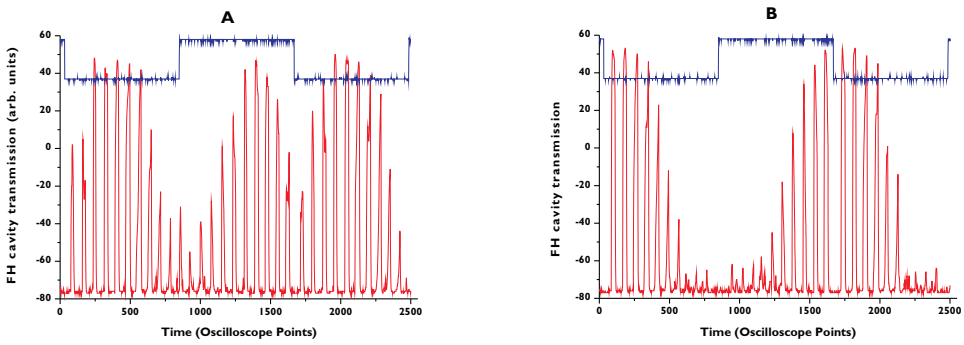

Figure 6.9: Illustration of the effect of manual movement of the piezo-electric transducer on the cavity transmission; all other parameters were kept the same between data sets A and B.

coupling mirror, M_0, was replaced by a mirror of much greater transmission in the 425–435 nm region; this mirror was specified with $R > 95\,\%$ at 860 nm and $R < 15\,\%$ for the blue radiation. So as to achieve focussing of the beam in the centre of the crystal to improve the interaction efficiency, the cavity was re-set into an asymmetric configuration so that the crystal could interact with the radiation at the beam waist. The same total cavity length of 9 cm was retained, but now with $L_1 = 3\,\text{cm}$ and $L_2 = 6\,\text{cm}$. As such, the beam waist was 1.5 cm away from the folding mirror, allowing the crystal to be mounted with its centre at this point. The optimised experimental arrangement is illustrated in Figure 6.10.

Mode matching calculations were also performed in order to match the fundamental beam spatially to the TEM_{00} mode of the resonator. Since the diode laser output is approximately Gaussian, no reshaping of the beam other than by focussing was considered. A generalised scheme is shown in Figure 6.11. The calculated beam waist in the cavity was $w_{cav} = 64\,\mu\text{m}$; the corresponding beam parameter is therefore:

$$q_{cav} = i\,\frac{(w_{cav})^2\pi}{\lambda} \tag{6.12}$$

which returns a value of $q_{cav} = 0.015i$. An experimental value for the incident beam waist before the cavity was determined by imaging the beam on a CCD camera [*Watec WAT-902A*] and analysing it on commercial beam-profiling software [*LBA-*

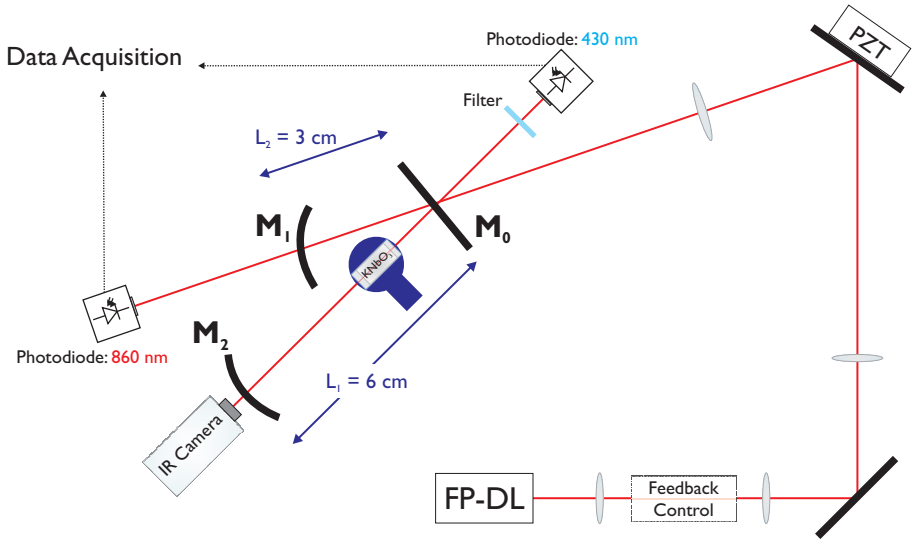

Figure 6.10: The asymmetric cavity setup; FP-DL is the Fabry-Pérot Diode Laser, and PZT indicates the piezo-electric transducer.

PC, Spiricon Inc.]. The beam was found to have equal widths of 1 mm in the horizontal and vertical directions; the corresponding beam parameter was $q_{in} = 3.653i$. The relevant matrices in order to build the $ABCD$-matrix for the complete system are as follows:

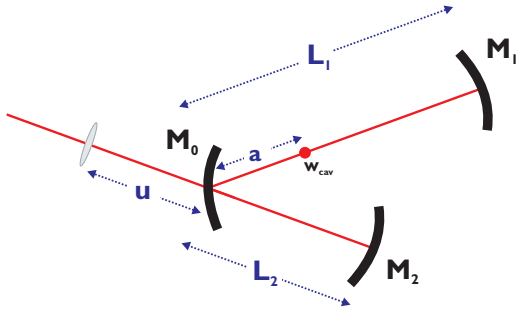

Figure 6.11: A generalised setup for the mode-matching calculations; a is the distance from the folding mirror to the beam waist, L_1 and L_2 are the respective V-cavity arm lengths, and u is the distance separating the lens and the cavity folding mirror.

F_{M_0}	Reflection at mirror M_0	$\begin{pmatrix} 1 & 0 \\ -\frac{2}{r_{M_0}} & 1 \end{pmatrix}$
$T_{L_{1,2}}$	Translation through the distance a	$\begin{pmatrix} 1 & a \\ 0 & 1 \end{pmatrix}$
F_u	Transmission through the lens (focal length f_u)	$\begin{pmatrix} 1 & 0 \\ -\frac{1}{f_u} & 1 \end{pmatrix}$
T_u	Translation along a distance u through free space	$\begin{pmatrix} 1 & u \\ 0 & 1 \end{pmatrix}$

This time, the overall ABCD matrix is given by:

$$ABCD = T_a F_{M_0} T_u F_u \tag{6.13}$$

The mode-matched beam parameter was then calculated using the Gaussian beam law (equation A.9), so that:

$$q_{mm} = \left(\frac{Dq_{in} - B}{Cq_{in} - A} \right) \tag{6.14}$$

$\mathrm{Re}(q_{mm})$ was then minimised by variation of the value of u, so that w_{mm} and w_{cav} would be as closely matched as possible, with w_{mm} given by:

$$w_{mm} = i\sqrt{\frac{\mathrm{Im}\,(q_{mm})\lambda}{\pi}} \tag{6.15}$$

Using the parameters associated with the asymmetric cavity configuration, a lens of $f_u = 25\,\mathrm{cm}$ was selected, to be placed 23.5 cm away from the folding mirror.

6.4 Feedback Control

As discussed in Chapter 3, the feedback in an optically-locked system must be carefully and controllably regulated. This can be achieved by attenuation, where the incident power *and* the feedback power are reduced, or by use of an optical

isolator, which serves to attenuate only the counter-propagating radiation. Each of these systems was investigated for use in the resonator-enhanced SHG setup.

6.4.1 Optical Attenuation

The optical attenuator comprised a half wave plate and a polarising beam-splitter, as in the OF-CEAS work of Chapter 3; the level of transmitted light in both directions is altered by rotating the half wave plate, so as to control the (mis-)match between the polarisation of the light and polarising beam splitter. In this realisation of the SHG setup, the non-linear interaction requires the highest incident radiation power possible – as according to equation 6.8, the output power transforms as the square of the incident power – and so the attenuation was generally set at the minimum possible level.

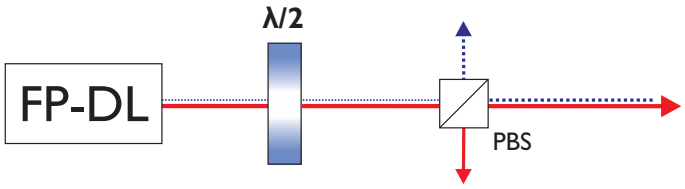

Figure 6.12: The variable optical attenuation setup. PBS indicates a polarising beam-splitter, and the dotted lines indicate the feedback light.

Using the optical attenuator setup, 16% of the incident light was coupled into the cavity; 52.3 mW of incident light at 858.8 nm produced 2.0 μW of blue light (adjusted for the filter transmission) after the resonator. This value is larger than in the single-pass setup, and the efficiency is partly limited by the radii of curvature associated with the resonator mirrors, meaning that the light cannot be focussed down to quite the beam waist size needed to achieve optimal conversion efficiency. The Boyd-Kleinman [326] focussing parameter, $h(\xi)$, took a value of 0.5 in this case, compared to 0.8 for the single-pass arrangement. An estimate of the expected conversion efficiency, accounting only for the *focussing effect* of the cavity, can be obtained by scaling the single-pass efficiency value by the ratio of the relevant focussing parameters. In this case, then, the cavity-enhanced efficiency is estimated

by:

$$\gamma_{CE} = 3.43 \times 10^{-4} \left(\frac{0.5}{0.8} \right) = 2.14 \times 10^{-4}\,\mathrm{W}^{-1} \tag{6.16}$$

An experimental conversion efficiency, γ_{exp} is simply taken as the ratio of the second harmonic power to the square of the incident fundamental power:

$$\gamma_{exp} = \frac{P_{SH}}{P_{FH}^2} = 7.31 \times 10^{-4}\,\mathrm{W}^{-1} \tag{6.17}$$

Comparing these two results indicates that there is an enhancement due to the cavity beyond the focussing effect, since the experimental result exceeds the efficiency expected for a single pass through a focussing arrangement analogous to the resonator.

Equation 6.17 does not take account of the coupling into the cavity, or the enhancement within it due to the cavity finesse. The circulating power within the resonator can be estimated from the result of equation 6.16:

$$P_{FH} = \sqrt{\frac{2P_{SH}}{\gamma_{CE}} \left(\frac{1}{0.85} \right)} = 148\,\mathrm{mW} \tag{6.18}$$

with P_{SH} giving the power of the second harmonic radiation transmitted by the cavity. This value is scaled to give the power of blue light within the cavity, by including the losses at the folding mirror, which has a specified transmittance of 0.85, and there are two loss routes for the blue light out of the folding mirror in a cavity of this geometry.

The enhancement in the circulating power is directly related to the cavity finesse, and so the latter value can also be estimated. With 16% coupling into the cavity, and an incident fundamental power of 52.3 mW, the finesse is:

$$F = \frac{P_{FH,circulating}}{P_{FH,incident}} = \frac{148}{0.16(52.3)} = 17 \tag{6.19}$$

That this value is so small is reasonable, and reflects the great losses when the crystal is introduced, causing the finesse to drop by a factor of approximately thirty

when the $KNbO_3$ is included. Others have implemented SHG within a "bow-tie" cavity configuration [330, 334]; in the work of Gibb [334], a finesse of 72 was calculated, although the experimental measurements suggested a lower value of 20. Nonetheless, it is sufficient to allow significant build-up of constructively-interfering waves on consecutive passes within the resonator, thereby giving rise to the enhancement in the observed conversion efficiency with respect to the single-pass case.

The structure of the cavity transmission of 858.8 nm (–) and 429.4 nm (–) light is shown in Figure 6.13. It can be seen in this figure that, compared to the case for the empty resonator without the crystal, the mode structure of the fundamental harmonic was found to be more chaotic once the crystal was used. Correspondingly, the blue light appeared as short, intense spikes.

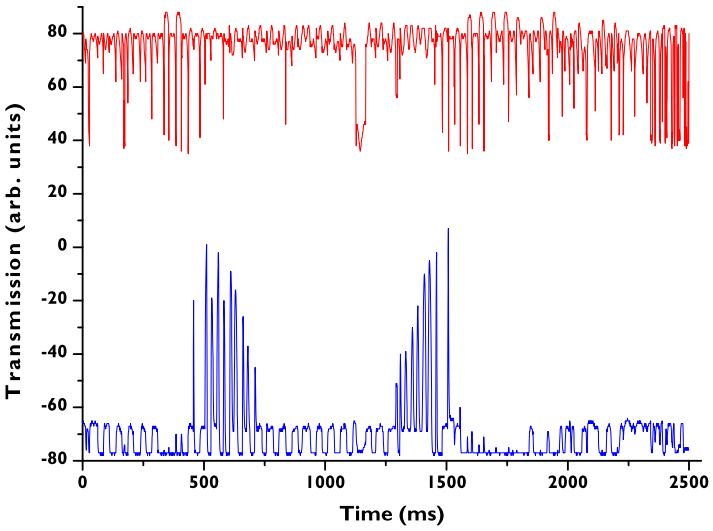

Figure 6.13: Transmission through the cavity of the fundamental (–) and second harmonic (–) using the optical attenuation system, showing intense spikes of the frequency-doubled blue light close to 500 and 1500 ms; the two traces are vertically offset for clarity.

6.4.2 Optical Isolation

A system involving an optical isolator was then investigated, aiming controllably to attenuate the level of optical feedback without reducing the level of light incident on the resonator. The crucial part of the optical isolator is the Faraday rotator; when the light is passed through this rod, which is encased within a strong magnet, it rotates the polarisation of the light propagating in both forward and backward directions through an equal angle and in the same *absolute* sense. As such, two polarisers set orthogonal to one another with a 45° Faraday rotator between constitutes a system whereby the forward beam is subject to maximal transmission, and the reverse-propagating light is rejected. Since the isolation is never total – imperfections in such a system are inevitable – a slightly-detuned isolator offers a useful way to attenuate (but not entirely eliminate) the feedback light without greatly depleting the light intensity incident on the cavity.

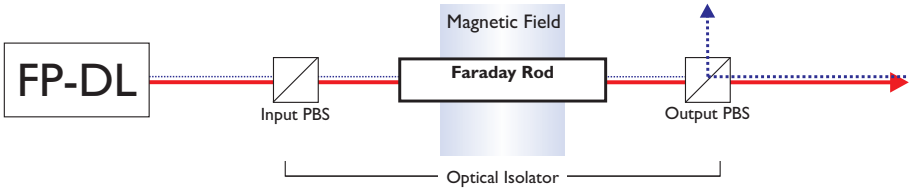

Figure 6.14: The optical isolator setup. As in Figure 6.12, PBS indicates a polarising beam-splitter, and the dotted lines indicate the feedback light.

On implementation of this system, the coupling efficiency into the cavity was improved to a value of 21%, and a total of 3.6 μW of blue, second-harmonic light was generated. This corresponds, through equation 6.17, to a value of $\gamma_{exp} = 2.62 \times 10^{-3}\,\mathrm{W}^{-1}$, which indicates a significant improvement with respect to the attenuator-based setup ($\gamma_{exp} = 7.31 \times 10^{-4}\,\mathrm{W}^{-1}$). Additionally, an improvement was seen in the spectral characteristics of the laser, as can be seen from the spectrum analyser trace in Figure 6.15, when the feedback level was reduced with the isolator. The broad peaks in that trace are consistent with the frequency locking of the laser to modes of the V-cavity as its frequency is being scanned.

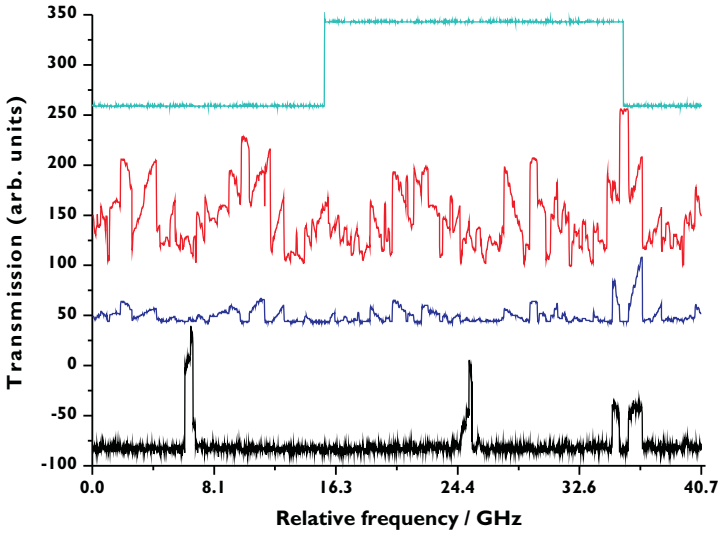

Figure 6.15: Cavity transmission and spectrum analyser (–) traces showing the fundamental (–) and second harmonic (–) light as the laser is ramped across a single scan (–).

The corresponding estimate for the cavity finesse (equation 6.19), treating this system in an analogous fashion to the treatment of the attenuator-based setup, is 25. This is consistent with the improvement in the action of the optical feedback, bringing about better frequency locking and the improved coupling efficiency of the fundamental light into the V-cavity.

The blue light generated using this optically-isolated arrangement remained somewhat chaotic in structure, as shown in Figure 6.15. Careful monitoring of the fundamental output of the laser on a wavemeter indicated that, when the resonator was blocked, the laser scanned consistently and without mode-hopping across the spectrum. However, once the resonator was uncovered, mode hops were seen in the laser output, especially near the ends of the laser scan. One explanation for this lies in the cavity bandwidth exceeding the laser bandwidth ($\sim 10\,\mathrm{MHz}$), meaning that the injection seeding is inefficient and not effective.

6.5 Conclusions and Outlook

The proof-of-principle work presented in this chapter has demonstrated the potential of an optically-locked resonator-enhanced second harmonic generation setup employing a V-shaped cavity. A V-cavity similar to that used in the OF-CEAS experiments of Chapters 3 and 4 was designed and implemented, with a combined cavity length of 9 cm, and a corresponding free spectral range of 1.7 GHz. Optical feedback locking of the fundamental output of an 860 nm Fabry-Pérot diode laser was demonstrated without active feedback phase control, and the expected effect of manual control of the feedback phase was observed. The cavity arrangement was optimised for the interaction between the fundamental radiation through the use of an input-output coupler with a greater transmission to the blue, second harmonic, radiation, and use of an asymmetric cavity configuration with simple mode-matching, so that the beam waist could be caused to occur within the centre of the PPLN crystal.

Optical attenuation (in both directions) and isolation (attenuation of the optical feedback only) were both implemented and investigated as methods to control the feedback level. Better coupling, optical locking, and therefore second harmonic light intensity were found for the optically isolated system, in the lower feedback regime. Evidence has been presented for successful locking of the diode laser during the production of blue second harmonic light.

The conversion efficiency, γ_{exp}, presented for each of a series of enhanced SHG systems in the literature [329–332] is typically close to 1 W^{-1}. As such, the best reported efficiency for this system of $2.62 \times 10^{-3}\,W^{-1}$ is several hundred times poorer than these. However, the measurements reported in this chapter were carried out without any impedance matching of the crystal and input coupler, and it was shown at section 6.2 that the crystal that was employed here had significant defects associated with it. Considering these issues with this preliminary setup, it is reasonable to expect a considerable improvement with respect to this preliminary value from a fully impedance-matched setup constructed with optimised, bespoke components.

Further improvement of the current setup might yield a more regularly-structured

output as well as a greater power of the second harmonic light. In this preliminary realisation, the bandwidth associated with the low cavity finesse (dominated by the crystal losses) is too great to injection-seed the laser effectively. Employing a custom input coupler with a transmission coefficient chosen to match the losses at the crystal would allow the achievement of a greater cavity finesse, reducing the associated bandwidth and increasing the effectiveness of laser injection seeding. This in turn would yield better optical frequency locking and a more stable, higher-power second harmonic output. A variable isolation system, reducing the power of the feedback without attenuating the light beam coupling into the cavity, as well as active feedback phase control, are additions to the setup that might also be expected to bring improvements. Use of a different type of diode laser, such as a DFB, which might be slightly less sensitive in its response to optical feedback, could further improve the stability of the resulting second harmonic light. An arrangement facilitating tighter focussing of the beam in the crystal, to bring it closer to the calculated optimum value of $\sim 15.2\,\mu$m, could bring great improvements to the observed conversion efficiency. Even modest improvements in this efficiency could yield a second harmonic power on the order of 0.1–0.5 μW of blue light, and powers of that order have been demonstrated to be sufficient for a successful implementation of CRDS [335].

The potential usefulness for this type of light source, after such improvements, is great. The light which is produced could be intense, is inherently pulsed and produced at a well-spaced frequency interval; as such, if the cavity transmission were stabilised according to some of the strategies outlined here, it could lend itself very well to use in a cavity ring-down experiment. The V-cavity strategy for resonator-enhanced SHG need not be limited to this wavelength, type of laser, or crystal. Indeed, one potential application of the principle shown in this chapter would be to generation of ultraviolet light from a shorter-wavelength laser in the red. In the ultraviolet region, there are strong electronic transitions associated with many small molecules of chemical and analytical interest.

In summary, the experiments presented in this chapter have shown the promise

associated with V-cavity-locked second harmonic generation for a spectroscopic source of great usefulness. By implementing such a system with some of the improvements outlined here, an enhanced-power, consistently-spaced sequence of second harmonic light pulses could be produced conveniently and economically, with many potential applications.

Appendix A

Ray-Transfer Matrices

In order to describe the propagation of light through an optical system composed of planar and spherical elements, we adopt the model [336] of a plane wave described by a wavevector k, where:

$$k = \frac{2\pi n}{\lambda} \tag{A.1}$$

with n being the refractive index of the medium through which the light is passing, and λ being the wavelength of the light. The finite size and non-planar nature of the optical elements means that the model of a plane wave cannot be exact; non-planar optical components bring about further deviations from the planar model of the wave, so the wave's direction varies across its wavefront. In an optical system with cylindrical symmetry, *paraxial* rays are those propagating at sufficiently acute angles to the optical symmetry axis that we may adopt a small angle approximation, such that $\sin\theta \approx \theta$. Within this *paraxial ray approximation*, we may formulate a ray tracing description simply by considering the reflection and refraction at each optical surface.

In both cases shown in Figure A.1, the distance $OA = S$ is the *object distance*, and $OB = S'$ is the *image distance*; the distance OC is the *radius of curvature*, R. From Figure A.1(a):

$$R\sin\theta = CA\sin\theta_1 = (S - R)\sin\theta_1 \tag{A.2}$$

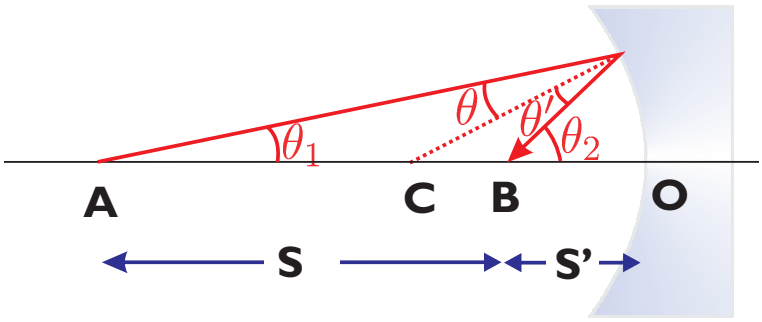

(a) Reflection at a mirror

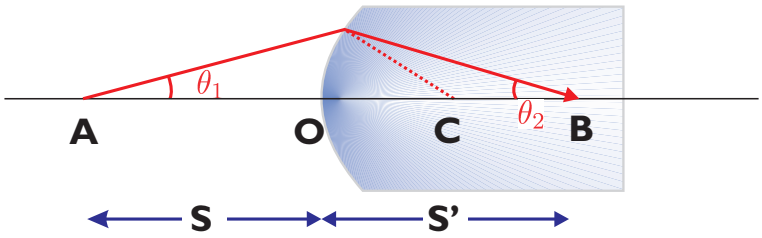

(b) Refraction at a lens

Figure A.1: Illustration of reflection at a concave mirror, and refraction at a convex lens.

$$R \sin\theta' = BC \sin\theta_2 = (R - S) \sin\theta_2 \tag{A.3}$$

Simply invoking the law of reflection, $\theta = \theta'$, and so:

$$\frac{\sin\theta_1}{\sin\theta_2} = \frac{R - S'}{S - R} \tag{A.4}$$

For the refraction system shown in Figure A.1(b), an analogous analysis leads to:

$$\frac{\sin\theta_1}{\sin\theta_2} = \frac{S' - R}{S + R}\frac{n_2}{n_1} \tag{A.5}$$

Within our model, we can describe a ray in terms of its distance, d, away from the symmetry axis ($\vec{z}$), and the angle, θ, that it makes with that same axis. Within the paraxial approximation, there is a linear relationship between the values describing

the input and output rays, respectively (d_1, θ_1) and (d_2, θ_2):

$$d_2 = Ad_1 + B\theta_1 \tag{A.6}$$

$$\theta_2 = Cd_1 + D\theta_1 \tag{A.7}$$

As such, we can use a matrix to describe the propagation through an optical system:

$$\begin{pmatrix} d_2 \\ \theta_2 \end{pmatrix} = \begin{pmatrix} A & B \\ C & D \end{pmatrix} \begin{pmatrix} d_1 \\ \theta_1 \end{pmatrix} = \mathbf{M} \begin{pmatrix} d_1 \\ \theta_1 \end{pmatrix} \tag{A.8}$$

where $\mathbf{M}$ is the *ray tracing matrix*, which has a determinant of $AD - BC = 1$.

There are some applicable conventions to the optical terms that make up a ray transfer matrix:

- The propagation direction is generally taken as left-to-right.
- The distance of the ray from the axis in the upward direction is taken to be positive.
- The radius of curvature of an optical surface is positive for a convex surface and negative for a concave one.

Some examples of the simplest ray-transfer matrices are given below:

$\begin{pmatrix} 1 & d \\ 0 & 1 \end{pmatrix}$	Translation along a distance d through free space.
$\begin{pmatrix} 1 & 0 \\ -\frac{1}{f} & 1 \end{pmatrix}$	Passing through a thin lens with focal length f.
$\begin{pmatrix} 1 & 0 \\ -\frac{2}{R} & 1 \end{pmatrix}$	Reflection at a curved mirror, with radius of curvature R.
$\begin{pmatrix} 1 & 0 \\ 0 & \frac{n_1}{n_2} \end{pmatrix}$	Refraction at a flat interface between media with indices $n_{1,2}$.

Accordingly, a ray-transfer matrix can be built up for an optical system comprising several components, allowing the complete system to be described in a convenient

mathematical form. The Gaussian ABCD law relates the beam parameters before (q_i) and after (q_f) tracing the path described by a given ray-transfer matrix [54]:

$$q_f = \frac{Aq_i + B}{Cq_i + D} \tag{A.9}$$

Appendix B

The Optical Stability Condition

The analysis of optical stability within the optical cavity begins with the formation of an $ABCD$-matrix for a single pass through a simple two-mirror cavity of mirrors with equal radii of curvature r, spaced by a length L:

$$\begin{pmatrix} d_1 \\ \theta_1 \end{pmatrix} = \begin{pmatrix} 1 & 0 \\ -2/r & 1 \end{pmatrix} \begin{pmatrix} 1 & L \\ 0 & 1 \end{pmatrix} \begin{pmatrix} d_0 \\ \theta_0 \end{pmatrix} \tag{B.1}$$

and therefore:

$$\begin{pmatrix} d_1 \\ \theta_1 \end{pmatrix} = \begin{pmatrix} 1 & L \\ \frac{-2}{r} & 1 - \frac{2L}{r} \end{pmatrix} \begin{pmatrix} d_0 \\ \theta_0 \end{pmatrix} \tag{B.2}$$

The confinement condition requires that the output vector be the same as the input vector for the light - *i.e.* each pass of the light through the cavity makes no alteration to the direction of the light's path. This allows us to set up an eigenvalue condition [54]:

$$\begin{pmatrix} 1 & L \\ \frac{-2}{r} & 1 - \frac{2L}{r} \end{pmatrix} \begin{pmatrix} d_0 \\ \theta_0 \end{pmatrix} = \lambda \begin{pmatrix} d_0 \\ \theta_0 \end{pmatrix} \tag{B.3}$$

This leads to a characteristic equation of the following form:

$$\lambda^2 - \mathbf{tr} \begin{pmatrix} 1 & L \\ \frac{-2}{r} & 1 - \frac{2L}{r} \end{pmatrix} \lambda + \mathbf{det} \begin{pmatrix} 1 & L \\ \frac{-2}{r} & 1 - \frac{2L}{r} \end{pmatrix} = 0 \tag{B.4}$$

wherein $\mathbf{tr}(\mathbf{M})$ is the *trace* of matrix $\mathbf{M}$, and $\mathbf{det}(\mathbf{M})$ is its *determinant*:

$$\mathbf{tr}\begin{pmatrix} 1 & L \\ \frac{-2}{r} & 1-\frac{2L}{r} \end{pmatrix} = 2 - \frac{2L}{r} \tag{B.5}$$

$$\mathbf{det}\begin{pmatrix} 1 & L \\ \frac{-1}{2r} & 1-\frac{L}{2r} \end{pmatrix} = 1 \tag{B.6}$$

We can simplify this equation by defining a *stability parameter*, g, so that:

$$\begin{gathered} \lambda^2 - 2g\lambda + 1 = 0 \\ \therefore g = \frac{1}{2}\,\mathbf{tr}\begin{pmatrix} 1 & L \\ \frac{-2}{r} & 1-\frac{2L}{r} \end{pmatrix} = 1 - \frac{L}{r} \end{gathered} \tag{B.7}$$

which has solutions of:

$$\lambda = g \pm \sqrt{g^2 - 1} \tag{B.8}$$

After N passes through the cavity, then, the condition becomes:

$$\begin{pmatrix} d_N \\ \theta_N \end{pmatrix} = \lambda^N \begin{pmatrix} d_0 \\ \theta_0 \end{pmatrix} \tag{B.9}$$

For a stable resonator, the value of λ^N cannot diverge, and this implies that λ cannot be purely real:

$$\begin{gathered} \mathrm{Im}\{\lambda\} \neq 0 \\ \Rightarrow g^2 - 1 < 0 \\ \Rightarrow |g| < 1 \end{gathered} \tag{B.10}$$

Given the form of g defined in expression B.7, this implies that:

$$0 < L < 2r \tag{B.11}$$

Appendix C

OF-CEAS Phase Control Electronics

At the end of this appendix, the full circuit diagrams relating to the feedback control electronics are given, without annotations.

Each of the major steps in the electronic circuit is carried out by an operational amplifier ("op-amp"). These are the components in the circuit diagram represented by the large triangular symbols. They are high-gain, dc-coupled differential amplifiers with a single output, represented as in Figure C.1.

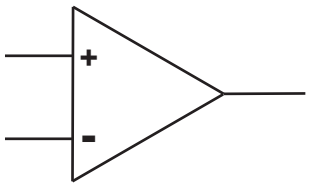

Figure C.1: Circuit diagram representation of an operational amplifier (op-amp).

Horowitz and Hill [337] enumerate two golden rules for the understanding and use of op-amps:

1. The output seeks to make the voltage difference between the two inputs zero.

2. The inputs draw no current.

Their first "rule" does not mean that the op-amp changes the voltage at the inputs– which would in any case be impossible without drawing current – but rather

that it changes its output signal such that the feedback network around the op-amp in the circuit brings the difference between the inputs closer to zero.

By way of example, applying Horowitz and Hill's "golden rules" [337], it becomes clear that the op-amp represented in Figure C.2(a) will function as a simple voltage follower, whilst that in Figure C.2(b) will produce an output that is the differential of the input signal. The latter type of op-amp essentially comprises the first major operational stage of the feedback circuit within the OF-CEAS servo loop.

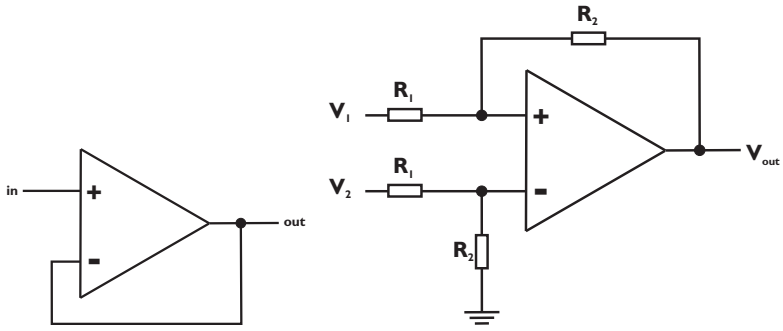

(a) Voltage follower (b) Differentiator

Figure C.2: Representations of two simple operational amplifiers (op-amps).

The gain value corresponding to the op-amp in Figure C.2(b) is simply R_2/R_1; the associated output voltage is given by:

$$V_{out} = \frac{R_2}{R_1}(V_2 - V_1) \tag{C.1}$$

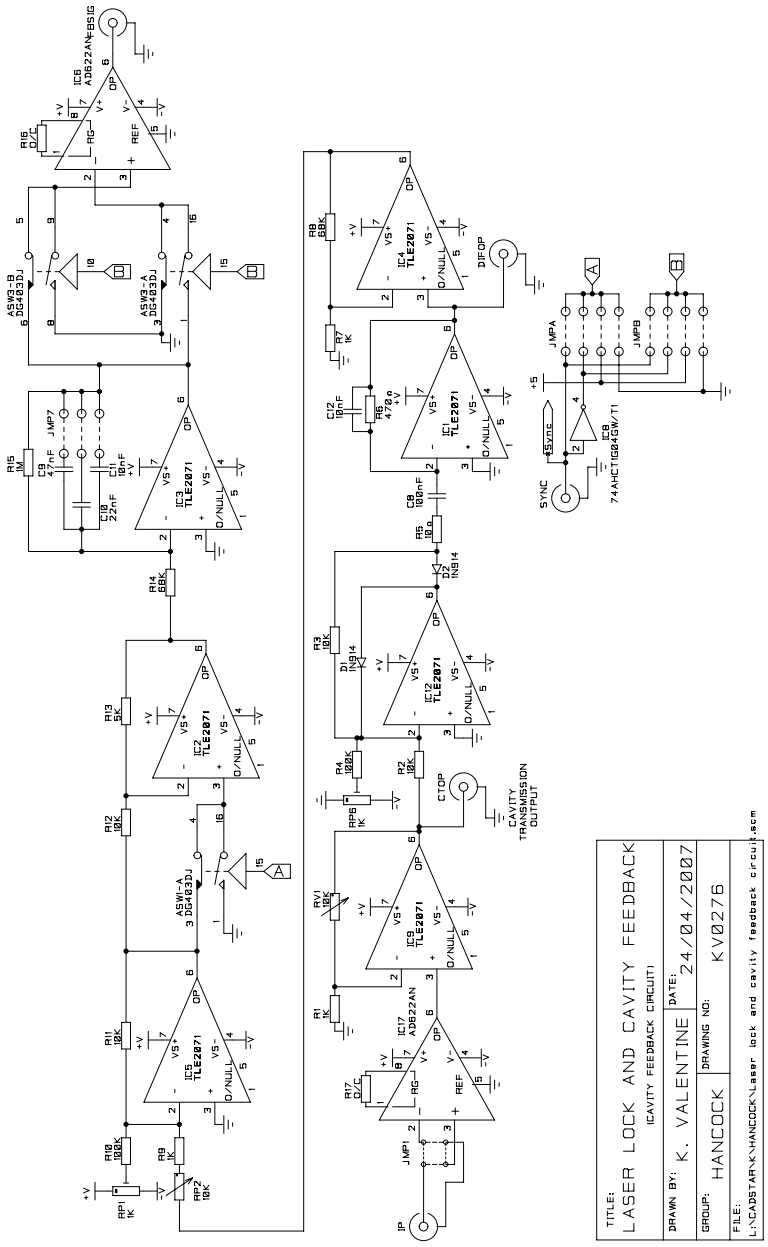

Figure C.3: The feedback phase error-signal circuit.

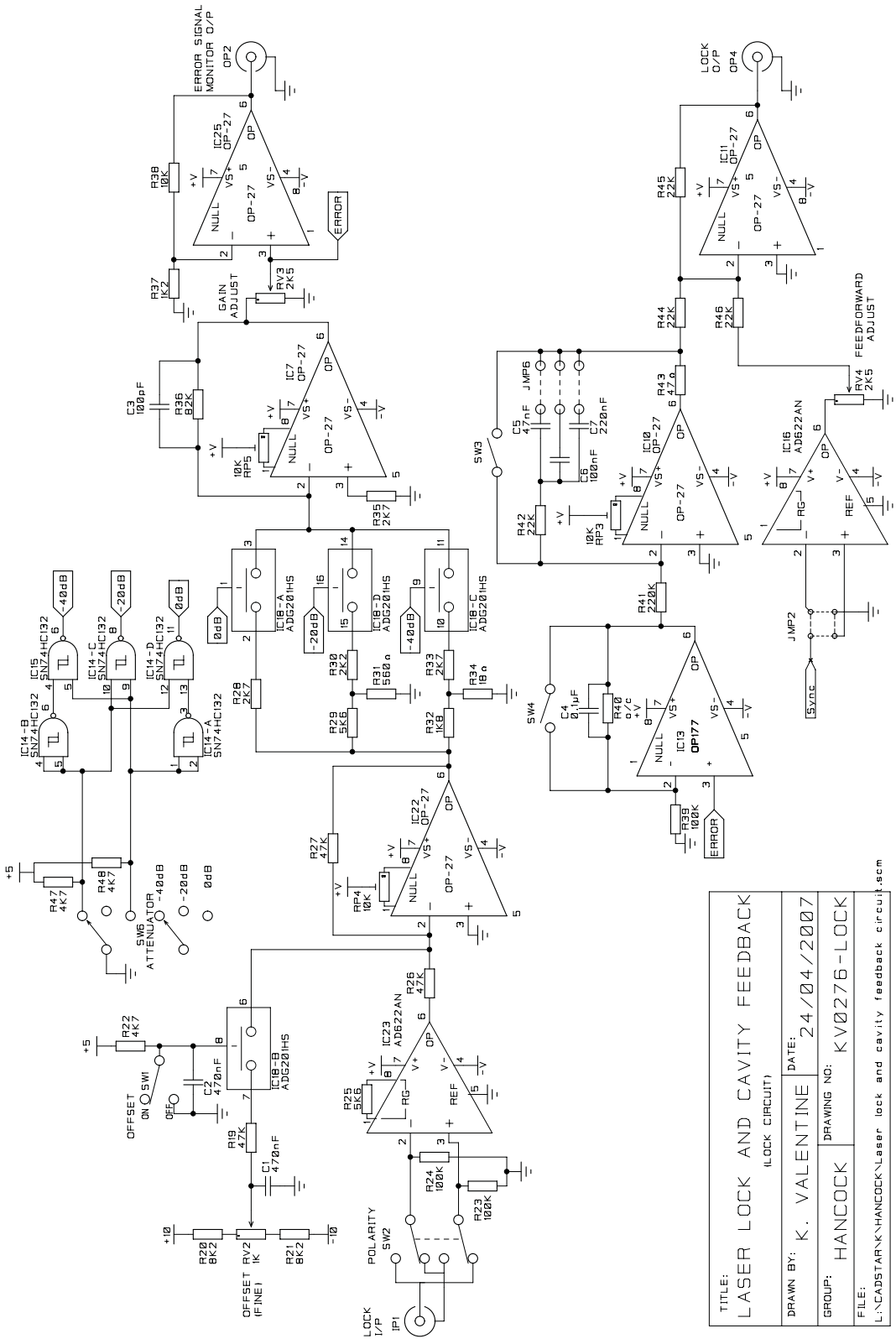

Figure C.4: The locking circuit.

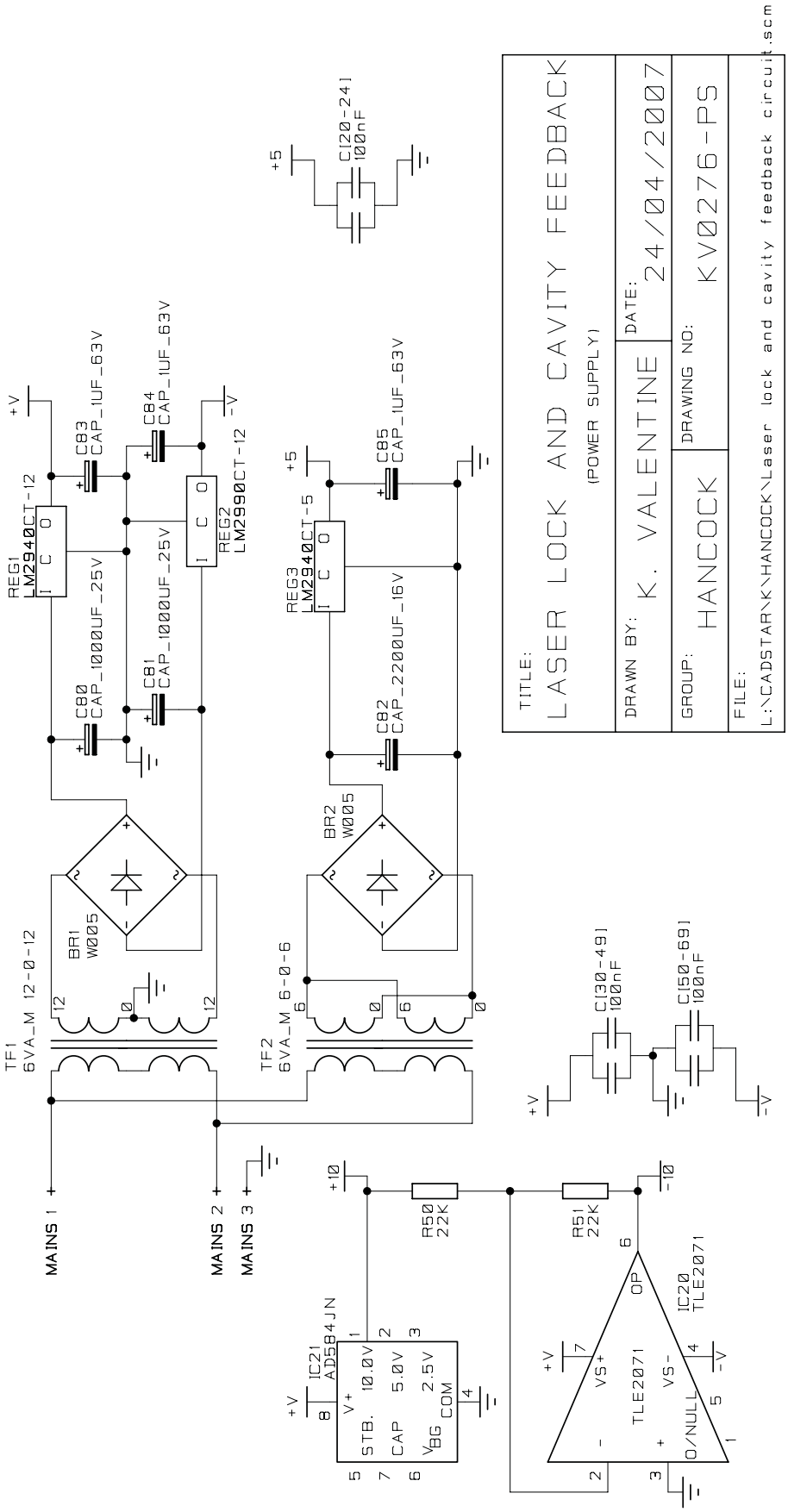

Figure C.5: The power supply circuit

Bibliography

[1] I. Linnerud, P. Kaspersen, and T. Jaeger, *Applied Physics B*, **67**(3), 297–305 (1998).

[2] P. A. Martin, *Chemical Society Reviews*, **31**(4), 201– (2002).

[3] P. A. Martin and R. J. Holdsworth, *Spectroscopy Europe*, **16**(5), 8–15 (2004).

[4] R. P. Wayne, *Chemistry of Atmospheres*, Oxford University Press, 3rd ed., 2000.

[5] D. J. Creasey, P. A. Halford-Maw, D. E. Heard, M. J. Pilling, and B. J. Whitaker, *Journal of the Chemical Society, Faraday Transactions*, **93**(16), 2907–2913 (1997).

[6] S. S. Brown, *Chemical Reviews*, **103**(12), 5219–5238 (2003).

[7] R. Ulber, J.-G. Frerichs, and S. Beutel, *Analytical and Bioanalytical Chemistry*, **376**(3), 342–348 (2003).

[8] A. Amann, A. Schmid, S. Scholl-Bürgi, S. Telser, and H. Hinterhuber, *Spectroscopy Europe*, **17**(3), 18–21 (2005).

[9] H. Dahnke, D. Kleine, P. Hering, and M. Mürtz, *Applied Physics B*, **72**(8), 971–975 (2001).

[10] H. Suto, T. Azuma, S. Ito, Y. Ito, H. Miyaji, Y. Yamazaki, Y. Kohli, and M. Kuriyama, *Journal of Gastroenterology and Hepatology*, **15**(2), 161–167 (2000).

[11] M. Mazurenka, A. J. Orr-Ewing, R. Peverall, and G. A. D. Ritchie, *Annual Reports on the Progress of Chemistry: Section C*, **101**, 100–142 (2005).

[12] D. C. Scott, R. L. Herman, C. R. Webster, R. D. May, G. J. Flesch, and E. J. Moyer, *Applied Optics*, **38**(21), 4609–4622 (1999).

[13] G. A. Bishop and D. H. Stedman, *Accounts of Chemical Research*, **29**, 489–495 (1996).

[14] W. Demtröder, *Laser Spectroscopy: Basic Concepts and Instrumentation*, Springer-Verlag, 1982.

[15] F. Graham-Smith, T. A. King, and D. Wilkins, *Optics and Photonics: An Introduction*, Wiley, 2nd ed., 2007.

[16] W. Demtröder, *Atoms, Molecules and Photons: An Introduction to Atomic-, Molecular- and Quantum-Physics*, Springer, 2006.

[17] S. M. Ball and R. L. Jones, *Chemical Reviews*, **103**(12), 5239–5262 (2003).

[18] J. W. Harder, E. J. Williams, K. Baumann, and F. C. Fehsenfeld, *Journal of Geophysical Research - Atmospheres*, **102**(D5), 6227–6243 (1997).

[19] T. Guanghua, X. Chuanlong, S. Litang, Z. Bin, Y. Daoye, P. Qi, and W. Shimin, *Measurement Science and Technology*, **20**(1), 015601 (2009).

[20] M. Buchwitz, V. V. Rozanov, and J. P. Burrows, *Journal of Geophysical Research - Atmospheres*, **105**(D12), 15231–15245 (2000).

[21] R. Wada and A. J. Orr-Ewing, *Analyst*, **130**(12), 1595–1600 (2005).

[22] R. E. Drullinger and R. N. Zare, *Journal of Chemical Physics*, **59**(8), 4225–4234 (1973).

[23] R. N. Zare and P. J. Dagdigian, *Science*, **185**(4153), 739–747 (1974).

[24] R. Altkorn and R. N. Zare, *Annual Review of Physical Chemistry*, **35**(1), 265–289 (1984).

[25] M. D. Wheeler, S. M. Newman, A. J. Orr-Ewing, and M. N. R. Ashfold, *Journal of the Chemical Society, Faraday Transactions*, **94**(3), 337–351 (1998).

[26] J. L. Kinsey, *Annual Review of Physical Chemistry*, **28**(1), 349–372 (1977).

[27] A. G. Bell, *American Journal of Science*, **20**(118), 305–324 (1880).

[28] A. Rosencwaig and A. Gersho, *Journal of Applied Physics*, **47**(1), 64–69 (1976).

[29] J. F. McClelland and R. N. Kniseley, *Applied Physics Letters*, **28**(8), 467–469 (1976).

[30] J. Davidsson, J. H. Gutow, and R. N. Zare, *Journal of Physical Chemistry*, **94**(10), 4069–4073 (2002).

[31] B. A. Paldus, T. G. Spence, R. N. Zare, J. Oomens, F. J. M. Harren, D. H. Parker, C. Gmachl, F. Cappasso, D. L. Sivco, J. N. Baillargeon, A. L. Hutchinson, and A. Y. Cho, *Optics Letters*, **24**(3), 178–180 (1999).

[32] C. N. Banwell, *Fundamentals of Molecular Spectroscopy*, McGraw-Hill, 3rd ed., 1983.

[33] A. Volkmer, P. P. Radi, A. M. Zheltikov, and A. Zumbusch, *Journal of Raman Spectroscopy*, **40**(7), 712–713 (2009).

[34] A. Bohlin, F. Vestin, P. Joubert, J. Bonamy, and P.-E. Bengtsson, *Journal of Raman Spectroscopy*, **40**(7), 788–794 (2009).

[35] A. M. Zheltikov, *Journal of Raman Spectroscopy*, **31**(8-9), 653–667 (2000).

[36] P. Ewart and S. V. O'Leary, *Optics Letters*, **11**(5), 279–281 (1986).

[37] R. L. Farrow and D. J. Rakestraw, *Science*, **257**(5078), 1894–1900 (1992).

[38] G. Hall and B. J. Whitaker, *Journal of the Chemical Society, Faraday Transactions*, **90**(1), 1–16 (1994).

[39] G. Chartier, *Introduction to Optics*, Springer, 1st ed., 2005.

[40] O. Svelto, *Principles of Lasers*, Springer, 4th ed., 1998.

[41] C. E. Wieman and L. Hollberg, *Review of Scientific Instruments*, **62**(1), 1–20 (1991).

[42] P. Werle, *Infrared Physics & Technology*, **37**(1), 59–66 (1996).

[43] P. Werle, *Spectrochimica Acta A*, **52**(8), 805–822 (1996).

[44] P. Werle, *Spectrochimica Acta A*, **54**(2), 197 – 236 (1998).

[45] A. J. Dempster, *Physical Review*, **11**(4), 316–325 (1918).

[46] J. B. Fenn, M. Mann, C. K. Meng, S. F. Wong, and C. M. Whitehouse, *Science*, **246**(4926), 64–71 (1989).

[47] P. R. Warburton, M. P. Pagano, R. Hoover, M. Logman, K. Crytzer, and Y. J. Warburton, *Analytical Chemistry*, **70**(5), 998–1006 (1998).

[48] H. Yan and C.-C. Liu, *Sensors and Actuators B*, **17**(2), 165–168 (1994).

[49] D. Pletcher, J. Evans, P. R. G. Warburton, and T. K. Gibbs, Acidic gas sensors and method of using same US Patent No 5 071 526, 1988.

[50] G. E. Collins and S. L. Rose-Pehrsson, *Sensors and Actuators B*, **34**(1-3), 317–322 (1996).

[51] C. P. Howard, Chemiluminescent gas analyzer for measuring the oxides of nitrogen US Patent No 4 822 564, 1989.

[52] A. J. Hills and P. R. Zimmerman, *Analytical Chemistry*, **62**(10), 1055–1060 (1990).

[53] J. Ye, L. S. Ma, and J. L. Hall, *Journal of the Optical Society of America B*, **15**(1), 6–15 (1998).

[54] A. Yariv and P. Yeh, *Photonics: Optical Electronics in Modern Communications*, Oxford University Press, 6th ed., 2007.

[55] M. S Keshner, *Proceedings of the IEEE*, **70**(3), 212–218 (1982).

[56] C. Fabry and A. Pérot, *Annales de Chimie et de Physique*, **16**, 115 (1899).

[57] H. Kogelnik and T. Li, *Proceedings of the IEEE*, **54**(10), 1312–1329 (1966).

[58] J. H. van Helden, R. Peverall, and G. A. D. Ritchie In *Cavity Ring-Down Spectroscopy: Techniques and Applications*, G. Berden and R. Engeln, Eds., Blackwell, *in press*, 1st ed., 2009.

[59] L. G. Gouy, *Comptes Rendus de l'Académie des Sciences, Paris*, **110**, 1251 (1890).

[60] A. Rubinowicz, *Physical Review*, **54**(11), 931–936 (1938).

[61] R. W. Boyd, *Journal of the Optical Society of America*, **70**(7), 877–880 (1980).

[62] J. J. Scherer, J. B. Paul, A. O'Keefe, and R. J. Saykally, *Chemical Reviews*, **97**(1), 25–52 (1997).

[63] D. Romanini and K. K. Lehmann, *Journal of Chemical Physics*, **99**(9), 6287–6301 (1993).

[64] R. T. Jongma, M. G. H. Boogaarts, I. Holleman, and G. Meijer, *Review of Scientific Instruments*, **66**(4), 2821–2828 (1995).

[65] G. Berden, R. Peeters, and G. Meijer, *International Reviews in Physical Chemistry*, **19**(4), 565–607 (2000).

[66] P. Zalicki, Y. Ma, R. N. Zare, E. H. Wahl, J. R. Dadamio, T. G. Owano, and C. H. Kruger, *Chemical Physics Letters*, **234**(4-6), 269–274 (1995).

[67] J. T. Hodges, J. P. Looney, and R. D. van Zee, *Applied Optics*, **35**(21), 4112–4116 (1996).

[68] J. Morville, D. Romanini, A. A. Kachanov, and M. Chenevier, *Applied Physics B*, **78**(3-4), 465–476 (2004).

[69] D. B. Atkinson, *Analyst*, **128**(2), 117–125 (2003).

[70] B. A. Paldus and A. A. Kachanov, *Canadian Journal of Physics*, **83**(10), 975–999 (2005).

[71] C. Vallance, *New Journal of Chemistry*, **29**(7), 867–874 (2005).

[72] K. K. Lehmann and D. Romanini, *Journal of Chemical Physics*, **105**(23), 10263–10277 (1996).

[73] D. Z. Anderson, J. C. Frisch, and C. S. Masser, *Applied Optics*, **23**(8), 1238–1245 (1984).

[74] J. M. Herbelin, J. A. McKay, M. A. Kwok, R. H. Ueunten, D. S. Urevig, D. J. Spencer, and D. J. Benard, *Applied Optics*, **19**(1), 144–147 (1980).

[75] D. Romanini, A. A. Kachanov, N. Sadeghi, and F. Stoeckel, *Chemical Physics Letters*, **264**(3-4), 316 – 322 (1997).

[76] J. W. Hahn, Y. S. Yoo, J. Y. Lee, J. W. Kim, and H. W. Lee, *Applied Optics*, **38**(1859) (1999).

[77] K. W. Busch and M. A. Busch, Eds., *Cavity-Ringdown Spectroscopy*, American Chemical Society, Washington, D. C., 1999.

[78] K. J. Schulz and W. R. Simpson, *Chemical Physics Letters*, **297**(5-6), 523–529 (1998).

[79] Y. Le Grand and A. Le Floch, *Applied Optics*, **29**(9), 1244–1246 (1990).

[80] J. D. Smith and D. B. Atkinson, *Analyst*, **126**, 1216–1220 (2001).

[81] A. Petterson, E. R. Lovejoy, C. A. Brock, S. S. Brown, and A. R. Ravishankara, *Journal of Aerosol Science*, **35**, 995–1011 (2004).

[82] V. Bulatov, M. Fisher, and I. Schechter, *Analytica Chimica Acta*, **466**, 1–9 (2002).

[83] A. W. Strawa, R. Castaneda, T. G. Owano, D. S. Baer, and B. A. Paldus, *Journal of Atmospheric and Oceanic Technology*, **20**, 454–465 (2003).

[84] W. R. Simpson, *Review of Scientific Instruments*, **74**(7), 3442–3452 (2003).

[85] S. S. Brown, H. Stark, and A. R. Ravishankara, *Applied Physics B*, **75**(2-3), 173–182 (2002).

[86] S. S. Brown, H. Stark, S. J. Ciciora, R. J. McLaughlin, and A. R. Ravishankara, *Review of Scientific Instruments*, **73**(9), 3291–3301 (2002).

[87] A. M. Parkes, B. L. Fawcett, R. E. Austin, S. Nakamichi, D. E. Shallcross, and A. J. Orr-Ewing, *Analyst*, **128**, 960–965 (2003).

[88] J. B. Wills, J. A. Smith, W. E. Boxford, J. M. F. Elks, M. N. R. Ashfold, and A. J. Orr-Ewing, *Journal of Applied Physics*, **92**(8), 4213–4222 (2002).

[89] C. J. Rennick, R. Engeln, J. A. Smith, A. J. Orr-Ewing, M. N. R. Ashfold, and Y. A. Mankelevich, *Journal of Applied Physics*, **97**(11), 113306 (2005).

[90] E. H. Wahl, T. G. Owano, C. H. Kruger, P. Zalicki, Y. Ma, and R. N. Zare, *Diamond and Related Materials*, **5**(3-5), 373–377 (1996).

[91] R. Evertsen, R. L. Stolk, and J. J. ter Meulen, *Combustion Science and Technology*, **157**(1), 341–342 (2000).

[92] P. Zalicki, Y. Ma, R. N. Zare, E. H. Wahl, T. G. Owano, and C. H. Kruger, *Applied Physics Letters*, **67**(1), 144–146 (1995).

[93] W. M. M. Kessels, J. P. M. Hoefnagels, M. G. H. Boogaarts, D. C. Schram, and M. C. M. van de Sanden, *Journal of Applied Physics*, **89**(4), 2065–2073 (2001).

[94] W. M. M. Kessels, A. Leroux, M. G. H. Boogaarts, J. P. M. Hoefnagels, M. C. M. van de Sanden, and D. C. Schram, *Journal of Vacuum Science and Technology A*, **19**(2), 467–476 (2001).

[95] L. Biennier, D. Romanini, A. A. Kachanov, A. Campargue, B. Bussery-Honvault, and R. Bacis, *Journal of Chemical Physics*, **112**(14), 6309–6321 (2000).

[96] M. Hippler and M. Quack, *Chemical Physics Letters*, **314**(3-4), 273–281 (1999).

[97] C. R. Bucher, K. K. Lehmann, D. F. Plusquellic, and G. T. Fraser, *Applied Optics*, **39**(18), 3154–3164 (2000).

[98] A. M. Parkes, A. R. Linsley, and A. J. Orr-Ewing, *Chemical Physics Letters*, **377**(3-4), 439–444 (2003).

[99] A. O'Keefe, *Chemical Physics Letters*, **293**(5-6), 331–336 (1998).

[100] R. Engeln, G. Berden, R. Peeters, and G. Meijer, *Review of Scientific Instruments*, **69**(11), 3763–3769 (1998).

[101] B. Bakowski, L. Corner, G. Hancock, R. Kotchie, R. Peverall, and G. A. D. Ritchie, *Applied Physics B*, **75**(6-7), 745–750 (2002).

[102] P. Zalicki and R. N. Zare, *Journal of Chemical Physics*, **102**(7), 2708–2717 (1995).

[103] K. An, C. Yang, R. R. Dasari, and M. S. Feld, *Optics Letters*, **20**(9), 1068–1070 (1995).

[104] M. J. Lawrence, B. Willke, M. E. Husman, E. K. Gustafson, and R. L. Byer, *Journal of the Optical Society of America B*, **16**(4), 523–532 (1999).

[105] J. Poirson, F. Bretenaker, M. Vallet, and A. Le Floch, *Journal of the Optical Society of America B*, **14**(11), 2811–2817 (1997).

[106] S. E. Fiedler, A. Hese, and A. A. Ruth, *Chemical Physics Letters*, **371**(3-4), 284–294 (2003).

[107] J. B. Paul, L. Lapson, and J. G. Anderson, *Applied Optics*, **40**(27), 4904–4910 (2001).

[108] H. R. Barry, L. Corner, G. Hancock, R. Peverall, T. L. Ranson, and G. A. D. Ritchie, *Physical Chemistry Chemical Physics*, **5**(15), 3106–3112 (2003).

[109] S. Williams, M. Gupta, T. Owano, D. S. Baer, A. O'Keefe, D. R. Yarkony, and S. Matsika, *Optics Letters*, **29**(10), 1066–1068 (2004).

[110] H. R. Barry, L. Corner, G. Hancock, R. Peverall, and G. A. D. Ritchie, *Physical Chemistry Chemical Physics*, **4**(3), 445–450 (2002).

[111] M. Staak, E. W. Gash, D. S. Venables, and A. A. Ruth, *Journal of Molecular Spectroscopy*, **229**(1), 115–121 (2005).

[112] D. M. O'Leary, J. Orphal, A. A. Ruth, U. Heitmann, P. Chelin, and C. E. Fellows, *Journal of Quantitative Spectroscopy and Radiative Transfer*, **109**(6), 1004–1015 (2008).

[113] L. Corner, H. R. Barry, and G. Hancock, *Chemical Physics Letters*, **374**(1-2), 28–32 (2003).

[114] P. Shixin, C. Fenping, G. Xiaoming, Z. Weixiong, Y. Yong, H. Teng, H. Wei, and Z. Weijun, *Vibrational Spectroscopy*, **40**(2), 192–196 (2006).

[115] V. L. Kasyutich, C. S. E. Bale, C. E. Canosa-Mas, C. Pfrang, S. Vaughan, and R. P. Wayne, *Applied Physics B*, **76**(6), 691–697 (2003).

[116] D. S. Baer, J. B. Paul, M. Gupta, and A. O'Keefe, *Applied Physics B*, **75**(2-3), 261–265 (2002).

[117] R. Peeters, G. Berden, and G. Meijer, *Applied Physics B*, **73**(1), 65–70 (2001).

[118] G. Hancock, R. Peverall, and G. A. D. Ritchie, Spectroscopic breath analysis – International Patent No. 03/015631, 2003.

[119] R. Engeln, G. Berden, E. van den Berg, and G. Meijer, *Journal of Chemical Physics*, **107**(12), 4458–4467 (1997).

[120] T. Müller, K. B. Wiberg, and P. H. Vaccaro, *Journal of Physical Chemistry A*, **104**(25), 5959–5968 (2000).

[121] T. Müller, K. B. Wiberg, P. H. Vaccaro, J. R. Cheeseman, and M. J. Frisch, *Journal of the Optical Society of America B*, **19**(1), 125–141 (2002).

[122] R. Engeln, G. von Helden, G. Berden, and G. Meijer, *Chemical Physics Letters*, **262**(1-2), 105–109 (1996).

[123] E. K. Lewis, D. Reynolds, X. Li, G. deVillele, C. Leduc, D. L. Cedeno, and C. E Manzanares, *Chemical Physics Letters*, **334**, 357 (2001).

[124] E. K. Lewis, C. J. Moehnke, and C. E Manzanares, *Chemical Physics Letters*, **394**(1-3), 25–31 (2004).

[125] S. DeMille, R. H. deLaat, R. M. Tanner, R. L. Brooks, and N. P. C. Westwood, *Chemical Physics Letters*, **366**, 383 (2002).

[126] J. M. Herbelin and J. A. McKay, *Applied Optics*, **20**, 3341 (1981).

[127] J.H. van Helden, D.C. Schram, and R. Engeln, *Chemical Physics Letters*, **400**(4-6), 320–325 (2004).

[128] L.S. Rothman, D. Jacquemart, A. Barbe, D. Chris Benner, M. Birk, L.R. Brown, M.R. Carleer, C. Chackerian Jr., K. Chance, L.H. Coudert, V. Dana, V.M. Devi, J.-M. Flaud, R.R. Gamache, A. Goldman, J.-M. Hartmann, K.W. Jucks, A.G. Maki, J.-Y. Mandin, S.T. Massie, J. Orphal, A. Perrin, C.P. Rinsland, M.A.H. Smith, J. Tennyson, R.N. Tolchenov, R.A. Toth, J. Vander Auwera, P. Varanasi, and G. Wagner, *Journal of Quantitative Spectroscopy and Radiative Transfer*, **96**(2), 139 – 204 (2005).

[129] S. M. Ball, I. M. Povey, E. G. Norton, and R. L. Jones, *Chemical Physics Letters*, **342**(1-2), 113–120 (2001).

[130] S. E. Fiedler, G. Hoheisel, A. A. Ruth, and A. Hese, *Chemical Physics Letters*, **382**(3-4), 447–453 (2003).

[131] E. Hamers, D. Schram, and R. Engeln, *Chemical Physics Letters*, **365**(3-4), 237–243 (2002).

[132] S. M. Ball, J. M. Langridge, and R. L. Jones, *Chemical Physics Letters*, **398**(1-3), 68–74 (2004).

[133] P. L. Kebabian, S. C. Herndon, and A. Freedman, *Analytical Chemistry*, **77**(2), 724–728 (2005).

[134] J. M. Langridge, S. M. Ball, A. J. L. Shillings, and R. L. Jones, *Review of Scientific Instruments*, **79**(12), 123110 (2008).

[135] A. Czyżewski, S. Chudzyński, K. Ernst, G. Karasinski, L. Kilianek, A. Pietruczuk, W. Skubiszak, T. Stacewicz, K. Stelmaszczyk, B. Koch, and P. Rairoux, *Optics Communications*, **191**(3-6), 271–275 (2001).

[136] J. J. Scherer, *Chemical Physics Letters*, **292**(1-2), 143–153 (1998).

[137] J. Orphal and A. A. Ruth, *Optics Express*, **16**(23), 19232–19243 (2008).

[138] R. R. Alfano, *The Supercontinuum Laser Source*, Springer, 2nd ed., 2006.

[139] W. H. Reeves, D. V. Skryabin, F. Biancalana, J. C. Knight, P. St. J. Russell, F. G. Omenetto, A. Efimov, and A. J. Taylor, *Nature*, **424**(6948), 511–515 (2003).

[140] P. S. Johnston and K. K. Lehmann, *Optics Express*, **16**(19), 15013–15023 (2008).

[141] J. M. Langridge, T. Laurila, R. S. Watt, R. L. Jones, C. F. Kaminski, and J. Hult, *Optics Express*, **16**(14), 10178–10188 (2008).

[142] L. van der Sneppen, G. Hancock, C. Kaminski, T. Laurila, S. R. Mackenzie, S. R. T. Neil, R. Peverall, G. A. D. Ritchie, M. Schnippering, and P. R. Unwin, *submitted to The Analyst* (2009).

[143] M. Schnippering, P. R. Unwin, J. Hult, T. Laurila, C. F. Kaminski, J. M. Langridge, R. L. Jones, M. Mazurenka, and S. R. Mackenzie, *Electrochemistry Communications*, **10**(12), 1827–1830 (2008).

[144] A. A. Ruth and K. T. Lynch, *Physical Chemistry Chemical Physics*, **10**(47), 7098–7108 (2008).

[145] M. J. Thorpe, K. D. Moll, R. J. Jones, B. Safdi, and J. Ye, *Science*, **311**(5767), 1595–1599 (2006).

[146] M. J. Thorpe, D. D. Hudson, K. D. Moll, J. Lasri, and J. Ye, *Optics Letters*, **32**(3), 307–309 (2007).

[147] M. J. Thorpe and J. Ye, *Applied Physics B*, **91**(3-4), 397–414 (2008).

[148] C. Gohle, B. Stein, A. Schlieeser, T. Udem, and T. W. Hänsch, *Physics Review Letters*, **99**(26), 263902 (2007).

[149] J. Mandon, G. Guelachvili, and N. Picqué, *Nature Photonics*, **3**, 99–102 (2009).

[150] K. Nakagawa, T. Katsuda, A.S. Shelkovnikov, M. de Labachelerie, and M. Ohtsu, *Optics Communications*, **107**(5-6), 369–372 (1994).

[151] L. Gianfrani, R. W. Fox, and L. Hollberg, *Journal of the Optical Society of America B*, **16**(12), 2247–2254 (1999).

[152] E. D. Black, *American Journal of Physics*, **69**(1), 79–87 (2001).

[153] R. W. P. Drever, J. L. Hall, F. V. Kowalski, J. Hough, G. M. Ford, A. J. Munley, and H. Ward, *Applied Physics B*, **31**(2), 97–105 (1983).

[154] B. A. Paldus, C. C. Harb, T. G. Spence, B. Wilke, J. Xie, J. S. Harris, and R. N. Zare, *Journal of Applied Physics*, **83**(8), 3991–3997 (1998).

[155] T. G. Spence, C. C. Harb, B. A. Paldus, R. N. Zare, B. Willke, and R. L. Byer, *Review of Scientific Instruments*, **71**(2), 347–353 (2000).

[156] J. Ye and J. L. Hall, *Physical Review A*, **61**(6), 061802 (2000).

[157] N. J. van Leeuwen, J. C. Diettrich, and A. C. Wilson, *Applied Optics*, **42**(18), 3670–3677 (2003).

[158] J. Morville, S. Kassi, M. Chenevier, and D. Romanini, *Applied Physics B*, **80**(8), 1027–1038 (2005).

[159] J. Morville *Injection des cavités optiques de haute finesse par laser à diode - Application à la CW-CRDS et à la détection de traces atmosphériques.* PhD thesis, L'Université Joseph Fourier - Grenoble I, (2001).

[160] V. Motto-Ros *Cavités de haute finesse pour la spectroscopie d'absorption haute sensibilité et haute précision: Application à l'étude de molécules d'intérêt atmosphérique* PhD thesis, L'Université Claude Bernard - Lyon I, (2005).

[161] L. S. Ma, J. Ye, P. Dubé, and J. L. Hall, *Journal of the Optical Society of America B*, **16**(12), 2255–2268 (1999).

[162] R. W. Fox, L. Gianfrani, and L. W. Hollberg In G. A. Lampropoulos and R. A. Lessard, Eds., *1998 International Conference on Applications of Photonic Technology III: Closing the Gap between Theory, Development, and Applications*, Vol. 3491(1), pages 794–798. SPIE, 1998.

[163] N. J. van Leeuwen and A. C. Wilson, *Journal of the Optical Society of America B*, **21**(10), 1713–1721 (2004).

[164] F. M. Schmidt, A. Foltynowicz, W. Ma, T. Lock, and O. Axner, *Optics Express*, **15**(17), 10822–10831 (2007).

[165] A. Foltynowicz, F. M. Schmidt, W. Ma, and O. Axner, *Applied Physics B*, **92**(3), 313–326 (2008).

[166] C.L. Bell, G. Hancock, R. Peverall, G.A.D. Ritchie, J. H. van Helden, and N. J. van Leeuwen, *Optics Express*, **17**(12), 9834–9839 (2009).

[167] S. G. Baran, G. Hancock, R. Peverall, G. A. D. Ritchie, and N. J. van Leeuwen, *Analyst*, **134**(2), 243–249 (2009).

[168] D. Romanini, M. Chenevier, S. Kassi, M. Schmidt, C. Valant, M. Ramonet, J. Lopez, and H.-J. Jost, *Applied Physics B*, **83**(4), 659–667 (2006).

[169] I. Courtillot, J. Morville, V. Motto-Ros, and D. Romanini, *Applied Physics B*, **85**(2-3), 407–412 (2006).

[170] E. R. T Kerstel, R. Q. Iannone, M. Chenevier, S. Kassi, H.-J. Jost, and D. Romanini, *Applied Physics B*, **85**(2), 397–406 (2006).

[171] R. Wehr, S. Kassi, D. Romanini, and L. Gianfrani, *Applied Physics B*, **92**(3), 459–465 (2008).

[172] V. Motto-Ros, M. Durand, and J. Morville, *Applied Physics B*, **91**(1), 203–211 (2008).

[173] V. Motto-Ros, J. Morville, and P. Rairoux, *Applied Physics B*, **87**(3), 531–538 (2007).

[174] T. J. A. Butler, J. L. Miller, and A. J. Orr-Ewing, *Journal of Chemical Physics*, **126**(17), 174302 (2007).

[175] M. D. Levenson, B. A. Paldus, T. G. Spence, C. C. Harb, J. S. Harris Jr., and R. N. Zare, *Chemical Physics Letters*, **290**(4-6), 335 – 340 (1998).

[176] J. Wieland, C. R. Mirasso, and D. Lenstra, *Optics Letters*, **22**(7), 469–471 (1997).

[177] A. M. Levine, G. H. M. van Tartwijk, D. Lenstra, and T. Erneux, *Physical Review A*, **52**(5), R3436–R3439 (1995).

[178] A. M. Levine, G. H. M. van Tartwijk, D. Lenstra, and T. Erneaux In *Summaries of Papers Presented at the Quantum Electronics and Laser Science Conference, 1996. QELS '96.*, pages 192–193, 1996.

[179] A. Ritter and H. Haug, *Journal of the Optical Society of America B*, **10**(1), 130–144 (1993).

[180] A Ritter and H. Haug, *Journal of the Optical Society of America B*, **10**(1), 145–154 (1993).

[181] G. H. M. van Tartwijk and D. Lenstra, *Quantum and Semiclassical Optics: Journal of the European Optical Society Part B*, **7**(2), 87–143 (1995).

[182] B. Dahmani, L. Hollberg, and R. Drullinger, *Optics Letters*, **12**(11), 876–878 (1987).

[183] S. Ohshima and H. Schnatz, *Journal of Applied Physics*, **71**(7), 3114–3117 (1992).

[184] W. Yang, A. Joshi, H. Wang, and M. Xiao, *Applied Optics*, **43**(29), 5547–5551 (2004).

[185] H. Patrick and C. E. Wieman, *Review of Scientific Instruments*, **62**(11), 2593–2595 (1991).

[186] H. Talvitie, A. Pietilainen, H. Ludvigsen, and E. Ikonen, *Review of Scientific Instruments*, **68**(1), 1–7 (1997).

[187] Z. D. Liu, D. Bloch, and M. Ducloy, *Applied Physics Letters*, **65**(3), 274–276 (1994).

[188] M. Kozuma, M. Kourogi, M. Ohtsu, and H. Hori, *Applied Physics Letters*, **61**(16), 1895–1897 (1992).

[189] A. L. Schawlow and C. H. Townes, *Physical Review*, **112**(6), 1940–1949 (1958).

[190] R. Paschotta, H. R. Telle, and U. Keller, *Noise of Solid State Lasers*, Solid-State Lasers and Applications (ed. A. Sennaroglu), CRC Press, 2007.

[191] H. M. Wiseman, *Physical Review A*, **60**(5), 4083–4093 (1999).

[192] C. Henry, *IEEE Journal of Quantum Electronics*, **18**(2), 259–264 (1982).

[193] C. H. Henry, R. A. Logan, and K. A. Bertness, *Journal of Applied Physics*, **52**(7), 4457–4461 (1981).

[194] J. Morville, D. Romanini, M. Chenevier, and A. Kachanov, *Applied Optics*, **41**(33), 6980–6990 (2002).

[195] J. M. Hollas, *High Resolution Spectroscopy*, Butterworths, 1982.

[196] G. Herzberg, *Molecular Spectra and Molecular Structure: II. Infrared and Raman Spectra of Polyatomic Molecules*, Van Nostrand Reinhold, 1945.

[197] A. Adel and D. M. Dennison, *Physical Review*, **43**(9), 716–723 (1933).

[198] D. M. Dennison, *Reviews of Modern Physics*, **12**(3), 175–214 (1940).

[199] E. Fermi, *Zeitschrift für Physik A*, **71**(3-4), 250–259 (1931).

[200] J. J. Olivero and R.L. Longbothum, *Journal of Quantitative Spectroscopy and Radiative Transfer*, **17**(2), 233–236 (1977).

[201] E. R. Crosson, K. N. Ricci, B. A. Richman, F. C. Chilese, T. G. Owano, R. A. Provencal, M. W. Todd, J. Glasser, A. A. Kachanov, B. A. Paldus, T. G. Spence, and R. N. Zare, *Analytical Chemistry*, **74**(9), 2003–2007 (2002).

[202] A. Hutchinson *Diode Laser Studies of Trace Species and their Reactions.* PhD thesis, University of Oxford, (2006).

[203] P. Bergamaschi, M. Schupp, and G. W. Harris, *Applied Optics*, **33**(33), 7704–7716 (1994).

[204] M. M. Baum, S. Kumar, A. M. Lappas, and P. D. Wagner, *Review of Scientific Instruments*, **74**(6), 3104–3110 (2003).

[205] D. E. Vogler and M. W. Sigrist, *Applied Physics B*, **85**(2-3), 349–354 (2006).

[206] S. A. Blankenship, R. W. Voight, J. A. Perkins, and J. E. Fried Jr., Process for selective hydrogenation of acetylene in an ethylene purification process US Patent No 6 509 292, 2001.

[207] M. Pradhan, R. E. Lindley, R. Grilli, I. R. White, D. Martin, and A. J. Orr-Ewing, *Applied Physics B*, **90**(1), 1–9 (2008).

[208] T. Y. Brooke, A. T. Tokunaga, H. A. Weaver, J. Crovisier, D. Bockelee-Morvan, and D. Crisp, *Nature*, **383**(6601), 606–608 (1996).

[209] R. P. Lucht, R. L. Farrow, and R. E. Palmer, *Combustion Science and Technology*, **45**(5), 261–274 (1986).

[210] B. A. Williams and J. W. Fleming, *Applied Physics B*, **75**(8), 883–890 (2002).

[211] H. Tai, K. Yamamoto, M. Uchida, S. Osawa, and K. Uehara, *Photonics Technology Letters, IEEE*, **4**(7), 804–807 (1992).

[212] D. B. Oh and D. C. Hovde, *Applied Optics*, **34**(30), 7002–7005 (1995).

[213] F. S. Pavone, F. Marin, M. Inguscio, K. Ernst, and G. Di Lonardo, *Applied Optics*, **32**(3), 259–262 (1993).

[214] M. De Rosa, A. Ciucci, D. Pelliccia, C. Gabbanini, S. Gozzini, and A. Lucchesini, *Optics Communications*, **147**(1-3), 55–60 (1998).

[215] W. Chen, G. Mouret, and D. Boucher, *Applied Physics B*, **67**(3), 375–378 (1998).

[216] G. Rusciano, G. Pesce, F. Pignatiello, and A. Sasso, *Optics Express*, **11**(23), 3010–3021 (2003).

[217] C. Hornberger, M. König, S. B. Rai, and W. Demtröder, *Chemical Physics*, **190**(2-3), 171–177 (1995).

[218] T. Ishiji and K. Takahashi, *Journal of Applied Electrochemistry*, **23**, 771–774 (1993).

[219] K. Nakagawa, M. de Labachelerie, Y. Awaji, and M. Kourogi, *Journal of the Optical Society of America B*, **13**(12), 2708–2714 (1996).

[220] R. Thapa, K. Knabe, M. Faheem, A. Naweed, O. L. Weaver, and K. L. Corwin, *Optics Letters*, **31**(16), 2489–2491 (2006).

[221] A. Onae, K. Okumura, Y. Miki, T. Kurosawa, E. Sakuma, J. Yoda, and K. Nakagawa, *Optics Communications*, **142**(1-3), 41–44 (1997).

[222] M. de Labachelerie, K. Nakagawa, and M. Ohtsu, *Optics Letters*, **19**(11), 840–842 (1994).

[223] C. S. Edwards, H. S. Margolis, G. P. Barwood, S. N. Lea, P. Gill, G. Huang, and W. R. C. Rowley, *Optics Letters*, **29**(6), 566–568 (2004).

[224] R. El Hachtouki and J. Vander Auwera, *Journal of Molecular Spectroscopy*, **216**(2), 355–362 (2002).

[225] J. Michael Hollas, *Modern Spectroscopy*, Wiley, 4 ed., 2004.

[226] J. M. Brown, J. T. Hougen, K. P. Huber, J. W. C. Johns, I. Kopp, H. Lefebvre-Brion, A. J. Merer, D. A. Ramsay, J. Rostas, and R. N. Zare, *Journal of Molecular Spectroscopy*, **55**(1-3), 500–503 (1975).

[227] P. W. Atkins and R. S. Friedman, *Molecular Quantum Mechanics*, Oxford University Press, 3rd ed., 1997.

[228] A. Thorne, U. Litzén, and S. Johansson, *Spectrophysics*, Springer-Verlag, 1999.

[229] M. Baranger, *Physical Review*, **112**(3), 855–865 (1958).

[230] D. H. Rank, D. P. Eastman, W. B. Birtley, and T. A. Wiggins, *Journal of Chemical Physics*, **33**(2), 327–328 (1960).

[231] P. Varanasi and B. R. P. Bangaru, *Journal of Quantitative Spectroscopy and Radiative Transfer*, **15**(3), 267–273 (1975).

[232] F. Thibault, D. Cappelletti, F. Pirani, G. Blanquet, and M. Bartolomei, *European Physical Journal D*, **44**(2), 337–344 (2007).

[233] M. Kusaba and J. Henningsen, *Journal of Molecular Spectroscopy*, **209**(2), 216–227 (2001).

[234] P. Minutolo, C. Corsi, F. D'Amato, and M. De Rosa, *European Physical Journal D*, **17**(2), 175–179 (2001).

[235] K. S. Bond, N. D. Collett, E. P. Fuller, J. L. Hardwick, E. E. Hinds, T. W. Keiber, I. S. G. Kelly-Morgan, C. M. Matthys, M. J. Pilkenton, K. W. Sinclair, and A. A. Taylor, *Applied Physics B*, **90**(2), 255–262 (2008).

[236] S. W. Arteaga, C. M. Bejger, J. L. Gerecke, J. L. Hardwick, Z. T. Martin, J. Mayo, E. A. McIlhattan, J. M. F. Moreau, M. J. Pilkenton, M. J. Polston, B. T. Robertson, and E. N. Wolf, *Journal of Molecular Spectroscopy*, **243**(2), 253 – 266 (2007).

[237] P. Soldan, E. P. F. Lee, and T. G. Wright, *Physical Chemistry Chemical Physics*, **3**(21), 4661–4666 (2001).

[238] M. Mazurenka, R. Wada, A. J. L. Shillings, T. J. A. Butler, J. M. Beames, and A. J. Orr-Ewing, *Applied Physics B*, **81**(1), 135–141 (2005).

[239] C. S. Parmenter and M. Seaver, *Journal of Chemical Physics*, **70**(12), 5458–5462 (1979).

[240] C. L. Bell, M. Dhib, G. Hancock, G. A. D. Ritchie, J. H. van Helden, and N. J. van Leeuwen, *Applied Physics B*, **94**(2), 327–336 (2009).

[241] D. Cappelletti, M. Bartolomei, E. Carmona-Novillo, F. Pirani, G. Blanquet, and F. Thibault, *Journal of Chemical Physics*, **126**(6), 064311 (2007).

[242] H.-M. Lin, M. Seaver, K. Y. Tang, Alan E. W. Knight, and C. S. Parmenter, *Journal of Chemical Physics*, **70**(12), 5442–5457 (1979).

[243] K. Shuler and C. E. Dykstra, *Journal of Physical Chemistry A*, **104**(19), 4562–4570 (2000).

[244] R. H. Dicke, *Physical Review*, **89**(2), 472–473 (1953).

[245] P. L. Varghese and R. K. Hanson, *Applied Optics*, **23**(14), 2376–2385 (1984).

[246] L. Galatry, *Physical Review*, **122**(4), 1218–1223 (1961).

[247] J. O. Hirschfelder, C. F. Curtiss, and R. B. Bird, *Molecular Theory of Gases and Liquids*, Wiley, New York, 1954.

[248] P. R. Bevington, *Data Reduction and Error Analysis for the Physical Sciences*, McGraw-Hill, 1969.

[249] C. Baird, *Environmental Chemistry, Ch. 3*, W. H. Freeman and Co, 1995.

[250] H. Fuchs, S. M. Ball, B. Bohn, T. Brauers, R. C. Cohen, H. P. Dorn, W. P. Dubé, J. L. Fry, R. Häseler, U. Heitmann, R. L. Jones, J. Kleffmann, T. F. Mentel, P. Müsgen, F. Rohrer, A. W. Rollins, A. A. Ruth, A. Kiendler-Scharr, E. Schlosser, A. J. L. Shillings, R. Tillmann, R. M. Varma, D. S. Venables, G. Villena Tapia, A. Wahner, R. Wegener, P. J. Wooldridge, and S. S. Brown, *Atmospheric Measurement Techniques Discussions*, **2**(5), 2539–2586 (2009).

[251] P.R. Hargreaves, J.U. Smith, S. Young, and K.W.T. Goulding, *Atmospheric Environment*, **39**(3), 409 – 417 (2005).

[252] A. Fontijn, A. J. Sabadell, and R. J. Ronco, *Analytical Chemistry*, **42**(6), 575–579 (2002).

[253] T. Okada, I. Karube, and S. Suzuki, *Biotechnology and Bioengineering*, **25**(6), 1641–1651 (2004).

[254] J. M. Sedlak and K. F. Blurton, *Talanta*, **23**(11-12), 811–814 (1976).

[255] J. M. Sedlak and K. F. Blurton, *Journal of the Electrochemical Society*, **123**(10), 1476–1478 (1976).

[256] K. F. Blurton and J. M. Sedlak, Method for the detection and measurement of noxious gases US Patent No 44 042 464, 1977.

[257] W. Weppner, *Sensors and Actuators*, **12**(2), 107–119 (1987).

[258] O. Ozden and T. Dogeroglu, *Environmental Monitoring and Assessment*, **142**(1-3), 243–253 (2008).

[259] S. I. Ohira, E. Wanigasekara, D. M. Rudkevich, and P. K. Dasgupta, *Talanta*, **77**(5), 1814 – 1820 (2009).

[260] T. Kida, A. Nishiyama, M. Yuasa, K. Shimanoe, and N. Yamazoe, *Sensors and Actuators B*, **135**(2), 568 – 574 (2009).

[261] J. Brunet, V. Parra Garcia, A. Pauly, C. Varenne, and B. Lauron, *Sensors and Actuators B*, **134**(2), 632 – 639 (2008).

[262] J. Tamaki, Z. Zhang, K. Fujimori, M. Akiyama, T. Harada, N. Miura, and N. Yamazoe, *Journal of the Electrochemical Society*, **141**(8), 2207–2210 (1994).

[263] S. K. Verma, M. K. Deb, and D. Verma, *Atmospheric Research*, **90**, 33–40 (2008).

[264] C. Dari-Salisburgo, P. Di Carlo, F. Giammaria, Y. Kajii, and A. D'Altorio, *Atmospheric Environment*, **43**(4), 970 – 977 (2009).

[265] F. Xu, Z. Lv, X. Lou, Y. Zhang, and Z. Zhang, *Applied Optics*, **47**(29), 5337–5340 (2008).

[266] T. Wu, W. Zhao, W. Chen, W. Zhang, and X. Gao, *Applied Physics B*, **94**(1), 85–94 (2009).

[267] V. L. Kasyutich, P. A. Martin, and R. J. Holdsworth, *Measurement Science and Technology*, **17**(4), 923–931 (2006).

[268] M. Triki, P. Cermak, G. Méjean, and D. Romanini, *Applied Physics B*, **91**(1), 195–201 (2008).

[269] R. M. Varma, D. S. Venables, S. Vaughan, J. Orphal, and A. A. Ruth, *Applied Optics*, **48**(4), B159–B171 (2009).

[270] T. Gherman, D. S. Venables, S. Vaughan, J. Orphal, and A. A. Ruth, *Environmental Science and Technology*, **42**(3), 890–895 (2008).

[271] A. Karpf and G. N. Rao, *Applied Optics*, **48**(2), 408–413 (2009).

[272] M. Pushkarsky, A. Tsekoun, I. G. Dunayevskiy, R. Go, and C. K. N. Patel, *Proceedings of the National Academy of Sciences of the United States of America*, **103**(29), 10846–10849 (2006).

[273] J. P. Lima, H. Vargas, A. Miklós, M. Angelmahr, and P. Hess, *Applied Physics B*, **85**(2-3), 279–284 (2006).

[274] A. Perrin, J. M. Flaud, A. Goldman, C. Camy-Peyret, W. J. Lafferty, P. Arcas, and C. P. Rinsland, *Journal of Quantitative Spectroscopy and Radiative Transfer*, **60**(5), 839 – 850 (1998).

[275] W. T. Raynes, *Journal of Chemical Physics*, **41**(10), 3020–3032 (1964).

[276] R. A. Toth and R. H. Hunt, *Journal of Molecular Spectroscopy*, **79**(1), 182 – 202 (1980).

[277] G. W. King, R. M. Hainer, and P. C. Cross, *The Journal of Chemical Physics*, **11**(1), 27–42 (1943).

[278] Y. Mine, N. Melander, D. Richter, D. G. Lancaster, K. P. Petrov, R. F. Curl, and F. K. Tittel, *Applied Physics B*, **65**(6), 771–774 (1997).

[279] K. P. Petrov, L. Goldberg, W. K. Burns, R. F. Curl, and F. K. Tittel, *Optics Letters*, **21**(1), 86–88 (1996).

[280] K. P. Petrov, S. Waltman, E. J. Dlugokencky, M. Arbore, M. M. Fejer, F. K. Tittel, and L. W. Hollberg, *Applied Physics B*, **64**(5), 567–572 (1997).

[281] D. G. Lancaster, D. Richter, R. F. Curl, and F. K. Tittel, *Applied Physics B*, **67**(3), 339–345 (1998).

[282] D. Richter, A. Fried, B. P. Wert, J. G. Walega, and F. K. Tittel, *Applied Physics B*, **75**(2-3), 281–288 (2002).

[283] H. Y. Clark, L. Corner, W. Denzer, G. Hancock, A. Hutchinson, M. Islam, R. Peverall, and G. A. D. Ritchie, *Chemical Physics Letters*, **399**(1-3), 102–108 (2004).

[284] P. Malara, P. Maddaloni, G. Gagliardi, and P. De Natale, *Optics Express*, **14**(3), 1304–1313 (2006).

[285] P. Weibring, D. Richter, J. G. Walega, and A. Fried, *Optics Express*, **15**(21), 13476–13495 (2007).

[286] L. Ciaffoni, R. Grilli, G. Hancock, A. J. Orr-Ewing, R. Peverall, and G. A. D. Ritchie, *Applied Physics B*, **94**(3), 517–525 (2009).

[287] R. W. Boyd, *Nonlinear Optics*, Academic Press, 2nd ed., 2003.

[288] D. S. Hum and M. M. Fejer, *Comptes Rendus Physique*, **8**(2), 180 – 198 (2007).

[289] M. M. Fejer, G. A. Magel, D. H. Jundt, and R. L. Byer, *IEEE Journal of Quantum Electronics*, **28**(11), 2631–2654 (1992).

[290] L. Goldberg, W. K. Burns, and R. W. McElhanon, *Optics Letters*, **20**(11), 1280–1282 (1995).

[291] D. G. Lancaster, D. Richter, and F. K. Tittel, *Applied Physics B*, **69**(5-6), 459–465 (1999).

[292] K. Fradkin-Kashi, A. Arie, P. Urenski, and G. Rosenman, *Opt. Lett.*, **25**(10), 743–745 (2000).

[293] T. Yanagawa, H. Kanbara, O. Tadanaga, M. Asobe, H. Suzuki, and J. Yumoto, *Applied Physics Letters*, **86**(16), 161106 (2005).

[294] P. M. Flaud and J. Orphal, *Infrared Physics & Technology*, **51**(4), 322 – 331 (2008).

[295] L.H. Deng, X.M. Gao, Z.S. Cao, W.D. Chen, Y.Q. Yuan, W.J. Zhang, and Z.B. Gong, *Optics Communications*, **268**(1), 110 – 114 (2006).

[296] M. M. J. W. van Herpen, S. E. Bisson, and F. J. M. Harren, *Optics Letters*, **28**(24), 2497–2499 (2003).

[297] V. L. Kasyutich, R. J. Holdsworth, and P. A. Martin, *Applied Physics B*, **92**(2), 271–279 (2008).

[298] P. Maddaloni, P. Malara, G. Gagliardi, and P. De Natale, *Applied Physics B*, **85**(2-3), 219–222 (2006).

[299] S. Stry, P. Hering, and M. Mürtz, *Applied Physics B*, **75**(2-3), 297–303 (2002).

[300] E. I. Moses and C. L. Tang, *Optics Letters*, **1**(4), 115–117 (1977).

[301] J. A. Silver, *Applied Optics*, **31**(6), 707–717 (1992).

[302] D. S. Bomse, A. C. Stanton, and J. A. Silver, *Applied Optics*, **31**(6), 718–731 (1992).

[303] J. M. Supplee, E. A. Whittaker, and W. Lenth, *Applied Optics*, **33**(27), 6294–6302 (1994).

[304] G. E. Hall and S. W. North, *Annual Review of Physical Chemistry*, **51**(1), 243–274 (2000).

[305] P. B. Davies, *Journal of Physical Chemistry*, **85**(18), 2599–2607 (1981).

[306] K. M. Evenson and M. Mizushima, *Physical Review A*, **6**(6), 2197–2204 (1972).

[307] M. Mizushima, K. M. Evenson, and J. S. Wells, *Physical Review A*, **5**(5), 2276–2287 (1972).

[308] R. F. Curl Jr., K. M. Evenson, and J. S. Wells, *Journal of Chemical Physics*, **56**(10), 5143–5151 (1972).

[309] G. Duxbury, *International Reviews in Physical Chemistry*, **4**(3), 237–278 (1985).

[310] R. N. Hager Jr. and R. C. Anderson, *Journal of the Optical Society of America*, **60**(11), 1444–1449 (1970).

[311] R. C. Anderson and R. N. Hager Jr., *Journal of the Optical Society of America*, **61**(9), 1269–1270 (1971).

[312] G. Bonfiglioli and J. Trench, *Optics Communications*, **10**(2), 207 – 210 (1974).

[313] G. C. Bjorklund, *Optics Letters*, **5**(1), 15 (1980).

[314] A. Schenzle, R. G. DeVoe, and R. G. Brewer, *Physical Review A*, **25**(5), 2606–2621 (1982).

[315] M. Gehrtz, G. C. Bjorklund, and E. A. Whittaker, *Journal of the Optical Society of America B*, **2**(9), 1510–1526 (1985).

[316] J. Reid, M. El-Sherbiny, B. K. Garside, and E. A. Ballik, *Applied Optics*, **19**(19), 3349–3353 (1980).

[317] Blu ray Disc Founders, Blu-ray disc format: White paper, 2004, `http://www.blu-raydisc.com/en/Technical/TechnicalWhitePapers/General.html` [cited August 2009].

[318] Risk, Gosnell, and Nurmikko, *Compact Blue-Green Lasers*, Cambridge University Press, 1st ed., 2003.

[319] I. R. MacDonald, J. S. Chu, F. F. Reilly II, M. Blincow, and D. Olivier In *OCEANS '95. MTS/IEEE. Challenges of Our Changing Global Environment. Conference Proceedings.*, Vol. 1, pages 555–565, 1995.

[320] S. Nakamura, T. Mukai, and M. Senoh, *Applied Physics Letters*, **64**(13), 1687–1689 (1994).

[321] E. Wiesendanger, *Ferroelectrics*, **1**(1), 141–148 (1970).

[322] E. Wiesendanger, *Ferroelectrics*, **6**(1), 263–281 (1974).

[323] B. Zysset, I. Biaggio, and P. Günter, *Journal of the Optical Society of America B*, **9**(3), 380–386 (1992).

[324] D. H. Jundt, P. Günter, and B. Zysset, *Nonlinear Optics*, **4**, 341–345 (1993).

[325] I. Biaggio, P. Kerkoc, L. S. Wu, Peter Günter, and Beat Zysset, *Journal of the Optical Society of America B*, **9**(4), 507–517 (1992).

[326] G. D. Boyd and D. A. Kleinman, *Journal of Applied Physics*, **39**(8), 3597–3639 (1968).

[327] O. Svelto and R. Polloni, *IEEE Journal of Quantum Electronics*, **4**(9), 528–530 (1968).

[328] R. G. Smith, *IEEE Journal of Quantum Electronics*, **6**(4), 215–223 (1970).

[329] G. J. Dixon, C. E. Tanner, and C. E. Wieman, *Optics Letters*, **14**(14), 731–733 (1989).

[330] A. Hemmerich, D. H. McIntyre, C. Zimmermann, and T. W. Hänsch, *Optics Letters*, **15**(7), 372–374 (1990).

[331] T. Senoh, Y. Fujino, Y. Tanabe, M. Hirano, M. Ohtsu, and K. Nakagawa, *Applied Physics Letters*, **60**(10), 1172–1174 (1992).

[332] C. Zimmermann, T. W. Hansch, R. Byer, S. O'Brien, and D. Welch, *Applied Physics Letters*, **61**(23), 2741–2743 (1992).

[333] L. Goldberg and M. K. Chun, *Applied Physics Letters*, **55**(3), 218–220 (1989).

[334] J. S. Gibb *Diode Laser Studies of Atmospherically Important Specie Diode Laser Studies of Atmospherically Important Specie Diode Laser Studies of Atmospherically Important Species* PhD thesis, University of Oxford, (2004).

[335] B. L. Fawcett, A. M. Parkes, D. E. Shallcross, and A. J. Orr-Ewing, *Physical Chemistry Chemical Physics*, **4**(24), 5960–5965 (2002).

[336] A. J. Orr-Ewing University of Bristol Graduate Lectures, (2003).

[337] P. Horowitz and W. Hill, *The Art of Electronics*, Cambridge University Press, 2nd ed., 1989.